GaN BASED HETEROSTRUCTURE GROWTH AND APPLICATION TO ELECTRONIC DEVICES AND GAS SENSORS

by

Eunjung Cho

A dissertation submitted in partial fulfillment
of the requirements for the degree of
Doctor of Philosophy
(Electrical Engineering)
in The University of Michigan
2009

Doctoral Committee:

Professor Dimitris Pavlidis, Co-Chair
Professor Khalil Najafi, Co-Chair
Professor Jerzy Kanicki
Professor Johannes W. Schwank

To my mother

ACKNOWLEDGEMENTS

I would like to thank Professor Dimitris Pavlidis for his guidance and support during the course of this work. His initiative and help are greatly appreciated. I am also grateful to my committee members, Professor Khalil Najafi, Professor Jerzy Kanicki and Professor Johannes W. Schwank for their suggestions.

I would like to acknowledge Dr. Seth Hubbard and Dr. G. Zhao for their advice and guidance on material growth and MOVPE system operation, as well as, the soon to be Dr. Sanghyun Seo. His support by fabricating devices from the grown materials and discussion about nitride processing are appreciated.

I would like to acknowledge the support from the members of my working group, Dr. Oktay Yilmazoglu, Jens Biethan, Laurence Considine, and Karin Boye. I am also grateful to Andreas Semrad and Peter Kiesslich for their engagement in solving technical problems in the MOVPE laboratory.

I would like to thank Dr. Stefan Flege and Dr. Ganhua Fu for SIMS and XPS measurements, as well as Euginio Siellero for his contribution to the analysis of the mechanical behavior of GaN/air gap based Fabry-Pérot filters (FPFs).

I also wish to thank Beth Stalnaker for administrative assistance. I am also grateful to close friends for their kind advices and help.

Last but not least, I would like to thank my family for their devoted love, endless support and encouragement to make this Ph.D completed. Specially, I am grateful to my husband Felix who always stands with me.

TABLE OF CONTENTS

LIST OF FIGURES

Figure

LIST OF TABLES

Table

LIST OF APPENDICES

Appendix

CHAPTER I

INTRODUCTION

Group III-Nitrides are important materials that can satisfy optical and electrical requirements which are not compatible with Si and traditional III-V materials properties. The direct bandgap of III-Nitrides and energy extending over a wide range of values (0.7$\sim$ 6.2eV) make them usable as very versatile light emitting sources as shown in Fig. 1.1. Beginning with blue light emitting diodes (LEDs) in the 1990s, the replacement of the incandescent light market with white LEDs has been ongoing and it is expected to save energy worth a 100 billion dollar annually. Other optical applications are data storage devices, laser diodes (LDs) and ultra violet (UV) LEDs for the detection of bio particles, air and water purification, medical treatment and missile warning systems.

Nitride alloys are also suitable for high power and high frequency applications. The high breakdown voltage of these materials makes them ideal for high power applications and their high saturation velocity is for high speed device operation. Figure 1.2 shows the position of GaN devices in terms of frequency and power performance in comparison with Si and traditional III-V materials. Applications include power amplifiers for wireless base stations, low noise amplifiers and high power switches.

Sensing devices are another important application of nitride materials espe-

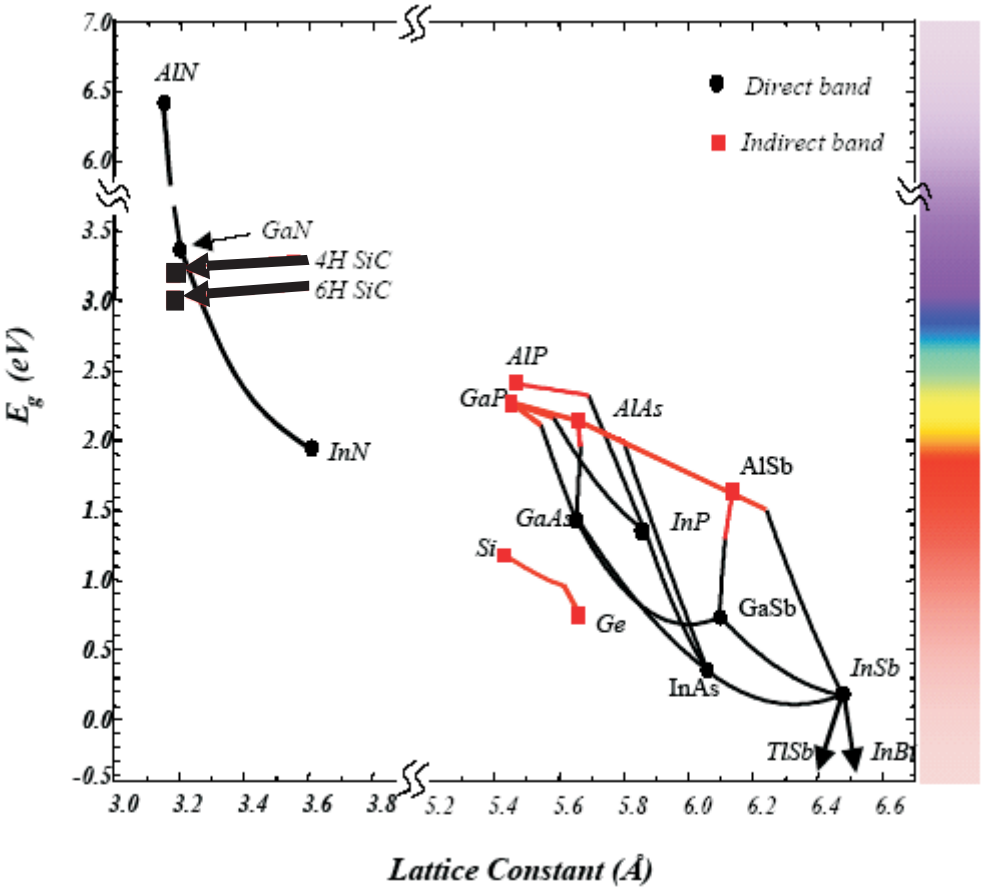

Figure 1.1: Energy bandgap and lattice constant of nitride materials. Recently the bandgap energy of InN is reported as 0.7eV.

cially for harsh environments as these materials are thermally and chemically stable. They also exhibit less intrinsic leakage and are capable of operating at high temperatures due to the larger bandgap and stronger bond energy. Furthermore, the possibility of sensor integration with nitride-based high power electronic devices is a clear advantage over oxide sensors.

III-Nitride device and growth technologies became mature since the birth of blue LEDs. However, there are still many problems that need to be addressed. This thesis is devoted to improving III-Nitride heterostructure materials and devices for electronic device and gas sensor applications. The approaches used for this

purpose include tailoring materials by optimization of material growth parameters, characterization of devices and materials and designing of novel structures through understanding of the material and device dependence.

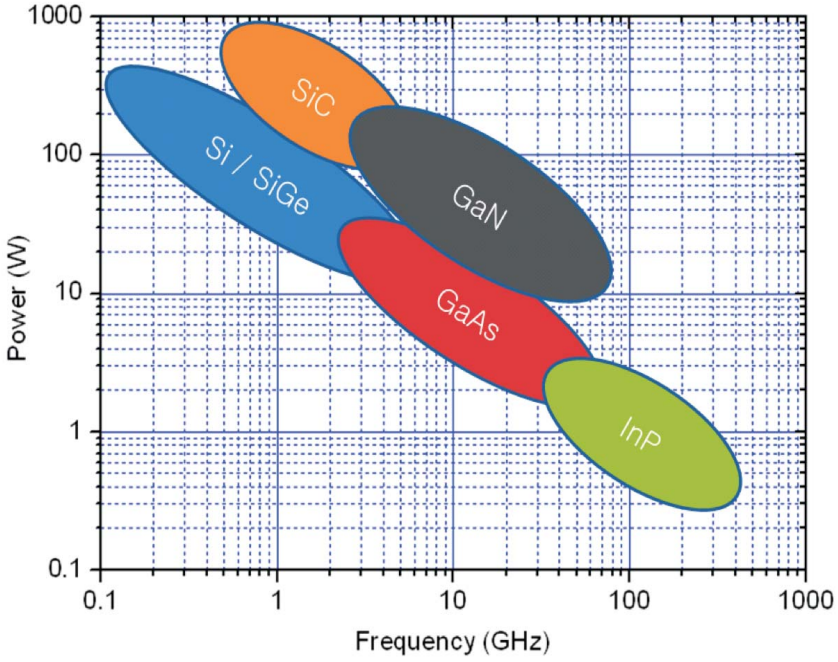

Figure 1.2: Frequency vs. power.

1.1 History of GaN growth

The first Gallium Nitride (GaN) material was produced by passing ammonia over hot gallium by Jusa and Hahn, in 1938. Small needles and platelets of GaN were synthesized from this process. After three decades, large area GaN was grown by hydride vapor phase epitaxy (HVPE) directly on sapphire by Maruska and Tietjen in 1969 [1]. Unfortunately, this GaN layer showed large n-type background doping and poor crystallinity due to heteroepitaxial growth on a non-native substrate.

In 1983, Yoshida employed an AlN intermediate layer and demonstrated that the cathodoluminescence efficiency of the overlaying GaN was improved [2]. Later this idea was developed further by Akasaki and Nakamura with a thin AlN nucleation

layer [3] or GaN nucleation layer [4] grown at low temperatures (500$\sim$ 750 °C) prior to the growth of high temperature bulk GaN. In this growth technique called a two step growth, a low temperature nucleation layer promotes the GaN growth mode from 3 dimensional islands to 2 dimensional growth mode and leads to a flat and smooth surface of the heteroepitaxially grown bulk GaN.

The success in p-type doping is another breakthrough in the history of GaN growth. As p-dopants, group II elements (Zn, Cd, Mg or Be) were used but the doped layers turned out to be very resistive. Amano and Akasaki observed that highly resistive Mg doped GaN became brighter during cathodoluminescence (CL) scanning. A further photoluminescence study revealed that low energy electron beam irradiation (LEEBI) converted an Mg-doped GaN layer to a p-type doped conductive layer [5]. A complex of Mg and hydrogen atoms produced during the growth is attributed to the impeding of p-dopant activation [6]. Releasing hydrogen atoms by either annealing above 750 °C (in vacuum or N_2 environment) or electron beam irradiation enables the realization of p-type conducting layers [7, 8]. However, only 1$\sim$ 5 % of the Mg atoms are expected to be ionized at room temperature even after a post annealing process due to its high activation energy (160 meV). Therefore, highly efficient p-type doping in GaN still remains a problem.

High-brightness blue LEDs with a brightness of over 1 cd were demonstrated by Nakamura in 1994 owing to the significant progress in nitride material growth and fabrication technology [9]. Nevertheless, the high density of threading dislocations (TDs) remained detrimental to the light emitting efficiency of laser diodes. In order to reduce the TD density ($1 \sim 10 \cdot 10^{10}\,\mathrm{cm}^{-2}$), various growth techniques were investigated. Among them, lateral epitaxial overgrowth (LEO) reduced the TD density down to mid of $10^6\,\mathrm{cm}^{-2}$ and laser diodes became commercially available with

a life time of 10,000 hours at the end of 1997 [10]. The efforts continue in order to accomplish high efficiency and long life time blue and UV violet LDs by means of producing GaN substrates or very thick GaN grown by HVPE.

1.2 MOVPE growth system

Metal organic vapor phase epitaxy growth (MOVPE) is a principal growth technique for III-Nitrides. It is distinguished from Molecular Beam Epitaxy (MBE) from the perspective of source materials, growth mechanism and growth pressure.

In MBE growth, the source materials are supplied as a beam of gas by heating high purity elements. The growth temperature is usually lower than MOVPE growth ($500 \sim 750\,^{\circ}\mathrm{C}$). Since the atoms of the necessary materials are delivered onto a substrate as a beam of gas, the MBE technique needs growth pressures as low as 10^{-10} torr for the efficient delivery of the atoms. Atoms react on a substrate surface and layers grow two dimensionally. A plasma is often used for supplying atomic source of nitrogen as ammonia cracking efficiency is quite low at the temperatures used. The possibility to control the interface on mono layer level is a great advantage of this growth technique.

In MOVPE growth, metal organics (TMGa, TMIn, TMAl) are used for group III (alkyl) source and ammonia is used as a group V (hydride) source. They are transported to a heated substrate by carrier gases (hydrogen and/or nitrogen) and gas phase reactions occur. Since MOVPE does not require ultra high vacuum (UHV), higher up-times are possible so that it can become a mass production tool to produce layers for solid state lighting and solar cell applications.

With MOVPE, GaN growth temperatures are usually above $1000\,^{\circ}\mathrm{C}$ due to the low cracking efficiency of ammonia. The substrate is heated by means of Radio Fre-

quency (RF), resistive or infrared lamp heating. Since thermal convection becomes serious at such high temperatures, appropriate reactor design is substantial to suppress gas turbulence and maintain laminar flow on the substrate. The consequence of improper reactor design is poor material uniformity and instability of growth. In order to address this problem, various type of reactors have been developed: the vertical type with high speed rotation (>1500 rpm), close space vertical rotating disc type, pancake (or planetary) type, barrel type, and horizontal type. In general, they are categorized based on the direction of the gas injection to the substrate surface (parallel or vertical), the rotation speed of the substrate, the space between gas injection and substrate. The benefits of each approach are as follows: The boundary layer is thin and uniform in a vertical reactor with high rotating speed. A close space reactor is good for operation under atmospheric growth condition because the small distance between gas entry and susceptor eliminates free convection. The planetary reactor type can operate under atmospheric condition and is capable of growing large volumes of wafers. A detailed review of reactor designs can be found in Ref. [11] and Ref. [12].

1.3 Crystal structure of nitrides

The common crystal structure of group III-Nitrides is wurtzite. Although the rock-salt or zinc-blende structure is possible depending on growth conditions and the type of substrates, the wurtzite form $P6_3mc$ (C_{6v}^4) is thermodynamically stable in ambient environment. The rock-salt structure is a structure transformed from wurtzite at high external pressure. The zinc-blende structure is metastable and may be stabilized by epitaxial growth on Si, GaAs, MgO and 3H SiC. Progress was made in improving the material quality of zinc-blende nitrides. Nevertheless, there are still

fundamental problems to be addressed such as rough substrate-epilayer interface, high density of planar defects, tendency of phase transformation into the wurtzite and poor optical quality. The work presented in this thesis focuses on the wurtzite nitrides exclusively.

Figure 1.3 illustrates the wurtzite structure. In this figure, the Ga atoms are represented by large black beads while the N atoms are represented by small white beads. The wurtzite lattice is characterized by two parameters: the edge length of the basal hexagon (a) and the height of the hexagonal lattice cell (c). The growth surfaces of GaN grown on c-plane sapphire substrates are depicted in Fig. 1.4. The growth surface is terminated by either Ga atoms or N atoms depending on the growth conditions. The Gallium terminated surface is termed Ga-face (or A face) and the nitrogen terminated surface is called the N-face (or B face). In MOVPE growth, the GaN surface is normally terminated by Ga atoms. In contrast, GaN grown with MBE can have either Ga-face or N-face controlling with nucleation layer or growth conditions. For the Ga-face, N has three dangling bonds but it has only one dangling bond in case of the N-face GaN [13]. Therefore, the face type can have profound effects on etching and impurity incorporation. Since all III-Nitride layer types (GaN, AlGaN, InGaN etc.) presented in this work are grown with MOVPE, the layers have Ga-face.

1.4 Substrates for nitrides

The challenge of nidride material growth lies in the heteroepitaxial growth. Since the melting condition for GaN requires high nitrogen partial pressure (45,000 Atm) and high temperature (about 2500 °C) [14], preparation of native GaN substrates is extremely difficult in comparison to Si and GaAs. To date, GaN native

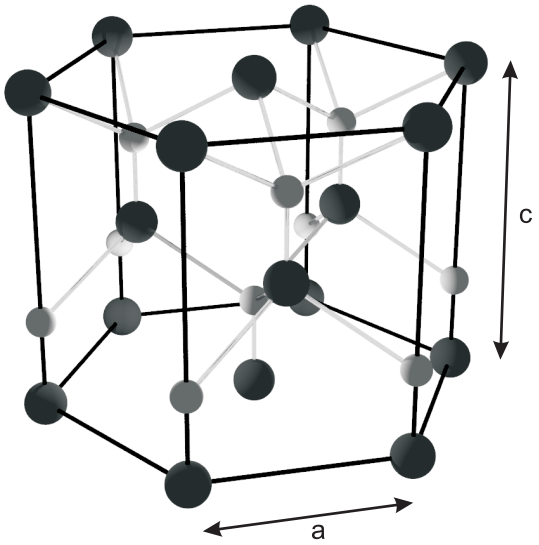

Figure 1.3: A unit cell of wurtzite GaN.

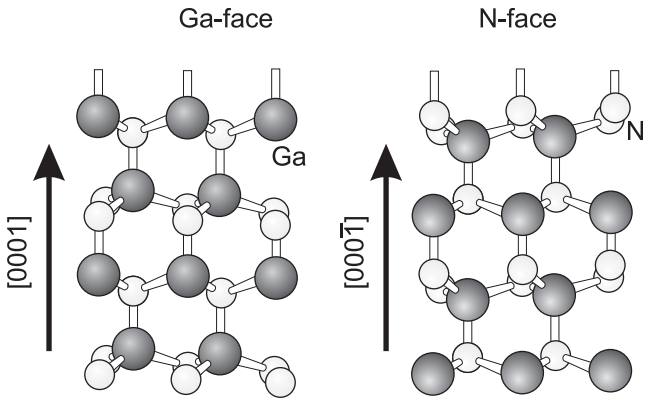

Figure 1.4: Atomic arrangement in Ga-face and N-face GaN.

substrates are available only in small sizes and their quality is still poor. Although free standing 2" GaN grown by HVPE with a TD density below $10^7\,\mathrm{cm}^{-2}$ is commercially available now, its price is between $1,500 and $6,000 per wafer depending on quality [15]. Therefore, the use of non-native substrates is still inevitable.

There is significant disparity of the thermal expansion coefficient and the lattice constant between nitride layers and substrates as shown in Table 1.1. This causes crystalline defects in the GaN layer in the form of threading dislocations, stacking faults and the electrical and optical performance of nitride devices will be degraded

accordingly.

Material	GaN	AlN	InN	6H-SiC	Si	Sapphire
Symmetry	Wurtzite	Wurtzite	Wurtzite	Wurtzite	Diamond	Hexagonal
Native Substrate	No	No	No	Yes	Yes	-
a (Å)	3.189	3.112	3.548	3.081	5.431	4.758
c (Å)	5.185	4.982	5.76	15.117	-	12.99
Lattice Mismatch with GaN (%)	0	2.48	-10.12	3.51	-16.96	13.9
α_a ($10^{-6}\cdot$ K^{-1})	5.59	4.2	5.7	4.2	3.9	6.7
α_c ($10^{-6}\cdot$ K^{-1})	3.17	5.3	3.7	4.68	8.5	-
Thermal Conductivity at 300K (W/cmK)	1.3	2.0	0.8	4.9	1.3	0.3
Melting point T_M °C	2500	3000	1100	2830	1412	2040

Table 1.1: Material properties of III-Nitrides, other semiconductor materials and sapphire.

The lattice mismatch of a semiconductor film with GaN is given by:

$$\Delta a(\%) = \frac{a_{GaN} - a_{film}}{a_{film}} \cdot 100 \tag{1.1}$$

Here, a_{film} is the in-plane lattice constant of the film. Although Eq. 1.1 shows that the lattice mismatch between GaN and sapphire is 33 %, the actual mismatch is 14 % because GaN basal plane rotates by 30 ° with respect to the c-plane of sapphire during the growth [16].

The choice of substrates can be determined by the targeted application. For high power devices, SiC will be the best candidate because of its good thermal conductivity. Besides, its better thermal and lattice match with GaN is an advantage over Si or sapphire. Nevertheless, the resulting structural defects are comparable to those obtained by growth on sapphire substrates in spite of all the advantages. Its inapplicability to UV devices and its relatively high price (>$1000 per wafer) impede its general use. Therefore, sapphire remains the common non-native substrate because of the relatively low price (about $50 per wafer), the mature manufacturing

technology and stability at high temperatures. Although Si has not been considered as a main substrate for III-Nitrides due to its large lattice mismatch with GaN, the significant quality improvement of GaN grown on Si spurred its use recently.

1.5 Electronic properties of nitrides

Table 1.2 lists the electronic properties of III-Nitrides and other semiconductors. The electron mobility for high quality unintentionally doped (UID) wurtzite bulk GaN ranges from $300 \sim 400\,\mathrm{cm}^2/\mathrm{Vs}$. The highest reported mobility for MOVPE grown GaN was $900\,\mathrm{cm}^2/\mathrm{Vs}$ [17] and $1245\,\mathrm{cm}^2/\mathrm{Vs}$ for free standing bulk GaN [18]. The maximum phonon limited mobility of GaN is predicted to be about $1350\,\mathrm{cm}^2/\mathrm{Vs}$ for electrons and $200\,\mathrm{cm}^2/\mathrm{Vs}$ for holes at 300 K. However, defects created from the heteroepitaxial growth hinder the achievement of such high values.

The breakdown field of nitride materials is one order of magnitude larger than that of Si and conventional III-V materials as shown in Table 1.2. Hence, Nitrides are promising for high power device applications. Moreover, their large bandgap allows one to obtain higher output power P_{max} ($\propto E_g^4$).

The current state-of-the-art power density of AlGaN/GaN heterostructure field effect transistors (HFETs) is about 32.2 W/mm at 4 GHz [19] and 10.5 W/mm at 40 GHz with a drain bias of 30 V [20]. In contrast, the maximum power density of GaAs is 1 W/mm. However, there are still some obstacles for the commercialization of such devices. Long term reliability, leakage current at shorter gate lengths, cost and maturity of substrates, fabrication processes and thermal management have to be resolved for mm-wave applications. A good review about the progress in III-Nitride based electronic devices can be found in Ref. [20].

Parameter	GaN	AlN	InN	6H-SiC	Si	GaAs
m_e^*	0.22	0.33	0.11	0.45	0.98	0.067
m_h^*	0.8	-	-	1.2	0.49	0.45
μ_e (cm^2/Vs)	$300 \sim 1000$	135	$1000 \sim 1900^*$	-	1350	8500
μ_h (cm^2/Vs)	200 *	14	-	50	450	330
v_s (x10^7cm/s)	2.5	1.4	2.5	2	1	2
Breakdown field (MV/cm)	5	4-12	5	3-5	0.3	0.4

* : theoretical values

Table 1.2: Electronic properties of nitrides and other semiconductor materials.

1.6 Polarization fields in III-Nitrides

Spontaneous polarization (P_{SP}) and piezoelectric polarization (P_{PE}) are very important features in nitride heterostructures. Due to P_{SP} and P_{PE}, a large amount of electrons can be created at the interface of nitride heterostructures even without intentional doping. Since the high electric field induced by the polarization confines the electrons two dimensionally, these electrons are referred to as a two dimensional electron gas (2DEG) or sheet charges. The advantage of this 2DEG is the remarkably high mobility compared to electron carriers produced by intentional doping in bulk nitride materials because the electron transport properties do not suffer from Coulomb scattering. In addition, a strong sensitivity to surface states of the 2DEG extends the application of nitride heterostructure devices to gas sensors and bio sensors.

1.6.1 Spontaneous polarization

Spontaneous polarization (P_{SP}) refers to the built-in polarization field caused by the lack of inversion symmetry of the crystal and the characteristics of the ionic bonds between Ga and N atoms. Due to the displacement of electron charge clouds towards one of the atoms, a net positive charge is present on one face of the crystal and a net negative charge on the other face as shown in Fig.1.5.

In III-Nitrides, asymmetry of inversion is present only along the c-axis. Hence, P_{SP} is parallel to this direction and c-plane nitrides are therefore called polar nitride materials. In contrast, m-plane $(1\bar{1}00)$ and a-plane $(11\bar{2}0)$ nitride materials are non-polar materials as they have inversion symmetry and equal numbers of Ga and N atoms are present in the planes.

P_{SP} is defined as a vector pointing from a metal cation toward a nitrogen atom. Thus, its direction depends on the growth face: P_{SP} points in the $[000\bar{1}]$ direction in case of Ga-face nitrides while it is parallel with [0001] in case of N-face nitrides.

Spontaneous polarization is screened by charges adsorbed to the surface of the material, as well as screened by free charges in the bulk. Therefore, it is assumed to be uniform or zero in a bulk. It is worth noting that if the interfaces are not atomically sharp and exhibit a certain degree of interdiffusion, the differences in spontaneous polarization would be reduced. Furthermore, if domains with inverted polarity exist, the overall polarization may be compensated.

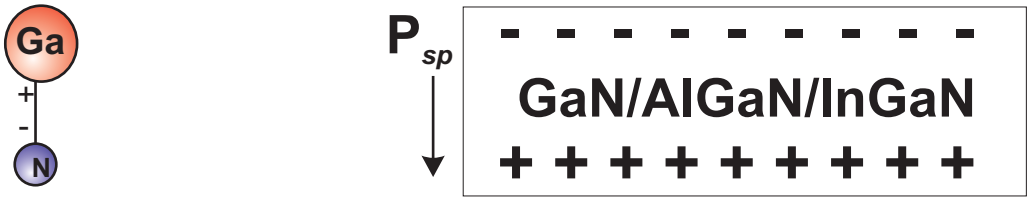

Figure 1.5: Ionic bond between Ga and N (left). Spontaneous polarization (P_{SP}) and sheet charges in nitrides with a Ga-face grown on c-plane sapphire (right).

1.6.2 Piezoelectric polarization

The nature of piezoelectric polarization P_{PE} is attributed to the strain caused by pseudomorphical growth between two lattice mismatched layers while spontaneous polarization is an inherent characteristic associated with crystal structures. When a layer is grown on a lattice mismatched substrate or layer, the top layer tries to fit its

in-plane lattice constant to the lattice constant of the layer underneath. This is called pseudomorphical growth. During this process, strain and stress will be developed in the top layer. Figure 1.6 depicts the compressive strain in InN and tensile strain in AlN when they are pseudomorphically grown on relaxed GaN.

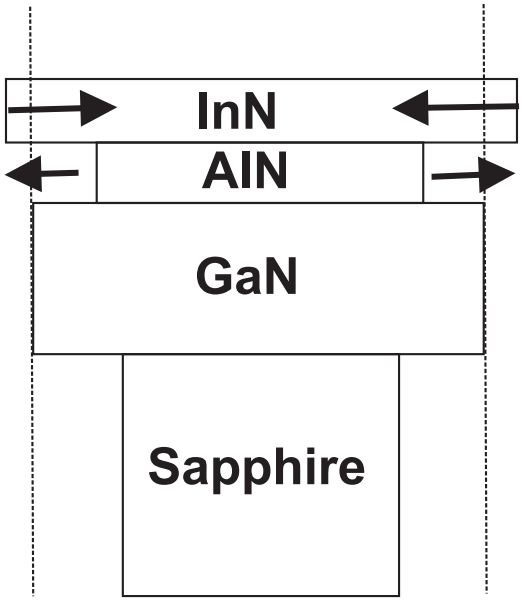

Figure 1.6: Strained AlN and InN grown on relaxed GaN. After Ref. [21].

However, pseudomorphical growth is only possible as long as the layer can accommodate the stress from the lattice mismatch. As the thickness of deposited layer increases, the stress in the layer also increases. Therefore, the layer will try to reduce the accumulated stress energy and finally grow with its original lattice constant. This process is termed relaxation. The relaxation may occur by the generation of dislocations, by delamination, cracking or a combination of some of them. When the layer is relaxed, P_{PE} becomes zero.

When biaxial stress is assumed in wurtzite nitrides, P_{PE} is given by:

$$P_{PE} = 2\frac{a - a_0}{a_0}\left(e_{31} - e_{33}\frac{C_{13}}{C_{33}}\right) \tag{1.2}$$

Here, a and a_0 represent the strained and the relaxed in-plane lattice constant of

the layer, respectively. e_{31} and e_{33} are the piezoelectric tensor components, C_{13} and C_{33} are elastic constants complying to Hooks law. The derivation of Eq. 1.2 can be found in Appendix A. From Eq. 1.2, the direction of P_{PE} will be dependent on the sign of $\Delta a = a - a_0$. P_{PE} will point in [0001] under tensile strain ($\Delta a > 0$). Otherwise it will point in the opposite direction when compressive strain ($\Delta a < 0$) is effective. In contrast, the direction of P_{SP} is independent of the sign of the strain.

1.6.3 Polarization induced charges

An electrostatic field is present in III-Nitrides due to the aforementioned polarization fields. In this section, the calculation of this field and its effects are presented as applied to AlGaN/GaN heterostructures which are the prime materials of interest in the thesis.

First of all, P_{PE} and P_{SP} of AlGaN with a Al composition x can be estimated by

$$P_{PE}^{AlGaN} = xP_{PE}^{AlN} + (1-x)P_{PE}^{GaN} + bx(1-x) \tag{1.3}$$

$$P_{SP}^{AlGaN} = xP_{SP}^{AlN} + (1-x)P_{SP}^{GaN} + bx(1-x) \tag{1.4}$$

The first two terms are given by linear interpolation between the values of GaN and AlN corresponding to Vegard's law. The last term is a nonlinear term and b is the bowing parameter. In favor of simplification, however, only linear terms are considered here. The relevant parameters such as lattice constants, P_{SP}, the piezoelectric tensor components, elastic constants are summarized in Table 1.1 and Table 1.3.

Therefore, P_{PE}^{AlGaN} and P_{SP}^{AlGaN} can be given by:

$$P_{PE}^{AlGaN} = 2\frac{a_{AlGaN} - a_{GaN}}{a_{AlGaN}}\left(-1.6 + 0.5x - (3.1 - 2.3x)\frac{390 - 6x}{398 - 21x}\right) \tag{1.5}$$

$$P_{SP}^{AlGaN} = (-0.056x - 0.034)Cm^{-2} \tag{1.6}$$

	GaN	AlN	InN
P_{SP}[1] (Cm^{-2})	-0.034	-0.090	-0.042
e_{31}[2] (pmV)	-1.6	-2.1	-3.5
e_{33}[2] (pmV)	3.1	5.4	7.6
C_{11}[2] (GPa)	390	396	223
C_{13}[2] (GPa)	398	373	224

[1] : in Ref. [13, 22]
[2] : theoretical values
[3] : theoretical values

Table 1.3: Spontaneous polarization of wurtzite III-Nitrides and polarization coefficients.

Since GaN is assumed to be relaxed on sapphire substrates, only spontaneous polarization is present in GaN while the total polarization field in AlGaN is the sum of P_{PE} and P_{SP}. At the interface between AlGaN and GaN, the disparity of the polarization field produces net charges given by

$$\pm\sigma = P_{Total}^{AlGaN} - P_{SP}^{GaN} \tag{1.7}$$

Accordingly, the sheet charge density is described by

$$n_s = \frac{\sigma}{e} \tag{1.8}$$

As illustrated in Fig. 1.7, the net positive charge is present at the bottom of the AlGaN surface due to the difference of the two polarization fields. In order to satisfy charge neutral condition, the positive charges must be compensated by electrons at the top of the GaN surface. These electrons form a Two Dimensional Electron Gas (2DEG) also called sheet charges which are confined in a potential well. The corresponding depth of the potential well is associated with the difference of electron affinity between the two layers.

Figure 1.8 depicts P_{PE} and P_{SP} existing in relaxed GaN, strained AlGaN and InGaN on the relaxed GaN. GaN and InN have similar P_{SP} values, but P_{SP} in

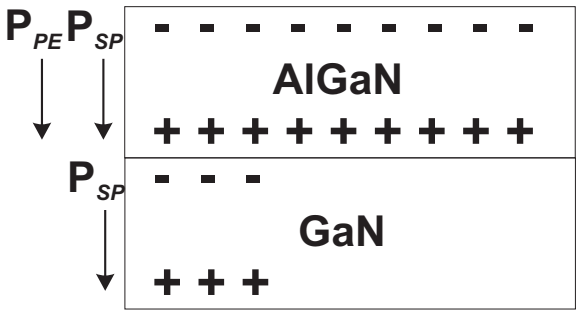

Figure 1.7: Polarization fields in AlGaN/GaN heterostructures.

AlN is two times larger than in GaN. Therefore both P_{SP} and P_{PE} are important in AlGaN/GaN heterostructures while P_{PE} contributes to the 2DEG dominantly in InGaN/GaN heterostructures. Besides, two dimensional holes will be formed instead of a 2DEG due to a net negative charge at the interface.

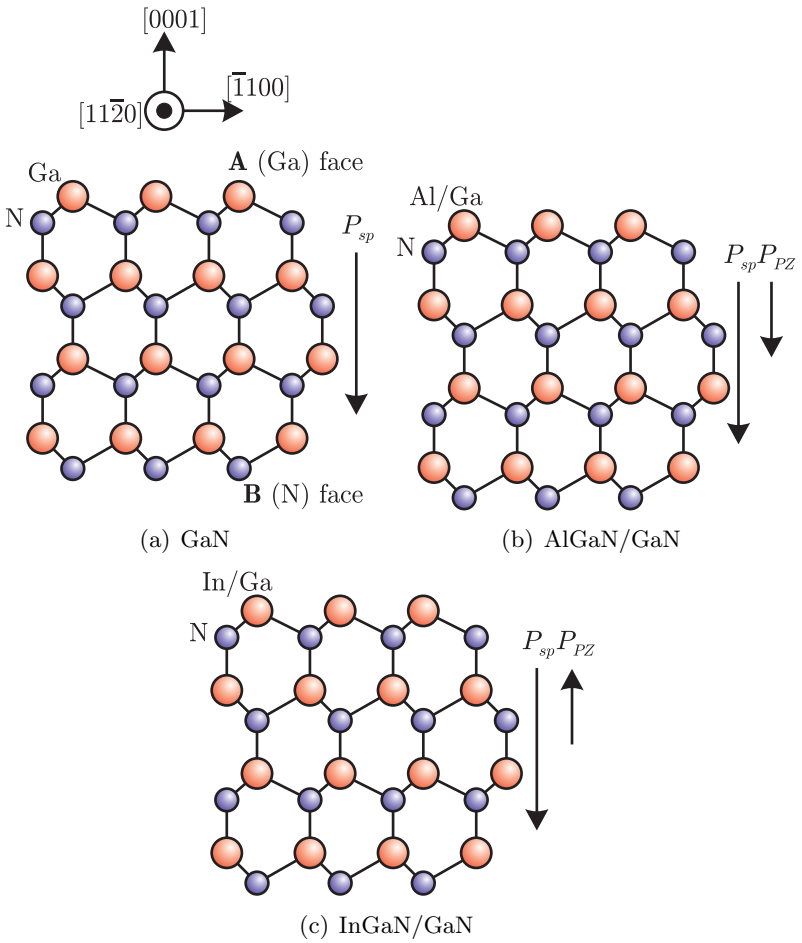

Figure 1.8: Spontaneous (P_{SP}) and piezoelectric (P_{PE}) polarization in nitride materials

1.7 Outline of this work

The objective of this work is to optimize the material quality of III-Nitrides grown on sapphire substrates by metal organic vapor phase epitaxy (MOVPE). Both polar and non-polar nitrides were studied for high frequency and high power transistors and gas sensors.

Following the introduction made in this chapter, chapter II presents the details of the MOVPE system recently set up in our laboratory along with an overview of the growth mechanisms. The electrical and optical characterization systems used for evaluating the nitride materials are also described.

The results on polar nitride material characteristics are presented in chapter III and chapter IV. The optimization process of bulk GaN is presented first in chapter III and followed by a discussion on nitride heterostructures in chapter IV. The growth and device characterization results of AlGaN/GaN and AlN/GaN heterostructures will be covered in chapter IV.

Growth of non-polar GaN will be discussed in chapter V. This chapter describes the characteristics of non-polar GaN and presents the optimization results using various nucleation layers along with results on devices fabricated on them.

Chapter VI is dedicated to the use of polar nitride materials in gas sensing applications. The first part of this chapter covers gas sensors based on nitride Schottky diodes. The gas sensing mechanisms and design parameters which impact the gas sensitivity are discussed. In the last part of this chapter, GaN/air gap based Fabry-Pérot Filters (FPFs) are discussed. The theory of distributed Bragg reflectors and a one dimensional mechanical model for FPFs are reviewed. Design and simulation results of GaN/air gap FPFs are presented together with growth and etching experiments.

A summary of the thesis work together with discussions on the observed results are presented in Chapter VII. The final chapter indicates suggestion on future work.

CHAPTER II

MOVPE GROWTH SYSTEM AND MATERIAL CHARACTERIZATION METHODOLOGY

This chapter describes the MOVPE growth system and material characterization tools used for this work along with a brief introduction of their principles.

The first half of this chapter focuses on the issues related to the operation of the MOVPE system. An overview of the MOVPE growth processes is presented first to allow better understanding of the hardware used. The description of the Thomas Swan MOVPE system used in this work is presented next. Since gas flow and material growth are sensitive to the temperature of the substrate, the temperature calibration process is also presented.

The second half of this chapter is dedicated to the characterization methodology. The importance of material characterization is significant since electrical, structural and optical characteristics serve as a feedback for the subsequently following steps necessary for layer design and quality improvement. Hall measurements and Capacitance-voltage measurements are conducted for the characterization of electrical properties. A Photoluminescence set-up is utilized in order to probe the optical properties of the materials. Structural characterizations are carried out with a X-ray diffraction system, atomic force microscopy, secondary electron microscopy and a surface profiler. Impurities and atomic composition in grown layers were analyzed

with secondary ion mass spectroscopy and X-ray photoelectron spectroscopy.

The laser interferometer, which allows *in-situ* monitoring of layer growth shall also be discussed, since it provides better understanding of the surface and interface roughness along with the growth rate.

2.1 Overview of reaction processes in MOVPE growth

There are many thermodynamic and kinetic processes involved with MOVPE layer growth. However, the key reaction process in III-V MOVPE growth can be expressed as follows.

$$A^{III}R_3 + B^{V}X_3 \longrightarrow A^{III}B^{V} + \text{organic by-products} \tag{2.1}$$

R is a radical such as methyl (CH_3) or ethyl (CH_2CH_5) or other organic groups and X is usually hydrogen. A^{III} and B^{V} are cations and anions, respectively. In case of GaN growth, the main reaction is described as below.

$$Ga(CH_3)_{3(g)} + NH_{3(g)} \longrightarrow GaN_{(s)} + 3CH_{4(g)} \tag{2.2}$$

Here, g and s stand for gas phase and solid phase, respectively.

Figure 2.1 illustrates the possible processes of the chemical reactions in III - Nitride growth [23]. The reactor design in this figure shows the design of the TS MOVPE system. MO sources and NH_3 are injected to the reactor through a showerhead and transferred to the substrate. Due to the high temperature ($> 900\,^{\circ}C$) in the reactor, the MO sources are decomposed completely and form various pyrolysis products. MO Sources and/or pyrolysis products are transported and adsorbed to the growth surface and then diffuse into growth sites. Finally the atoms are incorporated into the growth film. By-products flow out to an exhaust line.

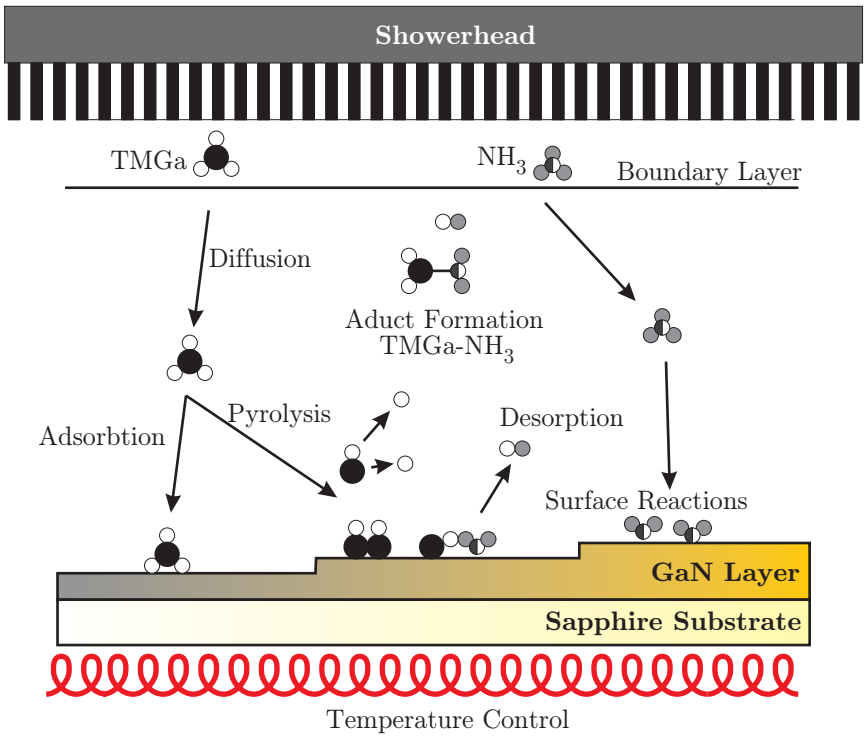

Figure 2.1: Reactions in a MOVPE reactor and on the substrate surface. After Ref. [23].

Pyrolysis and diffusion of a group III source through the boundary layer control the growth rate. During this process, solid adduct formation between NH_3 and the MO source can deplete the precursor concentration. As a result, the growth rate is reduced. A well known problem is the pre-reaction between NH_3 and TMAl. Parasitic deposition within the showerhead or on the reactor wall can also cause low growth rate and poor film quality. Therefore, the reactor design has evolved to suppress parasitic reactions and enhance the growth rate [24].

Depending on growth temperature, there are three growth regimes : (1) surface kinetically limited regime, (2) mass transported limited regime and (3) surface desorption limited regime [25, 26]. In the surface kinetically limited regime, the growth rate is dependent on temperature as the cracking efficiency of MO sources relies on temperature. Due to incomplete decomposition of the group III source, the surface reaction rate is slower than the diffusion rate. Complete pyrolysis of TMGa

is observed at temperatures above 500 °C and of TEGa for 300 °C in H_2 and N_2 environment [27]. However, the cracking efficiency of the alkyl sources depends on pressure and surface conditions as well. In presence of NH_3, full decomposition of TMGa is observed above 650 °C [28].

In the intermediate temperature zone (600∼1100 °C), mass transport of the alkyl source controls the growth rate dominantly. The temperature dependence becomes negligible. Surface kinetics are faster than the diffusion rate so this regime is termed also diffusion limited growth regime. Above 1100 °C, the growth rate decreases due to Ga and N desorption from the surface (desorption limited regime). Therefore, GaN growth is usually performed in the mass transported limited zone.

The amount of MO source supply to the reactor is given by:

$$f_{MO}(\mu mol/min) = \frac{f_{H_2}}{22414(sccm/\mu mol)} \cdot \frac{P_{MO}}{P_{Bubbler} - P_{MO}} \tag{2.3}$$

where, f_{H_2} is the net hydrogen flow into the bubbler from the input mass flow controller and $P_{Bubbler}$ is the back pressure on the bubbler set using the output pressure controller. P_{MO} is the vapor pressure of the MO as a function of temperature given from Eq. 2.4.

$$\log [P_{MO}] = B - A/T \tag{2.4}$$

where, constants A and B are empirically determined for each specific MO source. The properties of MO sources and their pressure and temperature coefficients are summarized in Table 2.1.

Symbol	Vapour pressure at 25 °C (torr)	A	B	Melting point (°C)	Remark
TMGa	238	1825	8.50	-15.8	Most common gallium source
TEGa	4.79	2530	9.19	-82.5	Best source for high purity but low growth rates
TMAl	14.2	2780	10.48	15	Most common aluminum source, high carborn incorporation
TEAl	0.041	3625	10.78	-52.5	Very low vapour pressure,
TMIn	1.75	2830	9.74	88	Most common indium source, high carborn incorporation
TEIn	0.31	2815	8.94	-32	Liquid indium source, pre-reaction
DEZn	8.53	2190	8.28	-28	n-doping material
Cp2Mg	0.05	3556	10.56	175	p-doping material

Table 2.1: Properties of metal organic sources.

2.2 Overview of the Thomas Swan MOVPE system

The vertical-type close space MOVPE reactor system set up for this work is given in Fig. 2.2 and its schematic is presented in Fig. 2.3. There are two separate gas delivery lines used in order to suppress gas phase pre-reaction between ammonia and the MO sources. The upper gas line carrying ammonia and silane is called the hydride line (Group V) and the lower gas line carrying the MOs is called the alkyl source line (Group III). Alkyl, hydride and carrier gases are directed into the run lines or vent lines through Epifold vent/run manifolds. Run lines are led to the reactor and vent lines are led to an exhaust system.

Two Epifold vent/run manifolds are fitted between the upper and the lower vent and run lines for stabilizing the input flow and pressure into the reactor. This ensures a smooth transition when the precursors are switched into or out of the reactor. Smooth transitions can be further enhanced by using a make-up line (LM1, LM2 for the lower gas line and UM1 and UM2 for the upper gas line, see Fig. 2.3) and a differential pressure control system.

Figure 2.2: Image of the 3x2" Thomas Swan MOVPE system used in this work.

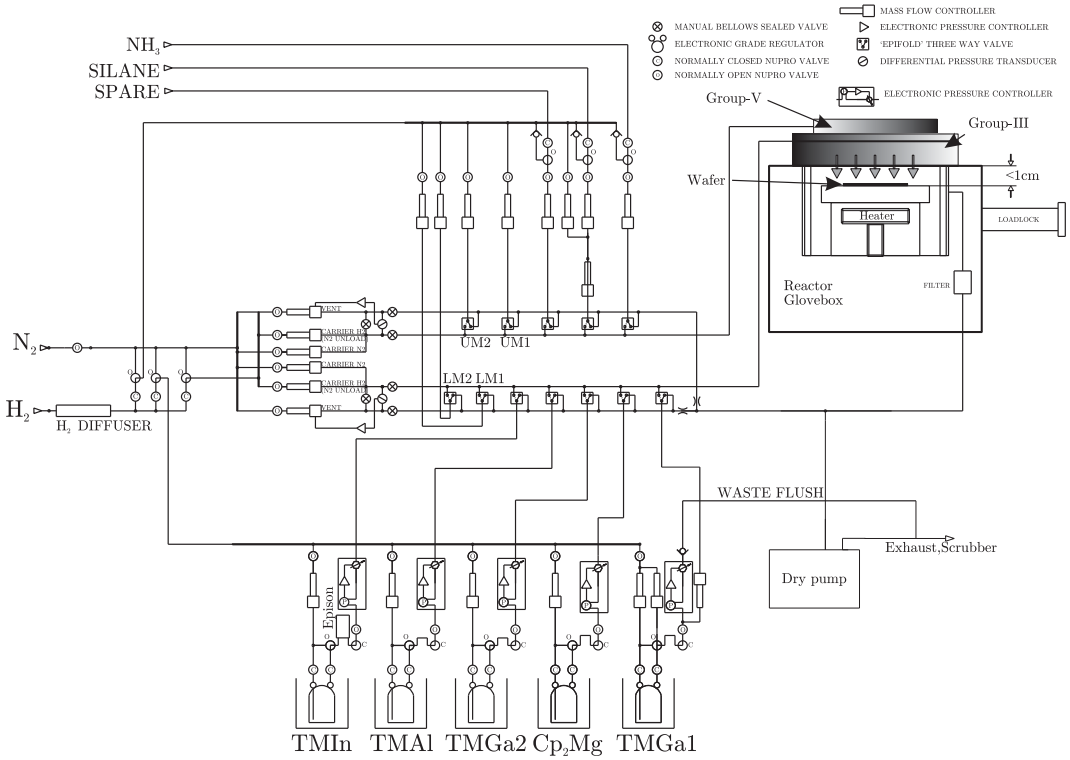

Figure 2.3: Schematic of the Thomas Swan MOVPE system used in this work.

An Epifold is a linear block of stainless steel with an axial 6 mm hole. Process gases flow with a high velocity along its length through this hole. The vent and run lines are connected to the Epifold by three way solenoid valves. When the valve is activated, process gases are directed into a run line or to the vent when the valve is in its normal state. The dead volume of the valve is as small as 0.02 cc so that efficient switching of MOs from a vent line to the reactor or vice versa is possible without interface smearing due to diffusion effects.

The purpose of differential pressure control is the prevention of any unwanted gas flow effects when the pressure in the vent line is not equal to the pressure in the run line. The pressure change occurs since the flow of the MOs, ammonia and carrier gas can be continuously changed during the growth process. The pressure difference in these two lines causes gas back-streaming, slow switching transition and unwanted mixing effects. In order to compensate the pressure difference, a differential pressure transducer (MKS Baraton type 223B) is fitted between the vent and the run lines. The zero differential pressure point between two lines can be set by adjustment of additional manual valves. The output voltage signal of the transducer is connected to an MKS 260 feedback control system. The output driving signal of the MKS 260 connected to a mass flow controller (MFC) of the vent line modifies the flow in the vent line corresponding to the differential pressure.

Despite the above described design considerations, the transient conditions may still affect the growth characteristics while the differential pressure is completely corrected. Especially in the growth of nitride heterostructures and alloys, pressure change becomes more serious due to abrupt and frequent switching of the flow of the MOs. The consequence of poorly controlled transitions is degradation of the electrical and optical performance. For example, in AlGaN/GaN heterostructures,

the mobility of the 2DEG is highly sensitive to the interface quality. In InGaN/GaN Multi Quantum Well (MQW) structures, the optical emission peak position is dependent on the accuracy of the In amount in the InGaN alloy and the peak intensity can be reduced by a poor interface quality between InGaN and GaN. Therefore, two make-up lines are implemented. The make-up lines compensate for the amount of precursor flow changes by flowing an equivalent quantity of hydrogen to either the vent or run line. The amount of make-up gas (H_2 in this system) is determined prior to the beginning of the process via the control software.

Two types of carrier gases are available for the described system: nitrogen and hydrogen. 99.999 % hydrogen, moisture of which is further removed by an absorber (supplied by Air Liquid), is used as carrier gas for bulk GaN and AlGaN/GaN heterostructure growth in our research. For InGaN MQW growth, 99.999 % nitrogen is used. The purity of the carrier gas affects the properties of the grown films by introducing impurities, defects and stress. Since the MOs strongly react with moisture and oxygen, the carrier gases must contain these elements as little as possible. The dew point of N_2 and H_2 are therefore monitored by a Panametric hygrometer to maintain a moisture level as low as a few ppm in our MOVPE system. As hydride source, 99.9999 % ammonia is used. 50 ppm silane diluted with 99.999 % hydrogen is used for n-type doping.

There are five MO sources installed in our system: two TMGa, TMIn, TMAl and Cp_2Mg. One of the TMGa sources is connected to a double dilution system and the other one is connected to a single dilution system. The double dilution system has an additional dilution MFC at the input MO lines. In case the dynamic range (maximum flow rate/minimum flow rate) of the process exceeds the dynamic range of a single MFC (20 in the given system) the second MFC is required to control

specially very low flow rates. TMGa connected to the single dilution system is used for bulk GaN growth or AlGaN growth. The other Ga source connected to the double dilution system is used only for the growth of GaN wells in InGaN/GaN MQWs which requires a dynamic flow range above 20.

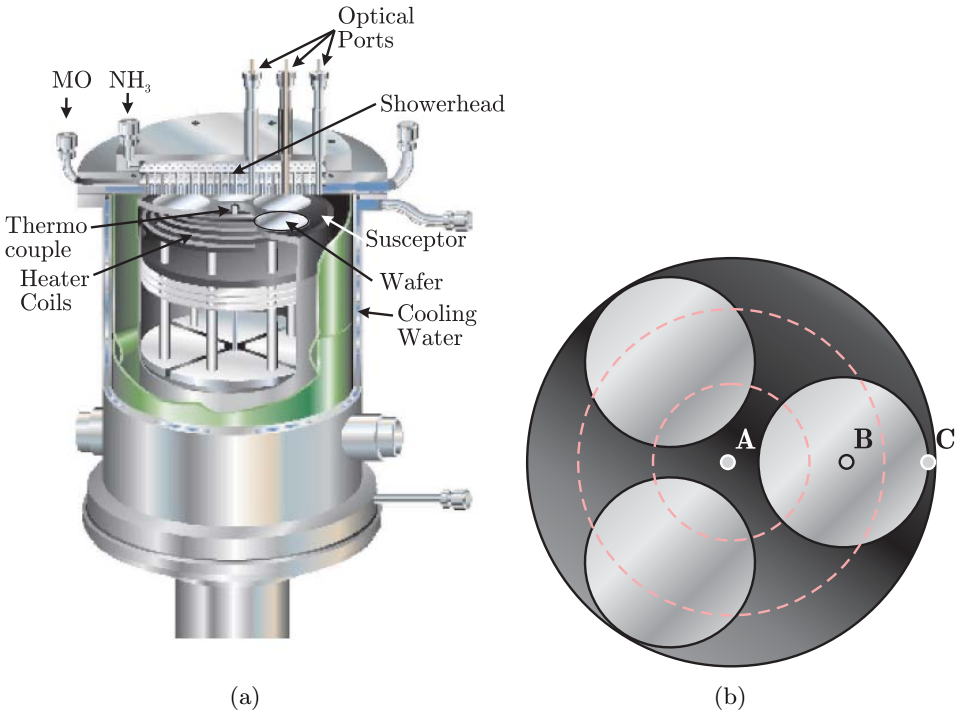

Figure 2.4: (a) Schematic of the TS reactor. (b) The top view of the susceptor. There are three 2" wafer pockets and three heating zones marked by A, B and C.

Hydride and alkyl sources flowing in the run lines are delivered into the reactor through the shower head. The schematic of the reactor is illustrated in Fig. 2.4(a). The shower head features many small size (about 1 mm diameter) holes, so called orifices. The density of these holes is about 100 per square inch. Orifices for the Alkyls and hydride sources are aligned side by side and distributed uniformly across the entire showerhead (S/H) in order to suppress pre-reaction between them. The distance between the S/H and the susceptor is less than 2 cm. It prevents recirculation of gases so that free convection can be reduced. This design improves uniform gas mixing and enhances the growth rate, interface abruptness and process

reproducibility.

Three 2" sapphire substrates sit on a graphite susceptor coated with thin silicon carbide (SiC) and rotate via a Ferrofluidic double magnetic fluid^{TM} bearing system during the growth. The rotation of the substrate enhances the uniformity of the gas flow. Underneath the graphite susceptor a resistive tungsten heater is mounted consisting of three separate tungsten coils. The heating zones are defined corresponding to the coil locations as Zone A (the center), Zone B (the middle) and Zone C (the outermost) as seen from Fig. 2.4(b) and the ratio of electrical power for each zone can be controlled. The substrate temperature is measured by a thermocouple (TC) which is located at the small recess underneath the susceptor. The TC output lead is connected to a feedback temperature controller (Eurotherm 2216) to maintain the growth temperature setpoint. However, the position of the TC is a few millimeter below the susceptor. Its position is adjusted manually. A significant difference exists, therefore, between the real temperature of the substrate and the TC reading temperature. In order to know the accurate substrate temperature and ensure temperature uniformity across the substrate, optical pyrometers are employed to monitor the surface temperature. There are three optical ports for checking the temperature of the three heating zones as shown in Fig. 2.4(b). Details about the temperature calibration process will be discussed in section 2.3.

The stainless steel jacket enclosing the reactor chamber and the S/H are cooled by water to ensure the rubber o-ring seals are not damaged. These o-rings can withstand up to $\sim$200 °C while the growth temperature is much higher than that. The cooling water temperature for the S/H is kept at 45 °C by using a heat exchanger so that deposition on the S/H and memory effects of Cp_2Mg are reduced. Normal tap water is provided to the reactor jacket in order to prevent parasitic reactions

with sidewall depositions. The TS system requires a constant water flow rate of more than 1 slm. Any interruption of the cooling water flow will trigger an interlock system so that the system is safely shutdown without any safety risk.

When over pressure builds up in the reactor, the pressure is relieved in two ways. If the reactor pressure reaches 950 torr for some reason without power loss, the system opens a normally closed (NC) valve and relieves the overpressure. On the other hand, if reactor over pressure occurs due to a power failure, pressure will be relieved by a normally open (NO) valve which is connected to the exhaust system via a 3 psi check valve. This check valve needs regular checking. Any damage to this check valve can lead to major leaks in the reactor. Figure 2.5(a) shows the image of the S/H of our system which was contaminated due to a reactor leak. The image of the normal S/H with regular GaN deposition is presented in Fig. 2.5(b).

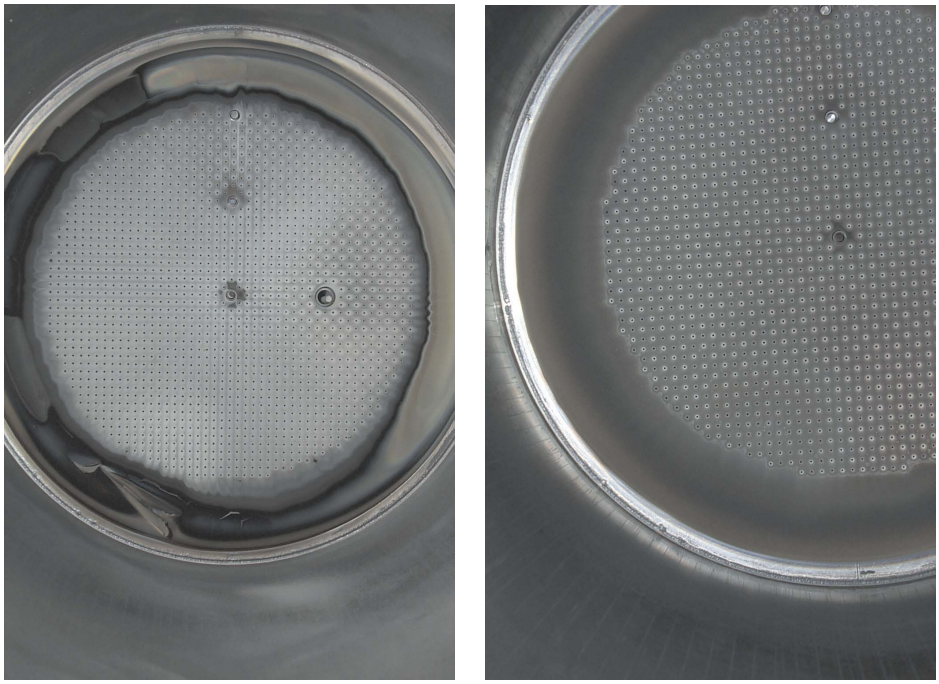

(a) (b)

Figure 2.5: Image of the showerhead taken (a) after reactor leak and (b) before reactor leak.

The reactor pressure is controlled using an MKS253 throttle control valve and a feedback controller (MKS651) connected to the reactor absolute pressure transducer with a range of $10 \sim 1000$ torr. The feedback controller is connected to the gate valve and controls the valve position in order to maintain set-pressure. The first system pump used was an Alcatel 200 mechanical oil pump. The downside of mineral oil pumps is oil back-streaming to the reactor and oil contamination in the exhaust line. Also this pump has a heating problem due to the aggressive ammonia. After several electrical failures due to the heating problem and damages to the shafts, it was replaced by an EDWARD QDP40 dry pump. Its capacity is $\sim$1200 slm and its body and motor are water-cooled. Since it does not need any oil lubricants, cleaner operation is possible. Excess gases and by-products in the reactor are directed to a pump. Two filters, a post reactor filter and a pall filter are installed in order to protect the pump. The post reactor filter is a stainless mesh filter. It traps relatively large particles during the nitrides growth. The second filter is a large area fine filter with a pore size of 6 μm.

Since MOVPE growth uses toxic gases and hydrogen, special treatment of any toxic chemicals from the reactor exhaust and vent line is necessary. Therefore a scrubber was set up which allows both thermal and wet treatment. In a ceramic heat chamber, H_2 and MOs are burnt into moisture and oxides at 750 °C. Most of the ammonia is diluted with water and then neutralized in a wet chamber.

In order to control the pneumatic valves for the MOs, carrier gases and ammonia, the pressure of the compressed air necessary always has to be maintained at 80 psi. An air pressure drop below this pressure leads to a failure of the valves. In order to ensure the operation of pneumatic valves, an N_2 bottle was connected to the air supply line via a 3 psi check valve. It allows to operate pneumatic valves even if

the pressure of the compressed air drops.

The gas and MOs valves can be controlled either manually or automatically. However, only manual setting is allowed to control the heater, substrate rotation and reactor purge gas flow. This is one of the drawbacks of our system. Ramp up and ramp down times for substrate heating and rotation are not automatically synchronized with other steps. This may cause instable purge gas flow and induce stress in the grown film. Many trial and error iterations are required in order to optimize these conditions. However, the possibility to handle gas and MOs valves manually during the process allows to correct the growth process for any reasons of safety or flaw in the growth recipe promptly.

The integrated interlock system returns the system into a safe state provided that any problem as follows occurs: water flow stop, reactor over pressure, low extraction flow, low pneumatic air pressure, system door open during the process, any abnormal events with the ammonia gas bottle cabinet, reactor open. In this event, the 24 V power controlling the pneumatic valve is cut and Epifolds switch the MOs and gases from the reactor to the vent line. The bubbler sources are disabled and then purged by nitrogen.

The reactor chamber is enclosed by a total loss glove box. 99.999 % N_2 flows constantly so that the moisture level inside is maintained at about ∼20 ppm. The separation of the reactor from the normal ambient environment reduces the possibility of contamination. However, a large amount of N_2 consumption is the downside of the total loss glove box.

The Thomas Swan (TS) system used in this work is equipped with an Epison controller. This equipment is based on ultrasonic velocity measurement and is able to control MO flow very accurately (∼ ppm). For the growth of any In alloys such

as InGaN MQW, this controller is very useful since very small amounts of different In incorporation can produce inhomogeneous quality.

2.3 Temperature calibration

Prior to the actual GaN growth, the susceptor temperature has to be calibrated. This procedure is important because of the discrepancy between the thermocouple (TC) reading temperature and the real temperature of the wafer which sits in the susceptor. Since the heater is controlled by the TC read-out temperature, the difference between these two values must be corrected. Otherwise, the material quality can be degraded in many ways. A small deviation of growth temperature of the NL layer is detrimental to its quality and consequently degrades the quality of high temperature GaN layer grown on top of it. In addition, accurate temperature calibration will improve the uniformity of the wafer since the temperatures of all three heating zones are calibrated to be equal or less than 1 % off.

The principle of the susceptor temperature measurement is the black body radiation. Infrared radiation from the heated susceptor surface propagates via the optical probes and is measured by an optical pyrometer. A minimum of three probes is necessary for a temperature calibration of the three corresponding heating zones (see Fig. 2.4(b)). The optical probes consist of a quartz rod inside a stainless steel jacket and an o-ring and have to be calibrated with respect to a reference system. An OMEGA CN920 black body furnace was used for this purpose. The radiation of the furnace was measured via the optical probes and the values were mapped to the furnace set temperature accordingly. From this relation, linear coefficients (slope and intercept) of the probes are extracted. Optical probes with ideal conditions will allow very small deviation from the set-values. Therefore, the slope will be close to

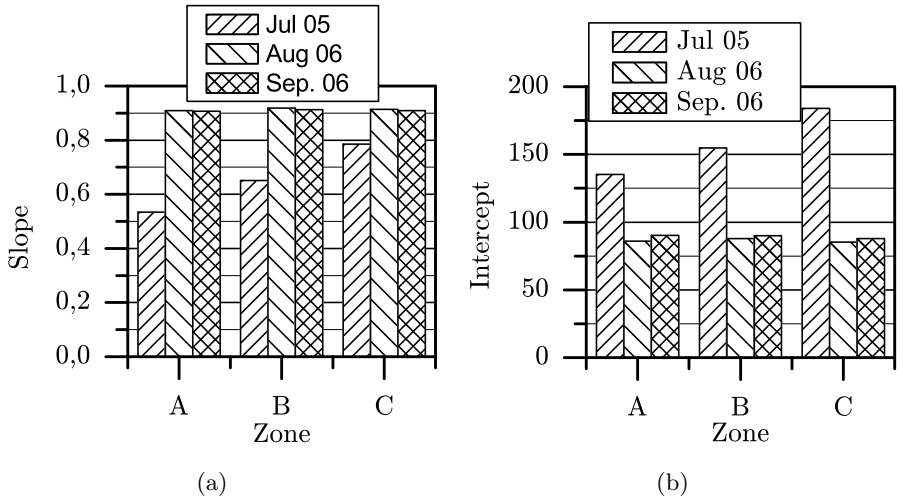

Figure 2.6: Linear parameters of the optical probes measured at different times. (a) Slope and (b) Intercept.

one and the intercept value will be very small.

Figure 2.6 shows that the linear coefficients of the optical probes are significantly different depending on the quality of the probes. With the probes used in our experiment in the year 2005, the quartz rod was chipped and the metal jacket was damaged. Due to this, the slope and the intercept of the probes are significantly off from the ideal case. Once these damaged quartz were replaced by new ones in the year 2006, better correlations were obtained. However, the optical probe characteristics drifted again in a second measurement in the year 2006 due to the thin coating of the quartz rod which occurred during the calibration process. After the calibration of the optical probes, they are inserted into the optical ports in the showerhead as seen in section 2.2 in order to be able to read the susceptor temperature. In this process, a temperature look-up table referring the real susceptor temperature to the TC setpoint was completed for the different growth temperatures (e.g. nucleation layer growth temperature and main layer growth temperature).

Although temperature calibration ensures the correct temperature of the substrates, several remaining problems with this method must be manifested. Firstly,

the temperature read by the optical pyrometer is highly sensitive to the actual state of the optical probe as mentioned above. Oxidation or any damage of the optical probes in the course of several growth runs must be accounted for.

Secondly, significant temperature deviation must be addressed among different susceptors due to the emissivity of the suscptor. Thirdly, the emissivity of a susceptor can even change due to the deposition of growth by-products. Especially, the impact of AlN deposition is significant by more than 200 °C. To overcome these issues, a quick and simple method is proposed [29]. The temperature of the three zones is calibrated with a reference susceptor which has not been used for growth at all. Since it has not been used for growth, no change of emissivity is ensured. For the susceptors being used, only the temperature of the growth pocket (zone B) is measured and calibrated with respect to the reference susceptor. This requires a spare susceptor and perfect uniformity of the suscptor is assumed. However, this method was evaluated to be adequate for this works purpose.

2.4 Material characterization methodology

2.4.1 Naked eye characterization

Naked eye characterization is a simple and quick method to evaluate layer quality as soon as a thin film is unloaded from the growth reactor. Good quality III-Nitride layers grown on sapphire wafers have smooth and transparent surface. Any quality degradation can be indicated by roughness and color of the surface. The drastic change of thickness across III-Nitride layers can be indicated by a color ring pattern on the surface.

2.4.2 Optical microscope

Another powerful visual inspection tool is an optical microscope. It can provide surface morphologies in detail: defects, scratches and particles. In particular, when it is equipped with a Nomarski differential interference contrast system, the surface feature contrast of the layer is enhanced further.

2.4.3 Hall effect measurement

Hall effect measurements give information about sheet resistance, carrier density and Hall mobility of semiconductor layers. In this work, Hall effect measurements are used to characterize bulk GaN and AlGaN/GaN heterostructures as will be presented in chapters III and IV.

The importance of RT Hall measurements for bulk GaN has three aspects. Firstly, an estimation of structural defects such as threading dislocations (TD) can be obtained in undoped GaN since the Hall mobility is strongly sensitive to TD densities. Secondly, the carrier density of undoped GaN given by RT Hall measurements provides information about the background carrier density associated with impurities and defects. Lastly, doping efficiency can be estimated for doped GaN by measuring the carrier density corresponding to the silane or Cp_2Mg flow.

In addition to room temperature Hall measurements, extensive information about the grown layers can be obtained by conducting temperature dependent Hall measurements. The electron Hall mobility is limited by different scattering mechanisms such as acoustic phonon, optical-phonon, ionized impurity, interface and dislocation scattering. These are strongly dependent on temperature. Ionized impurity scattering, interface scattering and dislocation scattering are, in particular, related to material quality and show different temperature dependence. Therefore, material

quality can be evaluated accordingly by the Hall mobility measured as a function of temperature. Measurement of carrier density as a function of temperature provides the activation energy of impurities and dopants. By comparing free carrier density and total impurity density, the compensation ratio can also be extracted.

Temperature dependent Hall measurement is a useful tool for confirming the presence of a 2DEG in AlGaN/GaN heterostructures. The effective mobility of both bulk and a 2DEG are limited by the polar optical phonon scattering at temperatures above 170 K. Below this temperature, however, the two mobilities show a different trend. The 2DEG mobility slowly increases as the temperature is reduced. In contrast, the mobility of bulk GaN decreases steadily due to ionized impurity scattering. In spite of all benefits from temperature dependent Hall measurement, in this work, only room temperature and 77 K Hall measurements are carried out due to the fact that our measurement system can be cooled effectively by liquid nitrogen but does not have the necessary compressor for controlling the operating temperature.

In our Hall measurement set-up, a standard electromagnet with a field strength of 1000 Gauss is used and a Keithley 236 source measurement unit is used as a current source. The current range of this equipment is 1 nA$\sim$1 mA. It can characterize materials having a sheet resistance of up to $10^6\,\Omega/\square$. For even higher resistive material, a low current source (pA) and additional effort to make good ohmic contacts are required. All the measurements were done in a dark environment in order to avoid noise induced by photocurrent.

For conductive materials, ohmic contacts are formed by Indium dots at the four corners of the wafer chip and consequently annealed at 400 °C for about 5 minutes. If the material is undoped bulk GaN and/or resistive, a Ti/Al/Ti/Au (25/120/12/300 nm) multi layer is deposited by e-beam evaporation and annealed at

850 °C for 30 seconds. The principle of Hall effect measurements is described below.

In order to measure the sheet resistance, the van der Pauw technique is used. This is a very useful method since it can be applied to any arbitrary sample shape. However, the ohmic contacts have to be located at the periphery of the sample (preferably at the corners) and the contact size and thickness of the thin film must be much smaller than the distance of two contacts. For the case of a rectangular sample, R_a and R_b must be measured to deduce the sheet resistivity as shown in Fig. 2.7. The resistances R_a and R_b are obtained by applying a constant current I through two contacts and measuring the voltage V at the other two contacts.

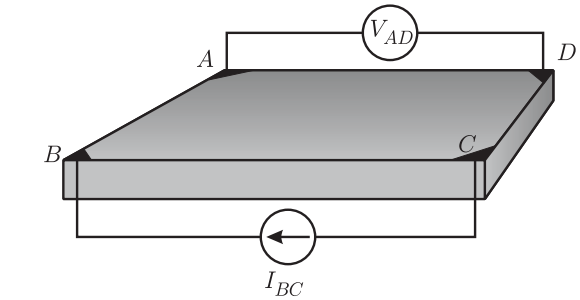

(a) measurement for R_a

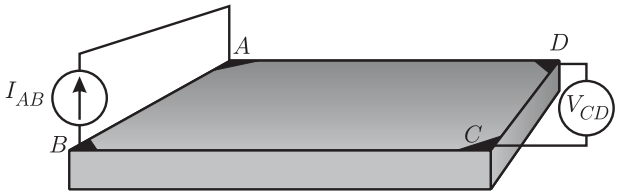

(b) measurement for R_b

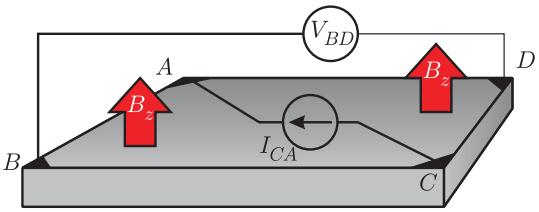

(c) measurement for Hall voltage

Figure 2.7: Configurations of van der Pauw measurement.

With the assumption that all ohmic contacts and the uniformity of the sample are good, two measurements of the resistance for two different polarities are enough

to determine R_a and R_b. From the relationship between R_s, R_a and R_b given in Eq. 2.5, the numerical solution of R_s is described by the measured voltages $V_{AB,DC}$, $V_{BC,AD}$ and their average voltage V_{avg} as shown in Eq. 2.6

$$exp(-\pi R_a/R_s) + exp(-\pi R_b/R_s) = 1 \tag{2.5}$$

$$R_s = d * \frac{\pi}{\ln 2} f \cdot \left(\frac{V_{AB,DC}}{V_{BC,AD}}\right)\left(\frac{V_{Avg}}{I}\right) \tag{2.6}$$

R_s is now replaced with the sheet resistivity ρ_s which is obtained by dividing R_s by the thickness d of the conducting channel. Here f is the van der Pauw geometry factor. Its solution can be numerically calculated from the following equation.

$$\frac{V_{BC,AD} - V_{AB,DC}}{V_{BC,AD} + V_{AB,DC}} = \frac{f}{\ln 2} \arccos\left(\frac{\exp(\ln 2/f)}{2}\right) \tag{2.7}$$

The DC current I applied to a sample should be controlled so that the power dissipation is no more than 5 mW. Heating the crystal increases phonon scattering and leads to a higher resistivity. Measurement in a dark environment avoids errors caused by photoconductive noise. This becomes very important when a high density of defects exists in the thin films.

In order to determine the carrier density N and the mobility μ, Hall voltage measurements are required along with van der Pauw method measurements. When holes and electrons are present in a semiconductor and the magnetic field B_z (coming out of the plane of the paper in Fig. 2.8) is applied to them in perpendicular direction to their movement, both electrons and holes move in y-axis direction due to the Lorenz force $F = qv_xB_z$. A pile of charges generates a counter electric field E_y which prevents further electrons or holes from accumulation. The differential voltage due to this electric field is termed the Hall voltage $V_H = E_y * w$.

From Fig. 2.8, the total net current density in y-direction (J_y) is zero at

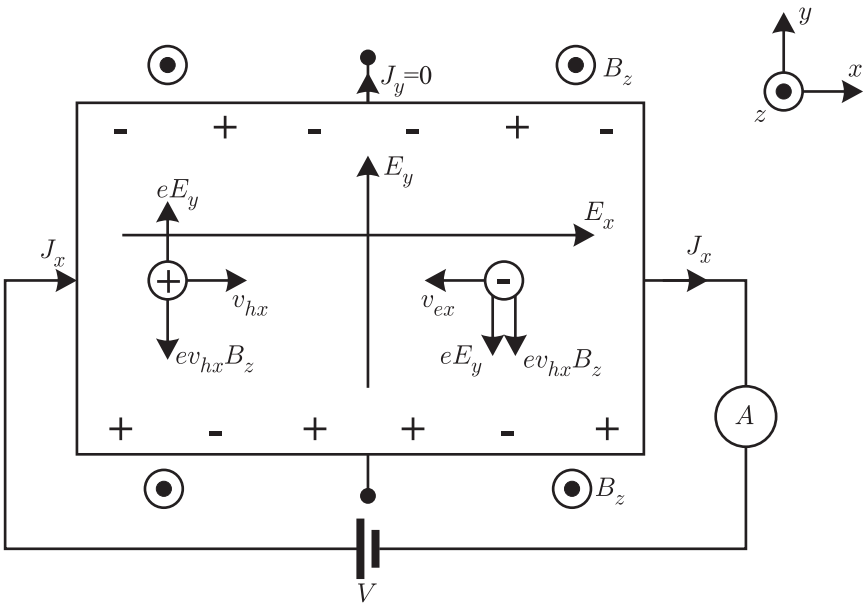

Figure 2.8: Hall effect in a semiconductor.

equilibrium state.

$$J_y = J_h + J_e = eN_p v_{hy} + eN_e v_{ey} = 0 \tag{2.8}$$

Here, N_p and N_e are the hole and electron carrier density, respectively. However, the net force on holes and electrons along the y-direction is given by the Lorenz force and the counter electric field as below.

$$F_{hy} = eE_y - ev_{hx}B_z \text{ and } -F_{ey} = eE_y + ev_{ex}B_z \tag{2.9}$$

Replacing the net force with the drift mobility and drift velocity terms and considering current equilibrium state from Eq. 2.8, Eq. 2.9 becomes,

$$E_y(N_p\mu_h + N_e\mu_e) = B_z E_x(N_p{\mu_h}^2 - N_e{\mu_e}^2) \tag{2.10}$$

When the total current density along the x-direction (J_x) is described in terms of E_x, the Hall coefficient R_H is defined as below.

$$R_H = \frac{E_y}{B_z J_x} = \frac{N_p{\mu_h}^2 - N_e{\mu_e}^2}{e(N_p\mu_h + N_e\mu_e)^2} \tag{2.11}$$

The sign of R_H shows the carrier type of the semiconductor and it depends on doping and temperature since drift mobility and carrier concentration are a function of temperature. Hall mobility and sheet carrier density are calculated from the known magnetic field and the change in voltage with and without the presence of the magnetic field as below.

$$\mu_{Hall} = 10^8 \left(\frac{\Delta V_{AC,BD}}{B_z \rho_s} \right) \text{ and } n = \frac{1}{q \rho_s \mu_{Hall}} \tag{2.12}$$

2.4.4 Capacitance-Voltage measurement

Capacitance-voltage (C-V) measurements can provide information about carriers and impurities in semiconductors. The carrier concentration profile versus depletion depth confirms the presence of a 2DEG explicitly as can also be confirmed by low temperature Hall mobility measurements. Besides, the location of the 2DEG can approximately be estimated.

Figure 2.9 shows a typical structure of a Schottky diode and its small signal equivalent circuit model. Since the substrate used in this work is resistive, the ohmic contact is placed on the same side of the Schottky contact. When reverse bias is applied to a Schottky contact, mobile charges move away and cause a depleted space charge region of the width w_d inside the semiconductor.

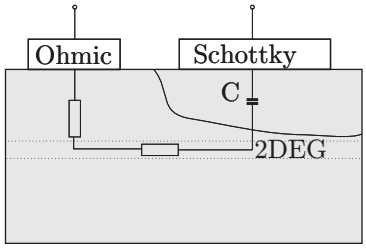

Figure 2.9: Small signal equivalent circuit model of the Schottky diode structure under reverse bias. After [30].

When the junction is assumed to be a parallel plate capacitance, the depletion

depth w_d is given by:

$$C = \frac{\epsilon_s \epsilon_0 A}{w_d} \tag{2.13}$$

where, A, ϵ_s and ϵ_0 are the area of the Schottky contact, the relative dielectric constant and the free space permittivity, respectively. In case where the semiconductor doping varies with distance, the space charge is not constant and will be given by:

$$Q = A \int_0^{w_d} N(w) dw = -CV \tag{2.14}$$

Here $N(w)$ is the doping concentration at the depth of w. Consequently, an increment in voltage dV results in an increment in Q_s. From the differential of Eq. 2.14 and by replacing dw/dV with $(dw/dC)(dC/dV)$, the following equation can be obtained [31].

$$N_d(w_d) = -\frac{C^3}{q\epsilon_s \epsilon_0 A^2 \frac{dC}{dV}} = -\frac{2}{q\epsilon_s \epsilon_0 A^2 \frac{d\frac{1}{dC^2}}{dV}} \tag{2.15}$$

The profile of the carrier concentration $N_d(w_d)$ can be plotted with respect to depletion depth w_d from Eq. 2.15.

2.4.5 Photoluminescence characterization

The principle of photoluminescence (PL) spectroscopy is construed by spontaneous emission from a given material. When electrons in a given material are excited by an external optical energy, they transit from a ground state to an excited state. Conversely when excited electrons return to the ground state, they will lose energy in some ways. This latter process is referred to a electron-hole recombination process. In particular, a recombination process involved with emitting light is termed as radiative recombination or spontaneous emission.

Figure 2.10 presents the various cases of electron - hole recombination. Radiative recombination occurs when an electron transits from the conduction band

to the valence band or from the donor to the valence band or from the conduction band to an acceptor via processes (a)-(c). These processes are related to the band edge emission since the corresponding photon energy is close to the bandgap energy of GaN. Defects at deep levels produce non radiative recombination by emitting phonons instead of photons in process (d).

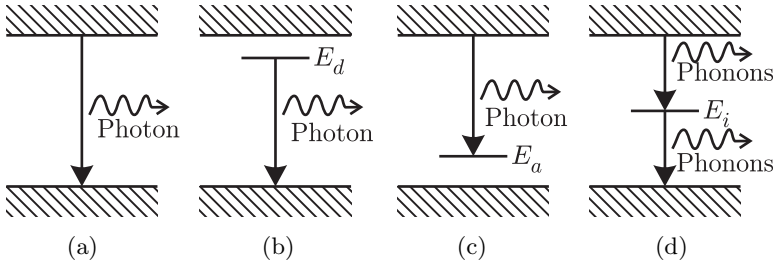

Figure 2.10: Recombination process of electrons and holes in GaN via (a) conduction band to valence band, (b) donor site to valence band, (c) conduction band to acceptor site, (d) non-radiative recombination. After Ref. [32].

If high quality undoped GaN is assumed, its PL spectra will show a sharp peak at the wavelength corresponding to the band edge emission. However, broad peaks are also in general observed beside the band edge peak. They are associated with impurities which are incorporated in UID GaN and occupy either donor or acceptor sites. Impurities can also create deep level defects so non-radiative recombination will occur. Hence, the PL intensity will decrease accordingly.

Since carriers at shallow defect states (close to the bands) are thermally inactivated at low temperatures ($<<300\,\mathrm{K}$), all three radiative recombination paths become stronger while they give very weak peaks in the RT PL spectrum. In low temperature PL spectrum data, the band edge spectrum provides information about strain, acceptors, donors, free excitons, binding energies by analyzing the position, intensity and full width at half maximum of the respective peaks. These features are strongly related to material quality. In undoped GaN, the presence of a strong

donor peak manifests a high background carrier density originating from intentionally or unintentionally incorporated impurities. On the contrary, if a peak related to acceptors exists in undoped GaN, this implies the existence of acceptor states from structural defects or intentionally or unintentionally incorporated impurities. Therefore, PL is another tool which verifies the resistive characteristics of GaN along with Hall measurements.

Although band edge PL spectra can give overall ideas about the type of impurities (either donor type or acceptor type), it is difficult to identify the origin of defects. Therefore it is necessary to measure the PL spectra below the band edge. This can give more detailed information about defects since specific defects are involved with different peaks shown in the range of wavelength from 380 nm to 700 nm.

The PL measurement set-up used in this work is illustrated in Fig. 2.11. A 55 mW He-Cd laser (center wavelength λ=325 nm) was used as an optical source in this work. Its power density at 325 nm is about 2 W/cm^2. The excitation energy of our source is equivalent to 3.82 eV. It can probe bulk GaN (E_g=3.4 eV) and AlGaN with Al compositions up to 12 %. A 325 nm line filter is used in order to block other ranges of wavelengths.

After the broadband dielectric UV mirrors and a UV silica convex lens, the light incidents on the sample (typically 7mm x 7mm) mounted in a cold stage. The temperature of the cold stage is controlled between 10 K and 320 K by a He recirculation cryostat and a heating element. Emitted light from the sample is focused by an UV lens into the spectrometer. A 340 nm long pass filter before the entrance slit of the monochrometer reduces diffuse laser reflections into the detection system. The PL signal is detected by a Spex 500M monochrometer which is connected to a photomultiplier tube (PMT). The grating inside the monochrometer has 1200 lines/mm

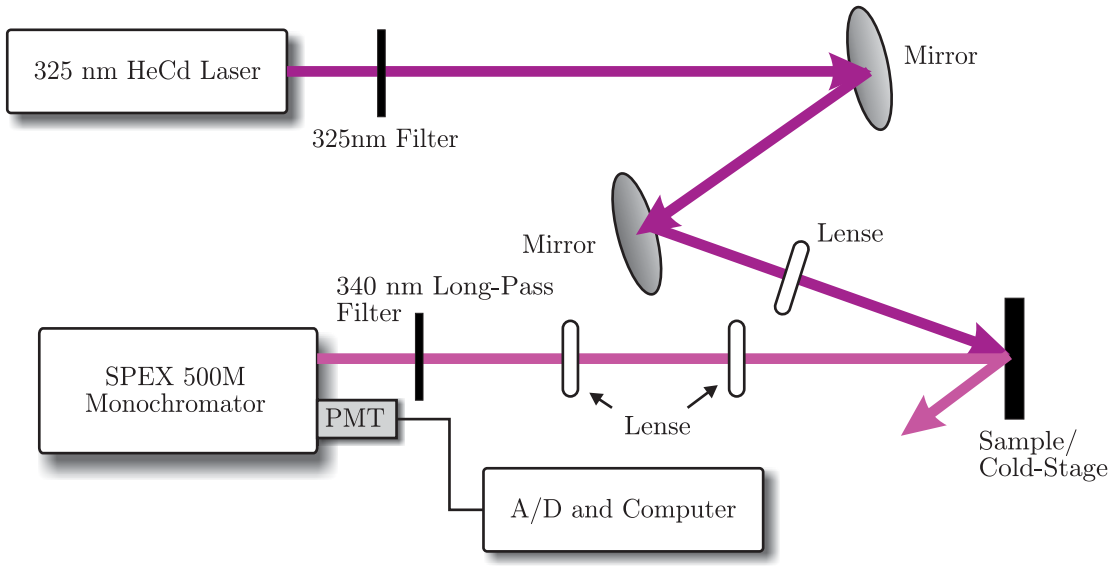

Figure 2.11: Schematic of the photoluminescence (PL) measurement set-up.

with 400 nm blazes.

In summary, PL is a non-destructive powerful technique to investigate electrical and optical characteristics of GaN. It provides not only the information of defects in GaN but also the information about surface roughness, interface roughness, impurity levels and alloy disorder since PL originates near the surface of the material. In this work, low temperature PL measurement was employed to confirm the presence of acceptors in resistive GaN. (see chapter III).

2.4.6 X-ray Diffraction

The X-ray Diffraction measurement technique is a powerful method to investigate crystalline quality, composition, thickness, strain, lattice mismatch, surface and interface roughness of grown layers. In this research, a BEDE D1 high resolution X-ray diffraction system (HR-XRD) was used in order to characterize the structural properties of nitride materials. The set-up configuration of this system is presented in Fig. 2.12.

The X-rays are generated from a 2.2 kW water-cooled Thales X-ray tube. Since

the X-ray beam scattered by the crystal-under-test is broadened by the geometrical and spectral divergence of the incident X-ray beam, a Si channel cut crystal (CCC) is used for beam collimation. In order to achieve very high resolution (about 5∼12”), two CCCs have to be used in the asymmetric configuration. However, it reduces beam intensity so it is not applicable to the measurement of nitrides.

Due to the relatively low intensity of the beam scattered from nitride materials, one CCC and a 100 μm precision slit after the CCC are used for beam collimation. The slit allows only passing of CuKα_1 (λ=1.54056 Å). Beam divergence due to the limitation of this set-up configuration is about 30∼40”. However, this is still acceptable for nitride materials because the resulting peak width in nitride materials is much larger than this beam divergence due to the high structural defects in this material system.

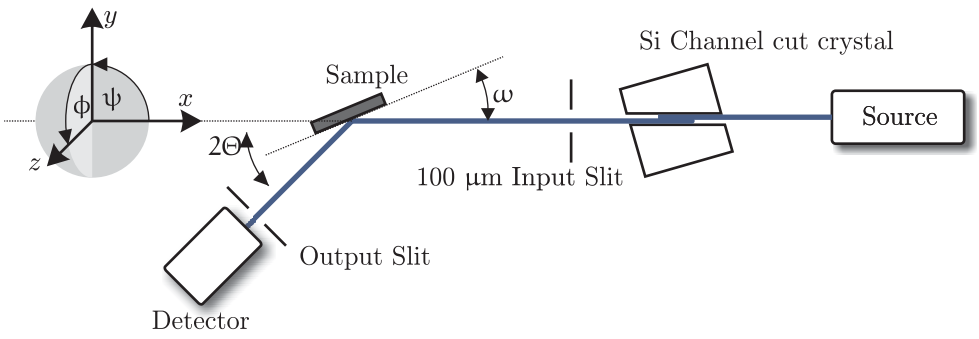

Figure 2.12: Schematic of X-ray Diffraction measurement set-up.

When X-rays scatter with atoms in adjacent crystal planes at a specific angle, the scattered X-rays interfere constructively (see Fig. 2.13). This angle terms as Bragg angle (θ_B) and the Bragg condition is given in Eq. 2.16.

$$m\lambda = 2d_{hkil}\sin\theta_B \tag{2.16}$$

where h, k, i and l are the Miller indices, d_{hkil} the spacing between neighboring planes and m is the order number of the reflection from the planes. In a hexagonal

structure, d_{hkil} is calculated as below.

$$d_{hkil} = \frac{1}{\sqrt{\frac{4}{3}\left(\frac{h^2+hk+k^2}{a^2} + \frac{l^2}{c^2}\right)}} \tag{2.17}$$

where a and c are the in-plane and out-of-plane lattice constants, respectively. The $hkil$ plane is equivalent to the hkl plane since $i + h + k = 0$ [33].

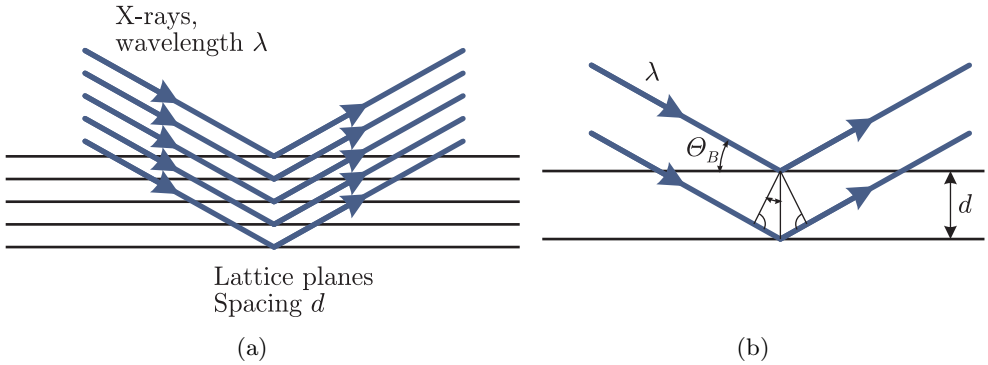

Figure 2.13: Schematic of (a) a X-ray beam scattered by a plane with lattice spacing d and (b) an incident and scattered beam under Bragg condition.

In order to evaluate the structural defects in bulk GaN, the ω-rocking curve is measured. With this measurement it is possible to estimate quality parameters such as lattice tilt, wafer curvature, screw-type dislocations, edge-type dislocations and mixed-type dislocations and mosaicity as depicted in Fig. 2.14. During the scan, only the sample is moving along the ω axis while the detector position is fixed at $2\theta_B$. Since the detector does not move, only one lattice plane spacing impacts the scan. It is important to note that at least two ω scans have to be performed. Scanning with respect to both the symmetric reflection plane and the asymmetric reflection plane is necessary in order to evaluate different types of dislocations.

XRD measurements together with Transmission Electron Microscope (TEM) studies for different qualities of GaN showed that the peak broadening in the symmetric rocking curve can be attributed to screw-type dislocations because the scattered X-ray beam is reduced by inconsistent lattice plane spacing (tilt of the mosaic struc-

ture). On the other hand, the asymmetric rocking curve is broadened by edge-type and mixed dislocations due to the twist of the mosaic structure. The origin of GaN mosaic structures and dislocations are sub-grains which form during the growth mode transition in heteroepitaxial growth of bulk GaN. Fig. 2.14(c) illustrates a mosaic structure consisting of many sub-grains. As sub-grains are tilted or twisted against each other, screw-type dislocations, edge-type and mixed dislocations are generated. Details about the growth mode transition will be presented in the following chapter.

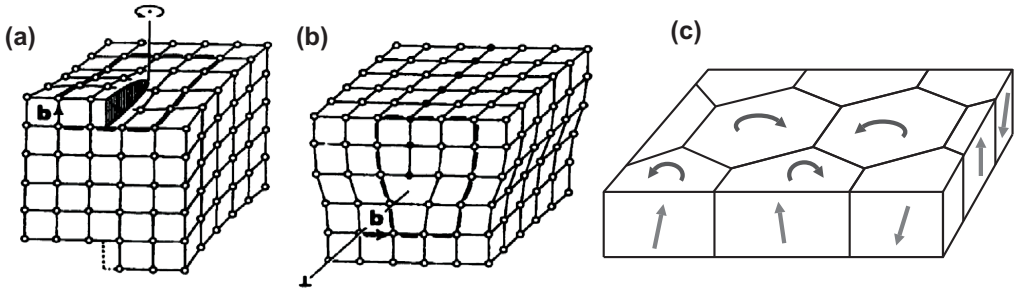

Figure 2.14: Structural defects in GaN. (a) screw-type dislocation, (b) edge-type dislocations, (c) mosaicity of GaN. After Ref. [34].

Symmetric rocking curve measurements are performed under the condition that the lattice plane is parallel to the surface normal. Planes interrogated here have Miller indices of $h = k = 0$ so for example [002] or [004]. θ_B of each symmetric plane is provided by the BEDE D1 software. In contrast, asymmetric measurements are more complicated than symmetric measurements, as the angle of the incident X-ray beam (θ_B) is set by the Bragg angle and ϕ being the angle between the surface normal and the diffraction plane normal. In a hexagonal crystal, ϕ is given as below.

$$cos\phi = \frac{l/c}{\sqrt{\frac{4}{3}\left(\frac{h^2+hk+k^2}{a^2} + \frac{l^2}{c^2}\right)}} \tag{2.18}$$

Two asymmetric rocking curve measurements are possible depending on how

the sample axis angle ω is determined. In Grazing Incidence (GI) system configuration or Grazing Exit (GE) system configuration, ω is given by either $\theta_B - \phi$ or $\theta_B + \phi$, respectively. Due to the limitation of the detector position, GI geometry is used in this research. Figure 2.15 illustrates a GI scan set-up.

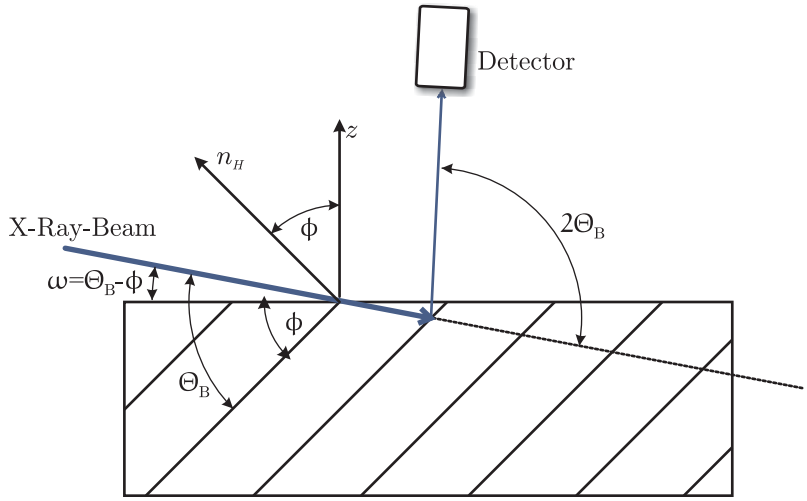

Figure 2.15: Schematic of Grazing Incidence (GI) XRD scan set-up.

Typical bulk GaN has an (002) FWHM of about 200∼300" and a (102) FWHM of about 400∼550". Since the FWHM of the symmetric and asymmetric plane is a measure of the TD density, the mechanism of sheet resistance change of bulk GaN was investigated in correlation with the (002) and (102) FWHM in this work. It will be discussed in section 3.3.

In this work, coupled ω-2Θ scans and X-ray reflectivity (XRR) are employed to characterize AlGaN/GaN heterostructures and optimize them accordingly. A coupled ω-2Θ scan is performed by moving both the sample and the detector in a 1:2 ratio simultaneously. In this case, various lattice plane spacings can be investigated. The scan is sensitive to the lattice constant and gives information about strain. Besides, the Al composition can be extracted from the peak separation between GaN and AlGaN layers (see also section 4.2). A series of coupled scans at different

sample angle offsets builds a reciprocal space map. This is a useful tool to analyze the AlGaN lattice relaxation in AlGaN/GaN heterostructures. Detailed discussion about stress analysis by XRD can be found in Ref. [35].

The grazing incident (GI) XRR method allows to measure thicknesses of 5$\sim$ 500 nm and a layer roughness less than 30 nm. Its principle is based on grazing incident X-ray scattering. At small incident angles, θ, below some critical angle θ_c, the X-ray beam is totally reflected from the solid surface because the refractive index for X-rays is less than one. θ_c depends on the electron density, scattering factor, atomic number of the material and the wavelength of the incident beam. Above this θ_c, the X-ray beam penetrates the surface and variations in electron density through the sample give rise to a distribution of the scattered intensity as the incident angle is varied. Using this method, the AlGaN layer thickness which is typically below 30 nm can be characterized. Since it is impossible to measure such ranges of thicknesses by a conventional SEM, XRD is a useful tool for the characterization of heterostructures.

2.4.7 Atomic Force and Scanning Electron Microscopy

Atomic Force Microscopy (AFM) allows to measure the surface topography on a scale from a few Å to 100 μm. While a cantilever probe holding a stylus with a radius of a few nm scans over the surface, the cantilever is deflected according to Hooke's law due to the interaction between the tip and the sample surface. The variation of the tip height is measured by a laser signal which is reflected from the tip into a photodiode. In order to avoid the tip being crushed by the surface in case of very rough samples, the interaction force between the tip and the surface can be held constant by an additional piezoelectric actuator.

In general, three scanning modes are available depending on the physical contact between the tip and the sample surface: contact mode, intermittent-contact

mode and non-contact mode. The contact mode is also known as repulsive mode due to the associated force between the tip and the sample. In this mode, an AFM tip gradually approaches the surface until the atoms are in contact. As a result of repulsive van der Waals forces between the tip and the atoms, the cantilever will bend to keep the tip away from the surface. The disadvantage of the contact mode are probable surface damage and lateral force due to the changes in friction and slope.

Intermittent-contact mode (tapping mode) is employed in order to address these issues. In this mode, the cantilever is oscillated at its resonant frequency in air or other gases and positioned above the surface. Therefore, it only taps the surface for a very small fraction of its oscillation period. Lateral forces are consequently reduced compared to the contact mode. Besides, it is useful for samples having a very soft surface since the duration of contact with the surface is very short. Finally, the non-contact mode is a powerful method to characterize magnetic force or electrostatic force materials with the assumption that the van der Waals force and the capillary force can be ignored.

In this study, a Digital Instruments Nanoscope IIIa AFM with a 20 nm SiN probe mounted was used. Figure 2.16 illustrates its schematic and a detail view of the optical head. It can operate either contact or tapping mode.

AFM provides information about surface roughness, growth mode changes and dislocation density. In this work, our bulk GaN grown on *c*-plane sapphire substrates measured by AFM showed a root mean square (RMS) surface roughness value of about 1.5$\sim$3 Å. In contrast, non-polar bulk GaN grown on *r*-plane sapphire substrates exhibited much rougher surfaces with a RMS roughness >2 nm. By counting the number of growth step termination defects at the surface, the mixed-type and pure

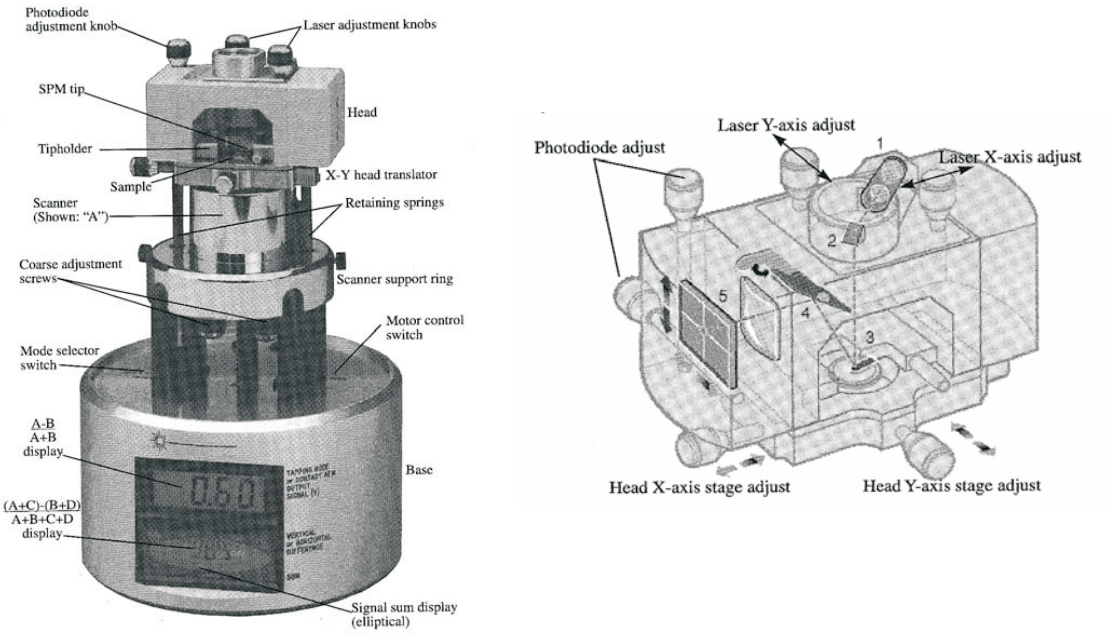

Figure 2.16: Schematic of AFM (left) and optical head (right). The main components of the optical head are: laser (1), mirror (2), cantilever (3), tilt mirror (4) and photodetector (5). After Ref. [37].

screw-type dislocation density was estimated to be about $10^9\,\mathrm{cm}^{-2}$ [36]. However, edge-type dislocations cannot be observed by AFM as they do not terminate at the surface and are usually too small to be resolved by AFM.

A Scanning Electron Microscope (SEM) was also used for the measurement of film thickness and surface topography. The basic principle of a SEM is projecting a focused electron beam on the sample surface and detecting electrons which are scattered after the collisions between the electron beam and atoms at or near the sample surface. A SEM consists of an electron gun, an anode, a vacuum chamber, electron lens and coils for focusing. The image of the sample surface is represented by brightness contrast. It is generated by photons as the emitted electrons from the surface collide with a scintillator material.

After the incident electron beam collides with atoms, electrons with various en-

ergies can be detected as shown in Fig. 2.17. Electrons with energies of 2∼10 keV are called secondary electrons and are typically used to probe surface morphology. Back scattered electrons and X-rays having higher energy are useful to analyze chemical composition contrast and material compositions.

A Philips XL30FEG and Zeiss DSM 950 were used in this work. The thickness of bulk GaN and AlGaN alloys was measured and consequently the growth rate of those was obtained. In this work, the typical growth rate of our GaN is about 2 μm/h and the AlN growth rate is between 0.5∼1 μm/h depending on growth conditions applied. Since the generation of secondary electrons is related to the topography of the respective sample, SEM is a good tool for characterizing the surface. The surface topography of bulk GaN and AlN was also studied to investigate their surface quality after chemical etching.

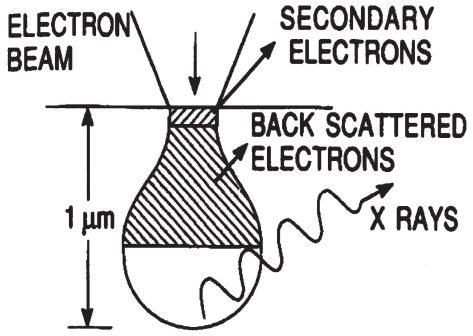

Figure 2.17: Signals emitted from interactions between the incident electron beam and the sample. After Ref. [38].

2.4.8 Secondary Ion Mass Spectrometer

The Secondary Ion Mass Spectrometer (SIMS) is a superior tool for determining impurity concentrations with respect to film depth. SIMS is a destructive technique, but provides accurate results for impurity profiles. It is based on the acceleration of heavy metal ions at a target sample and sputtering off constituent atoms. Atoms

from the target sample become then ionized, and are attracted to a charged detector. The sputtering ion used in this work was cesium (Cs+) with a primary ion energy of 4 keV.

2.4.9 X-ray Photoelectron spectrometer

The X-ray Photoelectron spectrometer (XPS) is a useful tool for elemental composition analysis of the surface in the range of 1∼10 nm. When a sample is irradiated by aluminum or magnesium X-rays, electrons gaining kinetic energy escape from the surface. By analyzing their kinetic energy, the elements present in the material and their chemical states can be obtained. In this work, a Thermo VG XPS system was used with Mg kα (1253.6 eV) in order to identify the presence of *in-situ* grown SiN_x.

2.4.10 Surface profiler

Surface profilometry is another common tool to characterize the surface topography. The vertical position of a diamond stylus tip varies as the surface of the sample changes. It can characterize etching depth, MEMS structures, and surface roughness including film stress. In this work, a Dektak 6M from Veeco was used for the measurement of the wafer curvature to estimate the film stress (section 3.3) and the calibration of the AlN etching rate (see also section 6.3).

The Stoney formula as given in Eq. 2.19 shows that the stress built in a deposited film due to lattice and thermal mismatch can be calculated from the mechanical properties of the film and the curvature change of a wafer before and after the film deposition.

$$\sigma_r = \frac{E d_s^2}{6(1-\nu) d_f} \left(\frac{1}{R_o} - \frac{1}{R_f} \right) \tag{2.19}$$

In Eq. 2.19, E and ν is Young's Modulus and the Possion ratio of the film, re-

spectively, and d_s and d_f is the thickness of the substrate and the deposited film, respectively. R_o and R_f is the radius of the wafer before and after film deposition. In this work, E and ν of GaN were set 345 GPa and 0.25, respectively. In order to obtain accurate results, the sample shape must be approximately a sector of a circle and the same points on the wafer must be measured for all scans.

2.5 Interferometer

In this section, the laser interferometer is introduced. It is not a direct characterization technique. However, it allows real time *in-situ* monitoring of III-Nitrides growth which provides information about the growth rate, surface roughness change and growth interruption.

The principle of a laser interferometer is based on Fabry-Pérot interferometry. In multiple layers consisting of substrate, grown film and air, the reflectance is given by:

$$R = \frac{{r_1}^2 + {r_2}^2 e^{-\alpha d_f} + 2 r_1 r_2 e^{-\alpha d_f} \cos\Delta}{1 + {r_1}^2 {r_2}^2 e^{-\alpha d_f} + 2 r_1 r_2 e^{-\alpha d_f} \cos\Delta} \tag{2.20}$$

$$r_1 = \frac{n_f - 1}{n_f + 1},\ r_2 = \frac{n_s - n_f}{n_s + n_f} \tag{2.21}$$

where r_1 and r_2 are the Fresnel coefficients for the air/film and film/substrate interfaces and Δ is the periodicity of the interference pattern (peak to peak). α is the absorption coefficient which is dependent on the extinction coefficient of the film at the probe wavelength λ. When n_f and n_s are the index of refraction for the film and the substrate and d_f is the film thickness, Δ is given by:

$$2\pi = \Delta = \frac{4\pi d_f n_f}{\lambda} \tag{2.22}$$

The incident angle of the laser beam is assumed to be normal to the surface. The thickness corresponding to one period can be verified afterwards by SEM measurements. Approximately, one oscillation corresponds to 135 nm GaN in this work.

Accordingly, n_f is calculated to be about 2.135. This value is a little off from 2.39 at a growth temperature of 1000 °C as reported by Thomas Swan. The difference is due to our higher growth temperature (1030 °C) and the measurement error of the SEM.

The reflected intensity will be attenuated as the thin film growth progresses. The relevant terms for the attenuation are the exponential terms in Eq. 2.20. The absorption coefficient α is described by the film extinction coefficient k_f

$$\alpha = \frac{4\pi k_f}{\lambda} \tag{2.23}$$

If the probing wavelength is chosen where III-Nitrides have very low k_f, the attenuation of the signal is ascribed to other factors such as the surface roughness rather than the film absorbance.

In this work, a commercial laser interferometer built by Thomas Swan is used. Its working principle and setup within the reactor is shown in Fig. 2.18. The red diode laser (λ=635 nm) is mounted at the top of the S/H. At this wavelength, k_f is less than 0.01 so that the film absorbance effect can be ignored.

Prior to use, a calibration must be performed with a 100 % and a 0 % reflectivity material, for example a mirror and a black surface. The laser was aligned in order to maximize the reflectivity from a bare sahppire wafer by adjusting its x, y position and tilt angle. Typical reflectivity of a sapphire substrate used in this work was about 7.5 % depending on the roughness of the sapphire wafer. The aligned laser beam is split into two directions by a 1:1 beam splitter: to the center of the sample through an 1/4" optical port and to a photo diode as a reference signal. The reflected signals from the wafer are collected by a photo diode and sent to a lock-in amplifier for reducing background noise. A sensor and an associated gearbox mounted on the rotation drive motor provide a synchronisation pulse once per revolution to the

reflectometer control unit. Therefore, any point on the wafer or any wafer from the three wafer pockets can be monitored.

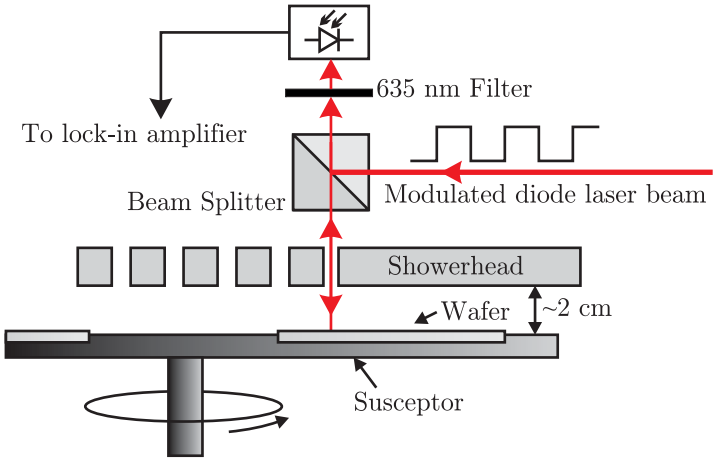

Figure 2.18: Schematic of the *in-situ* laser interferometer set-up. After Ref. [39]

Figure 2.19 shows a typical laser interferogram of GaN. The laser signal reflected from the surface changes as the growth proceeds. In order to help understanding these changes, six major growth events are indicated alphabetically. The temperature profile is presented along with the reflectance signal. The growth events of each step are as follows.

- A : Sapphire substrate cleaning

  The reflectance signal remains relatively constant which indicates the value of a bare sapphire wafer until GaN nucleation layer growth starts. Small variations observed here are due to the refractive index change corresponding to the temperature change.

- B : Nitridation and low temperature nucleation layer growth

  The reflectance signal increases once the growth of the NL begins.

- C and D : Temperature ramp up and nucleation layer annealing

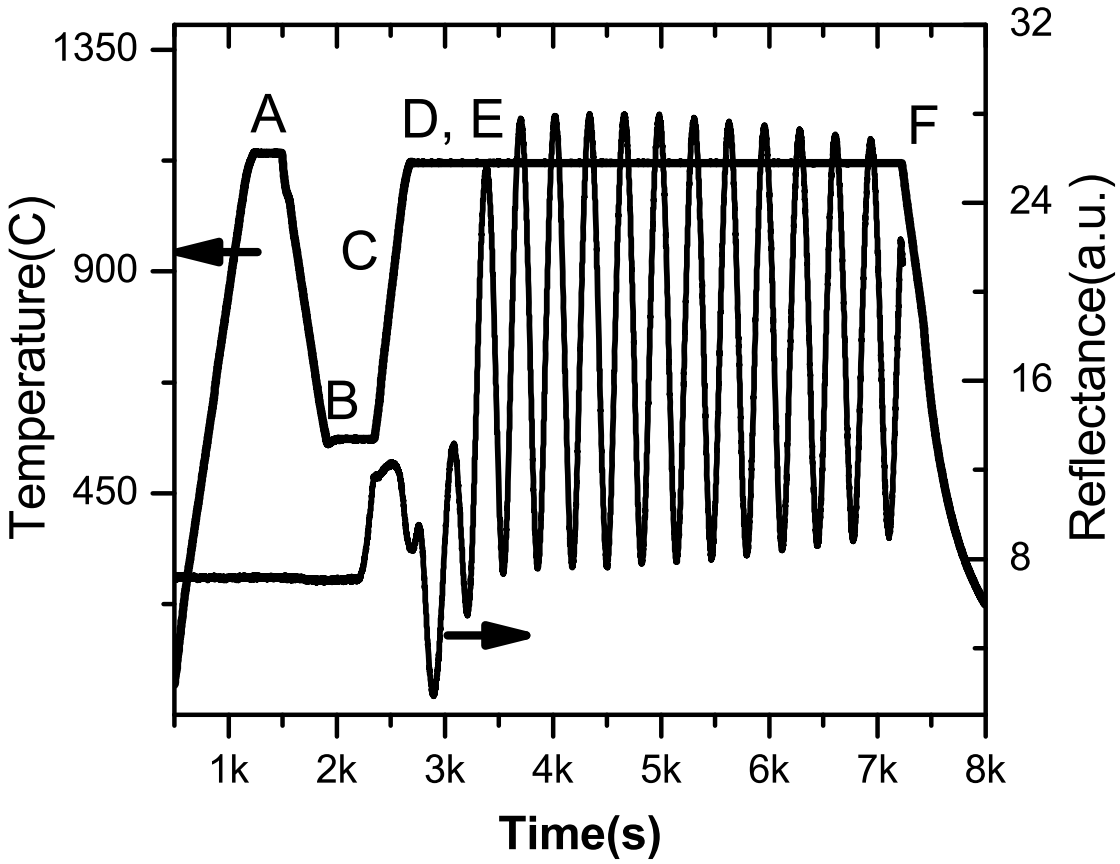

Figure 2.19: Profile of temperature and reflectance signal during GaN growth.

The signal drops during the process of temperature ramp up and NL annealing where no TMGa is fed into the reactor.

- E : High temperature GaN growth

  The reflectance signal recovers as high temperature GaN grows. Slow attenuation is observed.

- F : Growth stop and cooling down

  The monitoring of the reflectance signal is stopped.

Apparently, each growth event is distinguished by an associated interferogram pattern. Therefore, the interpretation of the interferogram helps understanding the evolution of the surface morphology at each stage. In case of bulk GaN growth, the features between B and E have tremendously important meaning which will be addressed later in section 3.1. By manipulating the surface morphology in this period, the quality of GaN is significantly affected.

2.6 Conclusion

The MOVPE system, which was set up for carrying out the work presented in this thesis, was described. The system used is a commercial system manufactured by Thomas Swan Scientific Equipment Ltd. It is equipped with a 3x2" Closed-Coupled Showerhead designed to improve layer uniformity and reduce gas mixing and residence time. Separate alkyl and hydride source injection lines were used for the suppression of pre-reaction between sources. Both pressure balancing and flow make-up systems are incorporated to improve the interface quality of the heterostructures.

The electrical and optical characterization systems were presented. Capacitance-voltage measurements and low temperature Hall effect measurements

were used to identify the presence of 2DEG in AlGaN/GaN heterostructures. Naked eye and optical microscope studies provided quick and qualitative information about the grown layers. Further investigations of the surface morphology were done using scanning electron and atomic force microscopy. Low temperature photoluminescence was utilized to study defects and conductivity of the layers grown in this work. Using an X-ray system, information about thickness, crystalline quality and the composition of ternary alloys was obtained. SIMS and XPS provided quantitative information about the depth profile of impurities. The built-in strain in nitride layers due to heteroepitaxy growth was estimated by using a surface profiler. *In-situ* growth monitoring was carried out with a laser interferometer.

CHAPTER III

POLAR GaN

Bulk GaN is a fundamental layer for all III-Nitride electrical and optical devices. The base GaN on which the device layers are grown is often referred to as buffer layer or template. Its thickness is usually between 2 μm and 3 μm. The key parameters characterizing its quality can depend on the application but in general smooth surface and good crystalline quality are required.

This chapter addresses the growth of bulk GaN with good crystalline quality and electron transport properties, low background carrier density and high sheet resistance. Several growth runs and material characterization were performed for this purpose and in particular for obtaining highly resistive GaN. The improvement in device characteristics associated with resistive GaN was confirmed by DC and high frequency electrical characterization. n-type intentional doping processes were studied in order to control the electrical conductivity of nitride based semiconductor devices.

The results and issues related to the aforementioned optimization processes will be described in this chapter. It should be noted that the bulk GaN discussed here is grown on c-plane sapphire substrates and is consequently polar GaN. The results of polar nitride heterostructures will be addressed in a subsequent chapter. Non-polar

nitrides will be discussed in chapter V.

3.1 Overview of bulk GaN growth

The understanding of the growth process is essential to apprehend the correlation between the quality of bulk GaN and growth parameters. Therefore, an overview of the bulk GaN growth process is given in this section before the growth details are discussed. Furthermore, the impact of the process parameters corresponding to each step are addressed.

Standard GaN growth consists of five main steps:

- Sapphire substrate cleaning
- Nitridation
- Low temperature nucleation layer growth
- Temperature ramp up and nucleation layer annealing
- High temperature GaN growth

The flow of these steps is illustrated in Fig. 3.1 as a function of time. Here, only the change of temperature, carrier gas H_2 flow, TMGa and NH_3 flow are shown because of their importance. The gas flow and the MO sources need to be optimized with respect to the design capacity and efficiency of the reactor. For the stabilization of the growth system, the response time of mass flow controllers, MO valves and gases and pressure controllers etc. must be considered in the ramp-up and ramp-down times of each parameter.

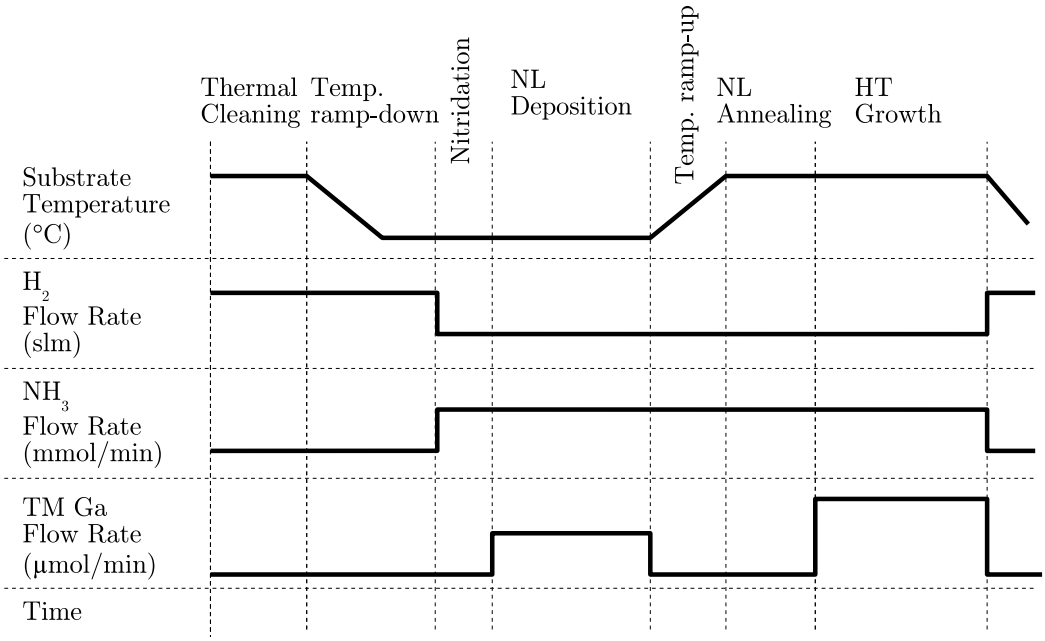

Figure 3.1: Standard growth sequence for bulk GaN.

3.1.1 Thermal cleaning and nitridation

The substrate cleaning is carried out with high hydrogen flow at a temperature higher than the main GaN growth temperature in order to remove contamination of the sapphire wafer especially with oxygen. The annealing time is typically 5∼10 min.

In the following nitridation step, the temperature ramps down to nucleation layer (or buffer layer) growth temperature, typically 530∼560 °C. Ammonia is fed into the reactor for a short period of time before the TMGa starts flowing. The nitridation process modifies the sapphire substrate to amorphous AlN_xO_{1-x} within a couple of mono layers [40] and promotes two dimensional nucleation layer (NL) growth. In addition, it eliminates the nucleation of misoriented GaN islands [41].

The grown NL layer is strongly dependent on the length of the nitridation time and ammonia flow. Since the transformation of the NL occurs after heat treatment, the impact of the nitridation step will be addressed together with the NL annealing process in the following section. The optimum nitridation time was found to be

between 5 and 60 seconds at 200 torr. More results and discussions about nitridation can be found in Refs. [42], [43], [44].

3.1.2 Nucleation layer growth and annealing

As reviewed in section 1.1, the use of low temperature (LT) AlN [45] or LT GaN layers [4] spurred the improvement of GaN quality. It allowed conversion of the three dimensional (3D) growth mode usually observed in the direct GaN growth on sapphire wafers to the 2 dimensional (2D) growth mode so that GaN with a smooth surface can be achieved.

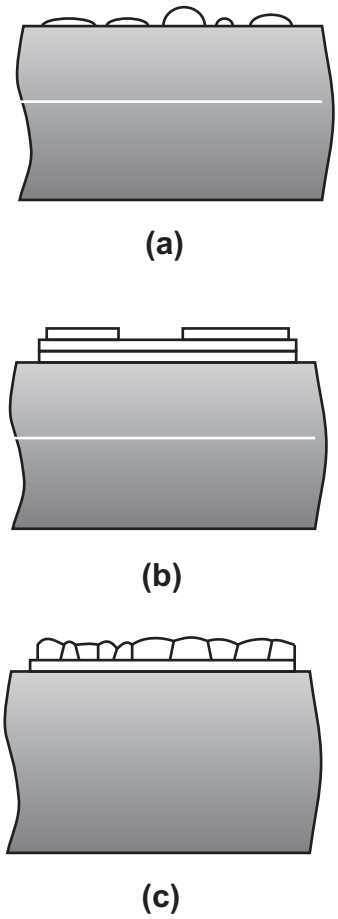

Figure 3.2: Three different growth modes. (a) Volmer-Weber mode : Island growth ($\gamma_f > \gamma_s + \gamma_i$), (b) Frank-van-der-Merwe mode : Layer by layer growth ($\gamma_s > \gamma_f + \gamma_i$), (c) Stranski-Kranstanov : Finite layer growth and island growth.

In general, heteroepitaxial growth is of one of the three growth mode types as

shown in Fig. 3.2. The growth mode is determined by the surface free energy of the substrate (γ_s), by the interface (γ_i) and by the deposited film (γ_f) [46, 47]. When γ_f is greater than $\gamma_s + \gamma_i$, Ga and/or N atoms diffusing from the boundary layer stick to the growth surface and form random islands or clusters. They coalesce with each other and result in a polycrystalline film being produced. This mode is called the Volmer-Weber (3D) mode of growth. The direct growth of GaN on a sapphire wafer at high temperature is of this type. Thermal treatment can change the orientation of the polycrystalline film.

On the other hand, Frank-van der Merwe (FM) mode occurs when γ_s is greater than $\gamma_f + \gamma_i$. An initial monolayer is formed on the substrate. The following layer will be deposited after the first monolayer is completely covered. In case the surface energy is greater than the strain energy in the deposited film, layer by layer (2D) growth continues. Otherwise, strain energy leads to defecting of the film by developing dislocations so that new nuclei or clusters are created.

The Stranski-Kranstanov (SK) mode is an intermediate growth mode between 3D and 2D growth modes. The growth begins with 2D but converts to 3D in order to release internal stress due to lattice mismatch after one or more monolayers. Quantum dots and wires are formed in this mode.

In this work, LT GaN NLs are exclusively used for the growth mode conversion from 3D to 2D mode. Since the NL growth is performed at relatively low temperatures (500$\sim$600 °C), the growth process is surface kinetically limited. In this growth regime, the growth rates strongly depend on the growth temperature. Therefore, the minimizing of the temperature difference across the wafer is extremely important for a uniform NL and GaN layer.

Early research about LT GaN NL growth reported that GaN NLs are also

amorphous like AlN NLs. However, structural investigations by X-ray diffraction (XRD) and transmission electron microscopy (TEM) revealed that GaN NLs grown after an optimum nitridation contain both a cubic phase with a high density of stacking faults and a hexagonal phase as shown in the left column of Fig. 3.3 [48].

During the NL annealing process, the NL recrystallizes and turns into a purely hexagonal crystal. Furthermore, GaN evaporates from the NL surface so that 3D islands are formed. Later these islands grow laterally and vertically and finally coalesce with neighboring islands. During this process, sub-grains develop and defects are generated. As addressed in section 2.4.6, the defects are edge-type, screw-type and mixed character TDs. Island coalescence completes after 0.3 μm [36] and the TD density is reduced dramatically above this region. Defects in the high temperature GaN, are therefore attributed to the characteristics of the NL. The pretreatment of the sapphire wafer, the thickness of the NL and its growth condition and annealing time are key factors determining the quality of the subsequently grown GaN.

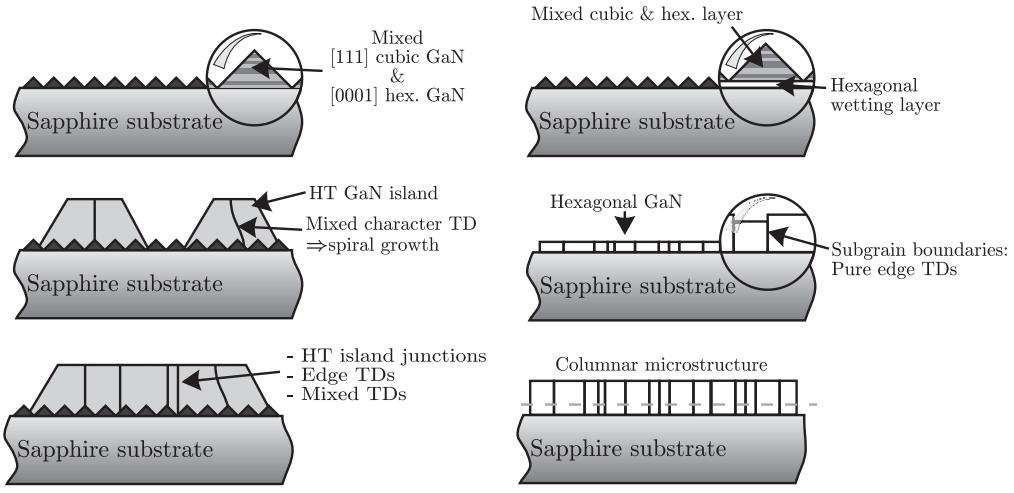

Figure 3.3: HT GaN growth evolution with GaN nucleation layer. The left column shows the GaN growth evolution with ideal nitridation conditions. The right column shows the case with long nitridation time. After Ref. [49].

An example of the above effects is the case of a long nitridation. Grain growth

is observed in this case due to the presence of a very thin AlN wetting layer which is formed during the long pre-ammonia treatment as shown in the right column of Fig. 3.3. This leads to lateral grain growth and growth of a highly columnar structure of GaN. GaN grown under such conditions is expected to have a high density of TDs. Its electron mobility will consequently be degraded because TDs act as scattering centers in the electron transport [50].

Due to the significant role of the nucleation layer for the quality of the grown GaN, a plethora of work has been done to optimize it. It is known that island size, its density, roughness, orientation and thickness determine the quality of the HT GaN. All these factors can be optimized by controlling the NL growth temperature [51], the V/III ratio by changing the Ga flow or the NH_3 flow [52], the growth rate [53], the NL thickness [54], the temperature ramp-up time and the duration of annealing [48, 55, 56]. More extensive studies can be found in Refs. [26, 57, 58]. The impact of the NL growth condition on the material properties are also reported by Nakamura in Ref. [4].

3.1.3 High temperature GaN growth

The next step following NL growth and its recrystallization is the growth of high temperature (HT) GaN. This layer is used as a template for further growth of ternary alloys such as $Al_xGa_{1-x}N$ and In_xGa_{1-x} N or is used directly for the fabrication of bulk GaN Schottky diodes etc. Either way, layers with good Hall mobility, low background carrier concentration, a smooth surface and low defect density are preferable for good electrical and optical performance. The quality of the HT GaN is affected by growth temperature, growth pressure, V/III ratio and the thickness of the GaN layer.

The growth temperature of HT GaN layers is typically in the range of

950∼1100 °C. In this temperature range, the growth rate is determined by the diffusion rate of Ga and N atoms. Since a high V/III ratio is maintained to prevent nitrogen vacancies, ammonia is assumed to be saturated compared to the group III materials. Therefore, the growth rate of GaN strongly depends on the TMGa flow. The growth rate drops slightly as the temperature exceeds 1030 °C due to Ga desorption from the GaN surface. The growth temperature is also known to affect the film resistivity by creating acceptor-like TDs during the NL annealing process [59, 60].

The pressure range of GaN growth is much wider than of AlN or InN growth. This is attributed to the different diffusion lengths of group III atoms. The diffusion lengths of the atom species involved can be classified as follows: In > Ga > Al. Therefore, much lower growth pressure is desirable for AlN growth than for GaN and InN growth in order to enhance the mobility of atoms on the growth surface. The advantage of low pressure (LP) growth for GaN is increased mass-transport over the boundary layer and lower residence time on the growth surface. At higher pressure, strain relaxation is much more suppressed so that lower TD densities are observed [61]. For the case of LP GaN, growth pressure is maintained between 100 torr and 300 torr for the GaN NL and bulk GaN.

Although high ammonia pressure is required to prevent nitrogen vacancies, extremely high V/III ratios can reduce the growth rate due to a parasitic reaction between ammonia and the metal organic materials. Typically, the V/III ratio is optimum in the range of 1000∼5000 .

As mentioned in section 3.1.2, the TD density in bulk GaN is decreasing remarkably after 300 nm where the coalescence of the NL is complete. In addition, a slight reduction of defects is expected as the film grows thicker because some of the TDs are bent laterally and their propagation through the layer is stopped [62].

This contributes to enhance the mobility and reduces the background carrier density. Reasonable quality of GaN is typically obtained for GaN thicknesses exceeding 2 μm.

3.2 Unintentionally doped (UID) GaN

UID GaN growth was carried out to evaluate the quality of material grown by our TS MOVPE system. The GaN layers were characterized by Hall, XRD and SEM in order to investigate their electrical properties, crystalline quality and growth uniformity.

3.2.1 Growth of UID GaN

c-plane sapphire wafers having a thickness of 430$\pm$25 μm, 2" diameter and polished on one side were used in this work. For the growth of the NL, the sapphire substrate must have an atomically flat and clean surface. Its root means square (RMS) surface roughness is less than $\pm$0.5 nm (manufacturer specification). The susceptor rotates with a speed of 100 rpm during the growth so that a uniform gas flow can be ensured over the wafers. A 10 slm total gas flow in the reactor is maintained throughout the entire growth process and 2.5 slm ammonia flow is used for both LT NL and HT GaN growth. A typical structure of bulk GaN grown in this work is depicted in Fig. 3.4.

Thermal cleaning of the substrate is performed at 1060 °C with high hydrogen flow for 5 min and then the growth temperature (T_g) and growth pressure (P_g) are set to 530 °C and 200 torr, respectively for the NL growth. After short nitridation, a 20$\sim$25 nm thick NL was grown. The temperature is then raised to 1040 °C to anneal the NL. Temperature ramp-up time (t_r) is 300 s. The NL is annealed at this temperature for t_a and the HT GaN growth follows. A summary of the growth

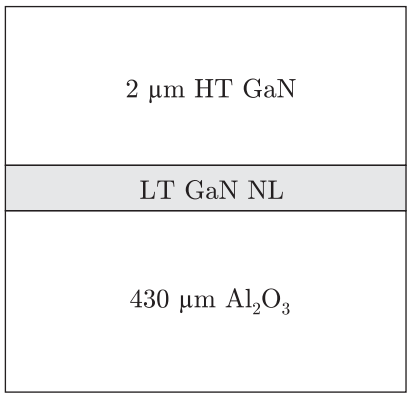

Figure 3.4: Typical structure of bulk GaN grown in this work.

conditions is tabulated in Table 3.1.

	P_g	T_g (°C)	V/III ratio	t_r (s)	t_a (s)
NL	200	530	3600	300	150
GaN	100	1040	920	-	-

Table 3.1: Growth conditions for NL and HT GaN.

The residual stress in the grown GaN was measured by a commercial laser ellipsometer (FSM 500). Here a laser beam with a wavelength of 650 nm scans across the wafer and allows measurement of the wafer curvature. This step is performed before and after the GaN growth. Four different directions are scanned to increase the measurement accuracy as described in Fig. 3.5. The surface profiles of the sapphire substrate with and without GaN on top were scanned from the top to the flat side (direction 2) and the results are presented in Fig. 3.6. The concave shape shown in the figure indicates that the stress present in the layer is compressive.

The residual stress is extracted from the Stoney's equation (see section 2.4.10 for details). The residual stress corresponding to these conditions is about -0.68 GPa. The origin of this stress is thermal and lattice mismatch between GaN and the sapphire wafer. Typical stress values of GaN grown on sapphire by MOVPE are in

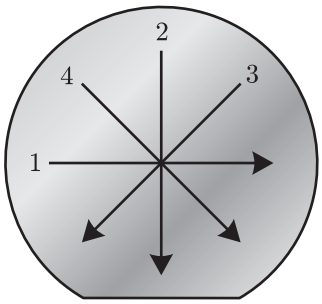

Figure 3.5: Diagram of the four scan directions for wafer surface curvature evaluation by a surface profiler.

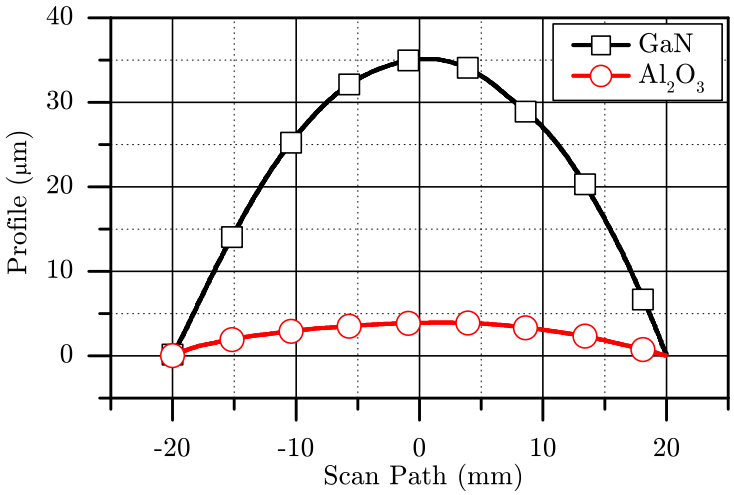

Figure 3.6: Example surface profiles of a wafer before and after GaN deposition (scan direction 2).

the range of -0.2 to -0.7 GPa [63]. This indicates that the GaN grown in this work is rather highly strained.

3.2.2 Characterization

In order to characterize the crystalline quality of the grown UID GaN, the BEDE D1 XRD system is used. The ω rocking curves of a sapphire substrate and of one of the first bulk UID GaN layers produced in this work are presented in Fig. 3.7. The measured full width at half maximum (FWHM) of the sapphire (006) reflection plane is about 44" showing that the substrate quality is high. The FWHM of the

GaN symmetric reflection plane (002) and of the asymmetric reflection plane (102) are 354" and 671", respectively as can be seen from Fig. 3.7. As mentioned before, screw and mixed TDs broaden the symmetric FWHM while the asymmetric FWHM reflects the total TD density including edge dislocations. Therefore, the density of screw and mixed TDs and of edge TDs can be expected to be around $10^8\,\mathrm{cm}^{-2}$ and $5 \sim 7 \cdot 10^{10}\,\mathrm{cm}^{-2}$, respectively[1].

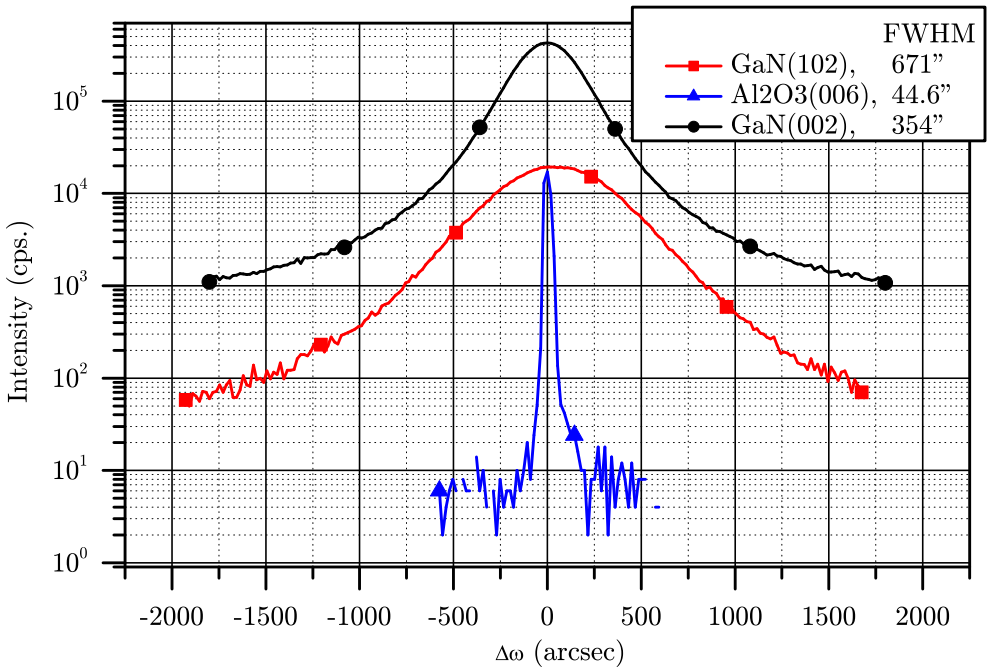

Figure 3.7: Symmetric and asymmetric ω rocking curve for GaN and Al_2O_3.

The thickness of the UID GaN was measured with a ZEISS DSM-940 SEM for the calibration of the growth rate. The average growth rate is $2.30 \pm 0.1\,\mu$m/h and its uniformity across the wafer is about $\pm 5\,\%$.

The range of the Hall mobility of UID GaN grown in this work is $126 \sim 138\,\mathrm{cm}^2/\mathrm{Vs}$ with a background carrier concentration of $0.7 \sim 1.28 \cdot 10^{17}\,\mathrm{cm}^{-3}$. Its sheet resistance ($R_s$) is mid $10^3\,\Omega/\square$. In good quality UID bulk GaN, the background carrier density is mid $10^{16}\,\mathrm{cm}^{-3}$. Since the UID bulk GaN grown in this work

[1] based on the correlation between FWHM and TD density as given in Ref. [64]

is rather conductive due to high background carrier densities, it is not directly suitable for high frequency devices. Therefore, growth optimization was performed with special focus on enhancing the sheet resistance, as will be discussed in the following section.

3.3 Resistive GaN

Even though the predicted intrinsic carrier density is $\sim 10^{-6}\,\mathrm{cm}^{-3}$ [65], epitaxially grown GaN has intrinsic n-type background carrier density of $>10^{16}\,\mathrm{cm}^{-3}$. This problem lies in nitrogen vacancies, oxygen and other impurities incorporated into the material during the growth. Nitrogen vacancies and oxygen are known to be residual donors in GaN. Such unintentionally doped (UID) GaN layers impede the electrical and optical device performance. Particularly in high electron mobility transistors (HEMTs) and heterojunction field effect transistors (HFETs), UID GaN degrades the high frequency performance and hinders good pinch-off because of the presence of a parasitic conductive channel formed through the UID GaN as shown in Fig.3.8. Therefore highly resistive (HR) or semi-insulating (SI) GaN layers are substantial for proper high frequency operation.

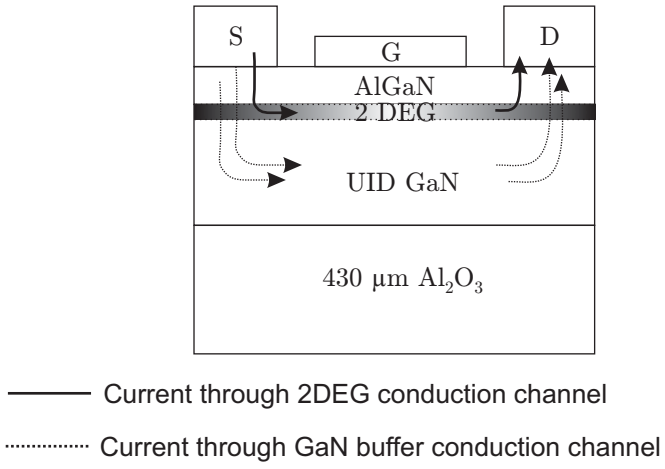

Figure 3.8: Two conduction channels in AlGaN/GaN HFET devices.

In order to obtain HR GaN, residual donors must be minimized by means of suppressing the impurity incorporation and residual donor compensation by either deep level acceptors or acceptor-like threading dislocations (TDs). However, since TDs are reported to be electron scattering centers, their density needs to be carefully controlled. Impurities in GaN should be minimized to achieve this objective. However, as will be reviewed in detail in the subsequent section, a significant part of impurities originate from carrier gases and MO sources, the reactor parts, and the reactor purging time after wafer loading etc. Parameters of this type are controlled through the hardware involved in MOCVD growth rather than the growth itself. This work focuses on the residual donor compensation method.

Residual donor compensation can be achieved by introducing deep acceptors created by intentional doping with transition metals such as Cr, Fe or Carbon. On the other hand, acceptor-like TDs are produced by controlling growth parameters without any intentional doping. In this work, resistive GaN was studied by adjusting the growth parameters since utilizing Fe or Cr may lead in reactor contamination [65]. An important aspect considered was the origin of the resistivity as described.

In our previous work, Hubbard *et al* achieved a GaN sheet resistance as high as $10^{10}\,\Omega/\square$ by optimizing growth parameters, especially the NL annealing temperature and the nucleation layer (NL) thickness [60]. However, the limitation imposed in this approach was a very narrow growth temperature window. A high sheet resistance could be obtained only at a specific annealing temperature (1030 °C) and the sheet resistance dropped significantly at higher or lower temperature. Moreover, the residual donor compensation mechanism were not clear.

Assuming that the donor compensation in the UID GaN grown here is ascribed to TDs where acceptor carbon impurities segregate, it is not possible to explain

the lower sheet resistance of GaN annealed at 1050 °C. Although GaN annealed at 1050 °C has a higher TD density than GaN at 1030 °C, its sheet resistance was only $10^6\,\Omega/\square$. This chapter provides further experiments and clarifications regarding the origin of the GaN resistivity.

The goal of this work is to obtain resistive GaN over a wide growth parameter window with high reproducibility. Therefore, the growth parameters were studied at a fixed annealing temperature of 1040 °C. Furthermore, the same processes were applied to numerous growth runs to ensure process reproducibility. Hall measurements, *in-situ* laser interferometry, photoluminescence measurements and XRD measurements were utilized to characterize background carrier density, crystalline quality and to identify the compensation mechanism. The impact of the optimized resistive GaN on HFET devices will be presented in chapter IV.

3.3.1 Impurities in UID GaN

1) *Nitrogen (N) vacancy*

GaN contains always N vacancies due to the high equilibrium pressure of nitrogen. N vacancies are considered to be the dominant source of donors in UID GaN. However, good resistive GaN with low background electron concentration was obtained without suppressing N vacancies later. It implies that N vacancies are not a dominant donor source in GaN.

2) *Silicon*

Si is believed to be a shallow donor since it occupies the energy state between 22 meV and 42 meV from the conduction band minimum [66, 67, 68] as shown in Fig. 3.9 when Si substitutes Ga sites (Si_{Ga}). The source of silicon in UID GaN can be from decomposition of SiC substrates or SiC coating of a susceptor. Since sapphire substrates were used in this work, the main source of Si in UID GaN is

considered to be the susceptor.

3) *Oxygen*

Oxygen incorporated in the nitrogen lattice site (O_N) is known to be the major source of background donors by donating its extra valence electron. A more complex form involved with V_{Ga} (O_N-V_{Ga}) is also proposed as a donor [69]. Figure 3.9 shows the donor levels related to oxygen in GaN occupying the shallow donor state between 2 and 34 meV from the conduction band minimum [70, 71, 72].

The possible origins are moisture or oxygen remaining in ammonia and the MOs or water produced during the sapphire thermal cleaning process as the sapphire substrate is etched by hydrogen at high temperatures. The exposure of the reactor to air during the wafer loading process is probable source. The use of pre-baked sapphire and purging the reactor chamber for a long time prior to the growth effectively reduced background donor concentration down to $2.28{\cdot}10^{16}\,\mathrm{cm}^{-3}$ [73].

4) *Carbon*

Carbon is a common impurity in MOCVD grown GaN films because of the use of metal organic group III precursors. SiC coated graphite susceptors or SiC substrates are plausible sources, too. Unlike Si or oxygen, carbon exhibits a more complicated behavior and it is known as a amphoteric dopant. It acts like a shallow donor with an ionization energy of 200 meV when carbon substitutes Ga (C_{Ga}). Conversely, it becomes a shallow acceptor if it incorporates into the nitrogen site (C_N). Interstitially placed carbon (C_i) is more interesting. Its energy level is mid-gap and its electrical characteristics are determined by the Fermi level positions. Therefore, carbon is often used for donor compensation in UID GaN. However, a

non-optimized quantity of carbon can haunt the device performance. Its presence in the active region can play the role of a scattering center and has been also implicated in gate leakage and dispersion in HFET devices [74].

5) *Hydrogen*

Hydrogen can be incorporated during MOVPE growth of GaN through MO sources and hydrogen carrier gas. The issue related to passivating Mg acceptors is a well known problem. In contrast, the effect of hydrogen in n-type GaN is negligible because its solubility in n-type GaN is very low in comparison to that in p-type GaN [75].

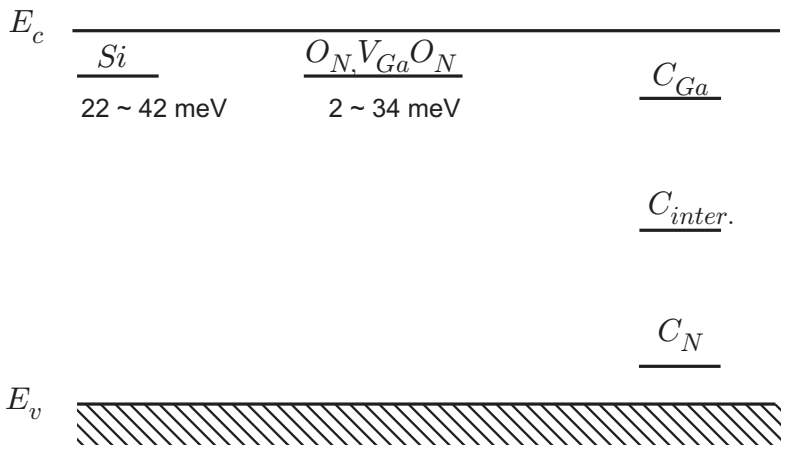

Figure 3.9: Energy state of impurities in UID GaN.

3.3.2 Optimizing resistive GaN

The aim of this work is to optimize growth conditions so that the residual donors unintentionally incorporated from the system can be compensated by acceptor like threading dislocations (TDs). The density of threading dislocations can be controlled by the thickness of the NL, growth temperature of the NL, growth pressure, growth rate, temperature ramp-up time, NL annealing time and temperature, V/III ratio [60, 76, 77, 78, 79]. Among them, the V/III ratio, ramp-up time and NL annealing time were considered as the key parameters to be studied due to the

profound effect they have on TDs.

Growth temperature and thickness of the NL were ruled out because a small variation of them profoundly impacts on the characteristics of GaN. Growth pressure and temperature for the high temperature GaN are also kept at the same values for UID GaN growth. Growth pressure is often adjusted to control the amount of carbon incorporation and strain. However, they are not of interest in the scope of this work. Growth temperature is chosen around 1040 °C considering the high quality of GaN and the limit of our heater system. A summary of growth parameters considered in this work is shown in Table. 3.2.

During the optimization process, the resistivity of GaN can be predicted at the growth stage - even before Hall measurements - by the *in-situ* laser interferometer. Although it is not a quantitative way of evaluating the resistivity as in case of sheet resistance or carrier concentration characterization, the profile of the interferogram, especially the recovery time, is known to be strongly correlated with the resistivity of GaN.

Fixed parameters	Controlled parameters
Temperature	V/III ratio
Pressure	Ramp-up time
NL thickness	NL annealing time
Growth rate	

Table 3.2: Growth control parameters for NL and HT GaN.

As introduced in section 2.5, the laser interferometer monitors the reflectance change of a grown layer during the growth process. Figure 3.10 demonstrates a typical interferogram of GaN. The x-axis indicates the growth time and the y-axis indicates the reflectance intensity. A significant change of reflectance occurs at five points labeled alphabetically from A to E.

At point A, the reflectance increases as the GaN NL growth starts and continues to do so until it reaches to point B. Between points B and C, the temperature is elevated to 1040 °C and NL annealing is initiated. During this process, the TMGa flow is stopped and only ammonia is fed into the reactor to prevent excessive decomposition of the GaN NL above 900 °C. As the GaN NL evaporates and becomes purely hexagonal NL islands are formed, a reflectance drop is observed. After NL annealing, TMGa is delivered to the reactor and HT GaN growth starts from point C. At the initial stage, growth mode conversion from 3D to 2D takes place. Islands grow vertically and laterally and coalesce with each other from point D. Finally the GaN surface becomes smooth and the reflectance intensity is fully recovered from point E. The recovery time is defined as the time for the complete 2D transition (between point D and point E). The length of the recovery time is known to be correlated with the resistivity of GaN in conjunction with the TD density.

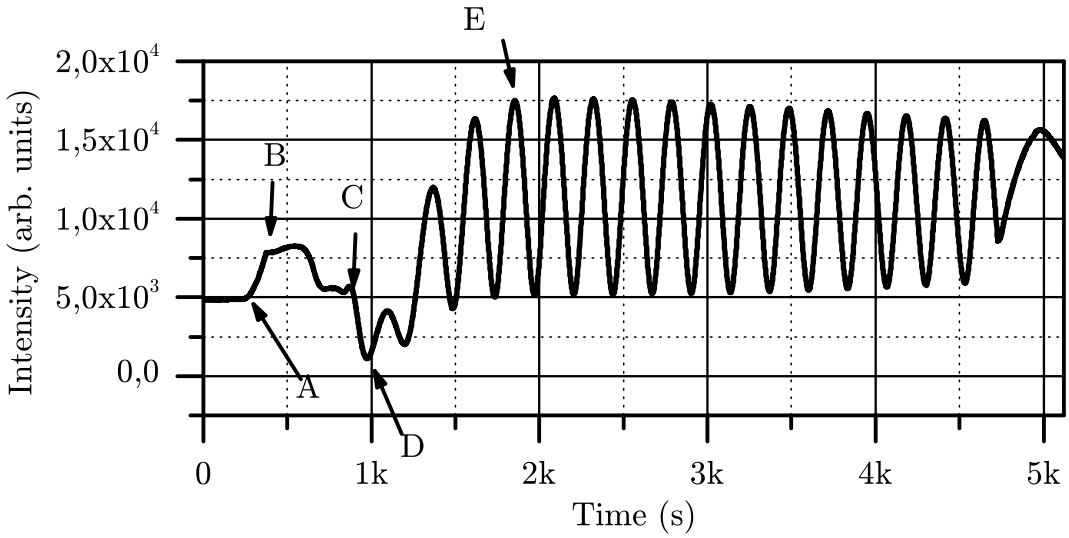

Figure 3.10: Typical interferogram of bulk GaN.

3.3.3 Experiments : Part I

In this experimental part, the investigation was performed with respect to the V/III ratio, NL thickness and temperature ramp up time (t_r). Samples were divided into three groups and different growth conditions were applied to them.

Table 3.3 summarizes the three growth conditions. In condition I, higher V/III ratios were applied for both NL growth and HT GaN growth than the values employed in UID GaN growth. The NL thickness was kept at 22 nm. On the other hand, in growth condition II, the V/III ratio was kept as for the UID GaN growth condition used but the thickness of the NL was increased by 3 nm which is in the range of the deviation of the NL thickness. Lastly, in condition III, the ramp-up time was varied. The V/III ratio remained the same as used in UID growth and the thickness of the NL was kept at 22 nm again.

	Condition I	Condition II	Condition III
NL thickness (nm)	22	25	22
V/III ratio (NL/HT GaN)	5700/1500	4200/1200	4200/1200
Ramp-up time(sec)	260	260	260, 280, 300
NL annealing time(sec)	40	40	40

Table 3.3: Three groups of growth conditions for NL and HT GaN.

Figure 3.11(a) and Figure 3.11(b) present the FWHM of the (002) and the (102) reflection plane of the samples and their recovery time versus ramp-up time. Both the (002) and (102) FWHM remain comparable for all samples except the samples grown under condition I. The (102) FWHM of sample group I is remarkably higher (688") than that of the other samples while its (002) FWHM is a little bit above the others. Since the (102) FWHM is broadened by pure edge-type dislocations and mixed-type dislocations, we can conclude that higher V/III ratio leads to a higher density of edge dislocations. The surface morphology of NL between point C and D

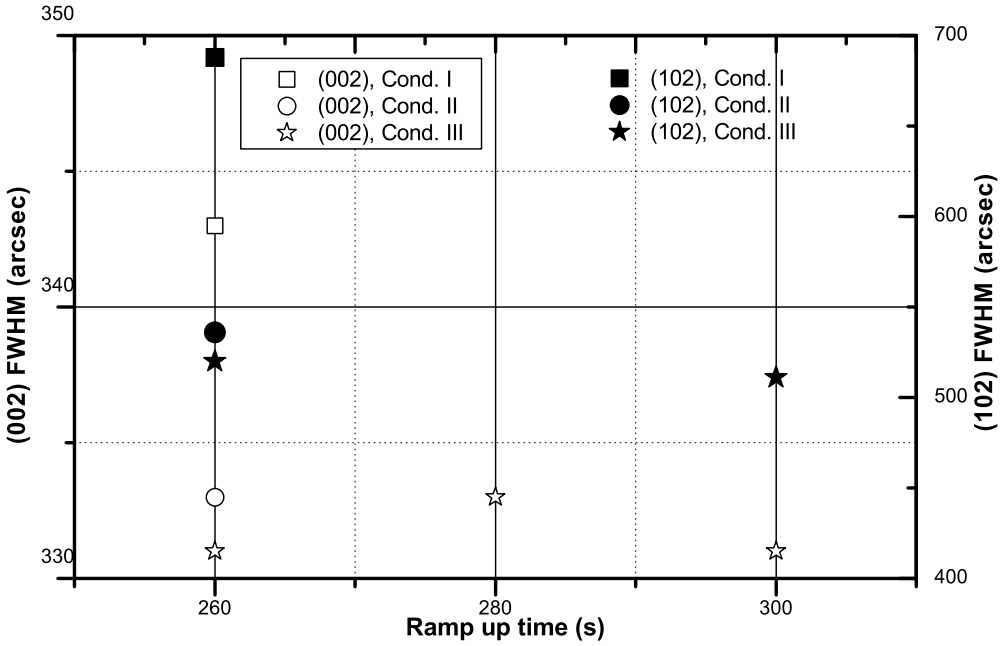

(a)

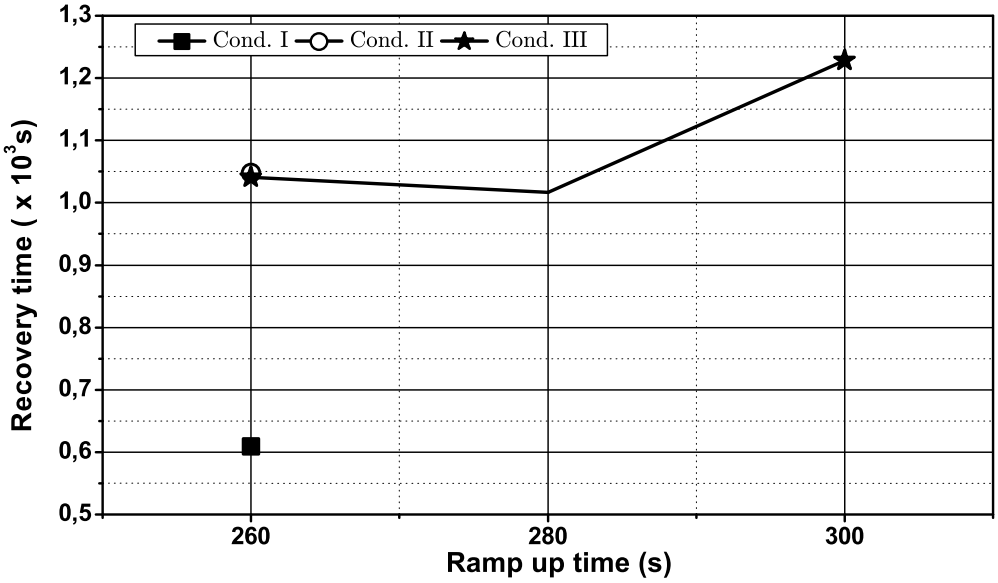

(b)

Figure 3.11: ω rocking curve measurement results and recovery time vs. growth condition. (a) The FWHM value of the (002) and (102) reflection plane. (b) Recovery time vs. temperature ramp up time.

in Fig. 3.10 was investigated with AFM and the results showed that ammonia rich conditions led to a higher density and a lower aspect ratio of the NL islands [80]. The observed high TD density and the quick recovery time under condition I in this work are therefore in agreement with Ref. [80].

There is no significant difference between samples grown under condition II and III in terms of recovery time and FWHM values. Only when the temperature is ramped up in 300 s, the recovery time was increased slightly and the (102) FWHM seems to be improved. Otherwise, stable oscillations in the interferogram are observed within 1025±20 s in most samples and the (102) FWHM is around 530". This allows to conclude that the crystalline quality does not change remarkably by a 2 or 3 nm NL thickness change and that the ramp-up time of 300 s enhances the crystalline quality slightly.

3.3.4 Experiment : Part II

In the following steps, the effect of the NL annealing time is investigated. The NL annealing time is varied between 10 s and 150 s while the other growth parameters were kept as under growth condition III. However, the temperature ramp-up time was chosen to be 300 s considering the improvement of crystalline quality reported in the previous section.

Figure 3.12 compares the interferograms of two samples annealed for short time (40 s) and long time (150 s), respectively. The points where the GaN coalescence is completed are also marked in the figure. Although the reflectances are slightly different at the point where the NL growth stops, this corresponds to even less than 1 nm difference in the NL thickness. Therefore, the recovery time is solely dependent on the annealing time.

Figure 3.13 shows that the FWHM (102) associated with edge and mixed TDs

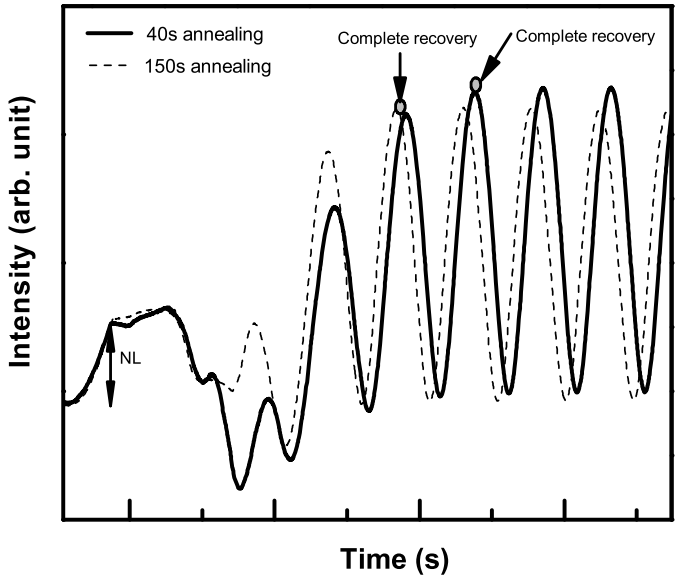

Figure 3.12: Interferograms of two samples annealed for 40 s and 150 s.

strongly relies on annealing time. In particular, either very short annealing times or long annealing times increase the FWHM (102) by a factor of 1.5. Since no significant change was observed in the FWHM (002), only the (102) FWHM and recovery time are presented here.

As the GaN NL is annealed longer, the number of NL islands increases due to further evaporation of GaN from the NL. Densely populated NL islands will quickly coalescence with neighboring islands once the high temperature GaN growth starts. Therefore, the coalescence (recovery) time will be reduced accordingly. In contrast, the density of TDs will increase as TDs are generated at the borders where islands coalescence. In this context, it can be understood that the GaN annealed for 150 s has a high density of NL islands and short recovery time.

The poor quality observed with the sample annealed for 10 s can be explained through the following process. Since the NL remains a relatively flat and continuous film rather than randomly distributed islands due to the very short annealing time,

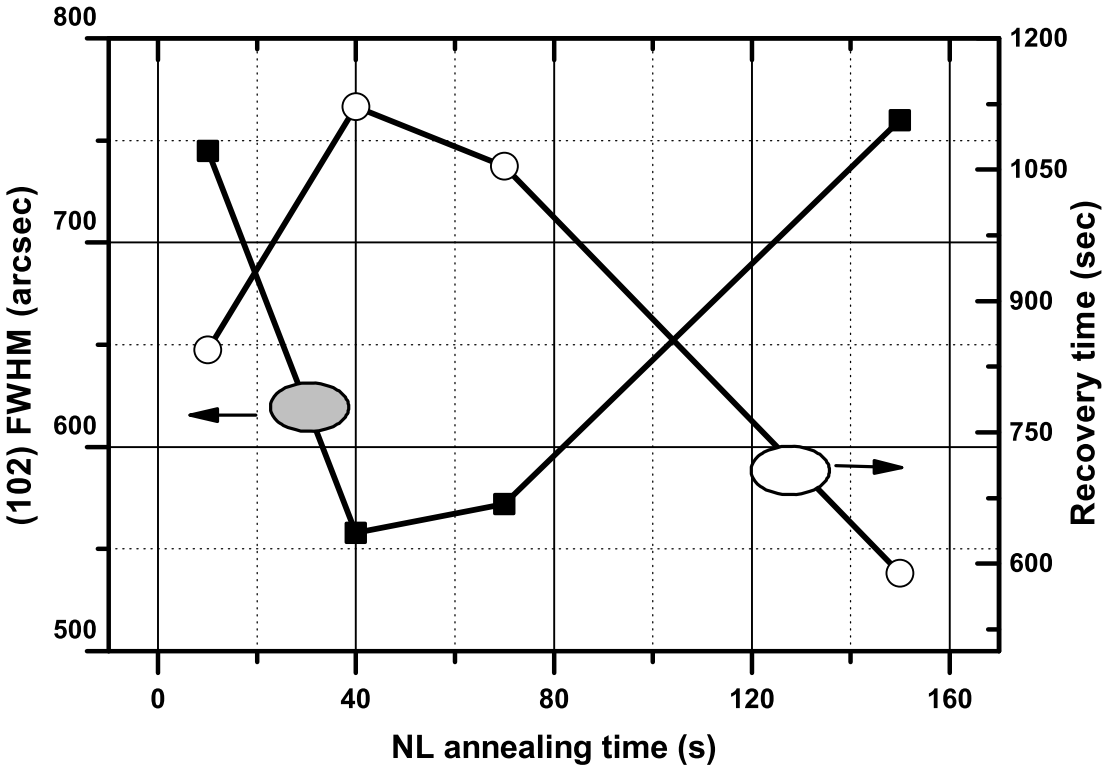

Figure 3.13: The FWHM value of the (102) reflection plane and recovery time vs. NL annealing time.

the polycrystalline structure of the NL leads to HT GaN of rather poor crystallinity similar to that of the sample annealed for a very long time. The recovery time is relatively shorter and the density of TDs is higher.

Intermediate annealing times result in a reasonable crystalline quality with a (102) FWHM value of about 550". This value indicates a TD density of about $10^9\,\mathrm{cm}^{-2}$. Since two to three additional oscillations were necessary to reach full intensity in the interferogram signal, the recovery time was in this case relatively long. Hall measurements results indicated that the sheet resistance of these samples is between $10^4\,\Omega/\square$ and $10^6\,\Omega/\square$. The highest R_s of about $10^6\,\Omega/\square$ is obtained with a sample annealed for 70 s. Although the sheet resistances of samples annealed for 10 s and 150 s are above this range, such high density of threading dislocation can impede the electron mobility because it acts as a center of scattering. Therefore, the

annealing time was chosen to be 70 s as a compromise between crystalline quality of GaN and sheet resistance. In chapter IV, HFET devices fabricated on GaN templates having comparable quality as the above analyzed template are compared in terms of their impact on device performance. A comparison with respect to materials with less resistive GaN is also made.

3.3.5 Band edge PL emission

PL characterization was performed with samples having various resistivity values (HR GaN, UID GaN and Si doped GaN) in order to study the origin of different resistivities. XRD, Hall measurement data and recovery time of the examined samples are presented in Table 3.4 together with their electrical characteristics. The carrier density of HR GaN is difficult to be measured accurately due to the used experimental set-up which is capable of measuring carrier densities up to high $10^{16}\,\mathrm{cm}^{-3}$. More precisely, the significantly high resistivity of these samples imposes the need for strong magnetic field and current control in the range of less than 1 nA. Poor quality of the ohmic contact also hinders accurate measurement. Detailed description of the used PL system and a discussion about the principle of PL can be found in section 2.4.5.

	HR GaN	UID GaN	Si-doped GaN
XRD FWHM (002)	310	320	-
XRD FWHM (102)	530	407	-
Recovery time (s)	624	2000	-
Carrier density (cm^{-3})	NA	$9 \cdot 10^{16}$	$1 \cdot 10^{18}$
R_s ($\Omega/\square$)	10^6	$4 \cdot 10^3$	$2 \cdot 10^2$

Table 3.4: PL sample list.

Figure 3.14 presents the 10K band edge PL emission (3.45∼3.52 eV) of HR GaN along with UID GaN and Si doped GaN. In order to compare their spectra

clearly, the PL spectra of HR GaN and Si doped GaN are rescaled by 10 and 25 respectively. Four well resolved peaks are observed in HR GaN and UID GaN while a very broad peak (donor related peak) is only found in Si-doped GaN. As indicated in the figure, each peak corresponds to the acceptor-bound exciton (A^0X), the donor-bound exciton (D^0X), the free exciton A (X_A) and the free exciton B (X_B).

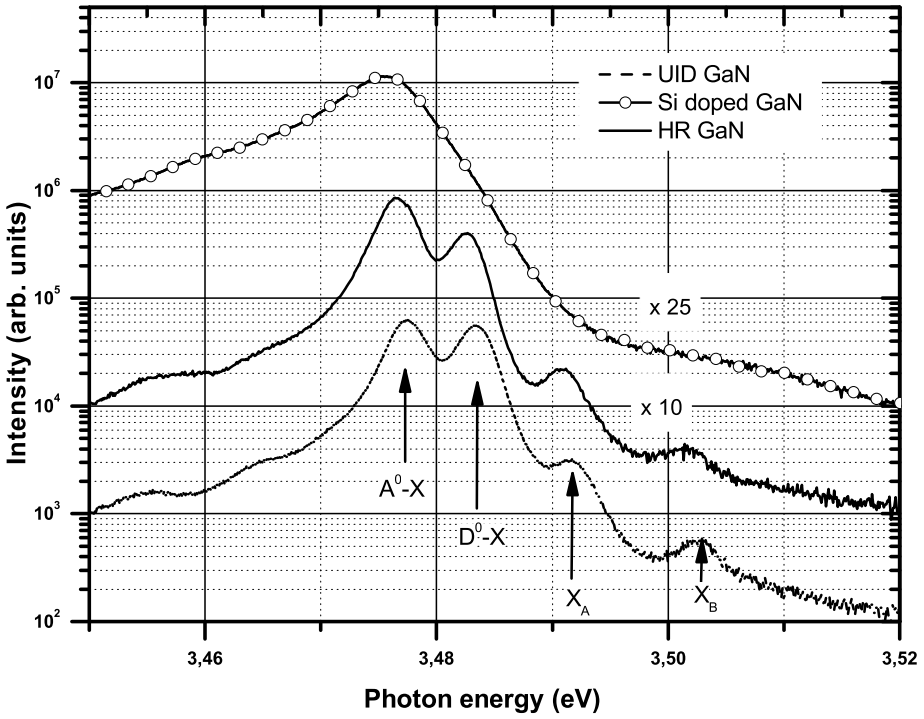

Figure 3.14: 10K band edge PL emission of UID GaN, Si doped GaN and HR GaN.

The exciton localization energies for donor and acceptor in the resistive samples are about 8 meV and 14.8 meV, respectively. Here, the exciton localization energy or binding energy is defined as the distance from the D^0X or A^0X peak to the peak of the X_A. These values resemble those reported for the binding energies of donor and acceptor in homoepitaxial grown GaN which are known to be 6.2 meV and 11.6 meV [81]. The deviation of the binding energy of our samples from the literature values is due to the strain caused by the growth conditions and the type of substrate used (sapphire). The peak position is also indicative of the strain in GaN. As bulk GaN

is strained more, the peak positions shift to higher energies (blue shift). The peak of Si-doped GaN is centered at 3.475 eV which also indicates the strain relaxation. This result agrees well with those of other groups. Significant strain relaxation was also reported for Si-doped GaN when the Si concentration is above $2 \cdot 10^{17}\text{cm}^{-3}$ [82]. Detailed information about the correlation between PL peaks and strain observed in various bulk GaN layers can be found in Ref. [83, 84]. Although not shown here, samples grown by our in-house MOCVD also show various peak positions depending on the growth condition.

It is worth noting that the A^0X peak shows a profound difference in all three types of GaN. As the sheet resistance of GaN becomes higher, the A^0X peak becomes more dominant than the D^0X. The peak ratios of A^0X to D^0X summarized in Table 3.5 are a very important measure of the GaN resistivity. Considering the fact that no *p*-type dopant was used in these experiments, the observation of an acceptor A^0X peak implies the presence of acceptors incorporated during the growth. The correlation between sheet resistance and the A^0X to D^0X ratio supports that the resistivity of GaN is increased by the compensation of background *n*-type carriers with acceptors. This result also agrees well with other reports [60].

Sample	$A^0 - X$	$D^0 - X$	X_A	X_B	$\frac{I(A^0-X)}{I(D^0-X)}$	R_s ($\Omega/\square$)
HR GaN	3.4767	3.4831	3.4915	3.502	2.45	10^6
UID GaN	3.477	3.483	3.4910	3.502	1.16	$4 \cdot 10^3$
Si doped GaN	-	3.476	-	-	-	$3 \cdot 10^2$

Table 3.5: Summary of PL peaks and the peak ratio of A^0X to D^0X in bulk GaN with various resistivities.

Although at first glance, the origin of resistive GaN can based on the 10K band edge PL emission, be understood by the compensation of acceptor like defects, the type of specific defects or impurities is not clear yet. In our previous work, the origin

of the A^0X peak may be caused by carbon impurities and its segregation at TDs in accordance with the results of Wickenden *et al* [60, 79]. However, this failed to explain the observation of low resistivity of GaN grown below 1030 °C in this work where a higher density of carbon can be incorporated.

The concentration of carbon impurities measured by Secondary Ion Mass Spectroscopy (SIMS) is affected adversely by growth temperature and growth pressure of the bulk GaN layer [77]. It was proposed that carbon is removed from the growth surface more effectively in a GaN decomposition environment in the form of methyl fragments [85]. High ammonia or high hydrogen flow, low pressure and high temperature are believed to enhance the GaN decomposition rate [85]. Conversely, the acceptor level is expected to increase together with carbon impurities at lower growth temperature, lower ammonia flow and higher pressure. Therefore, samples grown below 1030 °C were expected to demonstrate higher R_s compared to others annealed at 1030 °C as in Ref. [60] since all growth conditions were maintained the same except the temperature of the HT GaN.

Furthermore, HR GaN grown in this work at higher ammonia flow shows high sheet resistance R_s despite the low carbon concentration. Therefore, the resistivity of GaN cannot be explained simply by the presence of carbon and a high TD density. Because of the currently insufficient explanations, PL measurements were extended to longer wavelengths from the band edge to 700 nm in order to probe defect related emissions. The results obtained from these studies will be present in following section.

3.3.6 PL emission related to defects

In the previous section, the presence of the acceptor peak in UID and HR GaN was confirmed through high resolution band edge emission. Furthermore, the higher the resistivity of GaN is, the higher the acceptor peak is expected to be.

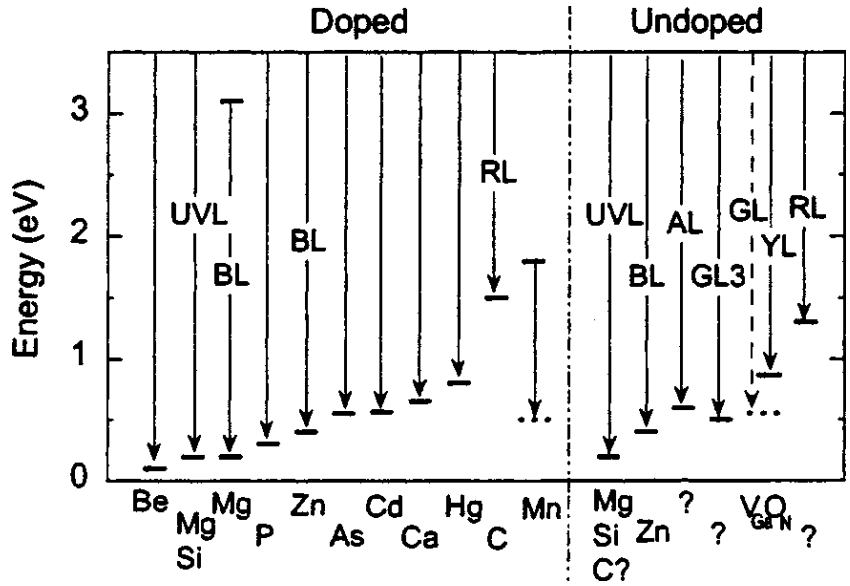

Figure 3.15: Various radiative transition paths in GaN. After Ref. [86].

However, this peak does not provide information about the type of defects related to unintentionally generated acceptors and how they are affected by the growth conditions. Since defects in GaN contribute to the PL emission in a pronounced way and their behavior strongly depends on temperature, the PL studies of this work were extended further in terms of wavelength and temperature compared to the simple band edge measurements presented in section 3.3.5.

Figure 3.15 illustrates the radiative emissions in doped and undoped GaN corresponding to the transition energies caused by various atoms incorporated in GaN. The first letter stands for the wavelength range, i.e. B for blue and Y for yellow etc. and the last letter **L** indicates luminescence. It is known that specific emission signatures appear depending on the growth system and material sources used, as well as on contaminants present during growth [86]. The Zn and Mg impurities shown in this figure can be excluded as possible dopants based on the SIMS results of the tested samples.

In this work, blue (BL) and yellow luminescence (YL) are of prime importance

since defects in HR GaN and UID GaN are closely related to those two emissions. The YL spectrum, which is nearly Gaussian shaped is centered at 2.3 eV with a FWHM of about 350 meV. The BL emission is caused by transition from the conduction band or the shallow donor to deep acceptor sites (0.34$\sim$ 0.4 eV). Its peak is centered around 3.0 eV with an FWHM of about 400 meV.

The PL emission of HR GaN, UID GaN and Si doped GaN from the previous section will be compared next in order to investigate the contribution of dominant defects to the GaN resistivity. The 10 K PL spectra from the three types of GaN are presented in Fig. 3.16. The spectra of HR GaN and Si doped GaN are rescaled for comparison. In addition to the band edge related emission, two broad band emissions can be observed in UID GaN and HR GaN. In contrast, BL is significantly low in Si doped GaN. Table 3.6 shows a summary of the peak ratios of blue luminescence (I_{BL}) to yellow luminescence (I_{YL}).

	HR GaN	UID GaN	Si doped GaN
I_{BL}/I_{YL} at 10K	8-9	10	$7 \cdot 10^{-3}$

Table 3.6: Ratio of the blue luminescence peak (I_{BL}) to yellow luminescence peak (I_{YL}) at 10K.

Yellow luminescence

Yellow luminescence (YL) in GaN is due to the transition from shallow donor levels to deep acceptor levels. Although it is also observable in UID GaN, the dominance of YL in n-type GaN is a well known phenomenon, too. Either the complex defects $V_{Ga}O_N$ or $V_{Ga}Si_{Ga}$ are believed to be the source of YL. Their binding energy is 1.8 eV and 0.23 eV and their energy levels are positioned at 1.1 eV and 0.9 eV from the top of the valence band, respectively [87]. As shown in this reference, the for-

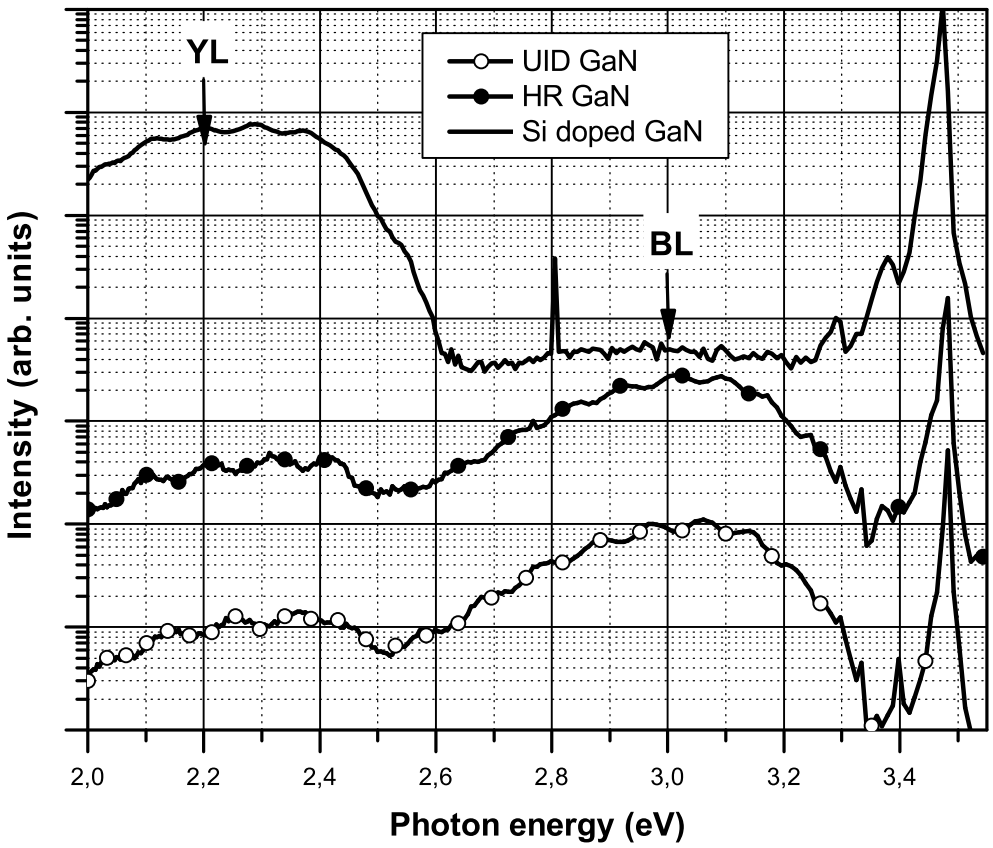

Figure 3.16: 10K PL emissions from UID GaN, HR GaN and Si doped GaN.

mation energy of Ga vacancy related defects is dependent on the Fermi energy level using first principle calculations; the less formation energy is necessary for the defects when the Fermi level is close to the conduction band, the higher the concentration of such defects will be in n-type GaN. Elsner *et al.* also proposed that a V_{Ga}-O defect is related to the acceptor level and also participates in the YL broadening near threading-edge dislocations [88]. Besides, Ga vacancies alone and complexes involving carbon (C_N) are believed to be the source of YL in UID GaN and carbon doped GaN [89, 90].

Blue luminescence

The defects and impurities associated with BL in un-doped GaN are $V_{Ga}O_N$ [91] and $V_{Ga}H_n$ [92, 93]. Albrecht ascribed it to the 60° dislocations forming a wide

band of half filled acceptor states in his cathodoluminescence study [94]. In C doped GaN, C_{Ga} contributes to the BL emission. Interestingly, BL emission is observed in samples grown by MOVPE and not in those grown by MBE [86], where no hydrogen sources are used.

Discussion

The significantly high intensity of YL observed in Si doped GaN studied in this work can be explained by the aforementioned V_{Ga} related defects. Although the presence of high carbon density ($> 10^{18}\,\mathrm{cm}^{-3}$) can also produce a strong YL peak, this is unlikely to be the case in this study. First, no intentional carbon doping was attempted and second, if such a high carbon concentration is incorporated unintentionally, its impact would have been seen from the PL results reported here for HR GaN and UID GaN.

Armitage showed that the intensity of the yellow luminescence band (I_{YL}) is almost equal to the intensity of the blue luminescence band (I_{BL}) when GaN is doped with carbon at $10^{18}\,\mathrm{cm}^{-3}$. Furthermore if its concentration raises above this level, YL emission increases accordingly [89]. However, the ratio of I_{BL}/I_{YL} is much higher than the value expected from GaN with high carbon concentration. It follows therefore that the concentration of carbon must be below $10^{18}\,\mathrm{cm}^{-3}$ in UID GaN and HR GaN samples studied here since the I_{BL}/I_{YL} ratio is much larger than one.

The presence of the A^0X peak in UID GaN supports this argument since the A^0X peak is missing in highly C doped GaN. The acceptor C_N prefers to form electrically inactive pair defects (C_N - C_{Ga}) in extremely high concentration of carbon. Consequently, carbon acceptor incorporation and compensation of residual donors becomes inefficient [95, 96].

The absolute intensity of the YL emission of HR GaN is slightly reduced in

comparison with UID GaN in Fig. 3.16. This might be due to the V_{Ga} related defects, which are the major source of YL band emission, being suppressed in resistive GaN ; the formation of these defects is implausible as the Fermi level is close to the valence band.

BL emission appears and competes with YL emission in UID GaN and HR GaN whereas no BL emission is observed in Si doped GaN. Although the absolute intensities of BL emission and YL emission from UID GaN is stronger than from HR GaN, the ratio between the two peaks is comparable between the two types of GaN as seen in Table 3.6. The lower emission efficiency in HR GaN is explained by its high density of threading dislocations predicted from the FWHM of the (102) reflection plane. Another role of TDs is to trap impurities.

West performed SIMS measurements for GaN layers in order to study the impact of growth pressure and TD density on impurity incorporation [97]. He showed significant effects of growth pressure on carbon incorporation presumably due to the stronger molecular integrations between carbon and hydride gases. As growth pressures become higher, less carbon is incorporated in GaN. However, no strong correlation was found between the density of threading dislocations and the amount of carbon incorporation. Although an intermediate density of TDs ($5.6 \cdot 10^9\,\mathrm{cm}^{-3}$) contained more carbon atoms than other samples having one order of magnitude lower or higher density of TDs [2], the dependence of TD density was vaguely observed. This implies that the complex defects of carbon and TDs are not the sole source of high resistivity of GaN layers.

The BL emission is, to some extent, also dependent on the V/III ratio. Figure 3.17 presents the PL spectra of the aforementioned UID GaN and HR GaN grown

[2] growth pressure for all samples were maintained at the same value

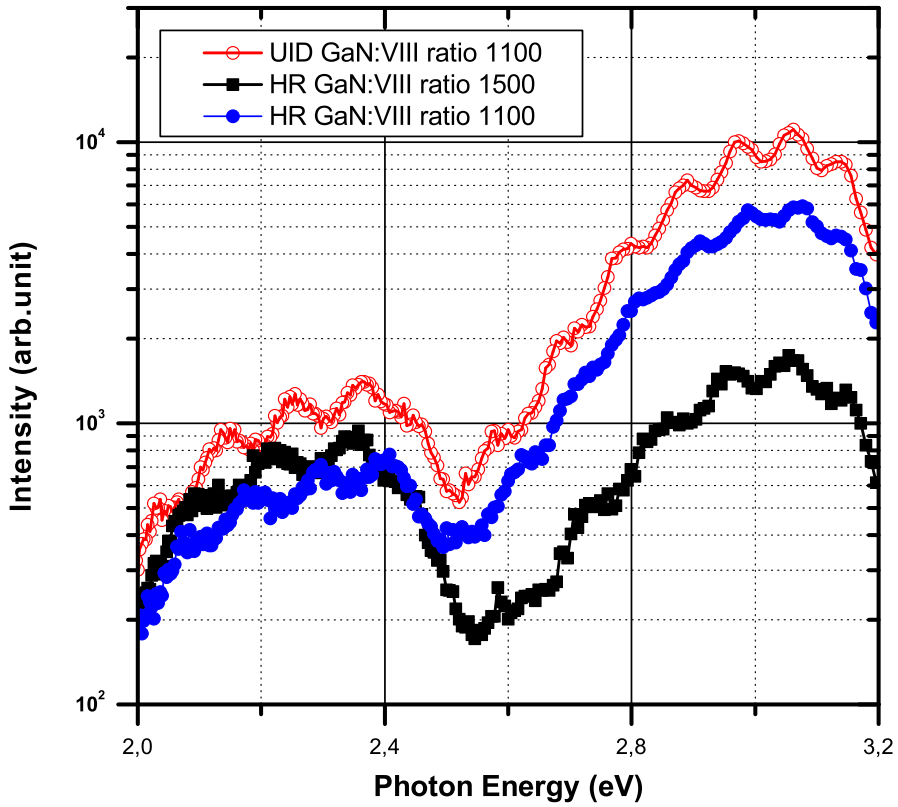

Figure 3.17: 10K PL emission of GaN layers grown under different growth conditions.

at a V/III ratio of 1100 along with the other HR GaN grown at a higher V/III ratio (1500). The sheet resistance of both HR GaN samples grown with different V/III ratios is as high as $10^6\,\Omega/\square$. The FWHMs of the (102) reflection plane is comparable; the values of the higher and lower V/III ratio sample are 688" and 745", respectively. However, a significantly lower BL emission is observed in HR GaN with high V/III ratio. The peak ratio of BL to YL is about 1.7 for this sample. Since high ammonia flow was adopted for a higher V/III ratio while the TMGa flow was kept the same, less carbon concentration was expected under this growth condition. Therefore, defects, specially originating from $V_{Ga}H_n$ [92, 93], seem to be responsible for the high resistivity of this HR GaN sample since it was grown with

high ammonia flow (high V/III ratio). This is consistent with the fact that ammonia rich conditions will generate more hydrogen dissociation from ammonia and also Ga vacancies.

The discussion presented so far addressed the correlation between PL spectra and possible defects incorporated under different growth conditions. Figure 3.16 implies a low radiative recombination rate due to TDs. Besides, the GaN layers grown under the same conditions except for the NL annealing time can have different sheet resistances because of different TD densities.

On the other hand, different types of defects can be responsible for the different values of measured resistivities. In Fig. 3.17, two HR GaN layers grown with different ammonia flow but having similar TD density and sheet resistance are compared. The significant suppression of BL emission by a factor of four indicates that the origin of high resistivity is different. Considering the fact that high ammonia flow enhances the removal of carbon from the growth surface, the carbon concentration is reduced effectively. Therefore, other defects such as $V_{Ga}H_n$ can be speculated as the origin of high resistivities in this work.

3.3.7 Process stability

Materials grown under the same growth conditions should exhibit similar electrical and optical characteristics. In order to ensure good growth reproducibility, the growth window should also be wide enough so that small variations of the growth parameters do not affect the material properties. In order to address this issue, numerous HR GaN growth runs were carried out.

The values of the (002) FWHM measured in this study were overall increased by more than 20". Since this variation is not drastically critical for the quality of GaN, data will not be presented here. These minor changes could be due to

the quality of the GaN which is observed to drift even though the same growth conditions are applied. This drift can also be caused by XRD measurement errors including probing position, wafer stress condition etc. or can be the consequence of a change in substrate quality, S/H and susceptor conditions.

Figure 3.18 compares the (102) FWHM values from two series of runs. Minor changes are observed at annealing times between 40 s and 90 s as indicated in the figure. The FWHM (102) is in the range of 500 $\sim$ 550 " for both series of runs and the sheet resistance is about $10^6\,\Omega/\square$. Therefore, the NL annealing time of this regime with a center value of 70 s seems to permit the establishment of a reasonable process window. However, remarkable difference was found between two runs when the GaN layers were annealed for 10 s and 150 s. Further investigation suggested that two major parameters can cause the instability of the process when no significant change of the reactor condition is assumed. The discussion of these two parameters follows in the next section.

1) *Nucleation layer*

The importance of the NL is profound as this layer determines the electrical and optical characteristics of subsequently grown GaN layers. The thickness of this layer must be tightly controlled. Otherwise, the same NL annealing time causes a different density of NL islands and number of TDs consequently. In the experiments reported in section 3.3.3, a thickness variation of about 3 nm was considered to be acceptable. In order to verify the thickness variations, the growth rate of the NL was carefully calibrated and its consistency was monitored from run to run as discussed next.

The growth temperature of the NL was kept at 530 °C. For the calibration of the growth rate, the growth of a very thick NL with a thickness of more than 500 nm

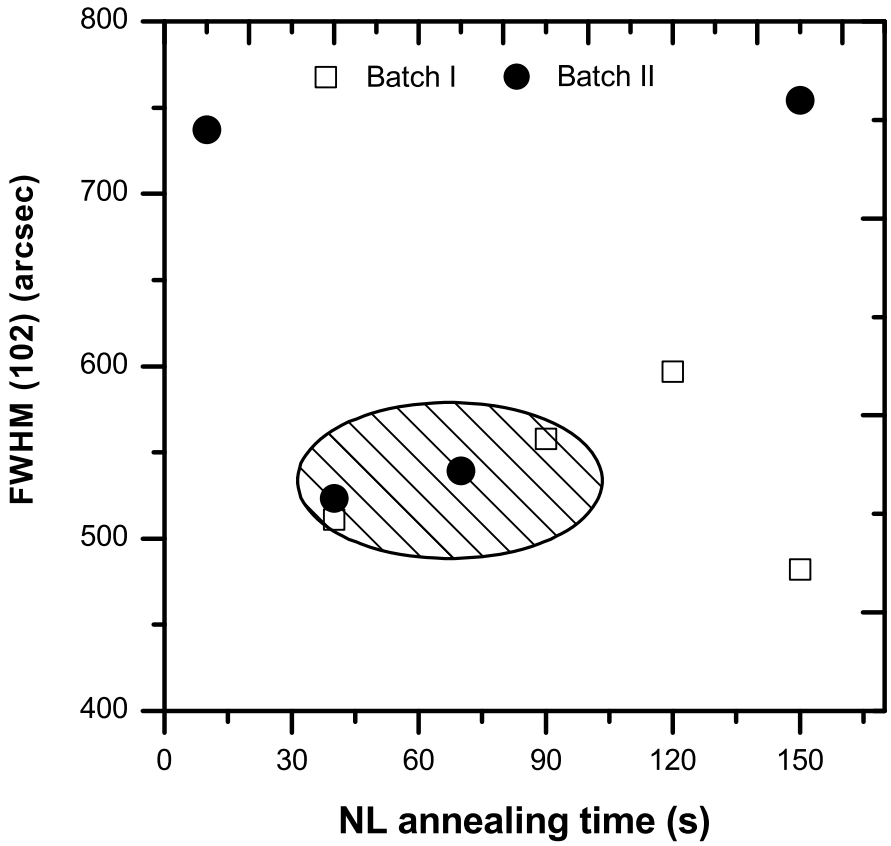

Figure 3.18: The FWHM value of the (102) reflection plane vs. NL annealing time.

was carried out. The SEM measurement results showed that the average growth rate was about 0.5 μm/h. Repeating the SEM measurements following each run was felt to be impractical since this is a destructive post growth characterization technique. Moreover, a nucleation thickness of less than 30 nm NL is below the 100 nm resolution of the system. Therefore, the NL thickness of each sample was extracted from the correlation between the SEM measurement and the interferometer data.

The extracted NL growth rates are presented in Fig. 3.19. It has to be noted that the values presented in this plot were measured only at the center of the respective wafer. The dashed line shows the growth rate of each run before the S/H and susceptor cleaning. The solid line indicates the monitored growth rate after cleaning of the S/H and the susceptor while the x-axis indicates the growth sequence follow-

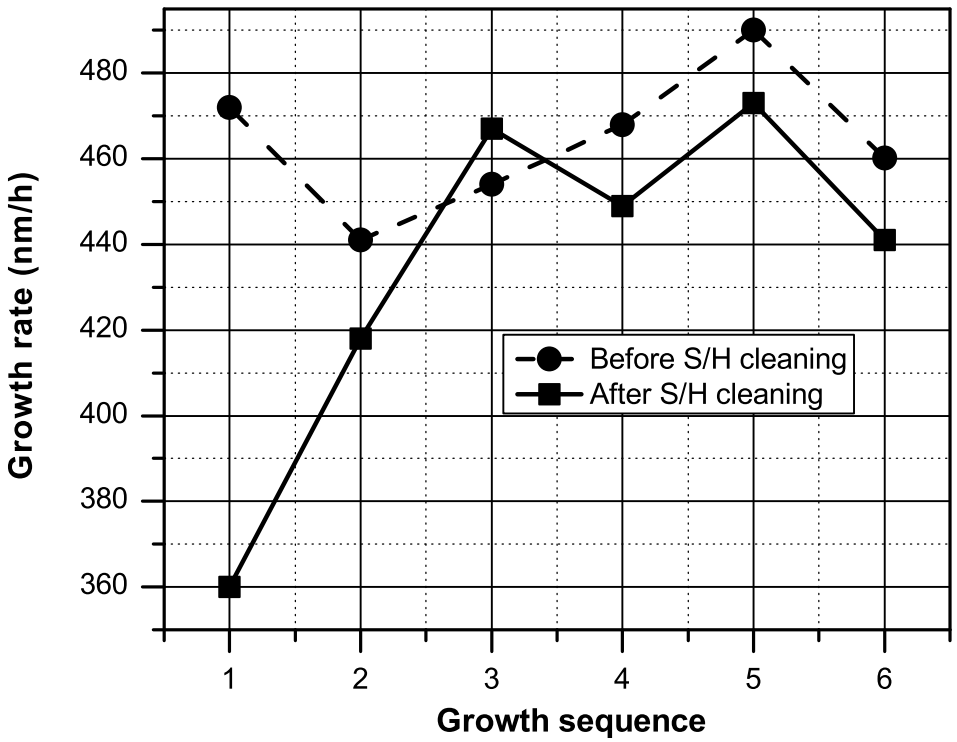

Figure 3.19: NL growth rate before and after S/H and susceptor cleaning.

ing reactor maintenance. A bake and coating run was performed between bulk GaN runs in order to keep the conditions of the susceptor and the S/H the same. The only exception was the case of the growth right after the maintenance of the S/H.

Before S/H and susceptor were cleaned, the average growth rate was about 460 nm/h. The maximum deviation of the NL growth rate was ±24 nm/h. Considering that the time for the NL growth is about 3 min, the resulting thickness deviation is about ±1.2 nm. This value is acceptable as it does not influence the quality of the HT GaN. Compared to the growth rates before the maintenance, a profound change was observed in the first three runs after the maintenance. In particular, the growth rate of the first run following the maintenance was only 75 % of the previous runs. This change can definitely cause the change of the resistivity of GaN. Nevertheless, the growth rate seems to recover after the growth of a few bulk GaN layers. Therefore, care must be taken to keep S/H and susceptor conditions consistent in order to

prevent drastic changes of the NL thickness.

2) *Substrate bowing*

The most remarkable quality change observed was for a sample annealed for 150 s. This cannot be understood just by nucleation layer thickness variations. Since no significant change of the MOVPE system occurred during the time of these experiments, the sapphire substrates were investigated as a possible source for these differences. In order to verify the effect of the sapphire substrate, their surface profile was measured by a commercial surface profiler (VEECO Dektak 6M). The sapphire wafers were randomly picked from a set of 50 wafers. The scan directions and positions are as shown in Fig. 3.5 on page 70.

	R1	R2	R3	R4	FWHM(002)	FWHM(102)
S 1	25	36	43	28	-	-
S 2	280	300	153	108	-	-
G 1	25	19	17	22	364	713
G 2	12	14	19	16	342	428

Table 3.7: calculated radius of two sapphire wafers and two consequently grown GaN layers on the same substrates (unit: m).

Four distinguished data sets of two substrates and GaN layers grown on them are provided in Table 3.7. The same growth conditions were applied for these two GaN layers. A symmetric concave shape and a relatively smooth surface profile were observed from the sapphire wafer 1 (S1) while sapphire wafer 2 (S2) showed an asymmetric convex shape with a relatively flat but rough surface. The average radius of S1 and S2 are 30 m and 190 m, respectively. The surface profile of both GaN layers is concave and the average radius is 20 m and 15 m for G1 and G2 respectively. Despite the little difference of the radius of the two GaN layers, the FWHM (102) of these two GaN layers confirms the impact of the substrates on the GaN layers. The GaN layer G2 grown on the flat sapphire substrate (S2) has a FHWM of 428" which

is 30 % less than that of G1.

The asymmetry observed from S2 could be deleterious because it causes a temperature gradient and a non-uniform gas flow, which results in non-uniform NL growth. However, its large radius implies that less stress will be caused by this substrate. On the other hand, enhanced stress contribution is expected from S1 because of its small radius as predicted by the Stoney equation (see Eq. 2.19 in section 2.4.10). As a result, a large number of TDs is generated. Therefore, the desired quality of the sapphire substrates should combine the features observed in two sapphire wafers, namely smooth, uniform and low stressed characteristics. In addition, its quality must be consistent in order to prevent profound quality changes.

3.4 n-doped GaN

The ability to modulate conductivity by doping allows the fabrication of various device types. In case of HFET devices, the importance of doping is relatively low compared with investigating the development of highly resistive GaN due to the fact that devices of this type are inherently doped through piezoelectric and spontaneous polarization effects while a highly resistive substrate is substantially essential for controlled current modulation. However, intentionally doped n- or p-type layers are needed for unipolar and bipolar devices and also for certain HFET designs. Precise doping control is in general considered a prerequisite for optimizing the device design and allowing production of devices with consistent performance characteristics.

The GaN conductivity can be controlled by intentional incorporation of dopant atoms into the Ga sites in the GaN crystal. As mentioned earlier, the common dopant for n-type GaN is Si and Mg is commonly used for p-GaN. Since n-type material is required to form good quality ohmic contacts for Schottky diode gas sensors and to

form 2DEG in a-plane HFETs in this work, the carrier density and Hall mobility was studied for various doping levels corresponding to the SiH_4 flow.

In good quality GaN material, the electron carrier density increases linearly with increasing silane flow as also can be seen in Fig. 3.20. This is due to the fact that mobility is, in this case, not limited by dislocation scattering. Consideration of Hall mobility data compared with the obtained carrier density showed that the materials investigated here are of moderate quality.

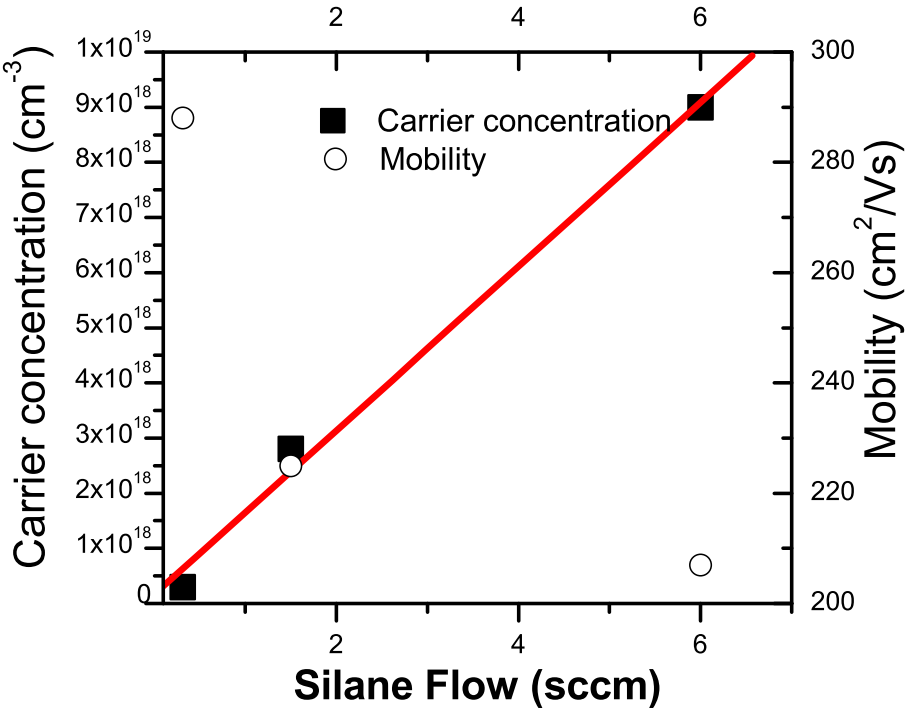

Figure 3.20: Carrier concentration and mobility vs. silane flow.

Temperature dependence measurements of the band edge PL emission were performed with a doped sample and the HR GaN sample in order to investigate the temperature evolution of peaks. The carrier concentration of doped sample II is $2 \cdot 10^{18}\,\mathrm{cm}^{-3}$ as measured by Hall measurement. In the doped sample, only D^0X is observed at $3.40 \sim 3.42\,\mathrm{eV}$. Figure 3.21 shows the temperature evolution of the peaks found in HR GaN and sample II. The free exciton A (X_A) peak, the D^0X and

the A^0X move to lower energies as temperature increases. Moreover, the donor and acceptor bound peak of HR GaN vanish above 60 and 80K. However, the free exciton A remains even at room temperature due to its high binding energy (28meV) [98].

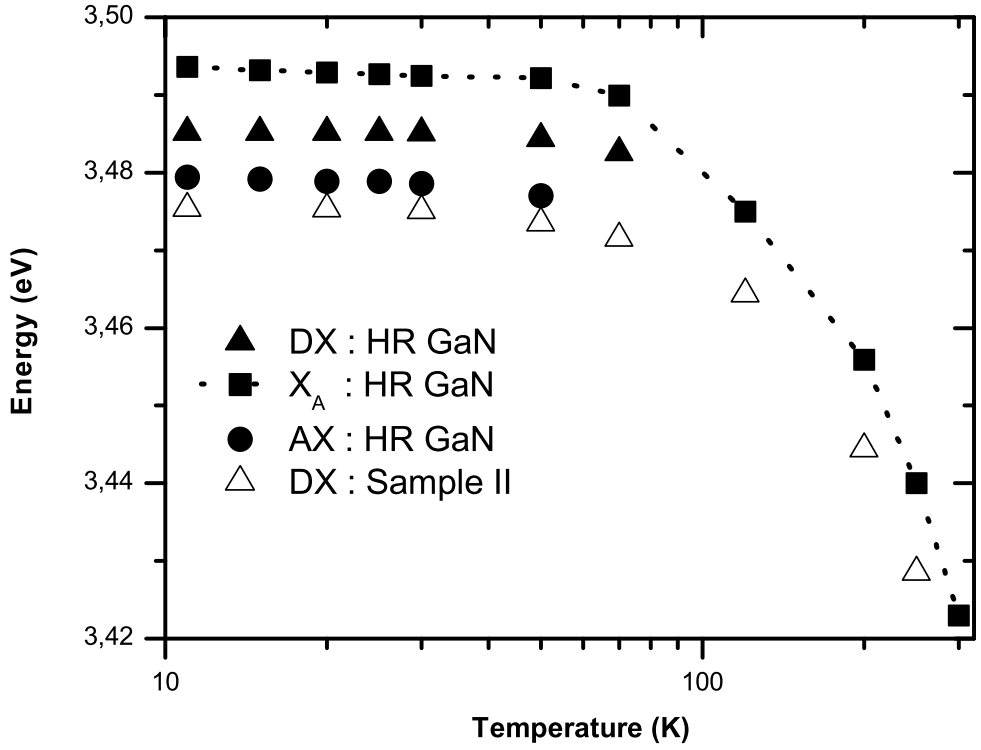

Figure 3.21: Temperature evolution of the peak position for HR GaN and sample II (N= $2 \cdot 10^{18}\,\mathrm{cm}^{-3}$).

3.5 Conclusion

The focus of this chapter was the growth and characterization of resistive bulk GaN. Due to the heater design of the TS MOVPE system, the importance of temperature calibration was addressed and its procedure was described. In order to minimize errors and temperature discrepancy, the emissivity of the susceptor and

the quality of the optical probes must be considered.

The first UID bulk GaN grown by the Thomas Swan MOVPE system in this work showed a screw and mixed TD density of $10^8\,\mathrm{cm}^{-2}$ and a edge TD density of $5 \sim 7 \cdot 10^{10}\,\mathrm{cm}^{-2}$. This implies that the crystalline quality of this unoptimized GaN was quite poor. Besides, the background carrier density was $\sim 10^{17}\,\mathrm{cm}^{-3}$ and the sheet resistance was as low as $10^3\,\Omega/\square$.

In order to improve the addressed issues of the first UID bulk GaN, a growth process optimization was performed. The control parameters were V/III ratio, temperature ramp up time and NL annealing time. As a result, a high R_s of about $10^6\,\Omega/\square$ was obtained. The edge TD density was estimated to be about $10^9\,\mathrm{cm}^{-2}$ which represents an improvement by about one order of magnitude.

The origin of the resistivity of our bulk GaN was studied with 10K and RT PL measurements with wavelengths in the range from 350 nm to 700 nm. The 10K band edge PL measurement confirms that the higher acceptor related peak exists in resistive GaN whilst the donor related peak is dominant in UID and n-doped GaN. In addition, BL emission related to TDs, $V_{Ga}O_N$ and $V_{Ga}H_n$ was observed and was stronger than the YL emission in the resistive GaN. On the contrary, BL emission was very weak compared to YL emission in UID or n-doped GaN. These PL results manifest that the acceptor like defects in our resistive bulk GaN originate from TDs as well as from $V_{Ga}H_n$.

CHAPTER IV

POLAR NITRIDE HETEROSTRUCTURES

III-Nitrides grown along the *c*-axis exhibit an internal polarization field due to the asymmetry and strain caused by the lattice mismatch in related heterostructures. As a result of the polarization field, electrons are confined in a well which is formed at the interface between GaN and the adjacent ternary alloy layer and form a 2DEG as described in section 1.6.

The 2DEG mobility in undoped heterostructures is 500∼2000 cm^{-2}/Vs at room temperature [99, 100] and 3000∼10000 cm^{-2}/Vs at low temperature [101]. Such high mobilities are ascribed to the fact that the transport of 2DEG is not affected by ionized impurity scattering since no doping is employed. The high breakdown voltages in conjunction with high mobilities make nitride heterostructures attractive for high frequency and high power electronic devices.

The scope of the work described in this chapter is to investigate the growth and characterization of various nitride heterostructures, and in particular undoped AlGaN/GaN designs including devices based on them. The optimization of AlGaN/GaN heterostructures was performed by controlling the thicknesses of the AlGaN layer and the Al composition in order to achieve a high mobility and high sheet charge densities. The 2DEG in AlGaN/GaN heterostructures was characterized by

Hall effect measurements. ω-2Θ scans and GI-XRR scans were used to analyze the Al composition, the thickness of the AlGaN layer and the interface roughness. Devices were also fabricated and their DC and RF characteristics were evaluated.

AlN/GaN heterostructures were explored as an alternative to AlGaN/GaN designs. The growth of them is more challenging due to the large lattice mismatch of AlN with respect to GaN (2.5 %) and the high risk of AlN oxidation. In order to address this issue, the use of *in-situ* SiN_x passivation was employed and its effects were investigated. This layer is expected to protect the surface of AlN and reduce strain relaxation.

Lastly, the growth of InGaN/GaN MQWs and their incorporation in Light Emitting Diodes (LEDs) was investigated. Since their light-emitting efficiency is highly sensitive to the interface quality, this is an adequate measure of the MOVPE system's capability for producing abrupt growth transitions and sharp interfaces. The effect of Indium composition and the quality of the heterointerface were evaluated by PL and XRD characterization.

4.1 AlGaN/GaN heterostructures

4.1.1 Surface states and energy band diagram

It was shown in sections 1.6.1 and 1.6.2 that the spontaneous and piezoelectric polarization in AlGaN/GaN heterostructures modifies the band diagram at the heterostructure interface and creates a 2DEG even without any intentional doping. The resulting 2DEG density is $10^{12} \sim 10^{13}\,\mathrm{cm}^{-2}$. In contrast to III-Nitrides, traditional III-V heterostructures, such as AlGaAs/GaAs require doping of the wide bandgap material in order to obtain a 2DEG. Although the polarization field is present in AlGaAs/GaAs, its value is smaller than that of AlGaN/GaN heterostructures by one order of magnitude and doping of the barrier layer is necessary in order to obtain a

2DEG. Experimental results demonstrate that surface states are also important for inducing the 2DEG. Therefore, this section is dedicated to the role and impact of surface states in AlGaN/GaN heterostructures.

When the AlGaN surface is assumed to be ideal i.e. no defects and no surface states are present, the polarization field only causes a linear band bending in the AlGaN layer and does not affect the band of the GaN layer underneath up to a certain AlGaN thickness. As the thickness of AlGaN increases further, the valence band of AlGaN approaches the Fermi level leading in an accumulation of holes at the surface. As a result, a positive sheet charge is formed. In order to compensate these positive charges, a 2DEG is formed at the heterointerface as shown in Figure 4.1(a).

However, the surface of a semiconductor layer is in general imperfect and the top surface of AlGaN is expected to contain vacancies or some other defects. Surface states (especially surface donor-like traps) in AlGaN layers were proposed to be a source of 2DEG by Ibbetson [102] and Smorchkova [103]. Figure 4.1(b) shows the way that the state of surface traps and the band diagram are changed by increasing the thickness of the AlGaN layer in a non-ideal surface case. Originally the surface states are below the Fermi level but they become ionized as the AlGaN thickness reaches the critical thickness. Electrons from the surface donor-like traps are transferred to the heterointerface by the polarization field and they form a 2DEG. It is worth noting again that the source of 2DEG and the energy band diagram are different in the non-ideal and ideal surface as shown by the schematics of Fig. 4.1. Koley investigated the surface potential of AlGaN/GaN heterostructures by using a scanning Kelvin probe and confirmed the contribution of surface states to the 2DEG formation [104].

The simulation results of $Al_{0.27}Ga_{0.73}N$/GaN heterostructures showed that the

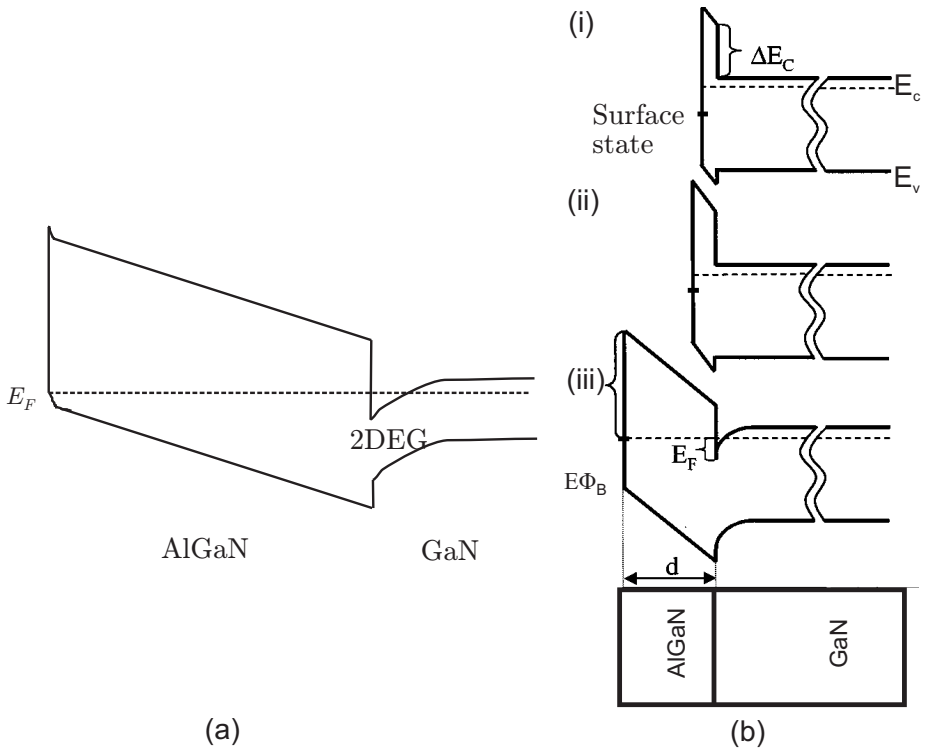

Figure 4.1: (a) Energy band diagram when a 2DEG is formed in an ideal surface case. After Ref. [105]. (b) Schematic diagram showing the development of the band structure in AlGaN/GaN heterostructures with increasing AlGaN barrier width in a non-ideal surface case. After Ref. [103].

2DEG density can increase by a factor of four when surface states are taken into account [106]. When the surface donor like states are filled by carriers originating from surface contamination-related phenomena or electrons arising by reverse biasing a gate, the associated sheet charge carriers are depleted and the related device performance is expected to be degraded as will be discussed in section 4.1.4 and 4.3.

The density of the 2DEG is not linearly proportional to the thickness of the AlGaN layer. Generally, the amount of the 2DEG increases abruptly up to a certain point and then saturates gradually. In particular, the relaxation of the AlGaN barrier layer leads to a decrease in the 2DEG density as the effect of the piezoelectric polarization is reduced. Therefore, the thickness of AlGaN should be optimized to ensure the maximum 2DEG density and pseudomorphic growth.

4.1.2 2DEG transport

When a gate metal is deposited on undoped AlGaN/GaN heterostructures with a Schottky barrier height $e\phi_b$ as shown in Fig. 4.2, the sheet charge density (2DEG) n_s is given by Ref. [107]:

$$n_s = \frac{\sigma_{pol}}{e} - (\frac{\varepsilon_{AlGaN}}{d_{AlGaN}e^2})(e\phi_b + E_F - \Delta E_C) \tag{4.1}$$

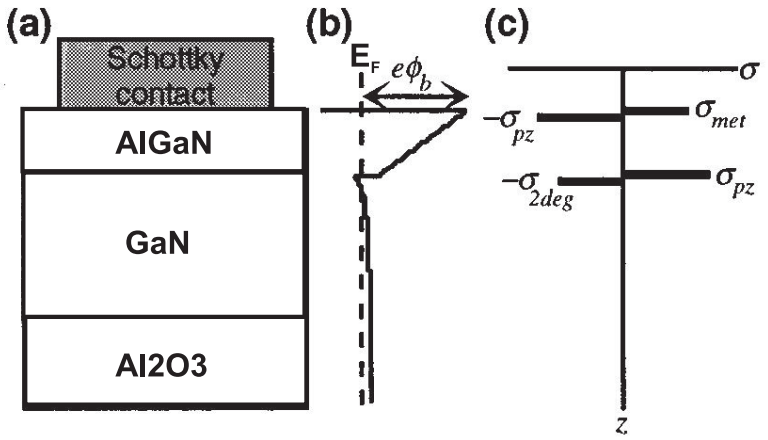

Figure 4.2: (a) Schematic diagram of a nominally undoped AlGaN/GaN HFET structure. (b) Conduction-band energy diagram for this structure. c) Schematic diagram of polarization induced and free-carrier charge distribution. After Ref. [107].

σ_{pol} is the charge induced by the polarization field, ε_{AlGaN} is the dielectric constant of $Al_xGa_{1-x}N$ and E_F is the Fermi energy at the heterojunction interface. d_{AlGaN} is the thickness of the $Al_xGa_{1-x}N$ barrier. ϕ_b and ΔE_C are the Schottky barrier height at the $Al_xGa_{1-x}N$ surface and the conduction band discontinuity between $Al_xGa_{1-x}N$ and GaN, respectively.

ΔE_C is related to the amount of n_s confined in a quantum well. The higher conduction band discontinuity present in III- Nitrides enhances the 2DEG density. ΔE_C can be calculated through the following equation:

$$\Delta E_C = 0.75(E_{g,AlGaN} - E_{g,GaN}) \tag{4.2}$$

as suggested by experimentally obtained data [108].

In general, the effective electron mobility (μ_{total}) is given by:

$$\frac{1}{\mu_{total}} = \sum_i \frac{1}{\mu_i} \tag{4.3}$$

Here, μ_i is a mobility defined by the various scattering mechanisms such as phonon, ionized impurities, alloy disorder, dislocations and interface roughness scattering. However, it should be noted that the temperature dependence of electron mobility in a quantum well is pronouncedly different from that in a bulk material. In Appendix B, Table B.1 summarizes the electron mobility mechanisms as defined for various scattering mechanisms in a bulk material and in a quantum well.

Figure 4.3 presents the electron mobility in $Al_{0.15}GaN_{0.85}$/GaN heterostructures [109]. In this calculation, the 2DEG is assumed to have a density of $1.6 \cdot 10^{12}\,\mathrm{cm}^{-2}$ and the doping concentration of the AlGaN layer to be $10^{18}\,\mathrm{cm}^{-3}$ while the dislocation density is set to $10^{9}\,\mathrm{cm}^{-3}$. Acoustic phonon and polar phonon scattering strongly depend on temperature whereas dislocation and remote donor scattering are relatively independent of temperature. Accordingly, the total mobility of the 2DEG is limited by the polar optical phonon scattering at temperatures above 170 K and acoustic phonon scattering is dominant at temperatures between 70 K and 170 K. The contribution of remote donors is relatively negligible in comparison with other scattering mechanisms. Therefore, the effective mobility of the 2DEG is characterized by a slow decrement at low temperatures and a drastic drop above 170 K. A similar trend was proposed by Bhapkar and Shur [110] who also showed a profound discrepancy between the effective mobility of bulk GaN and that of the 2DEG at temperatures below 170 K due to ionized impurity scattering. These distinct characteristics allows in fact temperature dependent mobility measurement to prove the

presence of a 2DEG.

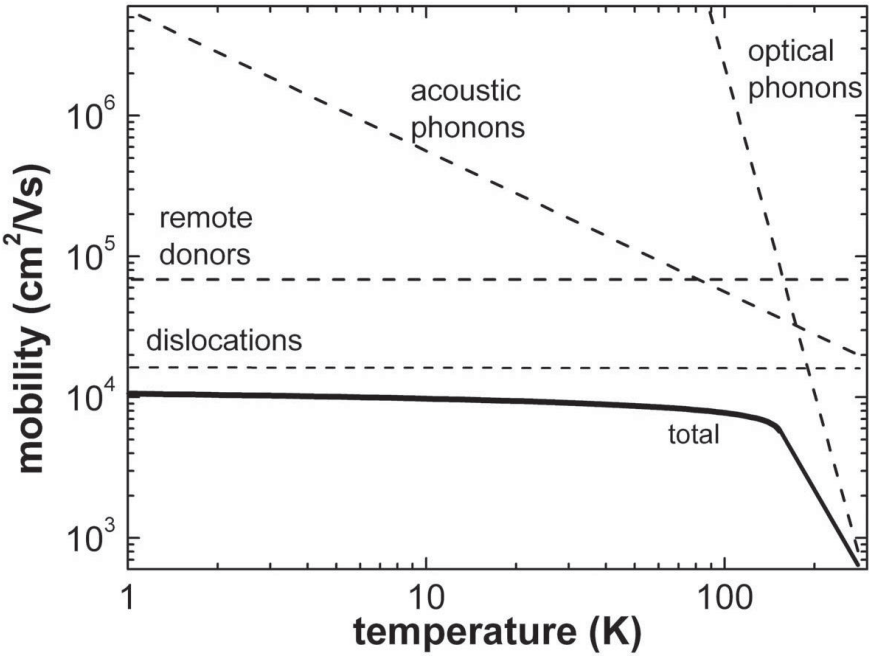

Figure 4.3: Electron mobility vs. temperature of $Al_{0.15}GaN_{0.85}$ modulation doped structure with the influence of different scattering processes. After Ref. [109].

Since electron transport takes place through the 2DEG channel in HFET devices, the sheet resistivity of AlGaN/GaN heterostructures is a key parameter dictating their performance. The sheet resistivity (ρ_s) is given by:

$$\rho_s = \frac{1}{en_s\mu} \tag{4.4}$$

and depends on both mobility and sheet carrier density of the 2DEG. In order to achieve low sheet resistivity, a high 2DEG density is preferable. However, as can be seen from Table B.1, the mobility is to some extent limited by n_s as well. A high n_s, consequently, reduces the mobility.

4.1.3 Heterostructure field effect transistors

A figure of merit (FOM or FM) is a quantized number which can be used for comparing materials in a specific application. Johnsen proposed that the basic

limit of the device performance of a transistor is set by the product of the critical breakdown field E_c and the saturated electron drift velocity v_{sat}. This is defined as $JM = (E_c v_{sat}/\pi)^2$ [111]. JM of GaN is larger by a factor of 800 and 80 in comparison with that of Si and GaAs, respectively. Various figure of merits for semiconductor materials were defined in terms of switching speed, power loss, etc. They are summarized in Table C.1 in Appendix C.

A typical HFET device structure and its circuit model are described in Fig. 4.4. A gate with the length L_G and the width W_G is placed between source and drain. The space between source and drain is defined as L_{ds}. The geometry parameters W_G and L_G are associated with the drain current and the maximum frequency limit for the devices, respectively. It is preferable to use small gate width designs for low noise and low current applications while large gate width designs are recommended for power applications.

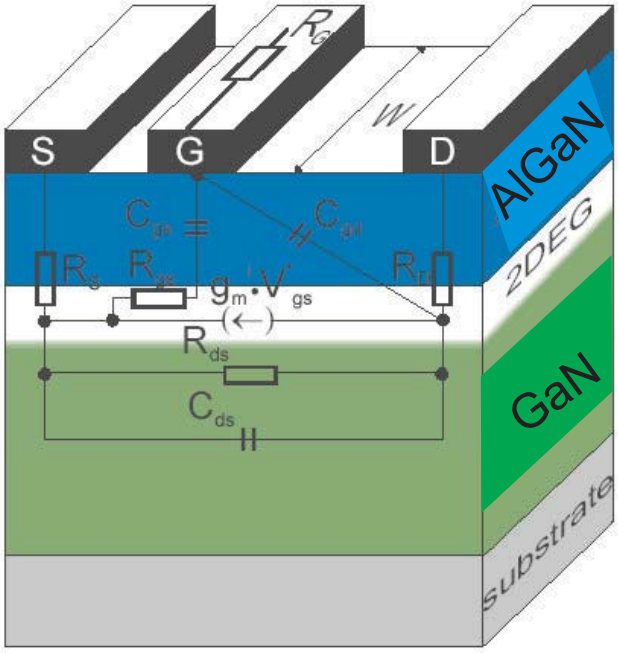

Figure 4.4: Schematic of a typical AlGaN/GaN HFET device and its circuit model [112].

Figure 4.5 represents the typical small signal DC output current voltage char-

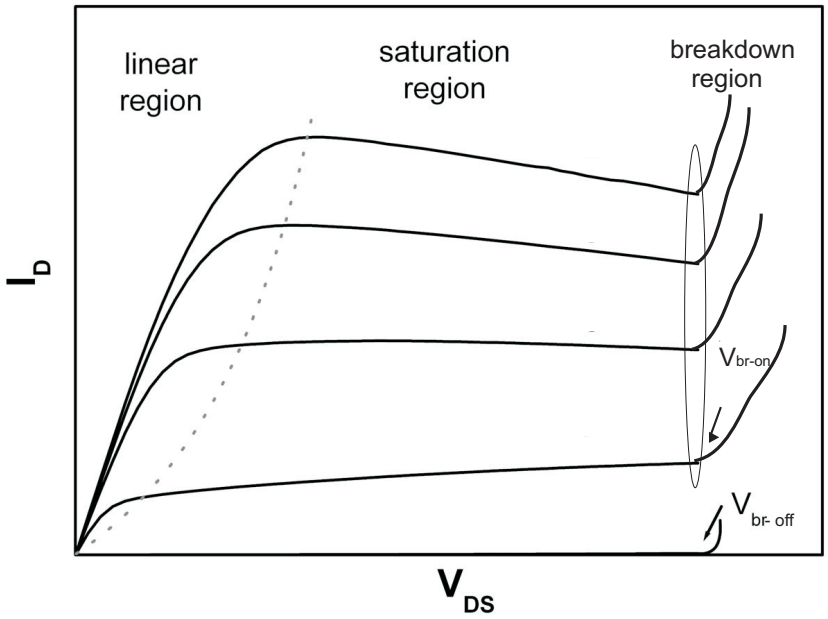

Figure 4.5: I_{DS}-V_{DS} characteristics of AlGaN/GaN HFETs. After Ref. [112].

acteristics of AlGaN/GaN HFETs. The output drain current I_{DS} is a function of the gate voltage and the drain-source voltage. The I-V characteristics can be divided in three regions: the linear region, where the drain voltage is small and I_{DS} is linearly proportional to V_{DS}; the saturation region, where the current is independent of V_D; and the breakdown region where the drain current increases rapidly with a slight increase of V_D [112]. The gate voltage (V_{GS}) controls the density of 2DEG concentration in the channel. The threshold voltage V_{th} is defined as the voltage at which the 2DEG concentration becomes negligible and the current channel is pinched off.

Devices used for microwave applications are qualified by the transconductance g_m which is strongly associated with the gain and high frequency properties. It is given by:

$$g_m = \frac{\partial I_{DS}}{\partial V_{GS}} \tag{4.5}$$

HFET devices utilized in this work have a short gate length ($<10\,\mu$m), so the devices

are assumed to operated in the saturation region. Accordingly, I_{DS} (normalized by the gate width) and g_m can be simplified to:

$$I_{DS} \approx en_s v_s \tag{4.6}$$

$$g_m = ev_s \frac{dn_s}{dV_{GS}} \tag{4.7}$$

The frequency at which the current gain becomes unity for short-circuit condition is called cutoff frequency f_T or unity current gain frequency. It can be described using g_m and the capacitance of the gate C_{gs} as below.

$$f_T = \frac{g_m}{2\pi C_{GS}} (= \frac{v_{sat}}{2\pi L_G}) \tag{4.8}$$

For power device applications, the breakdown voltage is one of the most important features. Two different breakdown phenomenon are observed depending on the bias condition: off-state breakdown and on-state breakdown. Off-state breakdown takes place under large positive drain bias and pinch-off conditions. Under such circumstances, empty surface states which are responsible for the 2DEG become filled with electrons from the negatively biased gate. Consequently, the 2DEG channel is depleted laterally toward the drain region. As the electric field increases, off-state breakdown occurs. At on-state breakdown, the contribution of impact ionization is dominant when the device carries a considerable amount of current.

4.1.4 Defects and *I-V* characteristics of heterostructure devices

In HFET devices, current collapse, which is also referred to as dispersion, DC/RF dispersion, current slump, has always impeded the high power performance. Possible sources of the current collapse are deep levels at the interface and/or in the buffer GaN layer, deep levels in the barrier layer under the gate metal and surface states in the barrier layer. Depending on the associated defects, the current dispersion can be classified into gate lag and drain lag.

Defects located at the interface and/or in the buffer GaN layer are responsible for the drain lag which is the current reduction at a given bias condition after a high drain-source bias has been applied while the gate voltage is kept constant. The mechanism of the drain lag is explained by electron trapping in the bulk GaN. High temperature or photo illumination can help releasing electrons from traps leading to partial recovery of the decrement of the drain current. Since no correlation between surface passivation with SiN_x and the current collapse was found, surface states are not involved with this current abnormality.

Interestingly, the drain lag is more serious in the HFET devices with a semi-insulating buffer layer than a conductive one [113]. Klein *et al* were able to identify the deep levels at 2.85 eV and 1.8 eV by varying the energy of the incident illumination [74]. The author showed that the concentration of deep levels associated with 2.85 eV is correlated with the carbon concentration in the buffer layer and the concentration of deep levels associated with 1.8 eV is related to higher dislocation densities. Considering that carbon incorporation around TDs enhances the resistivity of GaN buffer layers by compensating residual donors, the serious drain lag problem in a semi-insulating buffer can be explained well by the observation of Klein [74].

There is a considerable difference between the output power of HFET devices at RF frequencies and the values expected from DC *I-V* data. This phenomenon is known as gate lag and also called DC-to-RF dispersion, current slump, current compression, current collapse. For the RF characteristics, the knee voltage at which the drain current becomes saturated shifts to higher values and the maximum current is reduced in comparison to the DC *I-V* characteristics. Consequently, the RF output power ($P_{out} = 1/8 \cdot I_{DS,Max} \cdot (V_{BREAKDOWN} - V_{KNEE})$) is reduced.

Charge trapping in surface states is proposed as a responsible source of the

gate lag [21]. In fact, the significant impact of surface passivation substantiates this theory [114]. Figure 4.6 describes the mechanism of the gate lag. With negative gate bias applied, electrons flowing out of the gate electrode are captured by the free surface states at the area between gate and drain electrodes. Electrons captured by the surface states cause a virtual gate. The reduction of the net positive charge at the surface leads to a decrease in the drain-source current and transconductance g_m. Similar to the drain lag case, illumination can help detrapping charges from the surface states [21].

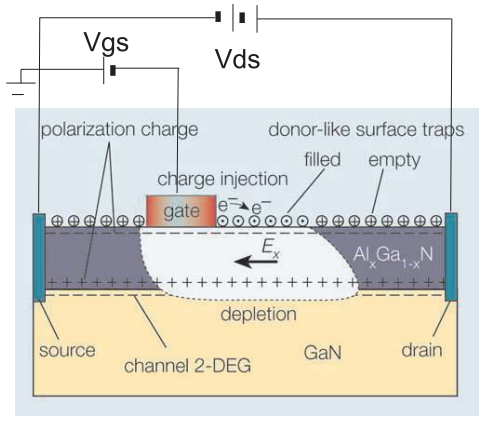

Figure 4.6: A negatively biased gate leads to trapping of electrons in surface states and formation of a virtual gate in the region between gate and drain. Consequently the drain source current is reduced and the current collapse effect occurs. After Ref. [21].

A gate lag measurement is an effective means to reveal this problem. In this measurement, the drain-source voltage is kept at a constant value, while a pulse is applied to the gate. Usually, this pulse is set to drive the transistor from below pinch-off to the on-state.

4.2 AlGaN/GaN heterostructures

4.2.1 Growth and characterization

The Al composition x along with the AlGaN barrier thickness are important in determining the characteristics of AlGaN/GaN heterostructures. The choice of Al percentage influences on the amount of polarization charges, the 2DEG mobility, and the depth of the quantum well where sheet charges are confined. A higher Al composition is beneficial to the induction of larger amounts of polarization charges due to the increased spontaneous and piezoelectric polarization field (see Eq. 4.1). Besides, the enhancement of the conduction band offset as a consequence of high x (see Eq. 4.2) helps that the 2DEG is confined in a way that carriers do not interact with other scattering centers in the bulk material. However, a high value of x causes difficulties in growing thick and good quality AlGaN layers since its lattice mismatch with GaN increases correspondingly. Large lattice mismatch leads to faster relaxation of the AlGaN layer bringing with its defects as for example layer cracks. These cracks limit the lateral transport capabilities of the 2DEG and degrade its mobility. Hence, the growth optimization of AlGaN/GaN heterostructures aims for high x while at the same time maintaining high quality of layer.

First, the Al incorporation issue was investigated. More, specifically, the correlation between ammonia flow and the efficiency of the Al solid incorporation x into AlGaN were investigated. In general, the pre-reaction between the aluminum source (TMAl) and ammonia is known to impede the growth rate and the Al incorporation. The depletion of TMAl caused by the pre-reaction makes Al incorporation less effective leading in a growth rate reduction [115].

Two different ammonia flows were chosen for the study of the impact of the Al composition: 1) 2.5 slm which is used also for bulk GaN growth and 2) 1 slm flow.

All other growth parameters, such as T_g, R_p, substrate rotation speed and total gas flow in the reactor etc, the contribution of which is relatively negligible, were kept the same.

The Al solid incorporation ratio in an $Al_xGa_{1-x}N$ layer was determined by XRD ω-2Θ measurements [116]. The relevant equation is given below.

$$\left(\frac{\Delta d}{d_s}\right) = -(\Delta\theta)cot\theta_B \tag{4.9}$$

Here, d_s is the substrate lattice plane spacing and θ_B is the corresponding Bragg angle. Δd is the difference in the inter-planar spacing of the layer and the substrate and $\Delta\theta$ is the separation of two peak positions. In this work, the layer to be characterized was AlGaN and the substrate was GaN. By employing sample and detector coupled scanning (ω-2Θ), the Bragg peaks of the substrate and the layer can be measured. For the simple case of the symmetric reflections (002) or (004) etc, the lattice mismatch ($\Delta d/d_s$) is obtained experimentally from the corresponding Eq. 4.9.

On the other hand, the in-plane lattice mismatch between AlGaN with Al composition x and GaN can be predicted. Since the strain present in AlGaN and GaN is biaxial, the in-plane lattice mismatch can be correlated with the out-of-plane lattice mismatch by the Poisson ratio ν as below.

$$\frac{\Delta a}{a_s} = \frac{1-\nu}{1+\nu}\frac{\Delta d}{d_s} \tag{4.10}$$

Assuming that the in-plane lattice constant of the AlGaN layer complies to Vegard's law, which assumes that the lattice parameter of the alloy layer varies linearly with the composition as given below in Eq. 4.11, the Al composition x can be calculated from Eq. 4.10.

$$a_{Al_xGa_{1-x}N} = (1-x)\cdot a_{\mathrm{GaN}} + x\cdot a_{\mathrm{AlN}} \tag{4.11}$$

In the gas phase, the Al composition (gas phase ratio) is driven by:

$$\text{Al gas phase ratio} = [M_{TMAl}]/[M_{TMAl} + M_{TMGa}] \tag{4.12}$$

M_{TMAl} and M_{TMGa} are the molar flows of TMAl and TMGa, respectively. These values are calculated by the related Eq. 2.3 on page 22.

The discrepancy between the gas phase Al ratio and x measured by XRD indicates the efficiency of Al incorporation. The correlation between Al gas phase ratio and the solid incorporation ratios are plotted in Fig. 4.7 with respect to two different ammonia flows (2.5 slm and 1 slm). In the ideal case, the Al solid incorporation will be equivalent to the gas phase ratio as indicated by the solid line in Fig. 4.7. However, experimental results show sub-linear behaviors. The Al solid incorporation ratio deviates from the theoretical values by about 15 % in the worst case. As the ammonia flow increases from 1 slm to 2.5 slm, its prereaction becomes more pronounced. Therefore, in this work, the ammonia flow was maintained at less than 2 slm for the AlGaN alloy growth in order to supress the pre-reaction.

The Al composition x was selected between $0.20 < x < 0.30$ in order to achieve high electron mobility and a reasonable 2DEG density. Low Al composition ($x < 0.15$) causes poor confinement of the 2DEG due to the small conduction band offset ($\Delta E_C < 0.28\,\text{eV}$). As a result, the 2DEG mobility is reduced because the wave function of the 2DEG penetrates into the bulk and its mobility is affected. An increase of Al composition improves the charge confinement and enhances the density of the polarization charges. However, this is accompanied by problems such as higher alloy scattering ($x > 0.3$) and layer relaxation.

The growth of AlGaN/GaN heterostructures with $0.2 < x < 0.3$ and $20\,\text{nm} < d_{AlGaN} < 40\,\text{nm}$ was followed by 2DEG transport characterization using Hall measurements at room temperature and 77K. The Hall samples were prepared by dicing

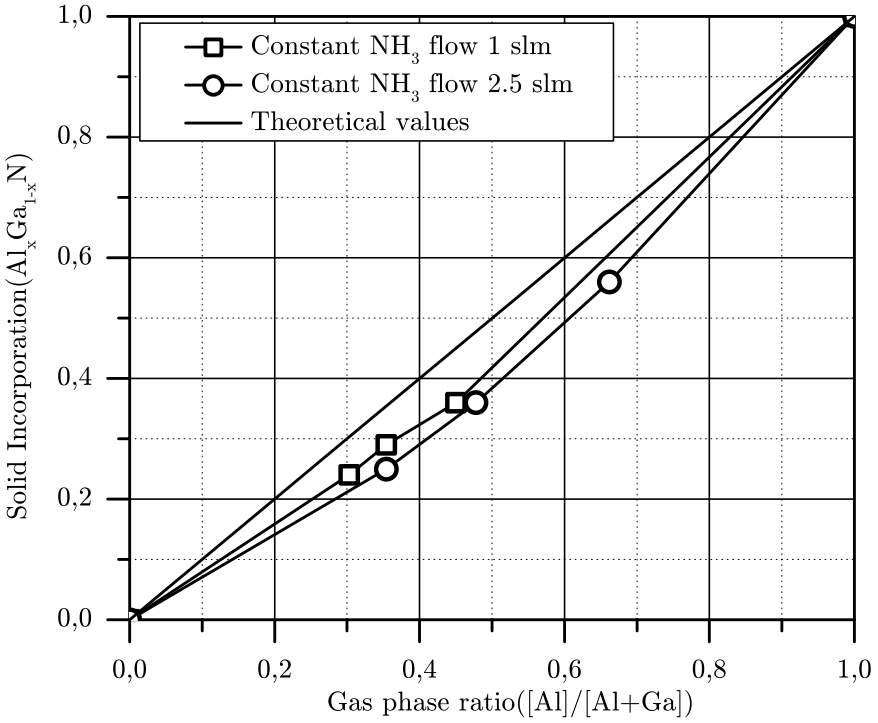

Figure 4.7: Solid Al incorporation vs. gas phase ratio in AlGaN layers with respect to two different ammonia flows.

the center region of a 2" wafer into 7 mm x 7 mm sized chips. Since the growth at the wafer edge is not uniform because of gas turbulence around the edge of the susceptor wafer pocket, the area within a few mm from the top and flat side of the wafer edge is excluded.

The average values of the room temperature Hall mobility and the 2DEG sheet charge densities obtained from various runs during our optimization are presented in Fig. 4.8. The Al composition was about 20±3 % and the thickness varied from 28 to 40 nm. The inverse relationship between Hall mobility and 2DEG density is observed as expected. A remarkable degradation of the Hall mobility (about 538 cm^2/Vs) and an extraordinarily high 2DEG density was found at a barrier thickness of 40 nm. It is worth mentioning that the observed high 2DEG density is attributed to the residual oxygen in the GaN template which was exposed to oxygen environment

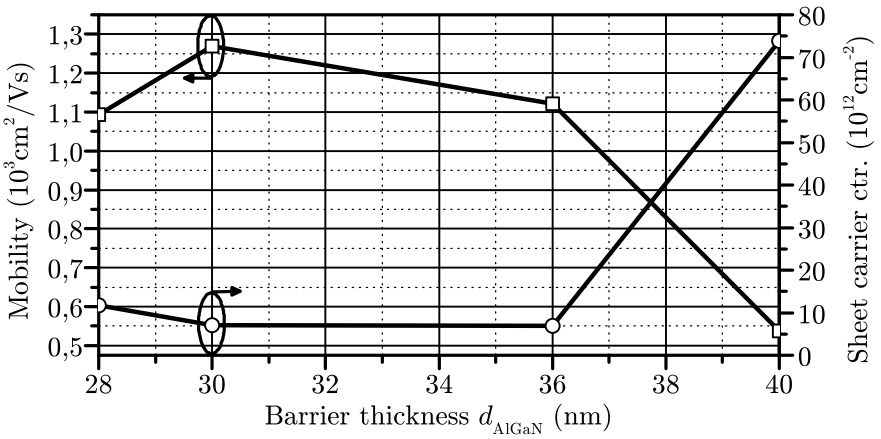

Figure 4.8: RT 2DEG mobility and sheet charge carrier density vs. d_{AlGaN}. Al composition was controlled at 20±3 %.

before the AlGaN growth, since the template was loaded into the reactor without removing the oxide layer. It can be speculated that the GaN underneath the AlGaN layer turnes into an unintentionally n-doped layer due to oxygen incorporation. In addition, the relatively thick AlGaN barrier (40 nm) reduces the mobility because of the delocalization of the 2DEG [117].

The best results obtained in this work at room temperature are an average Hall mobility and sheet charge density of about 1270 cm^2/Vs and 7.0·10^{12} cm^{-2}, respectively, with $Al_{0.17}Ga_{0.83}N$/GaN ($d_{AlGaN} \sim 30$ nm). This result is in good agreement with the theoretical and experimental work in Ref. [13]. The uniformity of the RT Hall mobility and sheet charge density is about ±7 %. The average of the 77K Hall mobility of this sample is about four times greater than the RT hall mobility (5020 cm^2/Vs) and the sheet resistance of the sample is about 680 Ω/□.

GI-XRR measurements of the corresponding samples were carried out to estimate the interface roughness. The measurement and simulation results are presented in Fig. 4.9. As a result, the surface and interface roughness is 0.7 nm and 0.5 nm respectively implying a very good interface transition from the GaN to the AlGaN

layer. In terms of material, the best Hall mobility and sheet charge density currently

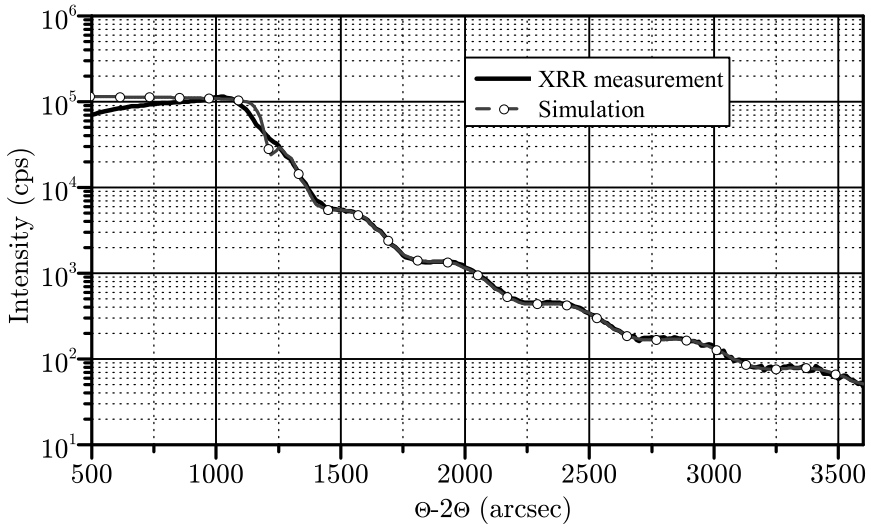

Figure 4.9: GI-XRR measurement and simulation result for a $Al_{0.17}Ga_{0.83}N$/GaN heterostructure.

reported is $\sim 2000\,cm^2/Vs$ and mid $10^{13}\,cm^{-2}$. Compared to these values, there is still room for improvement of the AlGaN/GaN heterostructure growth.

There are several possible approaches for improvement: 1) Increasing the channel confinement and polarization effect by raising the Al composition to 30 %, 2) inserting a very thin AlN interlayer between the GaN layer and AlGaN layer in order to enhance 2DEG confinement, 3) improving the interface roughness by controlling the quality of the GaN transition layer.

4.2.2 Device results

$Al_{0.17}Ga_{0.83}N$/GaN with a barrier thickness of $\sim 30\,nm$ was utilized for HFET device fabrication. The devices based on the in-house grown AlGaN/GaN heterostructures were compared with other devices fabricated on a reference sample in order to verify the impact of the resistive GaN buffer layer. The reference sample was grown externally. Table 4.1 is the summary of the structure parameters and Hall results of two samples.

	in-house HFET	Reference
d (nm)	30	16
x (%)	18	25
Sheet charge density (cm^{-2})	6.8x 10^{12}	-
μ at RT (cm^{-2}/Vs)	1280	-
R_s ($\Omega/\square$)	680	600

Table 4.1: Characteristics of in-house HFET sample and the reference sample.

The two samples were processed at the same time with the same fabrication process. The fabrication started with mesa isolation using reactive ion etching (RIE). Ti/Al/Ti/Au ohmic contacts were deposited followed by lift-off and rapid thermal annealing at 850 °C for 30s in N_2 environment. TLM measurements showed that the quality of the ohmic contact is good: contact resistance R_c is about $0.5\,\Omega{\cdot}mm$ and the specific contact resistance was in the low $10^{-5}\,\Omega \cdot cm^2$. 1 μm long gates were defined by optical lithography and Ni/Ti/Au metals were deposited by electron beam evaporation. The devices had two finger gates with a width of 150 μm and the distance between source and drain was 3.4 μm. Figure 4.10 illustrates the cross section and top view of device.

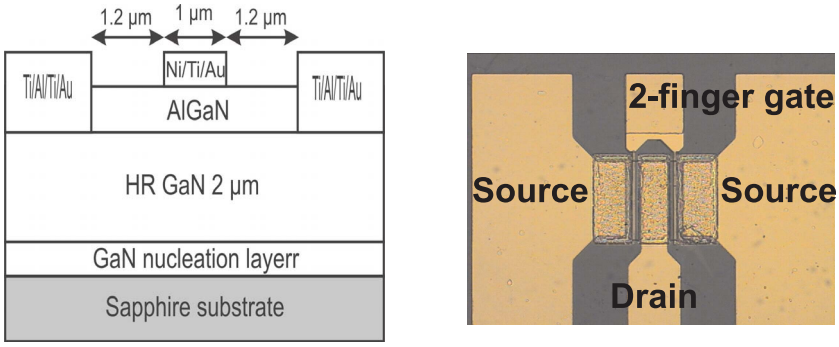

Figure 4.10: Cross section of AlGaN/GaN HFET devices and the microscope image of its top view (Courtesy of Sanghyun Seo).

The DC characteristics of two samples are shown in Fig. 4.11. The in-house devices show that g_m and I_{GS} are 138 mS/mm (at V_{GS}=-1 V) and 6 μA(at V_{GS}=-10 V),

respectively. The very small value of I_{GS} implies a very low leakage current. In contrast, the reference AlGaN/GaN HFETs exhibit a g_m and I_{GS} of about 105 mS/mm (at V_{GS}=0.5 V) and 0.2 mA (at V_{GS}=-10 V) respectively. In addition, the pinch-off current of the devices on the in-house wafer was 25 μA/mm (at V_{DS}=10 V, V_{GS}=-3 V) whereas the pinch-off current of the reference devices is higher by a factor of 20. The low pinch-off current observed from the in-house sample is indicative of the higher resistivity of the GaN buffer layer compared to the reference sample.

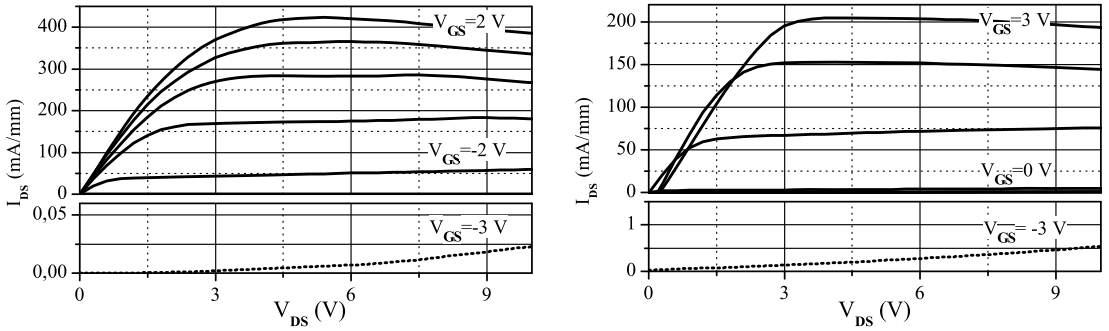

(a) The HFET device on the in-house sample

(b) The HFET device on the reference sample

Figure 4.11: I_{DS} vs. V_{DS} (gate voltage step = 1V).

Photoluminescence (PL) measurements of these two samples performed at 11K show that an acceptor bound peak is dominant in the in-house sample while a donor bound peak is stronger in the reference sample as shown in Fig. 4.12(a). Figure 4.12(b) shows the secondary ion mass spectroscopy (SIMS) results of the two samples. The concentrations of hydrogen, oxygen and carbon impurities are normalized with respect to the GaN concentration and compared. Since stable measurement requires a relatively long time, the data for several monolayers from the top surface (sputtering time upto 100 s) are discarded. However, this measurement can still provide valid information of the bulk GaN.

Overall, the concentration of hydrogen and oxygen is slightly higher in the in-house sample than in the reference sample. Since the TD density of the in-house

sample is also larger than that of the reference sample, defects such as $V_{Ga}O_N$ and $V_{Ga}H_N$ together with the TDs are responsible for the difference as proposed in chapter III. No discrepancy in the concentration of carbon is observed in the two samples except at a small degree at the surface. However, it is not sure that the high amount of carbon measured is due to surface contamination or not. In order to better understand those results, SIMS measurements need to be conducted after a SIMS system calibrations with samples of known impurity concentrations.

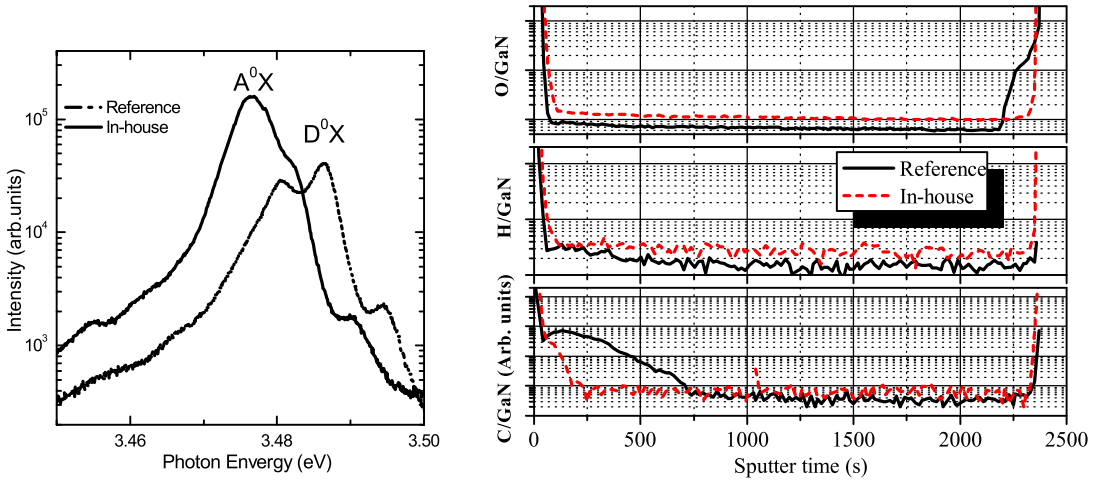

Figure 4.12: (a)11K band edge PL measurement and (b) SIMS results of the two samples of in-house grown $Al_{0.17}Ga_{0.83}N$/GaN heterostructure and the reference sample.

High frequency characterization of the devices was also carried out in order to obtain the two important parameters, f_T and f_{max}, the frequency where the current gain and the maximum stable gain become unity. The ratio of f_T to f_{max} was found to be in the range of two or three indicating good quality devices. f_T and a f_{max} of the in-house samples are about 11 GHz and 26 GHz, respectively and the associated f_T to f_{max} ratio is about 2.3. f_T and f_{max} of the reference sample are about 9 GHz and 20 GHz. The high frequency characteristics of the two samples are not significantly different. Nevertheless, an improvement of the device characteristics is observed

for the in-house grown sample which is likely to be attributed to the resistive GaN underneath the AlGaN layer. These values are comparable to device characteristics reported for such devices at the time this work was done [118].

4.3 AlN/GaN heterostructures

AlN/GaN heterostructures are attractive in many ways in comparison with AlGaN/GaN heterostructures. The alloy scattering observed in ternary alloys can be avoided while the very thin AlN barrier layer can enhance g_m and suppress the short channel effect [119]. Furthermore, devices of this type are possible to be operated at higher temperature and present reduced gate leakage due to their higher Schottky barrier compared with that of the AlGaN layer [120]. The AlN layer also present a small dielectric constant allowing therefore the reduction of the off-state capacitance in metal insulator field effect transistors (MISFETs) which may lead to higher cutoff frequencies compared to HFETs.

A 3∼5 nm thin AlN layer grown on GaN can lead in a high sheet charge density and high electron mobility values, which are comparable to the values obtained with AlGaN/GaN heterostructures due to the large polarization charge at the interface between AlN and GaN. Recently the highest sheet charge density ($n_s = 5{\cdot}10^{13}\,\mathrm{cm}^{-2}$) ever achieved was reported for AlN/GaN grown by MBE and corresponded to values close to the theoretical limit of $6{\cdot}10^{13}\,\mathrm{cm}^{-2}$ [121]. However, the achievement of high n_s is still challenging because of the relaxation of the AlN layer due to large lattice mismatch with GaN (2.5 %), AlN surface oxidation and the depletion of the 2DEG caused by surface degradation during subsequent fabrication processes.

In order to address such issues, *in-situ* or *ex-situ* SiN_x has been used as a passivation layer and device characteristics were found to be improved [119, 122]. How-

ever, these papers report on AlN MISFET with SiN_x grown by MBE and catalytic chemical vapor deposition (Cat-CVD). So far *in-situ* SiN_x grown by MOVPE was studied only with AlGaN/GaN heterostructure HFETs [123]. In this work, AlN/GaN MISFETs with *in-situ* SiN_x grown by MOVPE were studied to investigate its effects on the characteristics of MISFET.

4.3.1 Growth and characterization

AlN/GaN heterostructures were grown with the in-house MOVPE system on *c*-plane sapphire substrates. Trimethylaluminium (TMAl) and Trimethylgallium (TMGa) were used as alkyl sources and ammonia (NH_3) was used as hydride source. Silane (50 ppm SiH_4 in hydrogen) was used for the *in-situ* SiN_x growth. After cleaning and short nitridation of the substrate, the GaN nucleation layer was grown at 530 °C and subsequently annealed at 1040 °C. Finally, a 2 μm thick resistive GaN and 5 nm thick AlN layer was grown at 1020 °C. In order to grow an *in-situ* SiN_x layer, the temperature was reduced by 100 °C and silane was fed into the reactor until a few nanometers of SiN_x were grown on the top of the AlN layer. The growth rate of AlN and the *in-situ* SiN_x were characterized by Grazing Incidence X-ray reflectivity (GI-XRR) measurements using the BEDE D1 system. The growth rate was measured to be 143 nm/h and 10 nm/h, respectively. From the calibration of the growth rate, the thickness of SiN_x is found to be approximately 2$\sim$3 nm. As a reference sample, an externally grown AlN/GaN MISFET structure was prepared which did not have an *in-situ* SiN_x layer. Figure 4.13 illustrates the structures of the AlN MISFET with *in-situ* SiN_x and the reference sample.

The surface roughness of the AlN/GaN MISFET structures with and without *in-situ* SiN_x were measured by AFM and surface planarization was observed by *in-situ* SiN_x growth as shown in Fig. 4.14. The RMS surface roughness of the sample

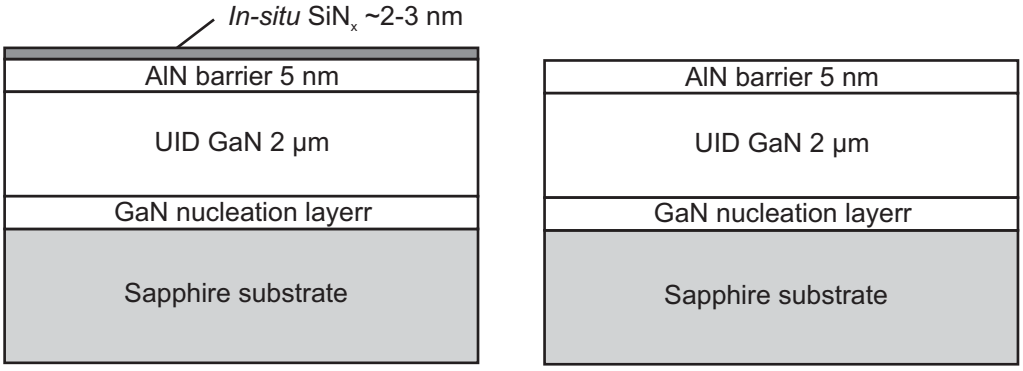

Figure 4.13: AlN/GaN heterostructure with *in-situ* SiN_x (left) and the reference sample (right).

with *in-situ* SiN_x is 0.17 nm while the corresponding value of the sample without *in-situ* SiN_x is 0.38 nm. This agrees well with the results in Ref. [123].

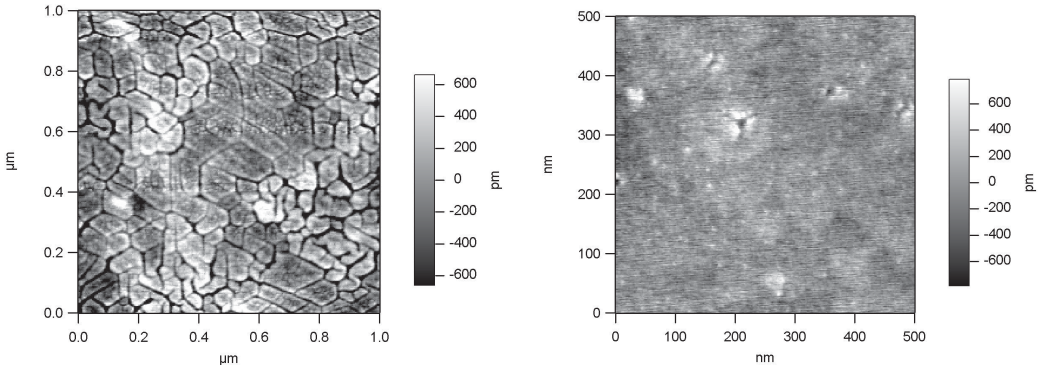

(a) (b)

Figure 4.14: AFM image of two AlN MISFET samples. The RMS roughness are (a) 0.38nm (without *in-situ* SiN_x passivation) and (b) 0.17nm (with *in-situ* SiN_x passivation).

Hall mobility at room temperature and 77K was measured using the Van der Pauw technique. Ohmic contacts were formed directly on the *in-situ* SiN_x by depositing Ti/Al/Ti/Au (25/120/12/300nm) using an e-beam evaporator system and subsequently annealed at 850 °C for 30s in N_2 in a rapid thermal annealing (RTA) system. However, removal of the AlN by KOH etching at 65 °C was necessary for the reference sample and ohmic contacts were formed directly on the GaN. A straight forward ohmic contact process by direct deposition of the ohmic metal on the *in-situ*

SiN_x MISFETs benefits from the absence of depletion of the 2DEG as well as the absence of an oxide layer between AlN and the metal layer. The expected good ohmic quality was confirmed by transfer length method (TLM) results which will be also presented after the Hall results.

The room temperature electron sheet concentration is $6.8 \cdot 10^{12}\,\mathrm{cm}^{-2}$ and the associated mobility is $950\,\mathrm{cm}^2/\mathrm{Vs}$. The 2DEG mobility at 77 K is $2610\,\mathrm{cm}^2/\mathrm{Vs}$. The 2DEG density of the reference sample is $9{\cdot}10^{12}\,\mathrm{cm}^{-2}$ and the mobility is $900\,\mathrm{cm}^{-2}/\mathrm{Vs}$. The observed higher 2DEG density might be due to weaker relaxation of AlN in the reference sample which was grown at low NH_3 flow. The ohmic quality of the devices was furthermore evaluated by TLM. Table 4.2 is the summary of the Hall and TLM measurement results of the *in-situ* SiN_x and the reference sample. Although the reference sample exhibits higher 2DEG density and slightly lower sheet resistance, its contact resistance and specific contact resistance are much lower than those of the reference sample. The contact resistance R_c and the specific contact resistance ρ_c of the *in-situ* SiN_x sample is $0.64\,\Omega{\cdot}\mathrm{mm}$ and $1.15 \cdot 10^{-5}\,\Omega{\cdot}\mathrm{cm}^2$, respectively. On the other hand, the reference sample exhibits an about three times higher contact resistance ($Rc = 1.75\Omega{\cdot}\mathrm{mm}$) and an one order of magnitude higher specific contact resistance ($\rho_c = 1.0{\cdot}10^{-4}\,\Omega{\cdot}\mathrm{cm}^2$). The high contact resistance of the reference sample is explained by the fact that the ohmic contact was formed directly on the GaN layer where no 2DEG is present. Therefore, its ohmic quality is relatively inferior to that of the *in-situ* SiN_x sample even though it shows larger 2DEG density.

Wet and dry etching of *in-situ* SiN_x were carried out with the Hall samples in order to investigate the quality of *in-situ* SiN_x and the way it affects the electron transport characteristics. First, the Hall samples were treated in 50 % BHF (buffered HF). The ohmic contacts were then masked in order to protect the metal and the

	in-situ SiN_x	Reference
n_{2DEG} (cm^{-2})	$6.8{\cdot}10^{12}$	$9{\cdot}10^{12}$
μ (cm^{-2}/Vs)	940	900
R_s ($\Omega/\square$)	600	570
R_c ($\Omega{\cdot}$mm)	0.64	1.75
ρ_c ($\Omega{\cdot}cm^2$)	$1.15{\cdot}10^{-5}$	$1.0{\cdot}10^{-4}$

Table 4.2: Hall and TLM measurement results of the *in-situ* SiN_x sample and the reference sample.

rest of the area was exposed to BHF. The Hall mobility and sheet charge carrier density were measured again after etching and values of 1100 cm^2/Vs and $6{\cdot}10^{12}$ cm^{-2} were obtained. The observed change is attributed to surface state changes [124, 125]. These values did not change even after more than one hour of etching. Since long time etching eventually degrades the ohmic contacts, there is presently no evidence of complete SiN_x etching by BHF. Additional studies using surface state characterization by X-ray photoelectron spectroscopy (XPS) are in progress for verification. However, the extremely slow etch rate of in-situ SiN_x is not a surprising result. Heying *et al.* reported that the etch rate of MBE grown SiN_x at 750 °C is one hundred times slower (4 Å/min) than the etch rate of PECVD SiN_x. Since the growth temperature of *in-situ* SiN_x grown in this work is around 950 °C, its etch rate can be extremely low. On the contrary, SF_6 etching led to substantial changes even after a few seconds of etching. The mobility dropped to 200∼300 cm^2/Vs which is close to bulk GaN values.

The etching effects were also studied by capacitance voltage (C-V) measurements. Standard Schottky diodes were fabricated with Ni/Ti/Au Schottky contacts. In order to achieve good ohmic quality, Ti/Al/Ti/Au multi layers were deposited on the *in-situ* SiN_x directly. Then, the *in-situ* SiN_x of half of the devices was etched by SF_6 and the Schottky contact step followed. Therefore, C-V characteristics of

Schottky diodes with and without SF_6 etching can be compared on the same wafer. The cross section of the Schottky diode is illustrated in Fig. 4.15(a).

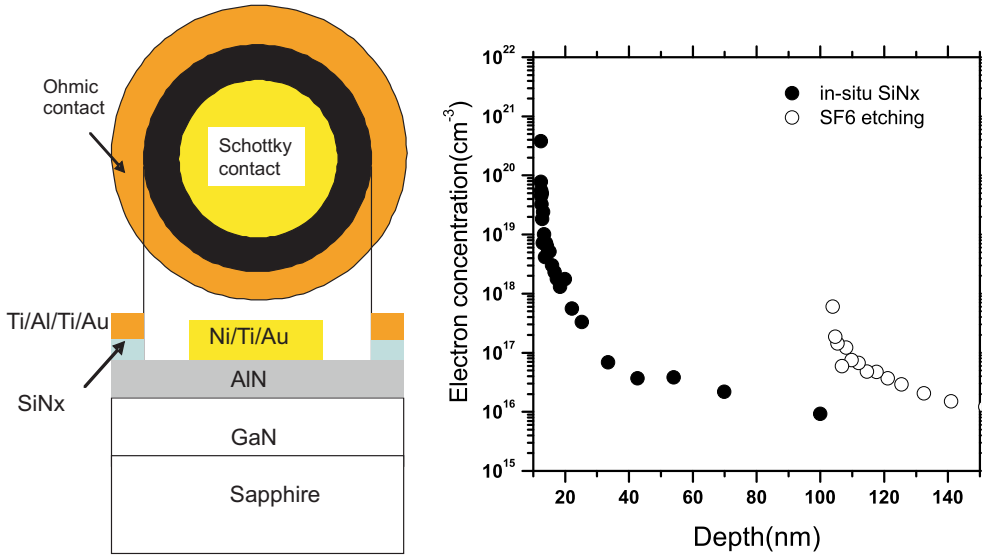

Figure 4.15: (a) Cross section of the Schottky diode fabricated after SiN_x etching. (b) Depth profile of the carrier concentration of as grown AlN MISFET structure with *in-situ* SiN_x and after SF_6 etching (right).

C-V characteristics were measured by an HP 4279A LCR meter at 1MHz. The carrier concentration versus depth profile confirms that the 2DEG is located at the interface between GaN and AlN in the MISFET with *in-situ* SiN_x as shown in Fig.4.15(b). However, the diodes treated by SF_6 etching do not show any 2DEG profile. The results are consistent with the observations from Hall measurements and imply that either the 2DEG is depleted as a consequence of the SiN_x etching or the AlN layer is removed by SF_6 together with SiN_x.

The impact of *in-situ* SiNx was also studied optically by PL measurements with a 325 nm continuous wave He-Cd laser. 11K band edge emission for three cases are compared in Fig. 4.16. These correspond to experiments without etching, BHF etching and SF_6 etching. In addition to three major peaks, A^0X, D^0X and X_A, a

very broad peak at 3.40 eV can be seen from the as grown AlN/GaN MISFET sample with *in-situ* SiN_x. The unusual peak shoulder also appears between 3.45 eV and A^0X. These shapes have not been found in either GaN or undoped AlGaN/GaN heterostructures. Although the peak at 3.4 eV becomes sharper and the peak shoulder becomes suppressed after BHF treatment, no discernible change was found. However, these two peaks disappear in the SF_6 etched sample. Therefore, they seem to be related to the 2DEG or the *in-situ* SiN_x layer. Since such peaks are not found in the reference sample, surface modification during growth resulting in a Si diffusion-like process is speculated as a plausible origin.

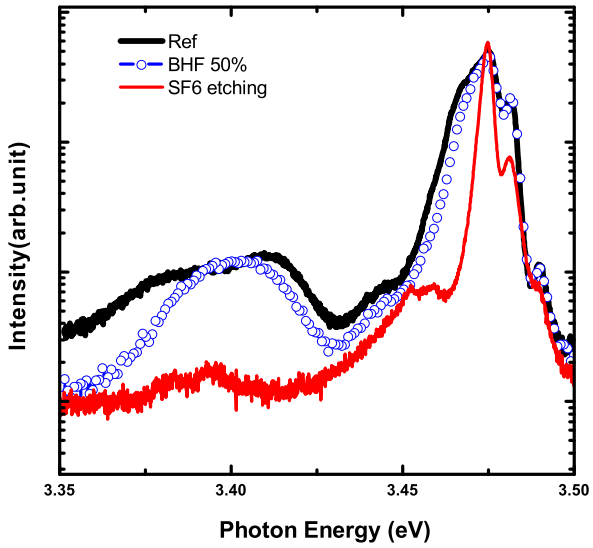

Figure 4.16: Band edge photoluminescence of the as grown AlN MISFET structure with *in-situ* SiN_x and after surface treatment by 50 % BHF and SF_6.

4.3.2 Device results

1 μm long gate devices were fabricated. The distance between source and drain was 3.4 μm. DC characteristics of the *in-situ* SiN_x device and the reference sample were measured at room temperature and are presented in Fig. 4.17. The *in-situ* SiN_x device exhibited a peak current density of 403 mA/mm at $V_{GS} = 1.5$ V and the

threshold voltage V_th was about -1.5 V. The peak extrinsic transconductance g_m was 206 mS/mm at V_{GS} = -0.6 V and V_{DS} = 5 V as shown in Fig. 4.18. This is almost a factor of three higher than 85 mS/mm obtained from the reference sample fabricated using the same technology.

The gate leakage current density was found to be around 1 mA/mm at a reverse V_{GS} of -30 V. This is one tenth of that of the reference sample. The small signal measurement results also show the superior performance of the *in-situ* SiN_x MISFET sample compared to the reference sample. The current gain cutoff frequency f_T and the maximum oscillation frequency f_{max} were found to be 10 GHz and 32 GHz, respectively. This is a factor of 2 to 3 improvement compared to the results of the reference sample.

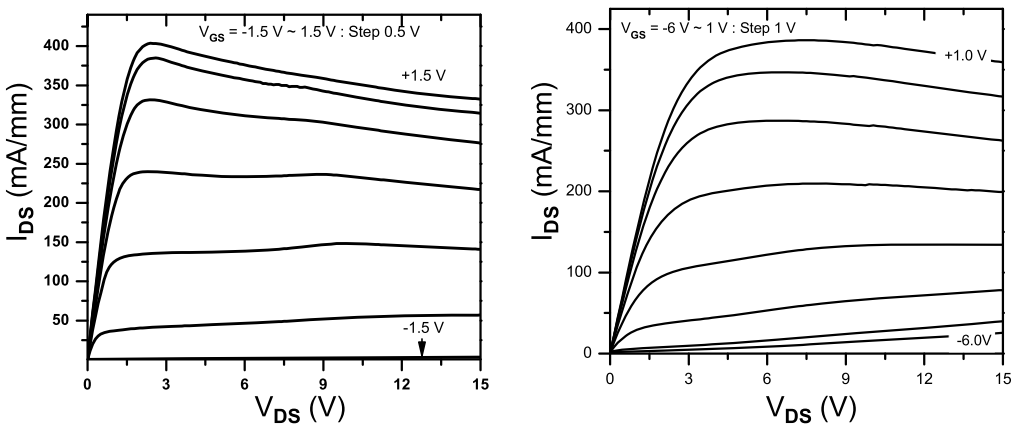

(a) (b)

Figure 4.17: I_{DS} vs. V_{DS} curves (a) of the AlN MISFET with *in-situ* SiN_x (b) of the reference sample [126].

4.4 InGaN/GaN alloy growth

The $In_xGa_{1-x}N$ alloy is a key material for blue and green light emitting devices. In addition, the implementation of an InGaN channel in HFET devices can improve the low-frequency noise behavior and the current collapse due to an increased con-

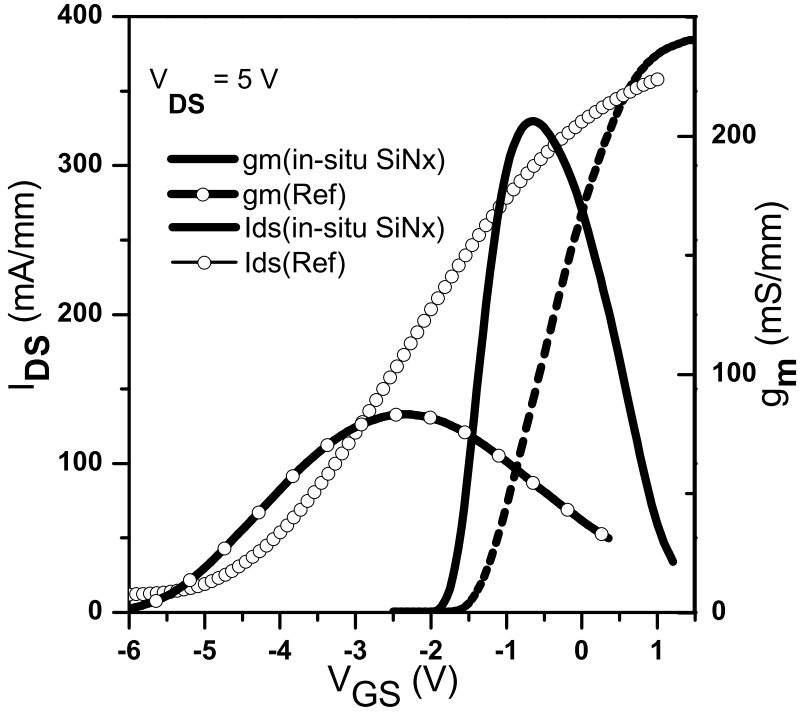

Figure 4.18: Transfer characteristics of the *in-situ* SiN_x MISFET and the reference sample at $V_{DS} = 5V$.

duction band offset between InGaN and GaN and a related carrier confinement improvement [127]. In this work, growth of InGaN/GaN multi quantum well (MQW) structures was attempted as part of the efforts made to investigate multiple heterointerfaces used in GaN/AlN DBRs (see section 6.3). Since the characterization methods for InGaN MQWs, for example PL and XRD, are non-destructive and provide accurate information about the quality of the heterostructure interface, they were used in order to obtain a quick quality estimation of the heterointerface.

The challenge in the growth of InGaN is Indium segregation from the growth surface since Indium is highly volatile and its bond energy with nitrogen is relatively weak. Surface segregated In grows and forms metal droplets which disturb the homogeneity of the film. Therefore, low temperature growth ($< 850\,^{\circ}C$) is necessary

[128]. The V/III ratio and the In molar fraction are also controlled in order to prevent Indium segregation. The growth parameters determining Indium incorporation are growth temperature, growth rate [4], carrier gas [129], TMGa flow [130] and ammonia flow.

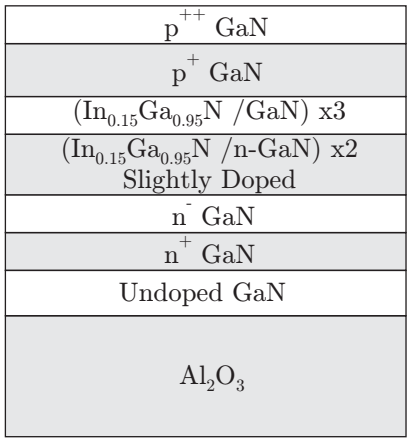

Figure 4.19: Schematic of the InGaN MQW structure.

The test structure was a 5 period $In_{0.15}Ga_{0.85}N$ MQW structure as shown in Fig. 4.19. The target InGaN well thickness and the GaN barrier thickness are 2.5 nm and 15 nm, respectively. To reduce the piezoelectric field which causes electron-hole (e-h) separation in the well, the GaN barrier was slightly doped with Si. The reactor pressure was fixed at 300 torr for the InGaN well and GaN barrier growth. For p-doped GaN, the reactor pressure was 100 torr. TMGa flow, T_g and growth time for the InGaN well were varied as shown in Table 4.3.

Sample	Peak position (nm)	T_g (°C)	TMGa Flow (μmol/min)	InGaN growth time(s)
M1	459	730	3.1	150
M2	419	750	2.1	150
M3	550	730	5.1	150
M4	491	730	3.8	150
M5	435	750	4.8	120

Table 4.3: Growth parameters for InGaN MQWs.

Room temperature PL measurements were performed for MQW structures

grown under various conditions. In all samples, a weak GaN band edge peak was found around 365 nm as can be seen in Fig. 4.20 and Fig. 4.21. In contrast, the peaks for the InGaN MQWs were found at different wavelengths depending on the growth condition. Sample M1 grown at a temperature of 730 °C had a peak at 459 ∼470 nm while the peak of sample M2 was found at 419 ∼425 nm.

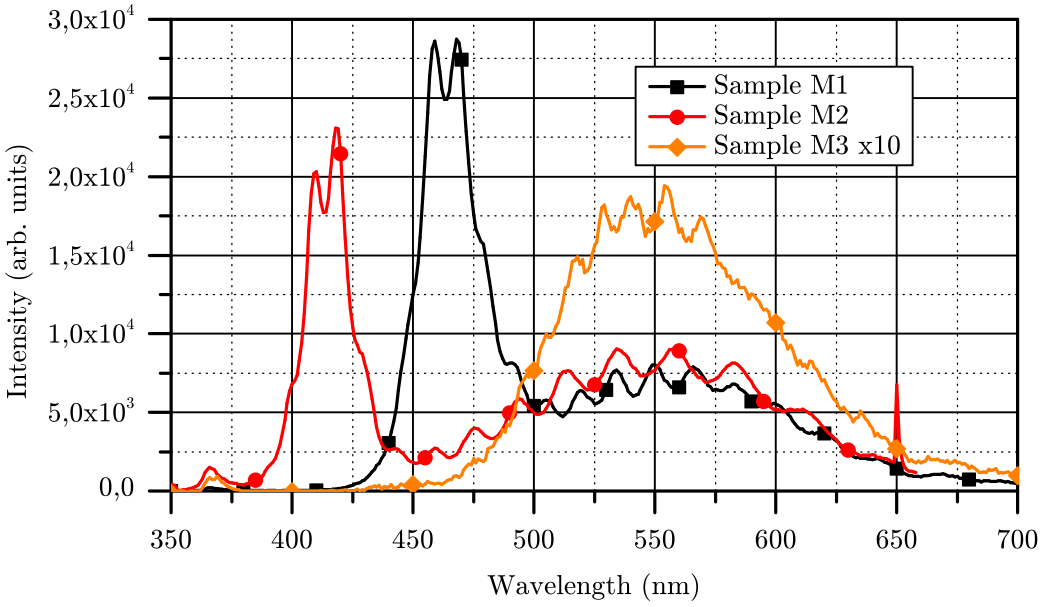

Figure 4.20: Room temperature PL measurement data of InGaN MQWs (I).

The blue shift of the PL peak in sample M2 indicates that the Indium incorporation is lower than in sample M1. Growth temperature differences between sample M1 and sample M2 (ΔT=20 °C) lead therefore to a 40 nm shift of the peak. The effect of TMGa flow can be found from the comparison between sample M1 and sample M3. Increasing TMGa flow from 3.1 μmol/min to 5.1 μmol/min shifts the peak position from 459 nm to 550 nm. High Ga flow contributes to efficient trapping of In and increases the InGaN QW thickness. Samples with thicker QWs usually show lower intensity and a broader peak because of separation of *e*-*h* pairs. The peak moved to green wavelengths (550 nm) and was broadened in sample M3 for these

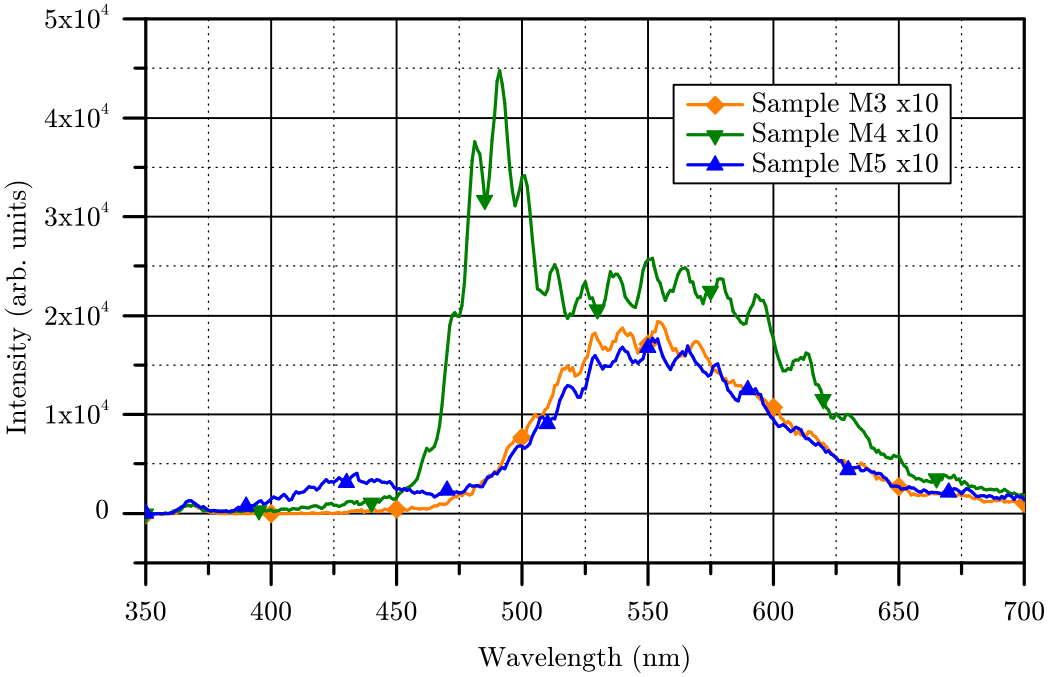

Figure 4.21: Room temperature PL measurement data of InGaN MQWs (II).

reasons.

In order to achieve good quantum confinement, the well thickness should be smaller than one Bohr radius (3.5 nm in case of InGaN). Figure 4.21 confirms the impact of the TMGa flow and the growth temperature on the PL characteristics. In sample M5, the effect of high TMGa flow and reduced well thickness was compensated by the effect of high growth temperature. Therefore, the red shift is smaller than for sample M3.

Although sample M1 presented a blue LED spectra, its FWHM is about 160 meV which is much broader than that of a typical blue LED. To obtain sharp peaks of about 20 meV, the well thickness should be further optimized. After annealing of sample M2 at 750 °C for 10∼20 min in N_2 environment, the Mg doped layer was found to be conductive. Blue emission was observed visually from this sample by applying electrical contacts to the top and bottom layer of the structure. Figure

4.22 (a) shows a typical result obtained from such tests. Electroluminescence was not observed from samples without high temperature annealing. The XRD characterization data in Fig. 4.22(b) illustrates well defined satellite peaks indicating a good interface between GaN and InGaN.

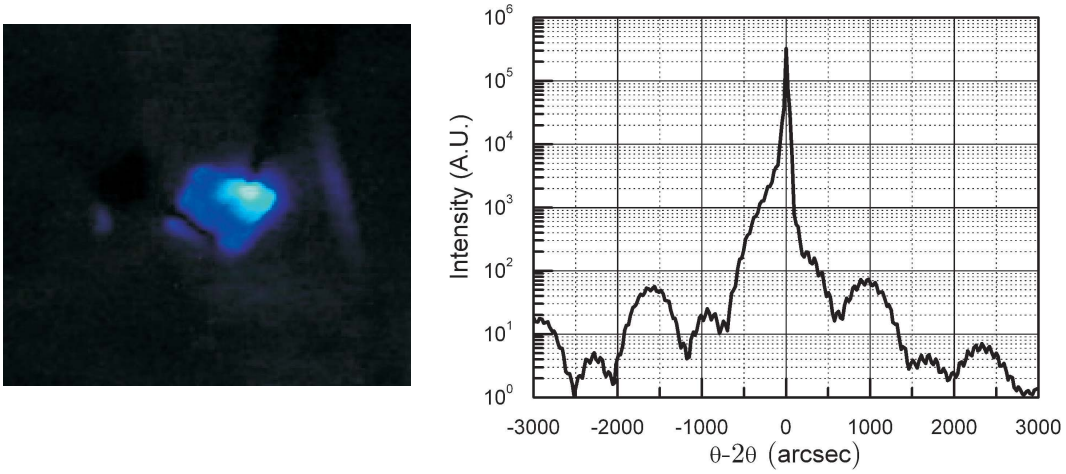

Figure 4.22: (a) Blue emission from sample M1 (left). (b) θ-2Θ measurement of a InGaN MQW (right) structure.

4.5 Conclusion

The focus of this chapter is the growth and characterization of nitride heterostructures such as AlGaN/GaN, AlN/GaN and InGaN/GaN.

The best electrical characterization results obtained from AlGaN/GaN heterostructures in this work were a room temperature average Hall mobility and sheet charge density of about 1270 $\mathrm{cm}^2/\mathrm{Vs}$ and $7.0{\cdot}10^{12}\,\mathrm{cm}^{-2}$, respectively. This material was also used to fabricate AlGaN/GaN HFET devices on a resistive bulk GaN template. Good pinch-off characteristics, a low gate leakage current and a good g_m value of 138 mS/mm were demonstrated while the f_T and f_{max} of these devices were about 11 GHz and 26 GHz, respectively. The obtained DC and high frequency characteristics imply that both the resistive bulk GaN and the AlGaN layers are of good quality.

AlN MISFETs with MOVPE grown *in-situ* SiN_x were investigated. Good ohmic contacts were possible without AlN etching. DC and RF characteristics of the devices were found to be improved in comparison with AlN MISFETs without a passivation layer by a factor of 2 to 3. f_T and f_{max} of these devices were about 10.2 GHz and 32.3 GHz, respectively. Moreover, these are comparable or superior to AlGaN/GaN HFETs presented in this work. Wet etching tests confirmed the high quality of the *in-situ* SiN_x. Significant depletion of the 2DEG was observed after SF_6 etching as evidenced by Hall, *C-V* and PL studies.

The growth of a InGaN/GaN MQWs (5 periods) structure was attempted to verify the capability of the growth system in terms of multiple heterointerfaces. As the result of optimizing the growth temperature and TMGa flow, a PL emission centered at 419 nm and electroluminescence were observed. This indicates that the TS MOVPE system used in this work is capable of growing multiple heterostructures with abrupt interfaces.

CHAPTER V

NON-POLAR NITRIDES

5.1 Introduction

Nitride structures grown on c-plane sapphire wafers have been presented in chapter III and IV. Polarization fields present in these structures result in a high sensitivity to surface state changes and strain. Therefore, polar nitride materials are attractive for sensor applications. In addition, 2DEG formation without intentional doping enables the fabrication of high frequency devices. However, polarization fields in III-Nitrides can also impede proper operation of certain device designs.

The strong polarization fields separate electron and hole (e-h) spatially in InGaN/GaN or AlGaN/GaN multi quantum wells (MQWs). As a result, the carrier recombination efficiency is poor and the emission wavelength is shifted due to the quantum confined Stark effect [131, 132]. The asymmetric energy band structure caused by the polarization field is also believed to hinder the realization of resonant tunneling diodes or varactors [133, 134].

In order to eliminate the polarization fields, the investigation of non-polar GaN growth is underway. Promising non-polar nitride growth results had been reported in early 2000 [135]. The schematic of the a-plane [$11\bar{2}0$] or m-plane [$1\bar{1}00$] crystal structures of GaN, which are referred to as non-polar GaN, are shown in Fig. 5.1(a).

The AlGaN/GaN heterostructure grown along the a-axis, for example, demonstrates that no spontaneous polarization is present due to the symmetric arrangement of atoms along this direction as depicted in Fig. 5.1(b). The piezoelectric polarization filed is present along the polar axis (c-axis) which is parallel to the growth surface. Therefore, heterostructures grown in either of these orientations are free of polarization-related electric fields. Figure 5.2 clearly shows that the presence of polarization fields impacts on the e-h recombination possibility and the emission wavelength in a AlGaN/GaN single quantum well.

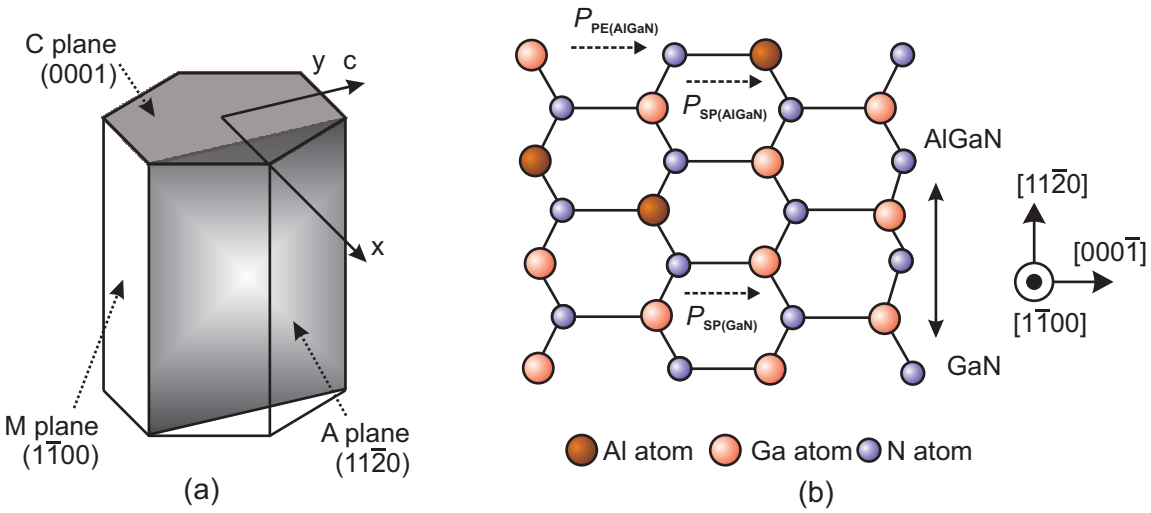

Figure 5.1: (a) Schematic of the hexagonal unit cell of wurtzite nitride semiconductors. The shaded and patterned areas present the c-plane and a-plane. The area without any pattern indicates the m-plane. (b) a-plane AlGaN/GaN heterostructure.

Superior properties of a-plane structures in comparison to conventional c-plane structures have already been reported and include a reduced shift of the emission wavelength with the injection current [136], a smaller turn-on voltage [137], and a strong polarization of the emitted light [138]. However, their application to electrical devices has barely been addressed.

This chapter describes the growth of a-plane GaN grown on r-plane [10$\bar{1}$2]

sapphire wafers for the realization of non-polar heterostructure electrical devices. In order to obtain good material, systematic studies of NLs were carried out first and then *a*-plane AlGaN/GaN heterostructures were grown.

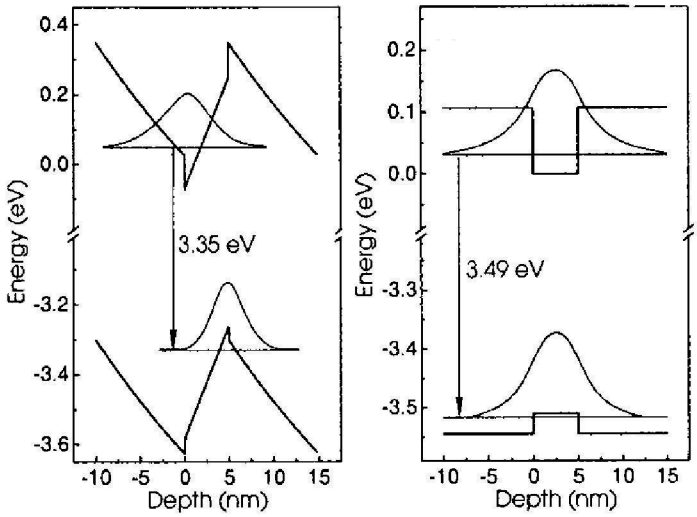

Figure 5.2: Energy band diagram of an AlGaN/GaN single quantum well with polarization field (left) and without polarization field (right) [135].

5.2 Growth and characterization

Compared with the featureless and smooth surface of *c*-plane GaN layers, the surface of *a*-plane GaN layers is quite rough and stripe features typically are observed. XRD rocking curve measurement results indicate that the in-plane crystalline quality of *a*-GaN layers is anisotropic. FWHM values are considerably different depending on the in-plane angle Ψ. This is due to the anisotropy of the in-plane thermal expansion and lattice mismatches [139].

Great efforts had been made in order to obtain smooth surface morphology and isotropic surfaces by optimizing the anisotropic strain, incorporation probability and adatom diffusion length. For this purpose, various techniques, including the conventional two step growth using NLs, have been proposed: 1) direct growth of GaN without NLs [140], 2) introducing N_2 as a carrier gas [139, 141], 3) SiN_x inter-

layer [142], 4) flow rate modulation growth [143] etc. In this work, prime importance was given to the optimization of NLs for the growth of *a*-GaN. SiN_x interlayers and modulation of the flow growth were not considered as the associated growth rate can be very low.

In chapter III, the significance of the NL in accommodating thermal mismatches and lattice mismatches between the main layer and the substrate was discussed. NLs were shown to promote the growth transition from 3D to 2D in the growth of *c*-plane GaN. Besides, the optical and electrical quality of the following layers is strongly dependent on the NL. Therefore, extensive experiments were performed in order to optimize low temperature grown GaN NLs. For the same reason, extensive studies were therefore also performed for the growth of NLs intended for *a*-plane GaN. Since the growth of GaN evolves in a completely different way depending on the orientation of the sapphire substrate, various types of NLs were explored as follows:

- Low temperature GaN nucleation layers
- Direct growth (without any NLs)
- AlN nucleation layers

The low temperature GaN nucleation layers used for the initial studies were of the same type of those for the growth process of *c*-plane GaN. The thickness and ammonia flow were varied in order to optimize the NL. The resulting low temperature GaN nucleation layers turned out to be less effective for the improvement of the surface morphology and anisotropy of *a*-plane GaN than for *c*-plane GaN. Therefore, direct growth of GaN was considered. The results obtained from these studies were comparable to those of *a*-plane GaN grown utilizing GaN NLs. As an alternative approach, AlN NLs were investigated and the results obtained from them indicated

improvement of the *a*-plane GaN quality.

5.2.1 Low temperature GaN nucleation layer

The standard reference growth conditions established for *c*-plane GaN were adapted for the growth of *a*-plane GaN. Trimethylgallium (TMGa) was used as an alkyl source and ammonia (NH_3) was used as hydride source. After cleaning and short nitridation of the substrate, the GaN nucleation layer was grown at 530 °C and subsequently annealed at 1040 °C. Finally, 2 μm thick GaN was grown. The growth conditions are given in Table 5.1.

	P_g	T_g (°C)	V/III	Ramp-up time (s)	Annealing time (s)
Substrate cleaning	100	1060	-	-	300
NL	200	530	3600	300	70
GaN	100	1040	920	-	-

Table 5.1: The standard *c*-plane GaN growth conditions.

Although the same growth process was employed for both *c*-plane GaN and *a*-plane GaN, a few differences were observed from the interferograms as presented in Fig. 5.3. In particular, the surface reflectance right after NL annealing is considerably different from that of *c*-plane GaN. In general, NL annealing causes a thin and continuous NL layer (20∼30 nm) to turn into NL islands and the reflectance from *c*-plane GaN is therefore quite low after annealing (see section 3.1.2). As the growth of GaN proceeds, the reflectance recovers within 1000 s. In contrast, the reflectance from the *a*-plane GaN remained high even after NL annealing.

Another discrepancy is that longer time (>1000 s) is needed for the reflectance recovery in case of *a*-plane GaN. Ni *et al.* investigated the surface evolution of *a*-GaN layers with GaN NLs utilizing SEM [144]. Complete coalescence was observed at a thickness of 1.5 μm. In general, the complete coalescence of *c*-GaN takes place at a thickness of 0.3∼0.7 μm. This result explains the longer recovery time of the surface

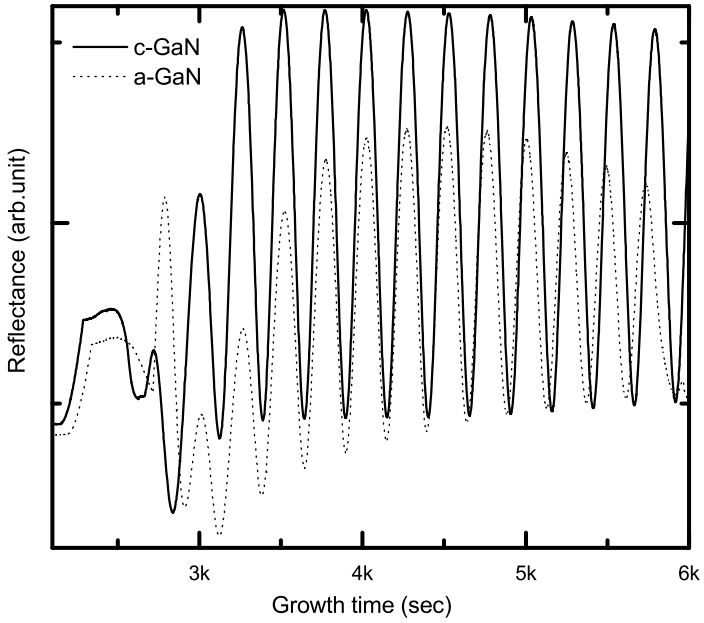

Figure 5.3: Interferograms of c-plane GaN and a-plane GaN. The standard reference recipe for c-plane GaN was used for both growths.

reflectance in a-plane GaN.

Lastly, the reflectance of a-plane GaN is much lower than that of c-plane GaN which implies that the surface of a-GaN is rough. This is consistent with the results of optical microscope and AFM measurements (see Fig. 5.4). Stripes along the c-axis can been seen and the surface undulates along the m-axis. This surface undulation is also observed from the r-plane sapphire substrate. However, its RMS roughness is 0.3 nm which is much less in comparison with 6.7 nm of a-GaN (20 x 20 μm). The typical RMS roughness of c-plane GaN (2 μm) is about 0.15$\sim$0.3 nm.

XRD ω-2Θ measurements confirmed that there is no peak related to the (002) reflection plane. The FWHM of the ω-rocking curve is $\sim$ 1000" when the incident X-ray beam is parallel to the c-axis while it is $>$ 2000" when the incidence beam is perpendicular to the c-axis (i.e. m-axis). This differs from c-plane GaN, where the typical FWHM value of in-plane ω rocking curves is about $\geq$ 300". Apart from the

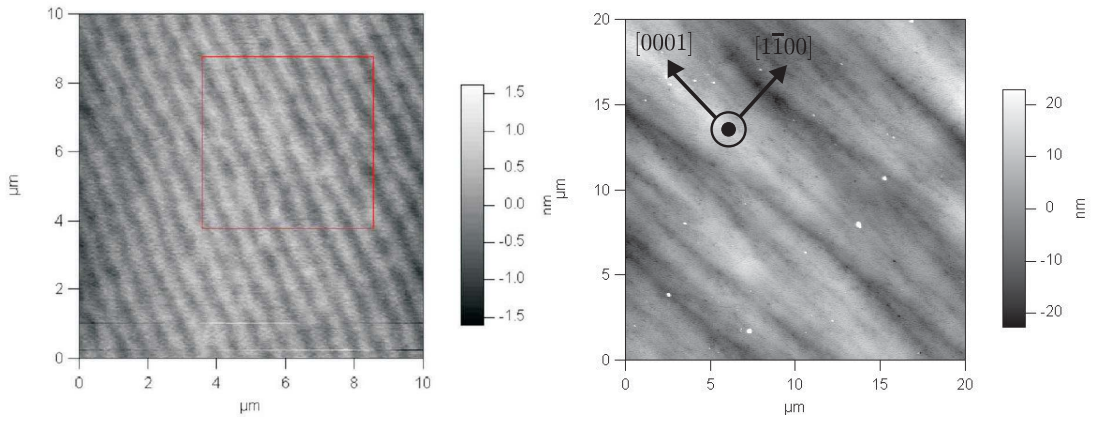

Figure 5.4: AFM images of r-plane sapphire substrate (left) and GaN grown with 25 nm NL (right). The RMS roughnesses are 0.3 nm and 6.7 nm respectively.

high value of the FWHM in comparison to c-plane GaN, the in-plane anisotropy was also found to present significantly different characteristics. The different migration length of adatoms along the two directions was speculated to be a possible reason [139].

It is worth mentioning that a-plane GaN is highly sensitive to the thickness of the low temperature GaN nucleation layer while relatively smooth surface morphology can still be achieved in c-plane GaN growth for a wide range of GaN NL thicknesses. Figure 5.5 and 5.6 present interferograms and microscope images of two a-plane GaN layers having different GaN NL thickness. The reflectance signal of the a-GaN layer with thick NL recovered very slowly after the high temperature annealing whereas the a-GaN layer grown on 25 nm showed quick recovery of the surface reflectance. As can be seen from the microscope image, the surface of a-GaN with thick NL was very rough and milky while a-GaN with relatively thin NLs had reasonable surface quality. It manifests that the growth window of a-GaN is very narrow.

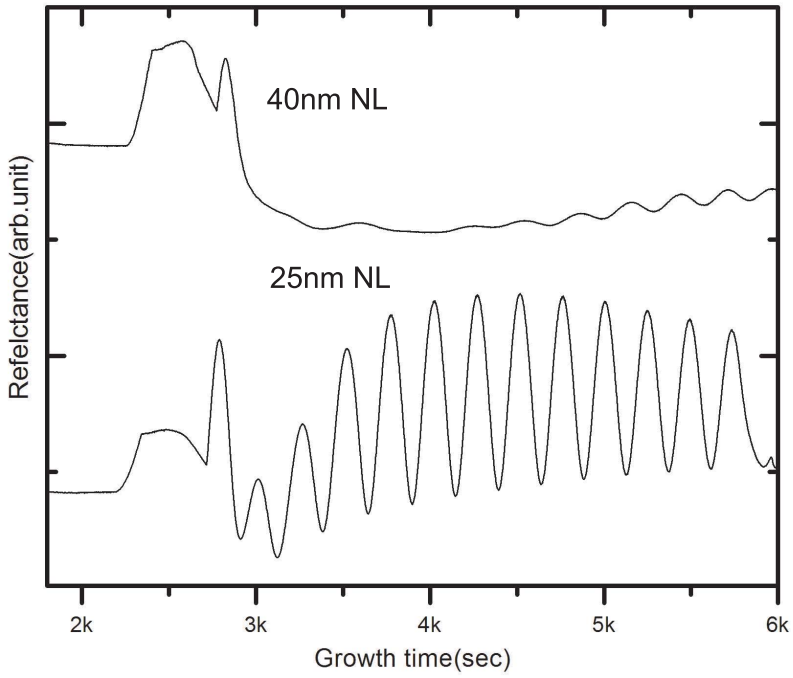

Figure 5.5: Interferograms of two a-plane GaN layers with two different GaN NL thicknesses. The top interferogram and the bottom one are associated with 40 nm and 25 nm NLs.

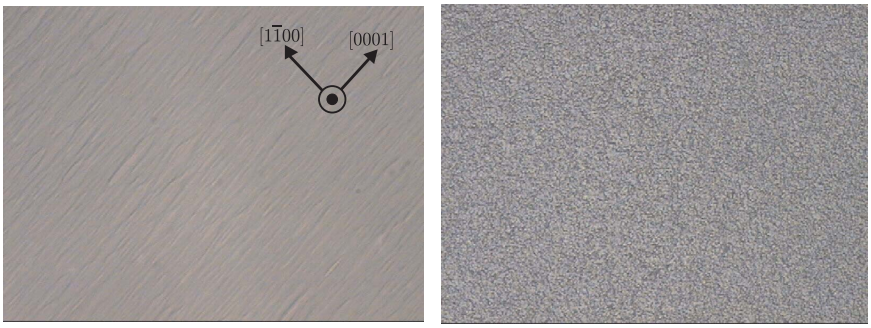

Figure 5.6: Optical microscope images of the two a-plane GaN layers grown on 25 nm NL (left) and 40 nm NL (right).

5.2.2 Direct growth

Our a-plane GaN grown on a GaN NL showed comparable quality characteristics with those reported in Refs. [139] and [144] but further improvements are necessary in order to achieve device quality layers. Higher temperature and lower

growth pressure than the current used growth condition are preferable for this purpose [144, 145]. However, growth temperatures used in this work are already quite close to the limit of the system. Therefore, a direct growth method was investigated as an alternative method. In this technique, *a*-plane GaN was grown without any nucleation layer.

Araki *et al* compared the direct growth of GaN on *c*-plane sapphire substrate and on *a*-plane sapphire after nitridation. The authors observed a very low-density nucleation of GaN islands and the Volmer Weber or three-dimensional (3D) growth mode on *c*-plane sapphire. In contrast, a high- density nucleation of GaN islands was observed on *r*-plane sapphire substrates. This implies that the initial layer grown after the nitridation step can function as a nucleation layer in case of *a*-plane GaN growth while *c*-plane GaN growth requires the deposition of a thin NL and subsequent annealing of it in order to form NL islands.

Nitridation was performed at 1040 °C after high temperature annealing of the *r*-plane sapphire substrate. The ammonia flow and the pressure were 1.8 slm and 100 torr, respectively. The temperature and the reactor pressure were reduced to 1020 °C and 50 torr for the first GaN growth. At this condition, the corresponding V/III ratio was 1280. The second step of the GaN growth was carried out at 1040 °C and 100 torr with a V/III ratio of 1520. The associated interferogram of *a*-GaN grown with the direct growth technique is illustrated in Fig. 5.7.

The surface reflectance recovered considerably faster than that of *a*-GaN layers with GaN NLs. Directly grown *a*-GaN layers fully coalescenced at about 0.5 μm which is quicker by a factor of three compared to *a*-GaN with GaN NL. The surface became rough rapidly above this thickness. The surface morphology was investigated at two thicknesses, $\sim$1.2 μm and $>$ 2.5 μm as marked on the interferogram. Figure

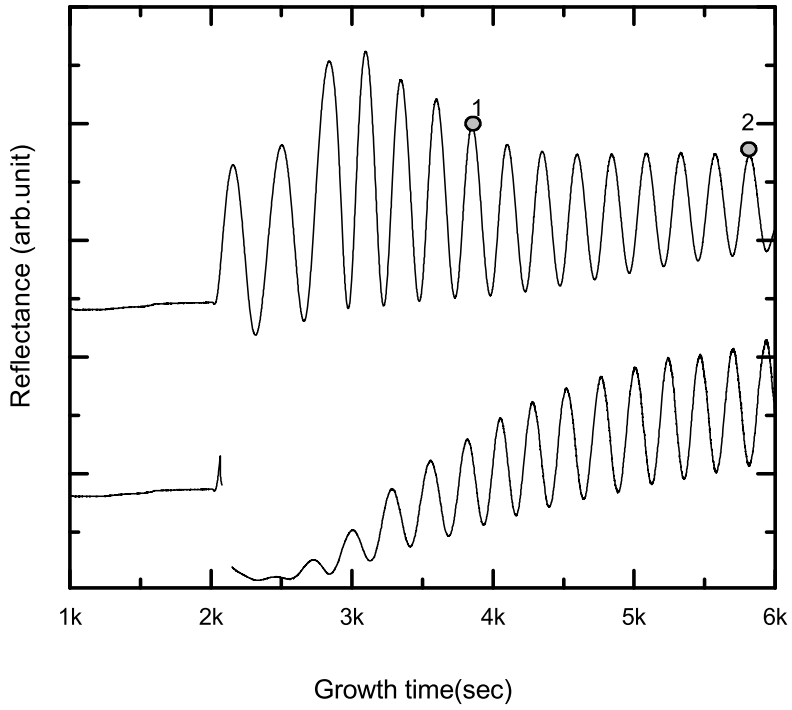

Figure 5.7: Interferograms of directly grown a-plane GaN layers with two different V/III ratios. V/III ratio was changed from 1280 to 1520 (at the top) and from 2100 to 1070 (at the bottom). The points where the surface morphology was checked are marked. Point 1 and 2 correspond to 1.2 μm and 2.5 μm, respectively.

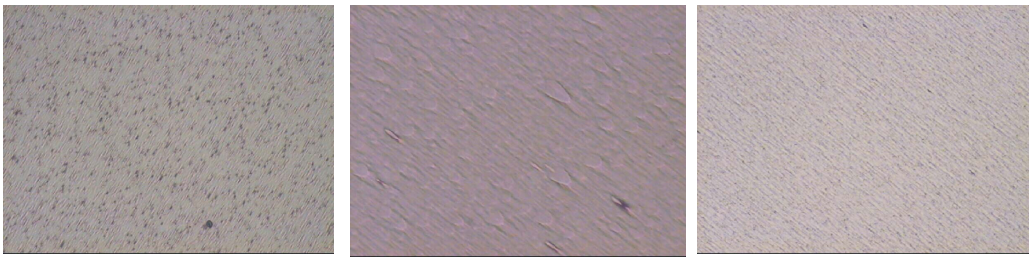

Figure 5.8: Optical microscope images of a a-plane GaN surface. (a) 1.2 μm, (b) 2.5 μm, (c) 2.5 μm thick a- GaN grown with high V/III ratio at the first growth step followed by a second step growth with low V/III ratio (from 2100 to 1070).

5.8 shows that the surface of the ~1.2 μm thick a-GaN is full of defects and pin holes. In contrast no such defects were found on the surface of the thick a-GaN (~2.5 μm) as the layer became fully coalescened. The FWHM of the rocking curve is 2250" and 1100" in m- and c- direction, respectively. The RMS roughness is about 6.2 nm

(10 x 10 μm) as shown in Fig. 5.9. This is comparable with the value of the a-GaN grown with GaN NL. However, more texture can be seen along c-axis.

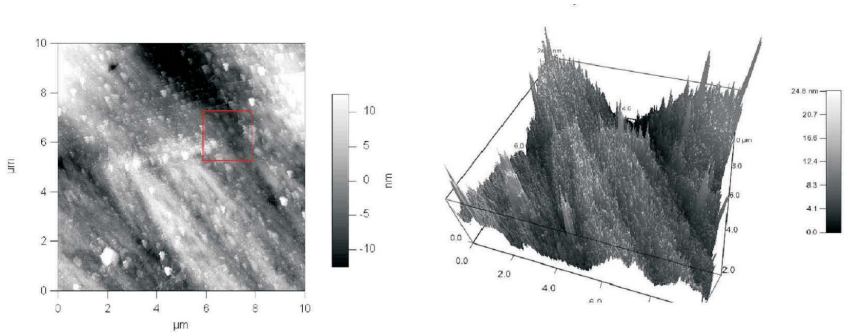

Figure 5.9: AFM image of a 2.5 μm a-plane GaN surface.

Direct growth was studied further by controlling the V/III ratio. Since high V/III ratio enhances the vertical growth mode and low V/III ratio promotes lateral growth, the ammonia flow was controlled to obtain a V/III ratio of 2100 and 1070 for the first and the second growth step, respectively.

The interferogram of this sample shows a completely different evolution of the surface morphology as presented in Fig. 5.7. The surface was very rough from the beginning and it slowly recovered. The GaN pit size was reduced, however, defects could be still seen on the surface. This might be due to the non-optimized V/III ratios.

The effect of the two step V/III ratio control in the direct growth method were investigated in Refs. [140, 146]. A high V/III ratio ($\sim$ 1350) was chosen for the growth of GaN following nitridation. In the subsequent growth, the V/III ratio was reduced below 150 for the growth of the main GaN layer. Voids found in the initial GaN can be reduced by a high V/III ratio. A low V/III ratio is believed to be beneficial in reducing the size of the pits due to the increase in lateral growth rate. Consequently flat and smooth surface could be obtained with a RMS roughness value

of 3.84 nm at 1.2 μm [146] which is smaller than that of the directly grown samples presented in this section.

The values set for the low V/III ratio in this work were by far greater than the literature values (1067 > 150) leading in less lateral growth. In order to obtain such a low V/III ratio, the TMGa molecular flow has to be set very high with respect to ammonia by means of increasing the flow or bubbler temperature or reducing ammonia flow to very low values. Changes of this type were however not possible due to the currently available hardware configuration of the TS system. Therefore, another method was considered as will be presented in the next section.

5.2.3 AlN nucleation layer

AlN nucleation layers were first proposed by Akasaki for the growth of *c*-plane GaN [3]. Although the growth window of AlN NLs is relatively narrow compared to GaN nucleation, it is widely used for the growth of GaN on SiC and Si whereas the use of GaN NLs is mainly limited to the growth on sapphire substrates.

Direct growth of GaN on AlN nucleation layers is known to lead to a higher triangular pit density which is sensitive to the GaN V/III ratio [147]. An intermediate layer was used between the GaN and the AlN NL layers to avoid this problems. Multiple buffer layers [148] and strained layer superlattice (SL) [149] approaches which have been proven an effective method in reducing dislocation densities in *c*-plane GaN epilayers were used.

In this section, the growth of *a*-GaN was carried out utilizing two step AlN layer growth and AlN/GaN superlattice layers. The growth sequence is summarized below.

- Substrate cleaning

- Nitridation
- Intermedium temperature AlN layer at 850∼1000 °C
- High temperature AlN layer at 1040 °C
- AlN/GaN superlattice layer (SL)
- GaN layer

During the growth, the reactor pressure was maintained at 60 torr. V/III ratio for AlN and GaN were 1800 and 1200, respectively. The thickness of the GaN was estimated to be around 2.0 μm. The associated interferogram showed that the surface reflectance recovered slowly after the AlN/GaN SL. The optical microscope image and AFM images are presented in Fig. 5.10. Although the RMS roughness is reduced by 20 % in comparison with other GaN layers grown by using GaN NLs and the direct growth method, many pits were found on the surface.

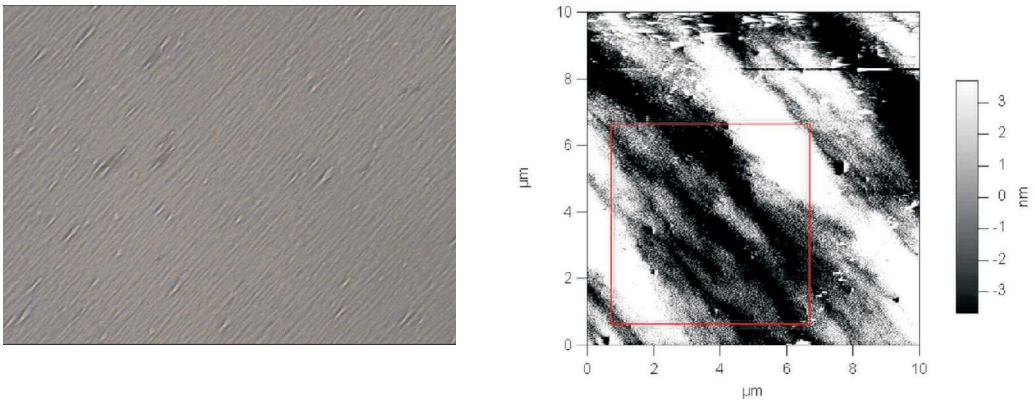

Figure 5.10: Microscope image (left) and the AFM image (right) of an a-GaN layer (2 μm). The RMS roughness is 5.7 nm.

The nitridation process can lead to a very rough sapphire substrate surface. Subsequently grown AlN NLs can for this reason be affected by this rough surface morphology. Therefore, growth experiments were carried out without nitridation.

The associated interferogram is depicted in Fig. 5.11 which also indicates the different growth phases. The growth of GaN was stopped when its thickness reached 1.2 μm in order to check the surface morphology and in-plane anisotropy by XRD measurements. After the characterizations, the wafer was cleaned and placed back in the reactor for a subsequent growth. During the 2nd growth step, 7 periods of AlN/GaN SL layers were used again for further improvement of the surface morphology of the following GaN layer.

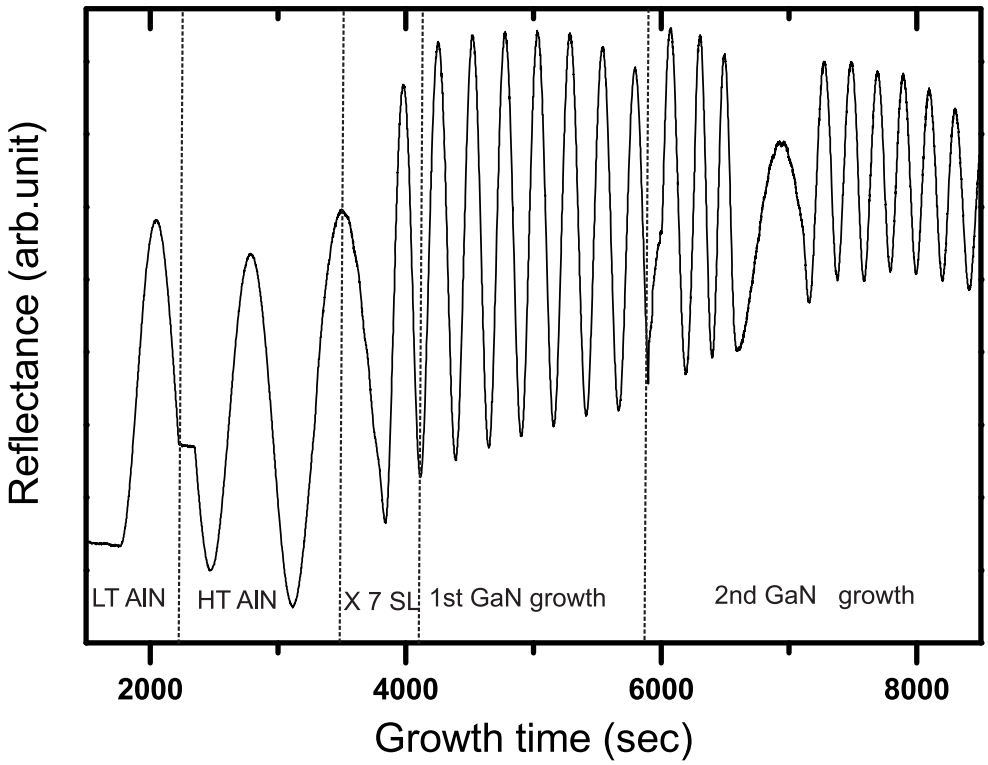

Figure 5.11: Interferogram of a-GaN monitored at two stages.

The surface images obtained for 1.2 μm and 2.4 μm thickness are compared in Fig. 5.12. Both images show relatively flat and smooth surfaces which is superior to previous layers grown with different methods. However, a stripe pattern along the c-axis is more obvious in the thin layer. This might be due to the less efficient lateral

growth in this axis than in the m-axis in the thin layer.

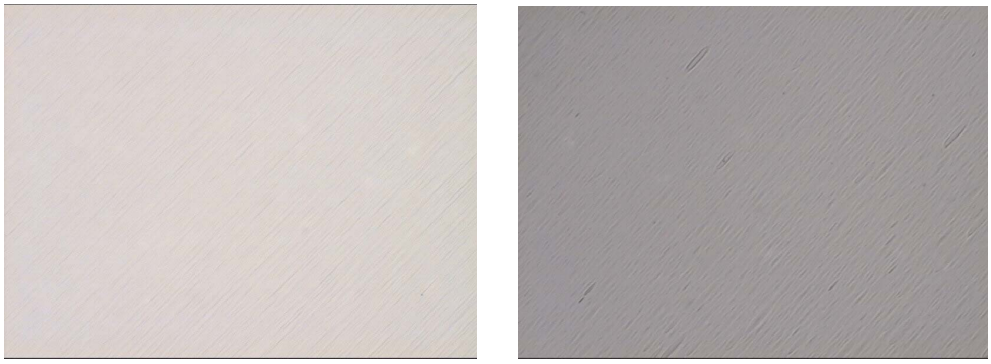

Figure 5.12: Surface images of a-GaN monitored at two stages. 1.2 μm (left) and 2.4 μm (right).

This argument is supported by XRD ω-rocking curve measurements. Figure 5.13 shows the plots of the FWHM values vs. the in-plane angle Ψ which were measured at two thicknesses, 1.2 μm and 2.4 μm. At the GaN thickness of 1.2 μm, the FWHM value deviates from 1600" to 1100". In contrast, the 2.4 μm GaN layer after the overgrowth shows less deviation (about 100") with an average of 1450". The measurements clearly demonstrate a decrease in surface anisotropy. However, the increase of the FWHM needs to be investigated further.

AFM measurement results are also very promising. Figure 5.14 shows a smooth surface of the 2.4 μm thick a-GaN. The RMS roughness of this layer is 2.2 nm which is by a factor of three less than the other values presented in section 5.2.1 and 5.2.2.

The impact of the AlN NL thickness on the surface anisotropy is shown in Fig. 5.15. The growth time of the high temperature AlN layer was kept constant and the growth time of the low temperature AlN layer was changed from 0 to 3000 s. The a-GaN grown with the direct growth method is presented as the reference sample. The thickness of the GaN in all samples is around 1.2 μm. A significant improvement of the surface isotropy is observed in the samples grown with AlN NL layers. The

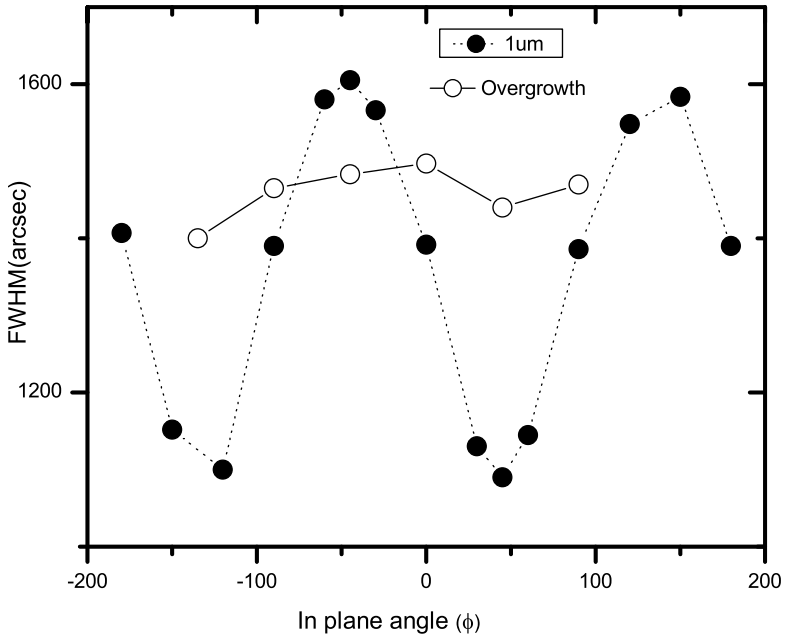

Figure 5.13: The FWHM values measured at different in-plane angles before and after overgrowth. In-plane angle 45 ° and -45 ° corresponds to the c-plane and m-plane respectively.

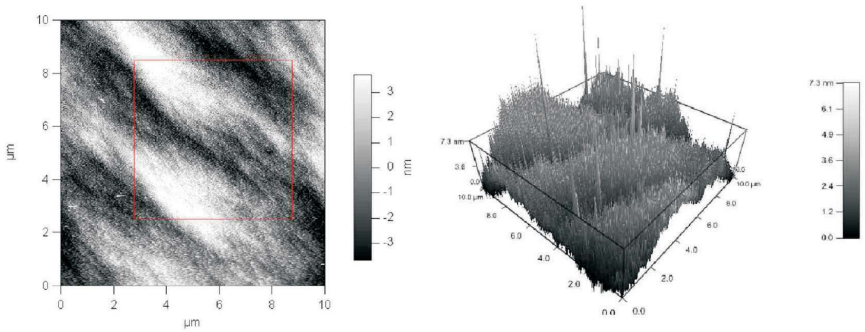

Figure 5.14: AFM images of 2.4 μm thick a-GaN grown with AlN NL and AlN/GaN SL layers. The RMS roughness is 2.2 nm

low temperature AlN enhances the surface isotropic characteristics and crystalline quality. Utilizing >300 nm thick (growth time 3000s) low temperature AlN grown at 950 °C reduces the average FWHM by 300∼ 600 ” compared to the other layers. The deviation between maximum and minimum FWHM value is also decreased to 350 ” from 600 ” (without low temperature AlN) and 1250 ” (direct growth).

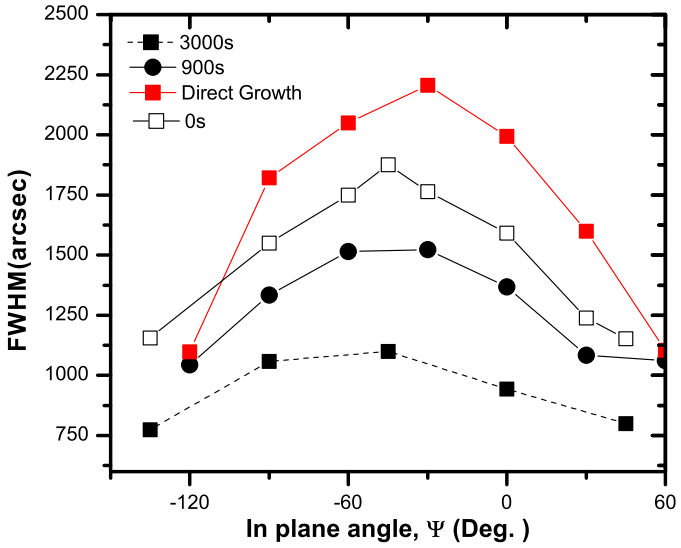

Figure 5.15: The FWHM values vs. the in-plane angle Ψ for *a*-GaN layers grown with direct growth technique and with a different thickness of AlN NLs. The growth time of AlN NL was varied from 0 s to 3000 s.

A similar improvement by using AlN buffer layers and SLs was recently reported by Armitage *et al*. The author introduced an AlGaN layer and AlGaN/GaN SL in *a*-plane GaN growth with high temperature AlN NL. As a result, the pits were much less of a problem and pit-free layers could be obtained over a wider range of V/III ratios (1000∼2000) [150] along with an improvement of surface morphology. The authors observed that the use of AlGaN interlayers results in a drastic reduction of screw dislocations by a factor of two. The results in this work are comparable to the reported values. Further increasing the thickness of the HT AlN NL can improve the quality of our layers.

5.3 Heterostructure growth

AlGaN/GaN heterostructure transistors are good candidates for high power switching applications due to their high breakdown voltage. Currently reported

c-plane AlGaN/GaN heterostructure field effect transistors operate commonly in normally-on mode, since the 2DEG originating from the polarization fields hinders normally-off operation. However, in practical power switching applications, normally-off operation is preferable because it provides safe operation even with a sudden release of the gate bias. It is also beneficial for power saving.

In order to address this issue, reduction of sheet carriers and employing a recessed-gate structure has been investigated. Reducing the Al composition or the thickness of the AlGaN layer leads to the decrement of sheet charge density [151]. This leads in an increase in sheet resistance and causes the increase of the parasitic resistance between the source and the drain [152].

A recessed gate by dry etching may be used to control the threshold voltage [153, 154]. This process may however cause surface damage [155]. Therefore, a polarization free heterostructure transistor is considered utilizing the growth on non-polar substrates [156]. The author demonstrated a non-polar AlGaN/GaN transistor with V_{th} = -0.5 V. The typical V_{th} of polar AlGaN/GaN transistor was demonstrated in this work to be about -4 V. However, the device performance still needs to be improved including the electron mobility which was reported to be 5.14 cm^2/Vs with a 2DEG density of $1.64 \cdot 10^{13}$ cm^{-2}. Considering that the typical mobility of *c*-plane AlGaN/GaN heterostructures is above 1000 cm^2/Vs, the quality of *a*-plane heterostructures needs to be significantly improved.

The work reported in this chapter aims to improve the properties of non-polar AlGaN/GaN HFET structures. The experience obtained from this work can be used to grow various non-polar heterostructure devices such as resonant tunneling diodes.

AlGaN layers were grown on an *a*-plane GaN buffer layer using an AlN NL and AlN/GaN SLs optimized in the previous sections. In order to investigate the

impact of the buffer GaN thickness, two GaN layers were grown, 1.2 μm and 2.4 μm. The thickness of the AlGaN layer and the Al composition are about 25 nm and 25 %, respectively. The AlGaN layer was doped with Si. Silane flow was 30 sccm which corresponds to a Si doping concentration of $6{\cdot}10^{19}\,\mathrm{cm}^{-3}$. A schematic of this structure and the corresponding XRD measurement results are presented in Fig. 5.16.

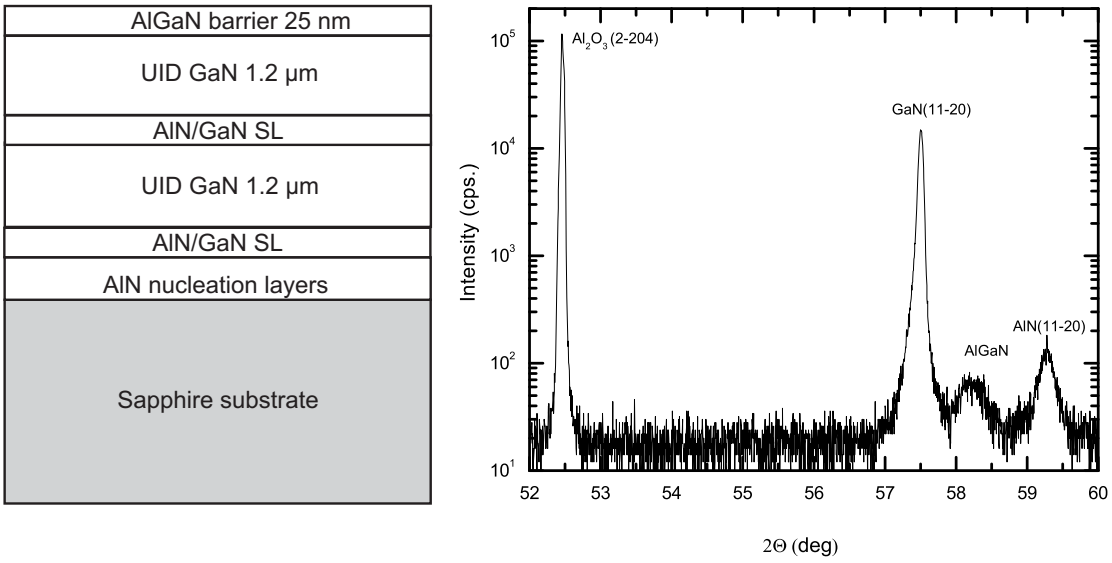

Figure 5.16: Schematic of the *a*-AlGaN/GaN heterostructure (left) and XRD ω-2Θ measurement results of 2.4 μm thick GaN.

The XRD ω-2Θ measurement shows three distinguished peaks for the *a*-GaN, *a*-AlGaN and *a*-AlN buffer layer. TLM results demonstrated that the two heterostructures grown on GaN layers having different thicknesses exhibited good ohmic contact quality. R_c and ρ_c are $0.7 \sim 0.9\,\Omega{\cdot}$mm and $0.5 \sim 1.5 \cdot 10^{-5}\,\Omega{\cdot}\mathrm{cm}^2$, respectively. All these values are comparable to the results from *c*-plane AlGaN/GaN heterostructures.

Hall measurement results of these two samples are summarized in Table 5.2. The sheet resistance measured was about $550{\sim}\ 750\,\Omega/\square$. Hall measurements indi-

cate that the sheet carrier concentration is about $1 \sim 2 \cdot 10^{14}\,\mathrm{cm}^{-2}$ with a mobility of $40\sim 50\,\mathrm{cm}^2/\mathrm{Vs}$. In comparison with *c*-plane heterostructures, this value is considerably low. Possible reasons for such low mobility is the remote ion scattering due to the heavily doped AlGaN layer and rough interface between *a*-AlGaN and *a*-GaN. However, this mobility is higher by a factor of 10 than that reported by other groups [156]. Since the samples investigated here were much more heavily doped than the samples in Ref. [156], the obtained higher mobility implies that the interface quality is better optimized. Hall and TML measurement results do not show clear dependence on the GaN buffer layer thickness.

	AlGaN/1.2 μm GaN	AlGaN/2.4 μm GaN
n_{2DEG} (cm^{-2})	$1.2 \cdot 10^{14}$	$1.7 \cdot 10^{14}$
μ (cm^{-2}/Vs)	50	40
R_s ($\Omega/\square$)	600±50	700±50

Table 5.2: Hall and TLM measurement results of the *a*-plane AlGaN/GaN heterostructures grown on 1.2 μm GaN and 2.4 μm GaN.

5.4 Conclusion

This chapter reports the growth and characterization of non-polar bulk GaN and AlGaN/GaN heterostructures on *r*-plane sapphire substrates.

Various growth techniques were used in order to obtain flat and smooth non-polar GaN surfaces. Both low temperature GaN NLs and direct growth without NL resulted in rough surfaces with a stripe pattern along the *c*-axis and in-plane anisotropy. In comparison with these two methods, thick AlN NL followed by an AlN/GaN superlattice improved the quality of non-polar GaN effectively. Using this method, the RMS surface roughness was reduced by a factor of three. Moreover, the deviation of in-plane on-axis FWHM values were reduced from > 1000" to < 500". As the AlN layer thickness increased and larger number of superlattice layers

were used, further improvement of surface morphology and in-plane anisotropy was observed.

Non-polar $Al_{0.25}Ga_{0.75}N/GaN$ heterostructures were grown and test structures were fabricated for evaluation their electrical characteristics. The sheet charge carrier concentration was $1\sim 2{\cdot}10^{14}\,cm^{-2}$ with a mobility of $40\sim 50\,cm^2/Vs$. The mobility of the sheet charge carriers is higher by a factor of 10 than the reported values in literature.

CHAPTER VI

GAS SENSOR APPLICATIONS

6.1 Introduction

Sensors are another application of GaN based heterostructures beside their two major applications in optical and electrical devices. III-Nitrides are believed to be a promising material for a wide range of chemical, biological, polar liquid, strain and pressure sensing applications because of their high sensitivity to surface state changes resulting from the polar nature [157]. The possibility of high power and high temperature operation as well as resistance to high radiation conditions make III-Nitrides sensors very attractive.

Considering the possibility of integrating sensors in circuits, solid state sensors have become more important over the last years. In this context, Si is the most popular material used for sensors. However, its intrinsic carriers become dominant as temperature is elevated above 300 °C imposing therefore the use of a cooling system. Since cooling of GaN-based devices is not necessary to maintain proper function at high temperatures, these devices can be a cost effective choice. SiC is an alternative to GaN but the material itself is quite expensive. Recent papers reporting GaN based gas sensors are summarized in Table 6.1.

In this work, the use of III-Nitrides for gas sensing was explored. Gas sensors

	Material	Device Type	Operating Temp.(°C)	Target Gas
G. Zhao [158]	AlGaN/GaN	HFET	250, 300	CO
E. Cho [159]	GaN	Schottky diode	250, 300	CO
F. Yun [160]	GaN	Resistive sensor	50	H_2
GE [161]	Si doped GaN	Schottky diode	700	NO
J. Song [162]	AlGaN/GaN	HFET	25∼800	H_2

Table 6.1: Research status of chemical gas sensors based on III-Nitride materials.

based on nitride Schottky diodes are investigated in section 6.2. Bulk GaN and AlGaN/GaN heterostructures were utilized for the sensing of hydrogen and carbon monoxide. The correlation of gas sensitivity and design parameters, temperature effects and material dependence was investigated.

Section 6.3 is dedicated to research on Fabry-Pérot filters (FPFs) for use in gas sensing. They consist of GaN/air gap distributed Bragg reflectors. The goal of this study is to realize GaN membranes which can be actuated for example by means of a voltage. By doing so, a filter with high resolution in the UV/VIS region can be obtained. This filter can be implemented in an optical gas sensing system as a part of a detector. Its resonant wavelength will be changed by membrane actuation, which will then lead to a change of air cavity length. This concept has already been demonstrated using Si and GaAs based resonators for gas sensing at infrared wavelengths. However, these materials are not transparent to Ultraviolet(UV)/Visible(VIS) wavelengths. Therefore, the successful use of Fabry-Pérot filters based on III-Nitrides can extend the current limit of wavelengths for probing gases or chemicals.

A theoretical research on the mechanical and optical characteristics of these structures was carried out in order to permit proper design of sensor structures and examine the feasibility of such devices. Experiments on growth and etching of the required structures were also performed.

6.2 Schottky diode gas sensors

The sensor sensitivity is measured by current, voltage or capacitance changes caused by the presence of testing gases. The associated mechanism is either a conductivity change or a Schottky barrier change. Resistor-type sensors detect gas species based on the first principle. On the other hand, the sensing mechanism of Schottky diodes or field effect transistors is based on the latter principle. Details about various gas sensing types and sensing mechanisms can be found in Refs. [163, 164]

The advantage of resistive gas sensors is a simple fabrication. However, they manifest relatively slow response and low sensitivity [160] in comparison with the Capacitance-type. Therefore, this work focuses on Schottky diode sensors. In this section, the principle of standard Schottky diodes will be reviewed briefly and experimental results and a discussion will be presented. The first part of experiments concentrates on comparing the gas sensitivity of bulk GaN and AlGaN/GaN heterostructures. Hydrogen and carbon monoxide (CO) were chosen as testing gases due to the fact that the detection of hydrogen is important because its explosive nature. Moreover, CO is a toxic gas and the control of CO is indispensable in combustion systems (e.g. automobile engines) in order to reduce CO_2 emission. The second part of the experiments is intended to investigate the effects of the catalytic layer thickness, diode size and operating temperature followed by a discussion of gas sensing mechanisms in Schottky diodes; a catalytic layer of Pt was used because it is known to be the efficient catalytic material and easy accessibility among Schottky metals.

The energy band diagrams for metal and n-type GaN before and after Schottky contact formation are shown in Fig. 6.1. For an ideal Schottky contact, the Schottky

barrier height $q\phi_b$ is given by:

$$q\phi_b = \Phi_m - \chi \tag{6.1}$$

where Φ_m is the work function of the metal and χ is the electron affinity of the semiconductor. In order to simplify the model, an ideal Schottky model is adopted without consideration of the image potential. The I-V characteristic of a Schottky diode is described by:

$$I = I_S \left[\exp\left(\frac{qV}{nk_BT}\right) - 1 \right] \tag{6.2}$$

$$I_S = A_e A^* T^2 \exp\left(-\frac{q\phi_b}{k_BT}\right) \tag{6.3}$$

where A^* is the Richardson constant, n the ideality factor, k_B the Boltzmann constant, T the temperature and A_e the area of the Schottky contact. The Richardson constant is calculated from

$$A^* = \frac{4\pi q m^* k_B^2}{h^3} \tag{6.4}$$

where h is Plank's constant and m^* the effective mass of an electron ($0.22m_o$ for electrons in the conduction band in GaN). From this, A^* is calculated to be $26.4\,\mathrm{Acm^{-2}K^{-2}}$. From the I-V or C-V characterization of a Schottky diode, the ideality factor and the Schottky barrier height can be obtained experimentally.

6.2.1 Bulk GaN Schottky diode sensors

Bulk GaN layers were grown on a c-plane sapphire substrate by metal organic vapor phase epitaxy (MOVPE). Standard precursors of trimethylgallium (TMGa) and ammonia (NH_3) were used as alkyl and hydride sources. After a high temperature (1100 °C) cleaning in H_2, a 25 nm thick GaN nucleation layer was grown at 530 °C. The temperature was then ramped up to 1040 °C for the growth of 3 μm GaN which is slightly doped with Si ($\sim 10^{17}\,\mathrm{cm^{-3}}$).

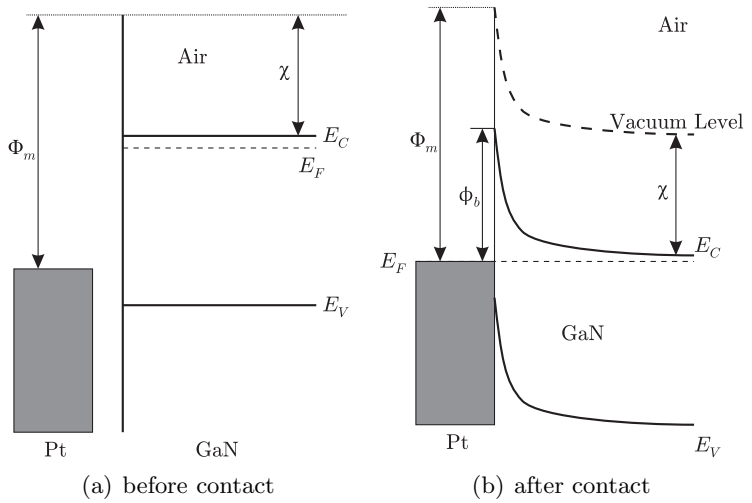

Figure 6.1: Energy band diagram of a metal semiconductor Schottky contact.

The gas sensor devices were fabricated based on a standard Schottky diode process. A cross section and a top view of the devices are shown in Fig. 6.2. Multiple devices of different sizes were fabricated on the same wafer. A Ti/Al/Au (400 Å/1200 Å/3500 Å) multi layer ohmic contact was deposited by e-beam evaporation and subsequently annealed at 850 °C for 30 s by rapid thermal annealing (RTA) in nitrogen environment. After a second photolithography step, a Pt Schottky contact with a thickness of 30 nm was formed.

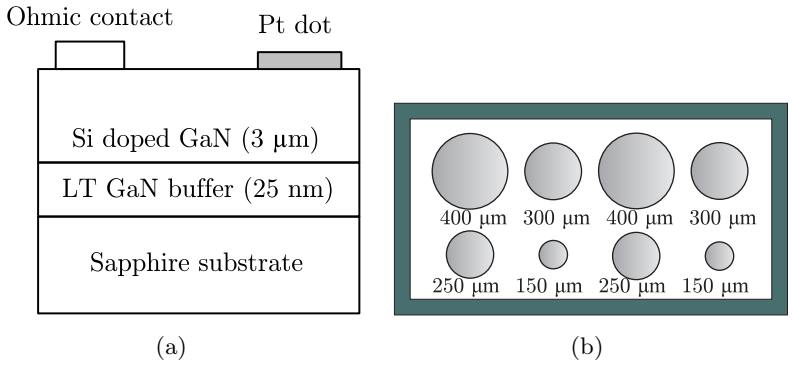

Figure 6.2: GaN Schottky diode sensors. (a) cross section and (b) top view.

Figure 6.3 depicts the schematic of the gas sensor measurement set-up. Testing gases are 0.9 % CO mixed with N_2 and 5.0 % H_2 mixed with N_2. N_2 is also used as

a carrier gas. All gases used in this work have a purity of more than 99.999 %. The gas flows into the gas cell where the sensors are placed and then flows out to an exhaust system. The Schottky diode sensor was mounted on an alumina holder. The Schottky and ohmic contacts of the sensors were connected to the gold pads of the alumina holder with a 25 μm thick Au bond wire. The device current was measured with the help of a constant voltage supply (Keithley source measurement unit 236).

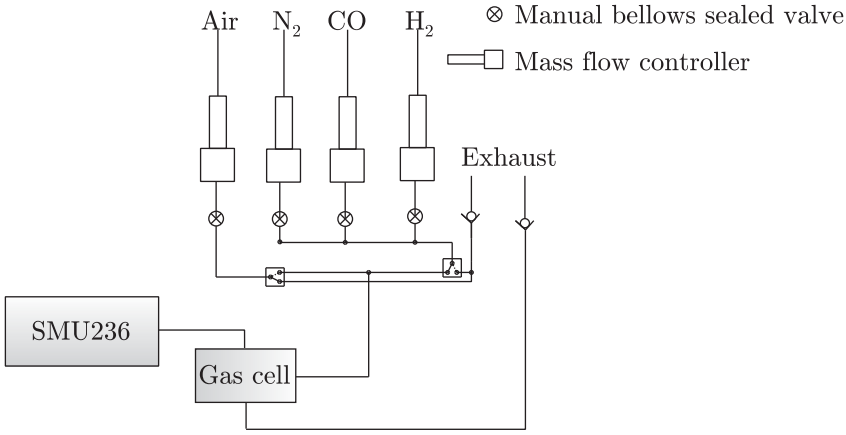

Figure 6.3: Schematic of the gas sensor measurement setup.

The I-V characteristics of the Schottky diodes were measured before and after gas exposure. Figure 6.4 presents the I-V curve changes with and without H_2 and CO. The dramatic current increase observed in the reverse bias region with the presence of gases implies Schottky barrier lowering. This is specially clear in Fig. 6.4(a), where the Schottky characteristics quickly transformed into ohmic in the presence of 25 ppm hydrogen at 240 °C. In contrast, a complete change to ohmic behavior was not observed in CO environment. Even at very high CO concentrations (400 ppm) at 300 °C, the device still worked as a Schottky diode as shown in Fig. 6.4(b). The change of I-V characteristics measured at 240 °C with CO exposure was negligible in comparison to the results measured at 300 °C which are presented here. The associated change of ϕ_b with the current increase at -2 V was about 0.2 eV in

25 ppm H_2 at 250 °C and 0.02 eV in 400 ppm CO at 300 °C.

Figure 6.5 summarizes the sensitivity of the bulk GaN Schottky diode sensors. During the tests, a reverse bias voltage of -2 V was applied. The bulk GaN Schottky diode gas sensors showed a strong response to H_2 rather than to CO. They are capable of sensing H_2 at much lower temperatures and lower concentrations. Since the sensitivity for H_2 is a couple of thousand %, the absolute value of the current change ΔI is plotted in Fig. 6.5(a). However, the sensitivity (%) is used for displaying the CO data in Fig. 6.5(b). The CO sensitivity shows a linear relationship to CO concentration at all measured temperatures and concentrations while the H_2 sensitivity becomes saturated depending on temperature and H_2 concentration.

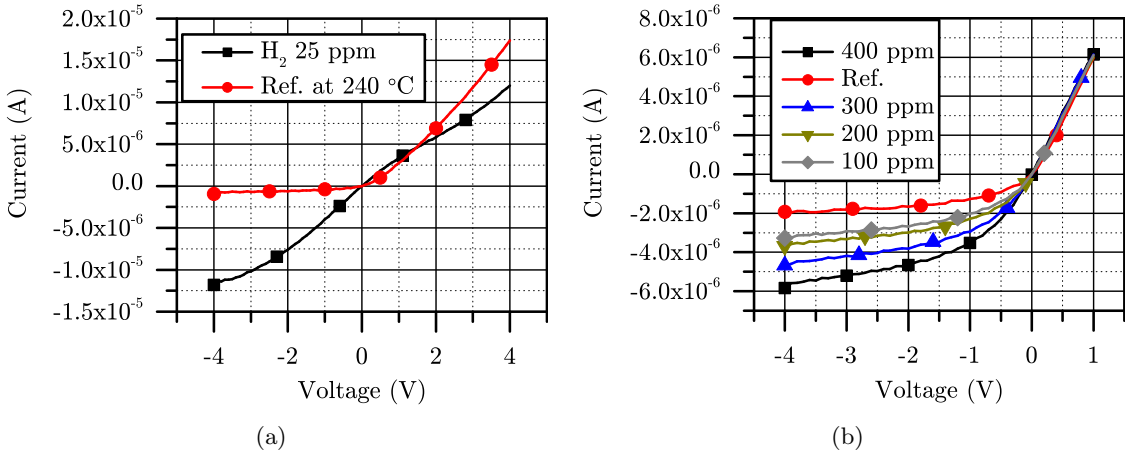

Figure 6.4: *I-V* characteristics of Schottky diode gas sensors. (a) measured at 240 °C in 25 ppm H_2 environment (b) measured at 300 °C in different CO concentrations. The curve labeled Ref corresponds to the *I-V* characteristics in the absence of gases.

The hydrogen detection mechanism in Si and Silicon carbide (SiC) based metal oxide semiconductor (MOS) gas sensors relies on the presence of an H-induced dipole layer at a Pd gate-SiO_2 interface [165, 166]. Such a dipole layer is formed at the insulator side due to hydrogen atoms absorbed by the Pd gate after dissociation of hydrogen molecules on the Pd surface. Hydrogen atoms can cross the 100 nm Pd

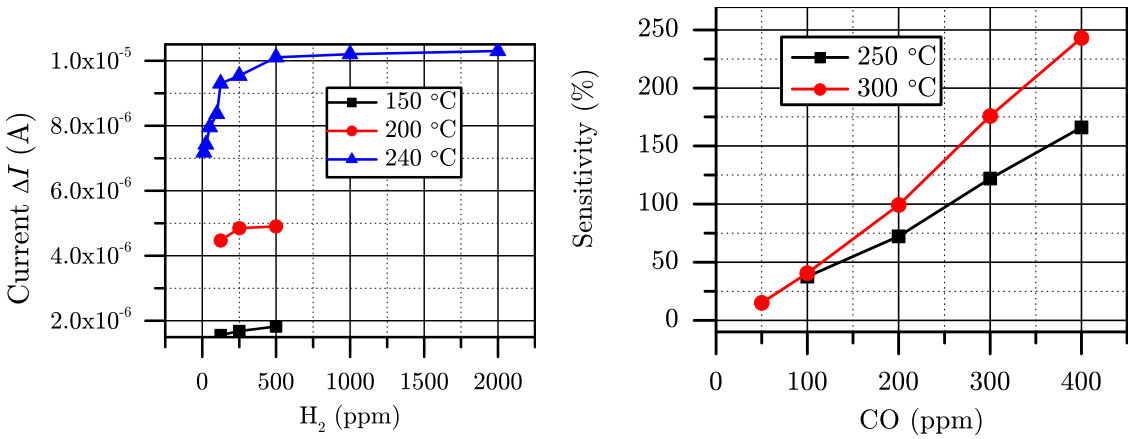

(a) (b) scale=0.9

Figure 6.5: Sensitivity vs. (a) H_2 concentration and (b) CO concentration.

layer within a time in the order of 10^{-5} s or smaller for temperatures around 150 °C. The gas diffusion time does not, therefore, influence the response time [165].

It was believed that the same mechanism applies to Pt GaN Schottky diode sensors as, for example, confirmed by Schalwig *et al* [167]. In their report, the authors observed an H concentration of about $10^{15}\,\mathrm{cm}^{-2}$ at the interface between Pt and GaN by elastic recoil detection (ERD) measurements.

Figure 6.6 shows the energy band diagrams of a bulk GaN Schottky diode with a Pt contact in air and in hydrogen environment. Without hydrogen exposure, the Schottky barrier (ϕ_b) of the Pt Schottky diode is determined by the Pt work function (Φ_m), by the electron affinity (χ) and by the Fermi energy level of GaN (E_F) as long as the GaN surface is not pinned by surface states. The typical ϕ_b value of Pt on GaN is 1.15 eV. The high Schottky barrier blocks the current flow at reverse bias. When the device is exposed to hydrogen, Pt, playing the role of a catalytic metal, dissociates hydrogen into hydrogen atoms. After the diffusion of hydrogen atoms into Pt, hydrogen dipoles form at the interface between Pt and bulk GaN and cause Schottky barrier lowering leading in an increase of reverse current.

Oxygen species introduced during device processing were found at the Pt/GaN interface. According to the work of Weidemann [168], this intermediate native thin oxide layer plays a very important role in gas sensing. In their experiments, *ex-situ* deposited Pd Schottky diodes exhibited 50 times higher sensitivity than *in-situ* deposited devices which did not have a thin oxide layer.

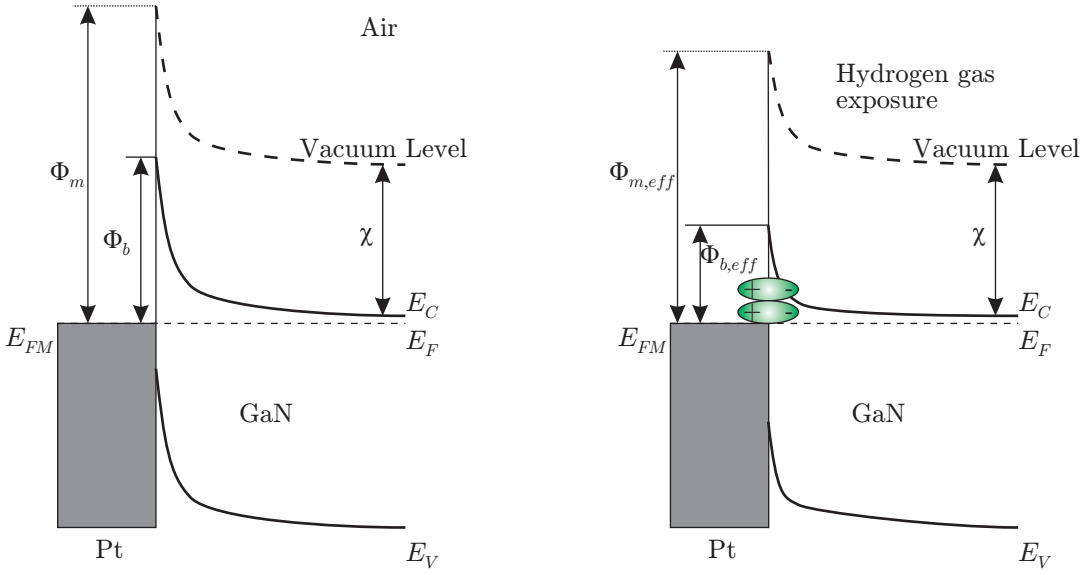

Figure 6.6: Schottky barrier change of a bulk GaN Schottky diode in H_2 environment.

Unlike hydrogen, in case of CO sensing, its adsorption on the reactive surface of a transition metal occurs in molecular form . The bonding strength between CO and the Pt surface is weak. When the temperature is elevated to dissociate CO molecules, desorption from the Pt surface occurs first [169]. Therefore, it is known that CO detection is very hard with sensors having a thick and continuous Pt layer. Increased CO sensitivity was observed in this work as the Pt layer became thinner and more discontinuous. This is a similar problem observed in ammonia detection.

Beside the effect of the dipole layer, the sensing mechanism for ammonia is known to be related to the polarization effect of the adsorbate or to reaction intermediates on the metal surface or to the exposed insulator [170, 171]. Other non-

hydrogen species, for example CO and NO, are also believed to follow this principle. Although H_2 sensitivity is mainly determined by the dipole layer regardless of the gate metal thickness, it should be noted that the effect of the catalytic metal thickness can not be ignored completely. A detailed discussion on the effect of catalytic layer thickness issues will be presented in section 6.2.3.

6.2.2 AlGaN/GaN heterostructure sensors

Schottky diode sensors made of AlGaN/GaN heterostructures were also investigated. An AlGaN layer with 25 % of Al and a thickness of 25 nm was grown on 2 μm thick UID bulk GaN using the TS MOVPE system. The diode design and the fabrication process are the same as in the aforementioned case of bulk GaN diodes.

C-V characteristics of the AlGaN/GaN heterostructure Schottky diodes were obtained using an HP 4175 LCR meter at a frequency of 100 kHz. The carrier concentration depth profile is extracted from Eq. 2.15. The large spike around 22 nm corresponds to the presence of a 2DEG at the interface between AlGaN and GaN as shown in Fig.6.7.

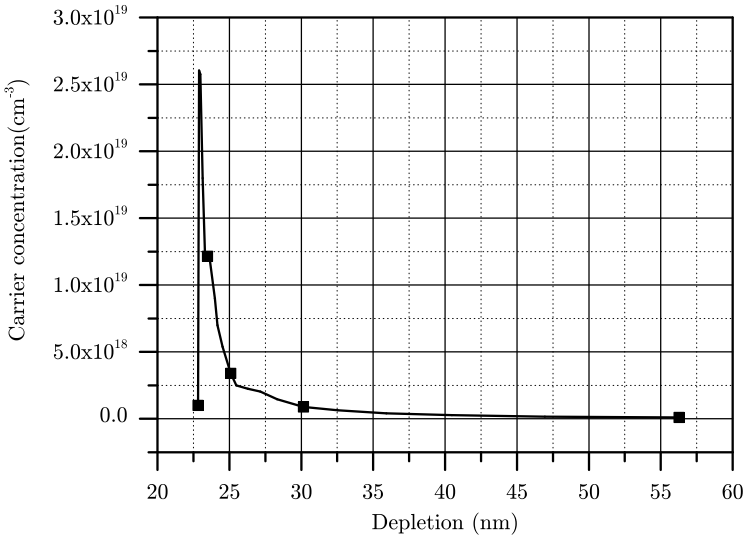

Figure 6.7: The depth profile of the carrier concentration in the AlGaN/GaN heterostructure.

The carrier gas N_2 flow was set to 4 slm and the on-time of the testing gas was 30 s except for the room temperature measurement. A forward bias of 1.0 V was applied to the AlGaN/GaN Schottky diodes as its leakage current was higher at reverse bias than that of bulk GaN devices.

Figure 6.8 illustrates the response of an AlGaN/GaN Schottky diode sensor to 100 ppm H_2 at different temperatures. The current transition curves are plotted from the moment when the hydrogen valve was opened. The current change is delayed due to the long path from the valve to the gas cell. The delay at room temperature is considerably longer than at higher temperatures. However, the response delay time between 150 °C and 250 °C are comparable.

A current change of about one order of magnitude (10^{-4} A to 10^{-3} A) was observed. Although the response time is relatively slow, the diodes also showed response at room temperature. The observed larger current change compared to the higher temperature is due to the longer gas exposure time (50 s vs. 30 s at high temperatures). Overall, it appears that high operating temperatures are advantageous for improving the response time and recovery time of the sensors.

The response of bulk GaN and AlGaN/GaN Schottky diode sensors are compared in Fig. 6.9. The current change of GaN is rescaled by a factor of 100. The thickness and size of the Pt contact for the two sensors were 30 nm and 200 μm. Regardless of temperature, the AlGaN/GaN hesterostructure gas sensor shows considerably higher sensitivity than the bulk GaN sensor.

The strong sensitivity of the AlGaN/GaN heterostructures can be attributed to the presence of a two dimensional electron gas (2DEG) formed at the AlGaN/GaN interface. Since the 2DEG is very sensitive to surface state changes as discussed in 4.1.1, it is expected that its conductivity will strongly depend on the presence of

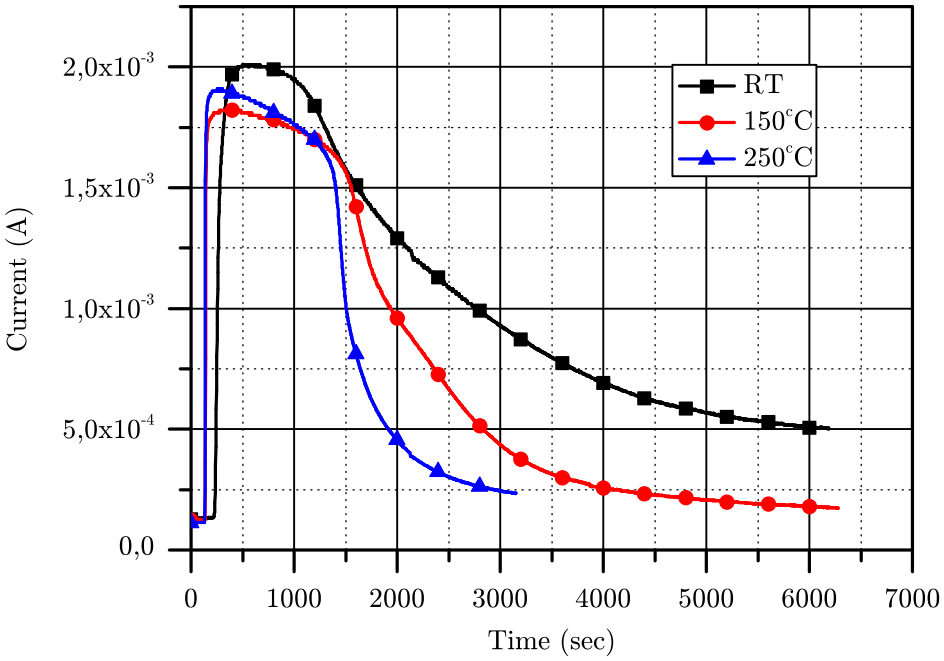

Figure 6.8: Sensor current time response in the presence of H_2 as a function of temperature measured with 100 ppm H_2 and 1 V bias.

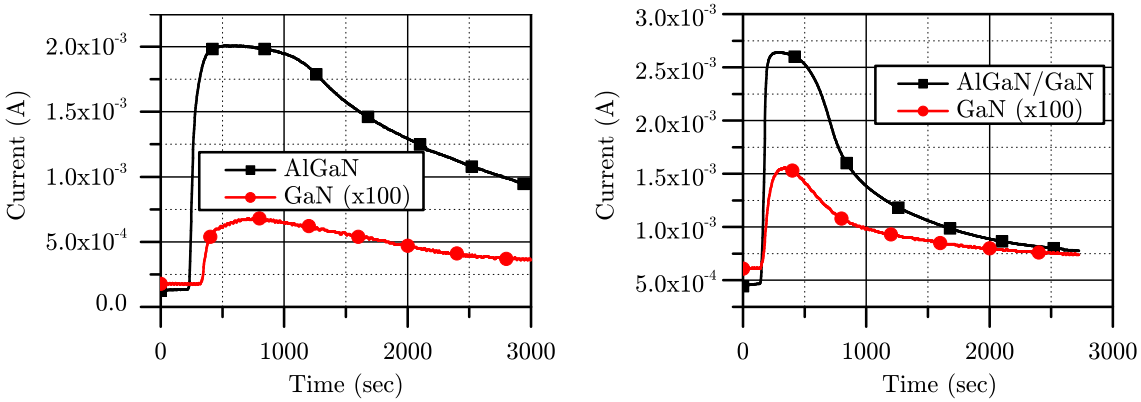

Figure 6.9: Transition curve for bulk GaN and AlGaN/GaN Schottky diode gas sensors measured (a) at room temperature with 8 sccm H_2 (b) at 250 °C with 1 sccm H_2.

gas species. Any polarity change on the surface caused by gases affects the surface potential and modulates the 2DEG density.

6.2.3 Impact of a catalytic layer on gas sensing

In this section, parameters impacting the gas sensing are investigated by utilizing bulk GaN Schottky diodes. Diodes with different Pt contact sizes and thicknesses were tested at different temperatures with various CO concentrations. The size and thickness of the Pt contacts are summarized in Table 6.2.

Before the actual gas sensing test, *I-V* measurements for each Schottky diode were performed using an HP 4145B semiconductor parameter analyzer. Figure 6.10 shows that a larger leakage current was observed for large diode sizes (sample A).

	Pt thickness (Å)	Pt contact diameter (μm)
sample A	300	400
sample B	300	150
sample C	500	400

Table 6.2: A sample list indicating the Pt thickness and diode diameter used.

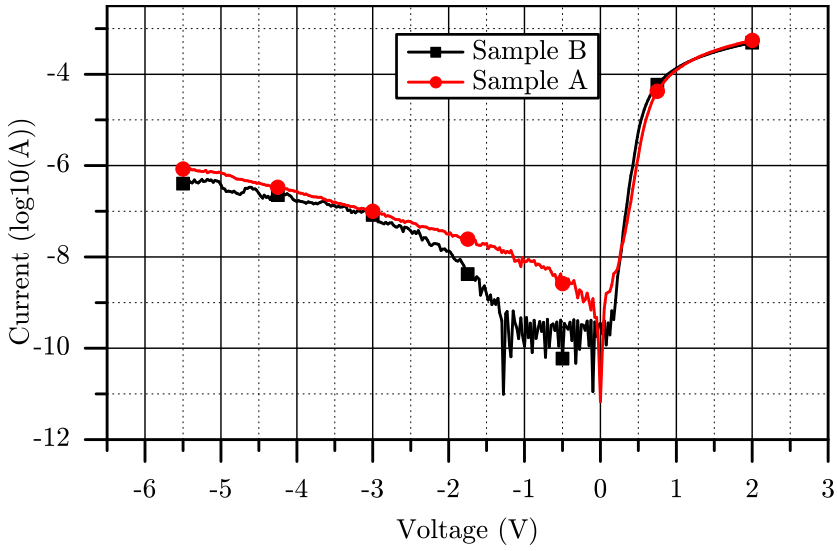

Figure 6.10: *I-V* curve for sample A (D=400 μm) and sample B (D=150 μm).

A more dramatic current change was observed at reverse rather than at forward bias [158]. The devices were therefore biased at -5 V when exposed to 0.9 % CO in

N_2. The carrier gas flow was 200 sccm N_2. The gas response was measured at 250 °C and 300 °C while the current was continuously monitored by a Keithley 236 source measurement unit controlled by a computer. The gas sensitivity is defined as the current change before and after gas exposure (ΔI) divided by the initial current (I_0).

The dependence of the gas sensitivity on the diode size is shown in Fig. 6.11. The thickness of the Schottky contact of sample A and B was 300 Å whereas the diameter was 400 μm and 150 μm, respectively. The sensitivity of sample B was as small as a few tenths of that of sample A at all measured operating temperatures (250 and 300 °C). A possible explanation for the higher sensitivity of sample A is the gas sensing mechanism associated with thin and discontinuous catalytic metals.

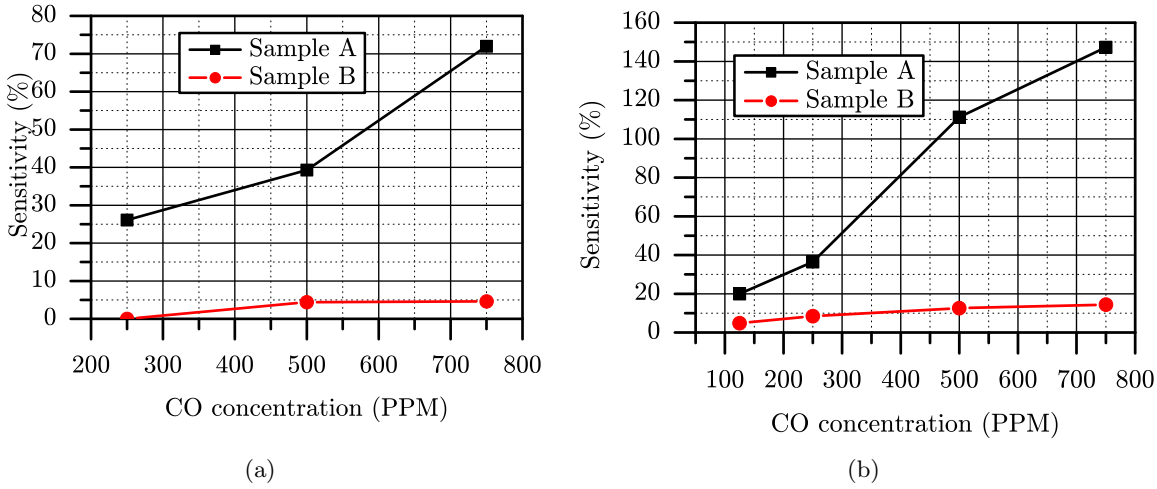

Figure 6.11: CO sensitivity of sample A (D=400 μm) and sample B (D=150 μm) measured at (a) 250 °C and (b) 300 °C.

In sensors with thin and discontinuous catalytic films, the change of the electrical characteristic is given by the sum of the polarization effects at the interface between metal and insulator (ΔV_i), the adsorbate or reaction intermediates on the metal surface (ΔV_s) and the exposed insulator (ΔV_a) as shown below [170].

$$\Delta V = g_i \Delta V_i + g_s \Delta V_s + g_a \Delta V_a \tag{6.5}$$

where the g's are the electrostatic coupling coefficients. ΔV_n and g_n are believed to be dependent on the structure of the metal film, but no detailed information about them is available so far [170]. Figure 6.12 illustrates different paths of gas reactions according to Eq. 6.5.

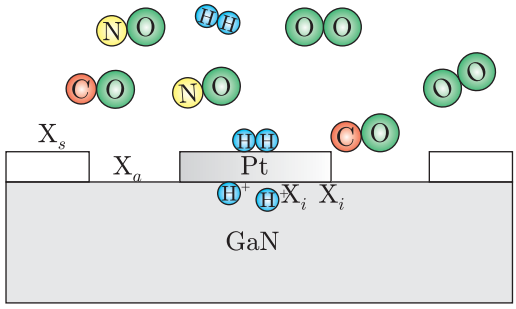

Figure 6.12: Reactions between gas species and surface and intersurface of the Schottky metal and bulk GaN.

The reduction of the catalytic metal thickness results in film discontinuity and in the shrinkage of the Pt grain size [172]. Hence, the porosity of the catalytic metal film enables the exposure of more metal surface to the gas. The number of grain boundaries increases as the grain size becomes smaller. Grain boundaries are believed to offer an additional route for gas diffusion [172] and the insulator layers are possibly exposed to gas through them. The number of grain boundaries is proportional to the surface area as long as the grain size is small enough compared to the Schottky contact size. Therefore, the $g_s \Delta V_s$ and $g_a \Delta V_a$ terms become important in Eq. 6.5. Accordingly, the sensitivity is dependent on the catalytic metal size. On the contrary, the impact of the diode size will be negligible in case of thick and continuous metal. Investigations on diode size vs. sensitivity for thick Pt Schottky diode sensors (>300 Å) could verify this point.

Sample A with a larger Schottky contact area also showed that the sensitivity increases linearly without saturation. Therefore, it was preferred to employ a larger

diode size to achieve high sensitivity without saturation over a broad detection range. However, the associated leakage current and the catalytic film thickness used must be considered in determining of the size of the Schottky contact.

Measurement of the transient gas response was performed with sample A and C at 250 °C. Figure 6.13 illustrates the results. In this test, the diode size was fixed at 400 μm and the Pt thickness was varied. Sample A (300 Å) responded 20 % faster than sample C (500 Å). Response time is defined as the time necessary to reach 90 % of the total current change. For the measurement setup used in this work, the response time is in the order of minutes. The sensitivity of sample A at 500 ppm was also two times higher (40 % vs. 20 %). These results confirm that the CO sensing mechanism discussed earlier agrees well with Spetz's results regarding the ammonia sensitivity of Pt gates [171]. However, since only two different Pt thicknesses were examined, it is not possible to predict precisely the CO sensitivity dependence on the Pt thickness at this stage. This could exhibit a broad range of maximum sensitivity for thin films and a rapid drop at thicknesses above 90 nm as observed in ammonia sensing or a steady increase by reducing the film thickness in H_2 sensing [171]. If further improvement of CO sensitivity turns out to be feasible by controlling the Pt thickness, this will open the possibility for CO selectivity over H_2. By employing a very thin Pt gate of about 3 nm in a Si MOSFET, good selectivity of ammonia towards H_2 was achieved [173]. Cross sensitivity between H_2 and CO can be improved further by employing other factors such as the type of the catalytic metal and operating temperature.

Although the dominant mechanism of H_2 sensing is based on the formation of a dipole layer at the interface, the sensitivity was also found to depend on the catalytic metal thickness. Tilak *et al* attributed this dependence to a higher density

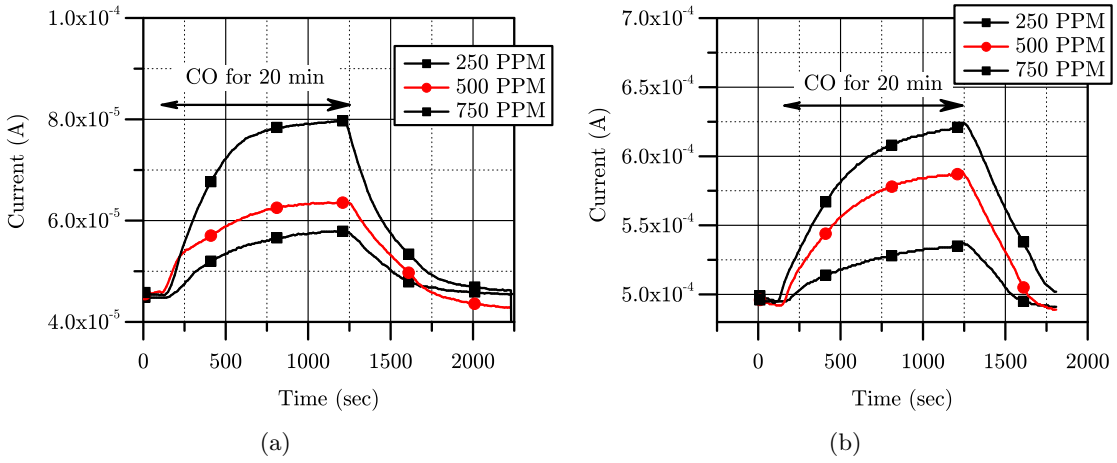

Figure 6.13: Transient response of (a) sample A (300 Å) and (b) sample C (500 Å) measured at 250 °C at different CO concentrations.

of grain boundaries measured by SEM in thinner Pt films [172]. Grain boundaries were believed to offer an additional route for hydrogen atom diffusion to the metal semiconductor interface so that sensitivity could be improved. It is not sure at this stage whether CO can penetrate through grain boundaries or not.

Beside the grain size change, Pt surface modification by thermal annealing was observed. XRD and AFM characterization in Fig. 6.14 showed restructuring and morphology changes of the 250 Å thick Pt film. After annealing at 600 °C for 30 min in a N_2 rich environment, the Pt (111) peak increased. Moreover, the smooth surface became rough and the RMS roughness value was increased from a couple of tenths of a nanometer to 3.75 nm. As a larger number of grain boundaries was found in thinner Pt films, one also expects severe surface restructuring and morphology changes for thinner films. In extreme cases, it was found that Pt islands with a very rough surface existed in 40 Å thick Pt films after annealing under the same conditions.

These surface modifications will play an important role in gas sensing. Hudeish *et al.* supports this argument [174]. In his work, the surface morphology evolution for different Pt thicknesses and annealing conditions was characterized by XRD and

AFM and discussed together with H_2 sensitivity data. Interestingly, thicker Pt responded to hydrogen better. These results are different from Ref. [172]. Since they investigated different ranges of Pt thicknesses, the dominant sensing mechanism might be different.

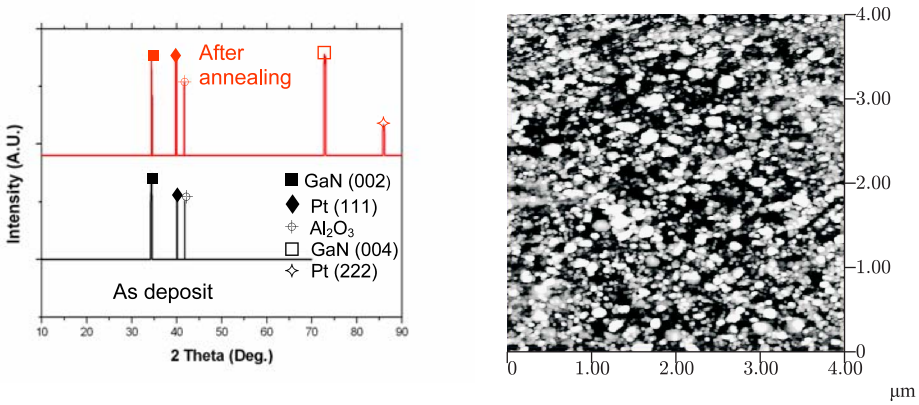

(a) (b)

Figure 6.14: (a) XRD measurement of a 250 Å Pt film for the as deposited film (bottom) and after annealing at 600 °C for 30 min in N_2 rich environment (top). (b) AFM image of a 40 Å thick Pt film.

6.3 GaN/air gap based Fabry-Pérot filters

Figure 6.15 shows the schematic of a typical set-up for optical gas sensor measurement. Gases are filled in a gas cell and an optical source and a detector are placed at either end of the cell. Light passing through the cell will be absorbed by the gas. The transmitted light will be detected by a detector. The measured spectra are differentiated according to gas species and their concentrations since each gas absorbs different wavelengths. In order to ensure high resolution measurements, the use of a spectrometer is preferable. However, this makes a sensing system bulky and expensive if a conventional spectrometer is used.

Micro-opto-electro-mechanical (MOEM) tunable Fabry-Pérot Filters (FPFs) have been developed for the replacement of bulky spectrometer systems. FPFs based

on conventional III-V materials or Si are already reported [175, 176]. These devices target the application of optical communication and IR gas spectroscopy systems as well. Similar spectroscopy applications are expected for GaN based FPFs because organic materials and chemicals are sensitive to UV and/or to the visible wavelengths. This spectroscopy system can be achieved with nitrides.

GaN photodiodes were reported for the detection of NO and CO in exhaust systems at wavelengths between 360 nm and 380 nm [177]. Since FPFs exhibit high resolution in the range of Å, they enable to distinguish different gases with higher precision than photo detectors usually offer. Besides, the integration with photo diodes and light sources (LED or LDs) will make a gas sensing system compact and cost effective as already demonstrated with Si FPFs [178].

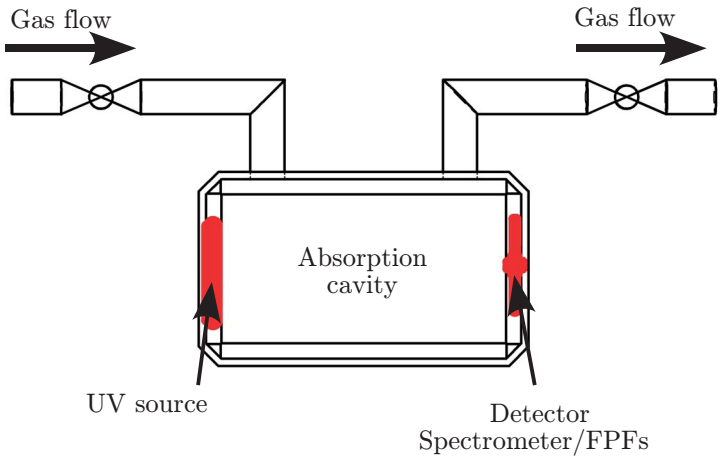

Figure 6.15: Schematic of an optical gas measurement set-up.

The GaN based FPFs proposed in this work consist of two GaN/air gap distributed Bragg reflector (DBRs) and an air cavity between them (see Fig. 6.23). The necessary air gaps can, for example, be formed by wet etching of a sacrificial layer. Dry etching can also be used as shown in several papers. Steckl presented horizontally stacked GaN gratings fabricated by focused ion beam (FIB) micromilling [179].

However, this approach is not appropriate for a vertical structure as the one used in this work. In most cases, wet etching of nitride materials is assisted by UV light since nitride semiconductors are very robust to conventional chemical treatment. The corresponding method is referred to as photo electrochemical etching (PEC) [180].

Although selective etching of nitrides is extremely difficult and rough surfaces resulting from etching are a problem, air gap based DBRs are attractive because only 3.5 periods are needed for 98 % reflectance due to the large refractive index contrast as shown in Fig. 6.16. In addition, FPFs consisting of two GaN/air gap based DBRs can tune the resonant wavelength by controlling the air cavity length electrostatically or thermally.[1]

Si or SiC is generally used for GaN MEMS devices. Nevertheless, AlN was chosen as a sacrificial layer in this work due to its suitability for building the multiple FPF membranes. Since selective etching between $Al_xGa_{1-x}N$ and AlN is possible for small amounts of Al content, it is feasible to replace GaN with $Al_xGa_{1-x}N$ layers so that sensors can be built for operation above the GaN absorption edge.

In the following sections, the theory of DBRs and FPFs and the optical and mechanical models used in this work are presented. Optical and mechanical simulation results for GaN/air gap DBRs and FPFs are reported. Residual stress and various designs are considered to investigate the effects of residual stress and the structure geometry. Finally experimental results of GaN/AlN heterostructure growth and etching will be discussed.

[1] A three-period GaN based air gap DBR was reported using band-gap-selective PEC etching with an InGaN sacrificial layer [181]. This structure was, however, not tunable.

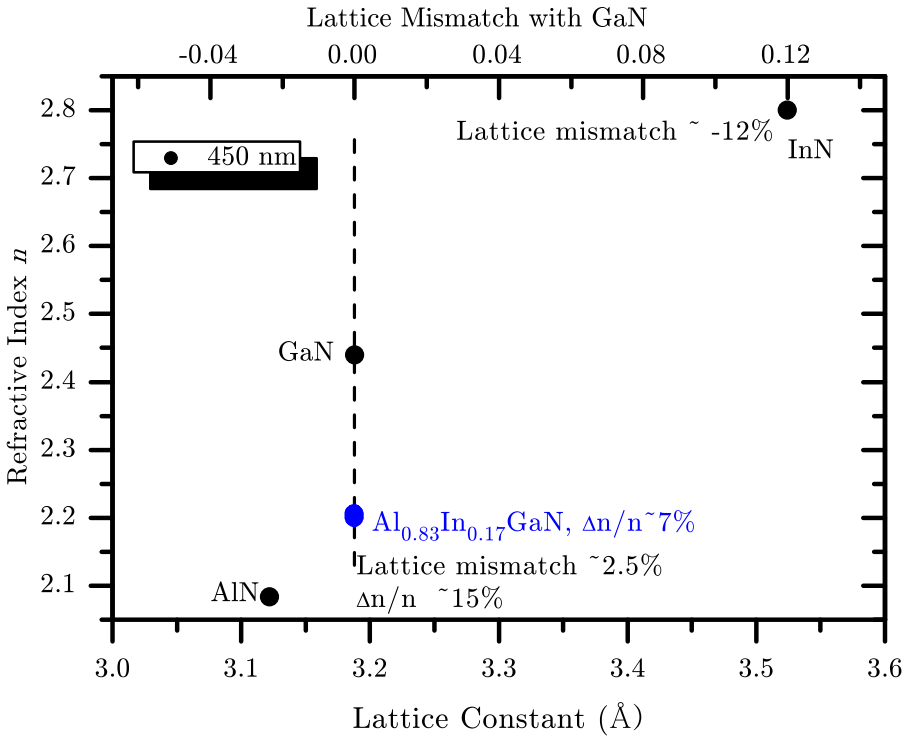

Figure 6.16: In-plane lattice mismatch and refractive indices of nitride materials.

6.3.1 Theoretical review

Distributed Bragg Reflectors (DBRs)

DBRs consist of multiple pairs of two layers having a different refractive index. A layer with a higher refractive index (n_H) and another layer having a lower refractive index (n_L) are stacked alternately as shown in Fig. 6.17.

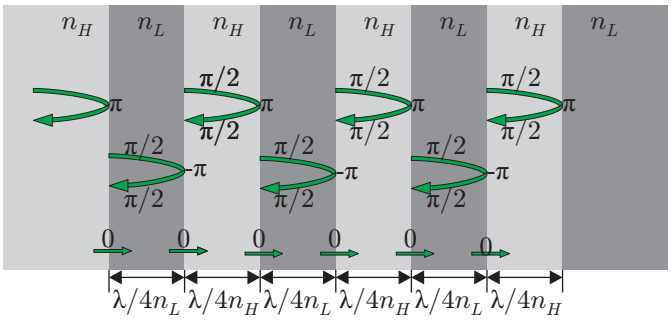

Figure 6.17: Phase delay in distributed Bragg reflectors with high (n_H) and low (n_L) refractive index materials.

When λ_0 is given as a center wavelength where maximum reflectivity is to be

achieved, the thickness of each layer has to be $\lambda_0/(4n)$. n is the respective material refractive index. The quarter wavelength layer thickness allows the reflected waves from each interface to build constructive interference. Considering a DBR with p pairs sandwiched between a substrate and an outside medium having the refractive indices n_s and n_o, respectively, its reflectivity R_0 at λ_0 with normal incidence can be calculated by the standard transmission matrix method (TMM) as given in Eq. 6.6.

$$R_0(p) = \left[\frac{1 - \frac{n_s}{n_o}\left(\frac{n_L}{n_H}\right)^{2p}}{1 + \frac{n_s}{n_o}\left(\frac{n_L}{n_H}\right)^{2p}} \right]^2 \tag{6.6}$$

When the angle of incidence is θ, the refractive index becomes $n\cos\theta$. The bandwidth with high reflectivity is called stop-band ($\Delta\lambda$) and is determined by:

$$\Delta\lambda = \frac{4}{\pi}\lambda_0 \left(\frac{n_H - n_L}{n_H + n_L} \right) \tag{6.7}$$

Therefore, a large refractive index contrast (Δn) and a large number of periods (p) are desirable to achieve DBRs with broad stop-band and high reflectivity. Since the maximum refractive index contrast between nitride materials is 15 % (GaN/AlN) as shown in Fig. 6.16, air is choosen to be the low refractive index material and GaN is the higher refractive index material. By doing so, the reractive index contrast is increased to 60 %. The number of periods required for 98 % reflectivity is only 3.5 while GaN/AlN needs more than 30 periods for DBRs with the same performance. More information about DBRs in general can be found in Ref. [182].

Fabry-Pérot Filters (FPFs)

Fabry-Pérot Filters (FPFs) are designed to reflect all wavelengths except the resonance wavelength (λ_0). The FPF design originates from the work of Fabry and Pérot in 1899. This type of filter is comprised of two DBR mirrors and a resonant

cavity with a refractive index n between a top and a bottom mirror as shown in Fig. 6.18. The distance between the two mirrors is called resonant cavity length (L) and is determined by λ_0. As L is tuned, a resonance wavelength can be shifted away from λ_0. The theory of FPFs will be described briefly based on an one dimensional electromagnetic field model.

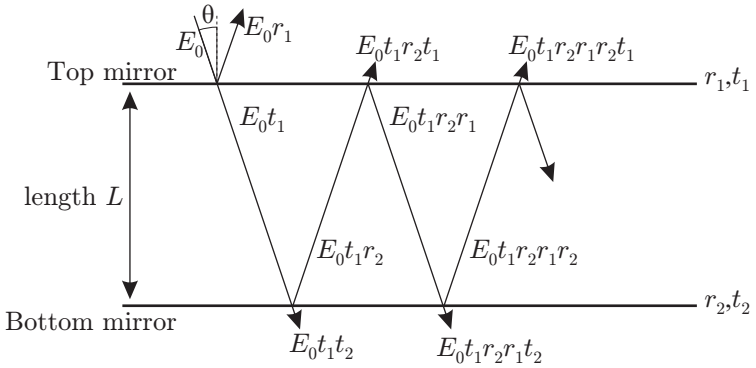

Figure 6.18: Schematic of a Fabry-Pérot cavity.

When the initial electric field E_0 is incident on the top mirror at an angle θ from the normal, the transmitted electric field is

$$E_t = E_0 t_1 t_2 \left[\sum_{d=0}^{\infty} \left(r_1 r_2 \mathrm{e}^{i2\phi} \right)^{2d} \right] = E_0 \frac{t_1 t_2}{1 - r_1 r_2 \mathrm{e}^{i2\phi}} \tag{6.8}$$

where E_t is the transmitted electric field and t_i and r_i are the field transmission and reflection coefficients of the mirrors. The phase shift after a cavity round trip is given by

$$2\phi = 2kL\cos\theta \tag{6.9}$$

where k is the amplitude of the wave vector in the cavity ($2\pi n/\lambda_0$). The maximum transmittance occurs when constructive interference is fulfilled. The power transmission coefficient for a Fabry-Pérot cavity is

$$T_{\mathrm{FP}} = \left| \frac{E_t}{E_0} \right|^2 = \frac{T_1 T_2}{1 + R_1 R_2 - 2\sqrt{R_1 R_2}\cos 2\phi} \tag{6.10}$$

where T_i and R_i are the power transmission and reflection coefficients with $T_i = |t_i|^2$, $R_i = |r_i|^2$ and $R + T = 1$ for lossless mirrors.

Generally, the medium of the cavity can be air or a dielectric film and the cavity length can be controlled by changing the refractive index or the physical position of one or two mirrors. A refractive index change can be obtained by electron injection but the tuning range is then limited to less than 10 nm wavelength. Spatial control of the mirror position can be achieved by electrostatic force or thermal actuation. In case of thermal actuation, tuning speed is in the millisecond range. Electrostatic actuation of mirrors offers advantages in speed compared to the thermal actuation but the design parameters have to be chosen carefully to achieve reasonably low actuation voltages.

The cavity between two DBR mirrors is designed to be air in this work. The DBR mirrors are moved by external force resulting in a ΔL. Since higher control speed is desirable in the actuation of the DBR mirrors, only electrostatic actuation is considered here. The mechanical model for the actuation of a membrane will be introduced in the following section.

Mechanical models for electrostatic actuation

In order to estimate the actuation voltage of a single GaN membrane, a simple model comprising a pair of parallel capacitor plates is employed. The two plates represent the GaN membranes and they are separated by an air gap as shown in Fig. 6.19. One or both of the plates are capable of moving. Although the FPFs considered in this work are of the type as depicted in Fig. 6.19(a) with two simultaneously moving mirrors, the results for a single movable membrane system as shown in Fig. 6.19(b) can easily be applied for this works purpose.

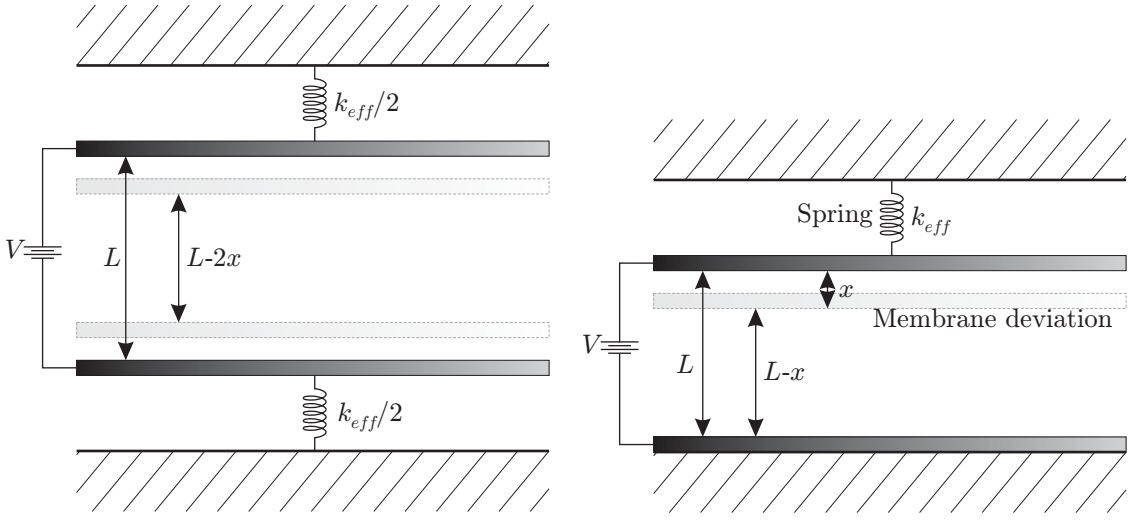

(a) Two movable membrane (b) One movable membranes

Figure 6.19: One dimensional spring model for the electrostatic actuation of a GaN membrane.

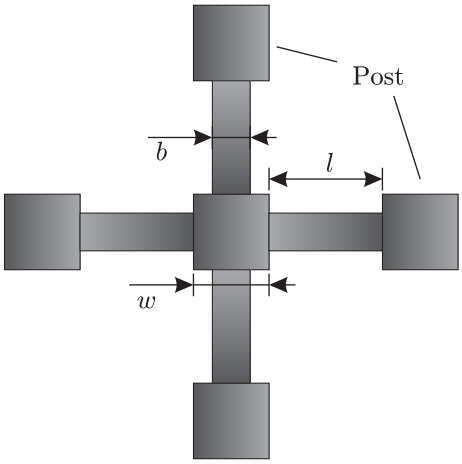

Figure 6.20: Schematic of the DBR membrane and support beams.

The membrane to be actuated with an area A separated by a short air cavity length of L from a second fixed membrane is considered. The membranes are supported by four beams with the length of l, width of b and thickness of d_b (see Fig. 6.20).

When a constant voltage V is applied to the top membrane in Fig. 6.19(b), the membrane is pulled down by x due to electrostatic force. This resulting electrostatic

force on the top membrane is given by:

$$F_E = \varepsilon_0 A \frac{V^2}{2(L-x)} + \varepsilon_0 bl \frac{2V^2}{L(L-x)} \tag{6.11}$$

ε_0 is the free space permittivity. The first term indicates the force distributed across the central plate while the second term describes the force generated along the length of the beams. In this expression, the central plate is assumed to experience negligible deformation upon actuation as compared to the suspensions. In addition, deformation of the beams is linear from post to the center.

A mechanical counter force corresponding to Hook's law exists to restore the plate to the original position. With the consideration of one degree of freedom, the elastic force is given as below when the suspension beams have intrinsic stress σ.

$$\begin{aligned} F_{\text{stress}} &= \pi^2 b\sigma \frac{d_b}{l} x \\ F_{\text{bend}} &= \pi^4 bE(\frac{d_b}{l})^3 x \\ F_{\text{stretch}} &= \pi^4 bEd_b(\frac{x}{l})^3 \end{aligned} \tag{6.12}$$

F_{stress} will be dominant if a very thin structure is fabricated from materials with high intrinsic stress. The second term is the linear bending force. The last term of F_{stretch} becomes important at large displacements. In our system, the Young's modulus E (345 GPa) and the stress are in the same order and the length of the beam (couple of tens μm) is much larger than the thickness of the beam (couple of tenth μm). Therefore, the first term related to stress is more dominant and considered to be balanced with the electrostatic force for a stable operation as below. Since only small displacement is accounted for, the last term is ignored. Details about the mechanical model can be found in Ref. [183].

At the equilibrium state, the electrostatic force and the mechanical elastic force

can be summarized as below.

$$\varepsilon_0 A \frac{V^2}{2(L-x)} + \varepsilon_0 bl \frac{2V^2}{L(L-x)} = \pi^2 b\sigma \frac{d_b}{l} x \tag{6.13}$$

From this equation, the displacement x corresponding to the applied voltage can be calculated. However, as the air gap is reduced by increasing the applied voltage, the electrostatic force becomes stronger. Due to this positive feedback, the top membrane will snap down into the bottom membrane. Normally such collapse occurs when the displacement x is larger than one third of L. This specific voltage is called pull-in voltage (V_{PI}). The commercial finite element analysis tool ANSYS is used for the simulation of the above given problem. The simulation results will be presented in section 6.3.2.

6.3.2 Simulation results

Optical simulation results

In this section, optical simulation results of GaN/air gap DBRs and FPFs designed with these DBRs are discussed. The number of DBR periods required in order to achieve 98 % reflectance is calculated in terms of GaN membrane thickness by employing the standard tansmission matrix method (TMM) [184]. The calculated reflectance spectra of GaN/air gap DBRs are presented and compared to those obtained with AlN/GaN DBRs. Subsequently, the reflectance spectra of FPFs are calculated corresponding to the change of the air cavity length.

The DBR designs presented in this work employ thick AlN sacrificial layer (about 0.7 μm) as a first layer on the sapphire substrate so that cracks in the following layers can be prevented [185]. The thickness of this first AlN grown layer should be optimized in consideration of the deformation of the GaN epilayer after etching (see section 6.3.2). The thickness of the GaN layer and of the sacrificial AlN layer

correspond to

$$d_{GaN} = i^* \cdot \frac{\lambda_0}{4n_{GaN}}, d_{AlN} = j^* \cdot \frac{\lambda_0}{4n_{air}} \tag{6.14}$$

where n_{GaN} and n_{air} are the refractive indices of GaN and air, respectively. i^* and j^* are odd integers. The center wavelength λ_0 was chosen to be 450 nm for NO_2 detection. The GaN absorption edge is below 400 nm and absorption was therefore excluded in this simulation. The refractive index data for GaN were taken from Ref. [186] and the value of 1.78 was used for sapphire [187]. The incident light was assumed to be normal to the surface and the incident medium was considered to be air.

Resulting from the TMM simulation, the number of periods vs. reflectance is presented together with experimental results from literature of nitride DBRs in Fig. 6.21. With DBRs having only 3.5 periods, 98 % reflectance is feasible. On the other hand, pure nitride semiconductor DBRs need more than 20 periods.

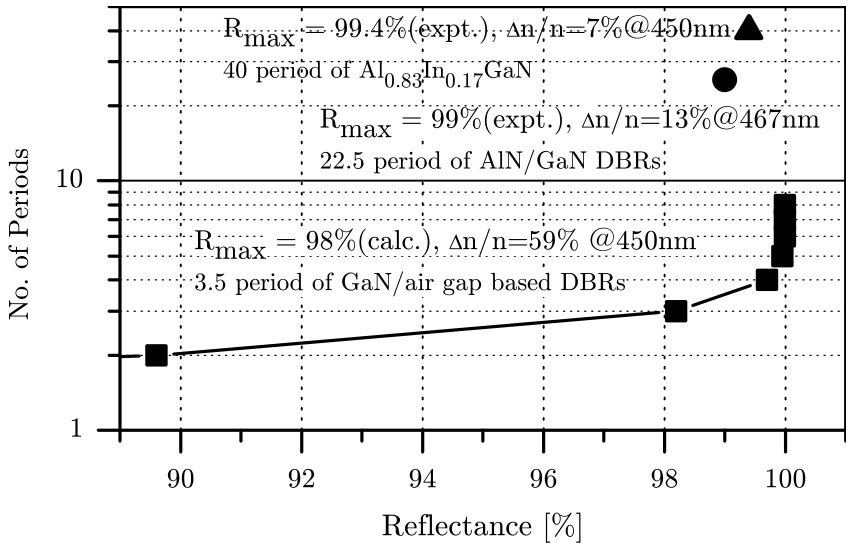

Figure 6.21: Reflectance vs. number of DBRs (triangle Ref. [188] and circle Ref. [189]).

The reflectance spectra of two GaN/air gap DBRs with different thickness and those of a 32-period GaN/AlN DBR (the thicknesses of each layer are given by a

quarter wavelength) are shown in Fig. 6.22. In all cases, the air gap was fixed to a quarter of λ_0 ($\sim$ 113 nm) and 3.5 periods were used. Regardless of the GaN thickness, the maximum reflectance remained above 98 % but the stopband was reduced to 63 nm as the thickness of GaN was increased from 230 nm to 322 nm. However, this design still shows a broader stop-band than that of a 32-period GaN/AlN DBR which is necessary to achieve high performance FPFs. If the GaN thickness is increased further to 507 nm the stop-band is decreased to 46 nm (not shown in Fig. 6.22).

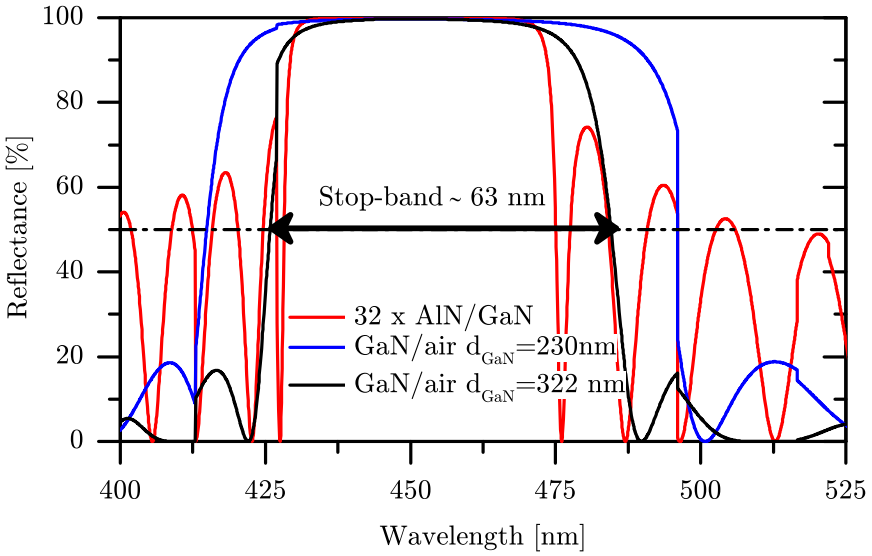

Figure 6.22: Reflectance spectra for a 32 period AlN/GaN DBR and two GaN/air gap DBRs having different GaN membrane thicknesses.

The Fabry-Pérot filter is designed with a simple square geometry of the DBRs supported by four beams as already shown in Fig. 6.20. The number of DBR periods is 3.5, for reasons given above. The cross section is shown in Fig. 6.23.

In order to assess the optical performance of FPFs, two different GaN membrane thicknesses were considered (Design I and II). The GaN thickness is 322 nm and 507 nm, respectively, for each design. The air resonant cavity of the FPFs is fixed at 230 nm. A larger cavity length is advantageous for achieving sharp FWHM but this is restricted by the AlN sacrificial layer whose growth is more difficult as

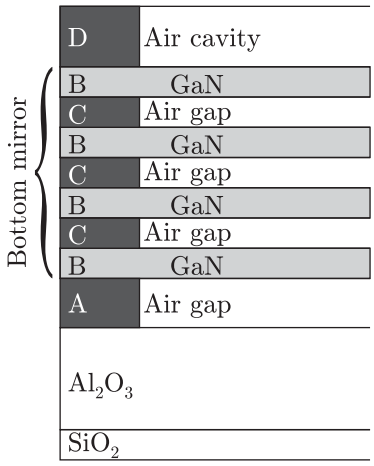

Figure 6.23: Cross sectional view of the bottom DBR including air cavity.

it becomes thicker. The thickness of each layer in the two designs is summarized in Table 6.3. Considering the deflection of the GaN membrane due to intrinsic stress, the thickness of layer A (see Fig. 6.23) is determined in order to avoid sticking of the first GaN membrane to the substrate. In the optical simulation, SiO_2 was included as an anti-reflection (AR) coating on the backside of the sapphire substrate.

Layer		Design I	Design II
A (AlN)	Post	720nm	720nm
B (GaN)	Membrane	322nm	507nm
C (AlN)	Air gap	113nm	113nm
D (AlN)	Air cavity	230nm	230nm

Table 6.3: Design parameters of GaN/air gap DBRs.

The reflectance spectra of the FPF (design I) corresponding to 322 nm thick GaN membranes is shown in Fig. 6.24(a). By controlling the resonant cavity length (ΔL) by up to 70 nm, the peak wavelength shifts from 451.35 nm to 432.89 nm and the FWHM is 0.08 nm and 0.21 nm, respectively. The optical tuning efficiency $\Delta\lambda/\Delta L$ is about 0.26. In design II shown in Fig. 6.24(b), the optical tuning efficiency is reduced to 0.18 due to the large thickness difference between GaN and air.

In terms of optical performance, these two designs are comparable. Therefore,

the thickness of the GaN is determined by considering the mechanical behaviors as discussed in the next section.

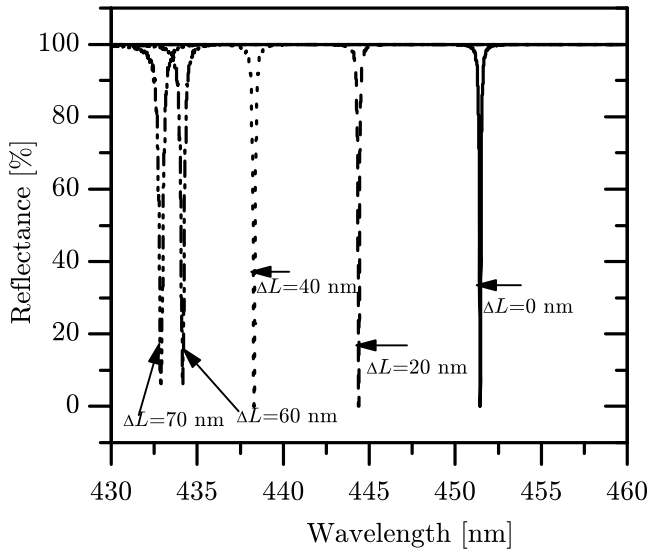

(a) Design I

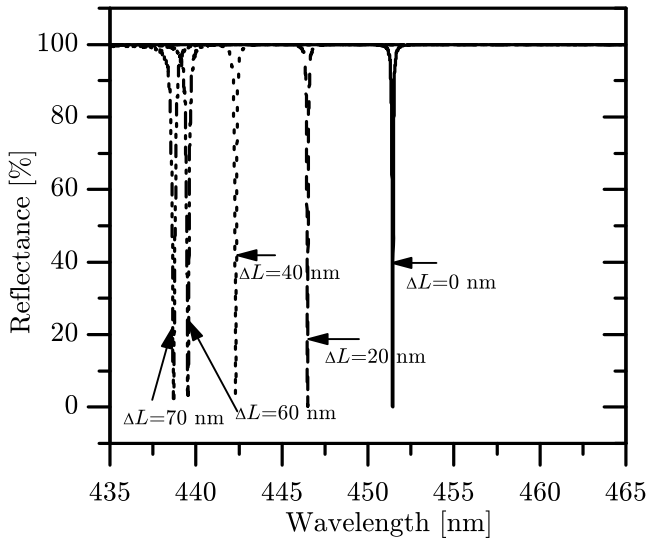

(b) Design II

Figure 6.24: Reflectance spectra of two GaN/air gap FPFs. By tuning the air cavity length, the reflectance dip position moves.

Finite element analysis

The electrostatic and mechanical analysis of GaN/air gap FPFs was performed in order to investigate the feasibility of membrane tuning and the effect of residual stress in the GaN membrane.

The in-plane residual stress σ_a was estimated roughly according to the relationship given in Eq. 6.15 [35],

$$\sigma_a = (c_{11} + c_{12} - 2\frac{c_{13}}{c_{33}}) * \varepsilon_a \tag{6.15}$$

where σ_a is the biaxial stress and $\varepsilon_a = \Delta a/a_0$ the in-plain strain. The following values were used for the elastic constants of GaN: $C_{11} = 390$ GPa, $C_{12} = 145$ GPa, $C_{13} = 106$ GPa, $C_{33} = 398$ GPa (taken from Ref. [190]).

Since residual stress data of GaN and AlN grown by MOVPE is not available at this time, two sets of plastic strain relaxation data of GaN on AlN epilayers grown by MBE were taken from Bellet-Amalric [191] for this purpose. Although stress relaxation in layers grown by MOVPE and MBE are very different, this estimation predicts the trends and parameter dependences applicable to the new scheme of GaN/air gap based MOEM FPFs.

In order to include the impact of growth conditions on the residual stress, two different MBE growth conditions were considered. In MBE growth, the residual stress in the GaN layer is dependent on the Ga flux conditions. Ga monolayer growth condition and bilayer growth condition were considered together with two different thicknesses of GaN (230 nm and 320 nm). The air gap was again fixed at about 113 nm. The cross section of this structure is the same as previously shown in Fig. 6.23. Strain data corresponding to the two design thicknesses were used as ε_a in Eq. 6.15 and bi-axial stress of each layer was calculated accordingly. Results are

presented in Table 6.4.

	Ga mono layer $d_{GaN} = 230\,nm$	Ga mono layer $d_{GaN} = 320\,nm$	Ga bi layer $d_{GaN} = 320\,nm$
1^{st} GaN bottom	-1.65	-1.65	-2.45
1^{st} GaN top	-0.60	-0.50	-0.69
2^{nd} GaN bottom	-1.36	-1.36	-2.05
2^{nd} GaN top	-0.43	-0.34	-0.51
3^{rd} GaN bottom	-1.35	-1.35	-2.0
3^{rd} GaN top	-0.42	-0.34	-0.51
4^{th} GaN bottom	-1.346	-1.345	-2.04
4^{th} GaN top	-0.42	-0.338	-0.51

Table 6.4: Calculated residual stresses of each membrane (unit: GPa).

The GaN membrane near the substrate is labeled 1^{st} layer. An epilayer grown under Ga bi-axial growth conditions shows a higher gradient relaxation above 20 nm thickness than under Ga (sub) monolayer growth condition [191] and consequently causes higher stress as can be seen from Eq. 6.15. With the same growth condition, relaxation occurs more gradually in thicker GaN membranes (320 nm) than in thinner ones (230 nm). Therefore, both growth conditions and thicknesses of the membranes lead to significant differences concerning the membrane deflection after etching of the AlN sacrificial layer.

The in-plane residual stress estimated above is taken into consideration for the calculation of the GaN membrane deformation using the FEA method. The purpose of this simulation is to investigate the effects of residual stress and geometrical parameters. For a single GaN membrane including the support beams, hexahedral meshing was adopted to apply the initial stress to each mesh node along the growth direction (z-axis).

When the membrane size and the length of the beam are a couple of hundred microns, more than 10 μm deflection caused by stress is expected. Hence, optimization of the beam width and the beam length and the reduction of membrane size

were considered. Table 6.5 shows the mechanical design parameters of the four FPF designs.

	Membrane size, A	Beam width, b	Beam length, l	Thickness, d_b	Growth cond.
Case 1	20 x 20	10	30	0.230	Ga mono
Case 2	20 x 20	10	30	0.322	Ga mono
Case 3	30 x 30	15	45	0.322	Ga mono
Case 4	20 x 20	10	30	0.322	Ga bilayer

Table 6.5: Various designs of FPF membranes (unit: μm).

The maximum deflection of each layer is compared in Fig. 6.25. The smallest deformation of the 1st GaN membrane is found to be about 0.6 μm for case 2 while the maximum value is 1.3 μm for case 4. Both cases have common geometrical design but different growth conditions were assumed. Therefore, this considerable difference of GaN membrane deformation found in these two cases indicates that the strain relaxation must be considered according to the growth conditions. Since higher rate of relaxation (Ga bilayer growth condition for case 4) results in rapid change of stress, the strain relaxation must occur slowly. This implies that the growth condition for GaN must be optimized to keep the change of the in-plane lattice of GaN slow so that the strain in GaN can be minimized. In MOVPE growth, stress in GaN can be controlled by the V/III ratio, TD density, growth pressure and growth temperature. In order to accomplish the slow relaxation, higher growth pressure and higher V/III ratio must be used.

Comparing the deflection values from case 1 to case 3, it is clear that a thick and smaller size GaN membrane is more resisting to bending. This result suggests that the beams should be designed short and wide enough to prevent buckling. Consequently the center GaN membrane (4th) is deformed 25 % less than the 1st GaN membrane based on a layer by layer analysis.

In addition to the deflection of the membrane, the control of the flatness of

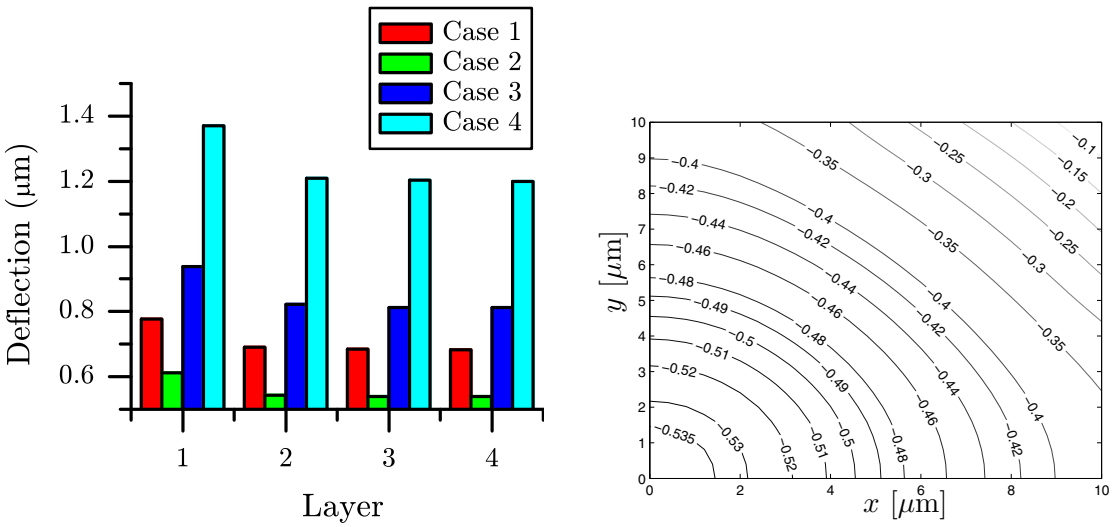

Figure 6.25: FEA results for residual stress vs. membrane deflection. (a) Maximum deflection of each layer depending on design. The number indicates the position of the membrane. The most top membrane is labeled 4$^{\text{th}}$. (b) Contour of top membrane deflection (4$^{\text{th}}$ layer) for case 2 [192].

the membrane is also important to achieve high quality FPFs. It was observed that a difference of 5 nm for the deflection of the top membrane (d_{GaN}: 322 nm) causes a resonant wavelength shift of about 2 nm. The difference between maximum and minimum deflection across the membrane is about 0.4 μm as shown in Fig. 6.25(b). By increasing the thickness of GaN from 322 nm to 507 nm, this value is reduced to 0.24 μm. The stop-band of a DBR with 507 nm GaN is still comparable to a 32 period AlN/GaN DBR and the characteristics of the FPF is not so much different from case 2 (see Table 6.5). Therefore, this could be a optimum design in terms of good optical and mechanical performance.

When the membrane design and growth condition are based on case 2, the simulation of the electrostatic actuation predicted a pull-in voltage (V_{PI}) of about 3.1 V for a 322 nm thick membrane and of 6 V for a 507 nm thick membrane. Figure 6.26 shows the membrane deflection corresponding to the applied voltage. Both

operating voltages are reasonable for real device applications.

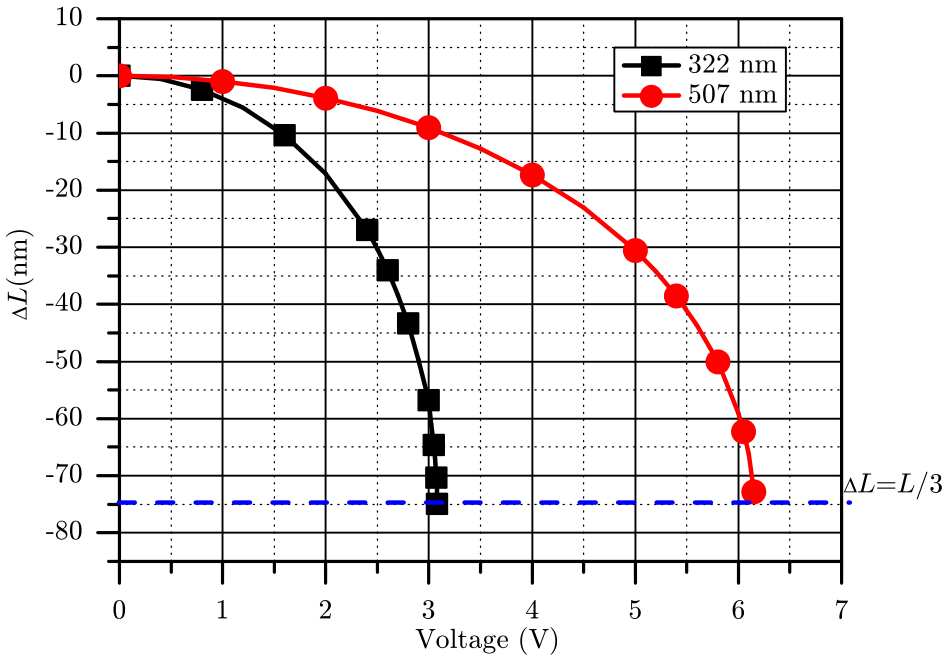

Figure 6.26: Air cavity length change vs. applied voltage.

6.3.3 Experimental results

GaN/AlN heterostructure growth was attempted to realize GaN/air gap DBRs. The growth sequence of the GaN/AlN heterostructure is LT AlN NL, LT AlN (the actual sacrificial layer), interlayers and HT GaN. It is worthy to note that there are several challenges in the growth of such a structure.

The AlN should not be of high quality to ensure easy removal upon etching since it is used as sacrificial layer. The second issue is that the GaN layer grown on top of the AlN has to relax slowly to prevent the membrane from snapping down to the sapphire substrate after etching. Lastly, the surface of the GaN must be smooth so that one can take full advantage of its optical properties. In order to overcome these problems, growth and etching tests have to be performed iteratively.

In the following section, the issues related to AlN growth will be discussed.

These include the growth rate of AlN, the growth of interlayers and the quality of GaN subsequently grown on top of AlN. The results of AlN etching will follow in the subsequent section.

GaN/AlN heterostructure growth for FPFs

As discussed in section 4.2, the pre-reaction between ammonia and TMAl in the gas phase influences the growth rate of AlN significantly. In addition, due to the long diffusion length of Al, the growth rate is sensitive to reactor pressure. Therefore, an optimization of the LT AlN growth rate was conducted with respect to growth pressure, TMAl flow and ammonia flow. Figure 6.27 shows the growth rate of AlN grown under various conditions. However, the growth temperature was fixed at 950 °C.

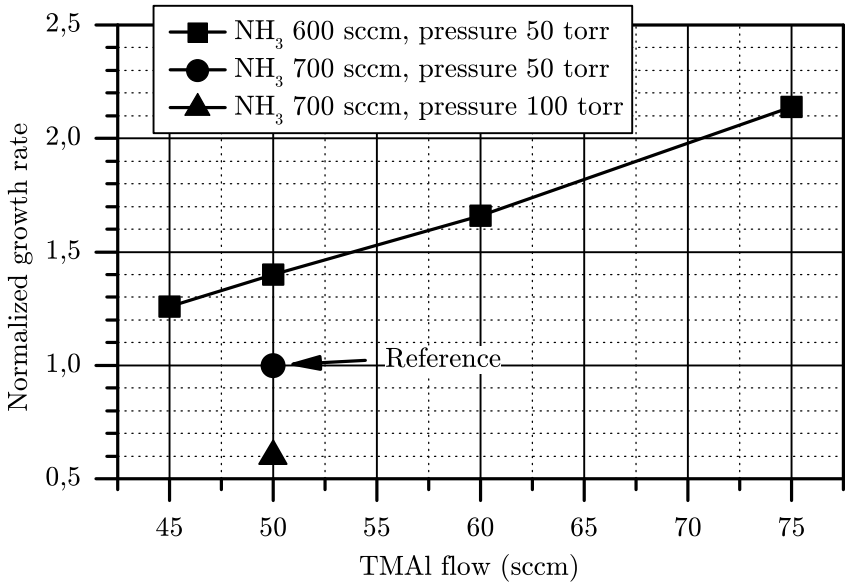

Figure 6.27: Normalized AlN growth rate in different growth pressure and ammonia flow. The growth temperature for all samples was 950 °C.

In this graph, the growth rate corresponding to different growth conditions is normalized with respect to a reference AlN sample. The growth condition for the reference sample was 50 sccm TMAl, 700 sccm ammonia and growth pressure

was 50 torr. For the normalization, the growth times, which are taken to make one interferogram cycle under different growth conditions, are compared to that of the reference sample. The absolute growth rate of the reference sample was about 0.6 μm/h as verified by SEM measurements.

The growth rate increased linearly with the TMAl flow since TMAl is completely decomposed[2] and the growth rate is limited by the mass transport of TMAl (see section 2.1). However, the growth rate was reduced by a factor of two as the growth pressure was increased from 50 torr to 100 torr. This is because the Al precursor diffusion length is reduced as growth pressure is getting higher. An equivalent change was also observed when the ammonia flow increased. The effect of prereaction between ammonia and TMAl is the reason for the low growth rate with 700 sccm ammonia flow as also addressed in section 4.2.

In order to obtain slow relaxation and good GaN quality layer on top of AlN, interlayers were considered before the growth transition from AlN to GaN occurs. Different types of interlayers were applied. Interlayers consist of a couple of periods of AlN/GaN or AlGaN/GaN superlattices (SLs). They contribute to compensate the strain between two layers having large lattice mismatch like AlN and GaN. The interferograms of two representative cases (sample D1 and sample D2) are presented in Fig. 6.28. The growth conditions for each layer of the two samples are tabulated in Table 6.6.

	D1	D2
Growth Temp. for LT AlN	800 °C	950 °C
Interlayer	$Al_{0.17}Ga_{0.83}N$/GaN	AlN/GaN

Table 6.6: Growth conditions for two GaN/AlN heterostructures

In sample D1, the about 600 nm thick low temperature AlN growth is followed

[2]Metal organic sources are decomposed completely above 350 °C.

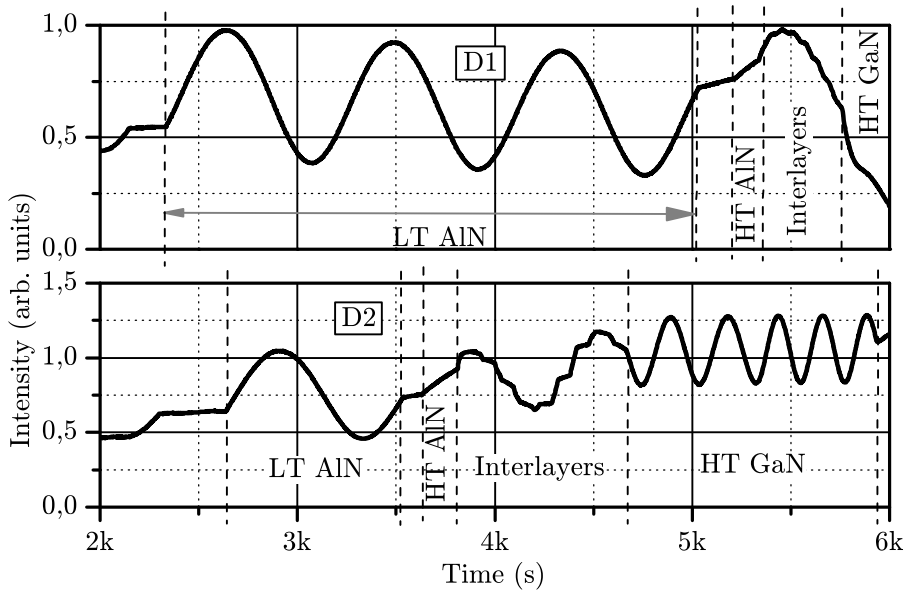

Figure 6.28: Interferogram of sample D1 and D2. The reflectance signal drop indicates that the surface of GaN in sample D1 becomes rough.

by the growth of a thin HT AlN and $Al_{0.17}Ga_{0.83}N$/GaN interlayer. The peak of the reflectance signal drops slowly because the surface of the LT AlN becomes rough during the growth. The top GaN was also observed to be very milky and rough which could also be predicted by the interferogram in Fig. 6.28.

On the other hand, sample D2 showed that the reflectance signal of the top GaN layer recovered fully and oscillated as typical HT GaN does. This indicates that the GaN layer grown on top of the AlN is of good quality. The results can be attributed to the presence of the GaN/AlN interlayer which compensates the strain between AlN and GaN successfully. The pronounced contrast of the growth rate of AlN and GaN is clearly demonstrated in this growth trace.

The failure of strain compensation in sample D1 has several reasons. An $Al_{0.17}Ga_{0.83}N$/GaN interlayer having a thickness of 2 nm/5 nm may be inefficient for compensating the strain. Since the Al composition is quite low, its lattice mismatch with AlN is as high as 2 % which is close to the lattice mismatch of GaN with AlN

(2.5 %). Much lower growth temperatures for AlN and the resulting very poor LT AlN quality in sample D1 have also to be considered.

Etching

In order to achieve good AlN etchability, different growth temperatures were investigated since the AlN quality strongly depends on them. The growth temperature was varied from 800 °C to 1040 °C. The etching for these layers was performed with 1 mol/l KOH solution diluted with DI water. The temperature of the etching solution was kept at 60 °C. During the etching a magnet stick was stirring the solution. The etching depth was measured by a surface profiler after DI water rinse of the samples. The etching rate of AlN versus the growth temperature is summarized in Fig. 6.29.

AlN layers grown between 950 and 1040 °C were barely etchable. Their etching rate was only about 1 nm/min due to the high bond strength between Al and N. Therefore it is difficult to use such a high quality AlN as a sacrificial layer. On the contrary, the AlN grown at 800 °C was etched by more than 10 times faster than the layer grown at 950 °C. By increasing the KOH concentration and the temperature of the KOH solution, the etching was further stimulated and a 200 nm/min etching rate was obtained with the sample grown at 800 °C. These etching results state the importance of AlN growth temperature in terms of etchability.

The correlation between etching rate and the concentration of the etching solution and etching temperature was also investigated. The sample used for this purpose was grown by a different MOVPE system. As can be seen from the cross section of this test structure in Fig. 6.30(a), 100 nm GaN was grown on 700 nm AlN. Its HR-XRD ω-2Θ measurement shows that the (002) FWHM of the AlN and GaN are 126" and 232", respectively (see Fig. 6.30(b)). The very broad GaN peak implies

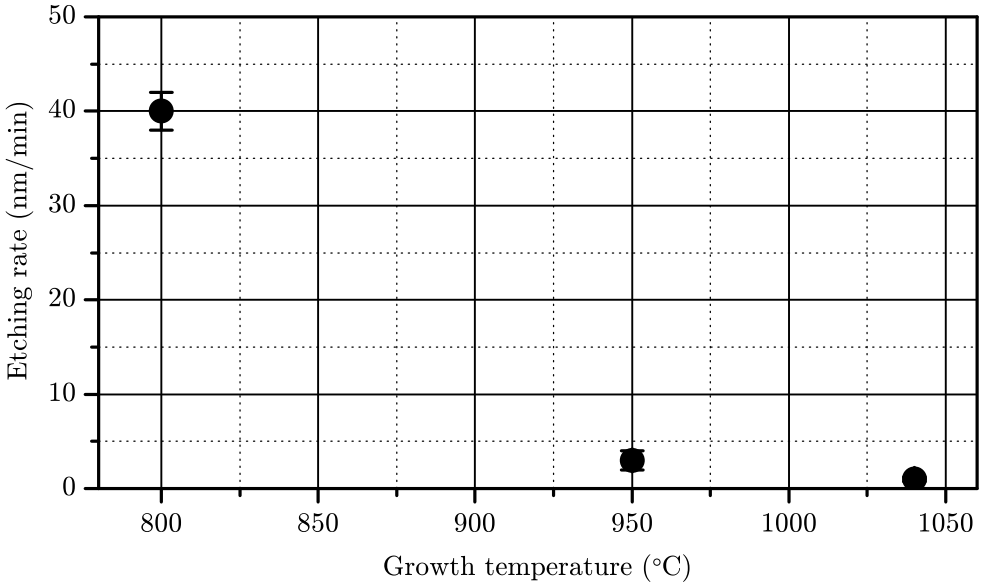

Figure 6.29: Etching rate vs. AlN growth temperature. AlN was etched with 1 mol/l KOH solution at 60 °C.

that the GaN quality is very poor. The (002) FWHM of 2 μm thick GaN is typically less than 50".

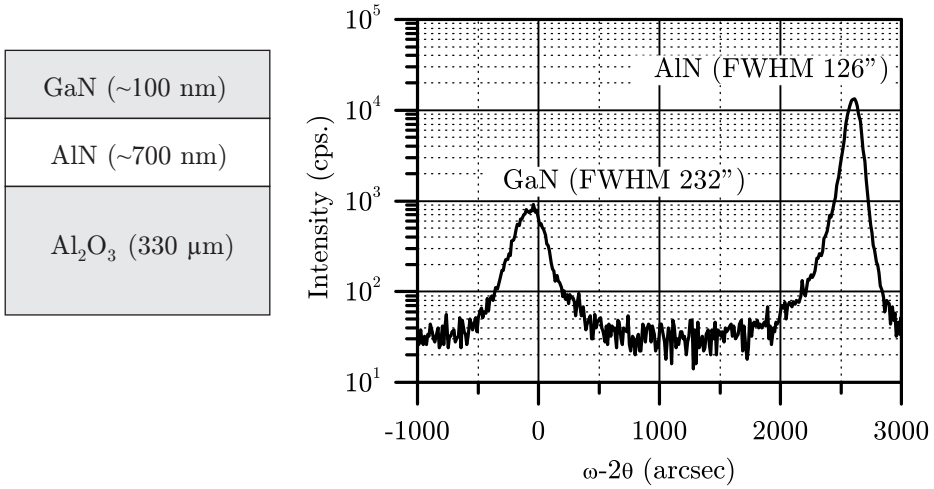

(a) (b)

Figure 6.30: (a) Structure of the GaN/AlN heterostructure for the selective etching test. (b) ω-2Θ measurement.

A photoresist layer was first patterned using photolithography. Etching of the top 100 nm GaN layer was achieved by reactive ion etching (RIE) using an Oxford

Plasmalab 80. The etching conditions were Ar 20 sccm at 50 mTorr for 5 min and the plasma RF power was set to 300 W. The resulting etching rate was 20 nm/min. The sample was then cleaned with acetone and isopropanole alcohol (IPA). Once all photoresist was removed, KOH etching tests were performed with various solution concentrations.

The best result is about 220 nm/min with 2 mol/l KOH at 80 °C as can be seen from Fig. 6.31(a). Figure 6.31(b) shows the Arrhenius plots of the etch rate. The reaction limited etch rate is given by:

$$R(T) = R_0 \exp(-\frac{E_a}{k_B T}) \tag{6.16}$$

where R is the etching rate at temperature T, E_a the activation energy of the etching reaction, k_B is the Boltzmann constant and R_0 is a constant dependent on the material quality. Therefore, an activation energy of 0.654 eV is obtained from the graph which is very close to the literature value of 0.67 eV [193].

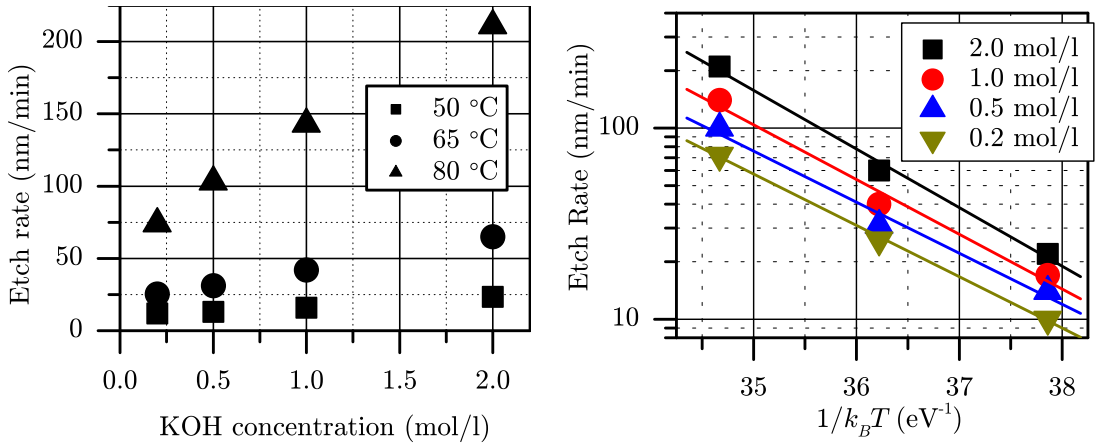

Figure 6.31: (a) Etching rate vs. KHO concentrations. (b) Arrehenius plots of the etch rate.

The desired lateral etching (about 2 μm) was observed as shown in Fig. 6.32(a). However, the SEM image illustrates that the GaN on top of the LT AlN was also

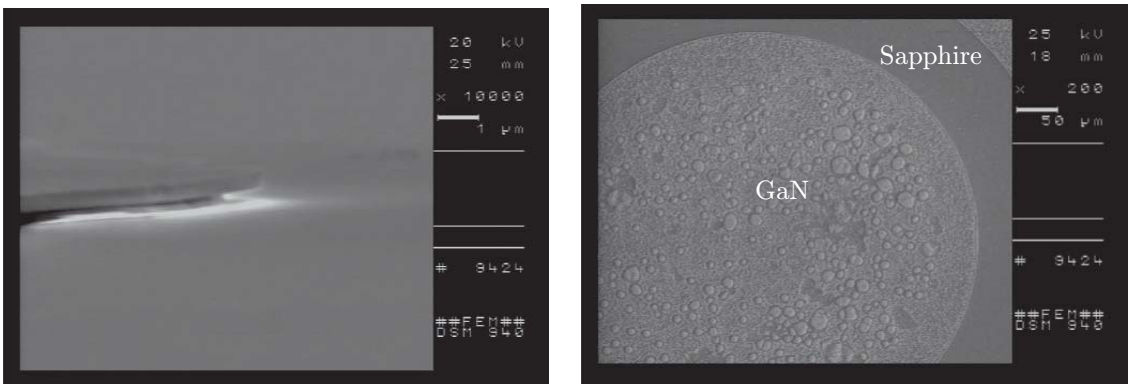

(a) (b)

Figure 6.32: SEM images of GaN/AlN sample after etching with 2 mol/l KOH at 80 °C. (a) Cross section. AlN lateral etching can be observed. (b) Top view of 100 nm thick GaN on AlN. Its surface is very rough.

affected by KOH (see Fig. 6.32(b)). Its surface was found to be very rough and some part of GaN seems to be etched. It indicates that growth transition from SL to the 100 nm thick GaN needs to be optimized in the future in order to achieve a reasonable GaN quality.

6.4 Conclusion

In this chapter, the use of III-Nitride materials in gas sensing applications was discussed. Devices investigated in this work were Schottky diodes and GaN/air gap based Fabry-Pérot filters (FPFs).

Bulk GaN and AlGaN/GaN heterostructures grown by the TS MOVPE system were used to fabricate standard Pt Schottky diodes. Optimizing size and thickness of the Pt Schottky contact lead to an improvement of the gas sensitivity. Bulk GaN Schottky diodes with larger sensing area and thinner Schottky metal showed six times higher sensitivity than a reference sample for CO detection. This supports that CO sensing occurs through the grain boundaries in porous metal films.

Schottky diodes based on AlGaN/GaN heterostructures demonstrated the ca-

pability of gas detection even at room temperature while bulk GaN sensors did not show any response. Their operation at forward bias showed an one order of magnitude current change with 100 ppm H_2 even at room temperature. Under reverse bias, the current change of the Schottky diode gas sensors was more than three orders. This excellent performance in comparison with bulk GaN Schottky diodes is due to the 2DEG formed by spontaneous and piezoelectric fields in nitride materials.

GaN/air gap based Fabry-Pérot filters (FPFs) were explored as a potential detector in an optical gas sensing system. Compared to nitride semiconductor DBRs (for example GaN/AlN), GaN/air gap based DBRs need only 3.5 periods to achieve 98 % reflectance due to the large refractive index contrast between GaN and air. This number is much smaller than that of GaN/AlN DBRs which need more than 20. TMM simulation results showed that a 63 nm stop-band can be achieved with DBRs consisting of 3.5 periods of 322 nm GaN and 113 nm air gap. This value is broader than that of a 32-period GaN/AlN DBR.

FPFs were designed with two DBRs separated by a 230 nm air cavity. Finite element analysis of this FPF showed that the residual stress can cause a deflection of the membrane as large as 0.6 μm when literature values from MBE growth are used for the calculation of the residual stress. The deflection difference across half of the membrane is expected to be about 0.4 μm. In terms of membrane actuation, the calculated pull-in voltage is about 3.0 V.

Increasing the thickness of GaN membranes is proposed to enhance the membrane flatness. FEA simulation results of a 507 nm thick GaN membrane showed 50 % less deflection and an improvement of the mirror flattness compared to the 322 nm thick GaN membrane. Although its stop-band is reduced from 63 nm to 46 nm and V_{PI} increases to 6.0 V due to higher stiffness, its optical performance is

still comparable to the 322 nm design.

In order to realize the AlN sacrificial layer, the correlation between etchability and AlN growth temperatures was investigated. An etching rate of about 200 nm/min was obtained for AlN grown at 800 °C. The etching rate of AlN grown above 950 °C is less than 3 nm/min with the same condition which makes this quality of AlN not applicable for sacrificial layers.

More etching experiments were conducted with various etching conditions as varying etching temperatures and concentrations of KOH. Lateral etching of about 2 μm was observed by SEM measurement. However, the crystallinity of the GaN was affected by KOH because the GaN layer was as thin as 100 nm and its quality was not optimized. This confirms that the GaN thickness is important not only in terms of the structural deformation of a GaN membrane due to residual stress but also in terms of etching resistivity.

CHAPTER VII

THESIS CONCLUSION

This thesis focused on the growth understanding and optimization of III-Nitride materials and their use in different types of devices. More specifically, the objective was to optimize layer growth for high power and high frequency devices based on $Al_xGa_{1-x}N$/GaN heterostructures and to explore the use of Nitrides in gas sensing applications. The following conclusions are drawn.

7.1 Polar Nitrides

Comprehensive growth optimization work was carried out to reduce the intrinsic high conductivity of undoped bulk GaN. The nucleation layer (NL) annealing time was found to be an effective parameter to control the resistivity of GaN layers grown at 1040 °C. Different annealing times result in different threading dislocation densities which play the role of acceptor-like defects along with impurities. 11K band edge photoluminescence measurements manifest that an acceptor-bound exciton peak (A^0X) is present with a donor-bound exciton peak (D^0X) in undoped bulk GaN. Hall measurements confirmed the proportional relationship between the ratio of the two peaks and the layer resistivity. Moreover, off-axis X-ray diffraction measurements showed that edge threading dislocations contribute to a certain extent to improve resistivity.

A similar conclusion was made for GaN grown at 1033 °C and carbon impurities segregated around TDs were speculated as the origin of resistivity increase [60]. However, in this work, PL measurements over the wavelength range of 350∼700 nm suggested that TDs as well as $V_{Ga}H_N$ are responsible for the resistivity of bulk GaN. The role of carbon seems to be insignificant in this work since blue emission and yellow emission caused by carbon were found to be relatively negligible. This is consistent with the growth conditions used since less carbon is expected in the reactor as the growth temperature and V/III ratio increase.

The use of resistive bulk GaN in AlGaN/GaN heterostructure field effect transistors resulted in the improvement of device pinch-off. Pinch-off current was reduced by a factor of twenty in comparison with devices fabricated with non-optimized bulk GaN. The associated f_T and f_{max} was about 11 GHz and 26 GHz, respectively. These DC and high frequency characteristics imply that both the resistive bulk GaN and the AlGaN layers are of good quality.

For a further improvement of the high power and high frequency device characteristics, AlN MISFET structures were investigated. MOVPE grown *in-situ* SiN_x was implemented in this structure to reduce the high risk of AlN oxidation and 2DEG depletion due to surface contamination. The effect of *in-situ* SiN_x was proved by good ohmic contact quality obtained even without AlN etching. Moreover, the leakage current of these devices showed a decrease of one order of magnitude in comparison to AlN MISFET reference samples having no passivation layer. DC and RF characteristics of the devices were also improved by a factor of 2 to 3

7.2 Non-polar Nitrides

The growth of non-polar III-Nitrides was carried out using r-plane sapphire substrates in order to remove polarization fields in AlGaN/GaN heterostructures and realize normally off mode transistors. In-plane anisotropic characteristics were observed in terms of crystalline quality. The FWHM along the m-axis was two to three times larger than the values along the c-axis. Surface undulation was also observed along the m-axis. A comprehensive study of how the NL affects the overall growth rate manifested that AlN nucleation layer can improve the surface roughness and anisotropy in comparison to low temperature bulk GaN NLs or direct growth without NL.

7.3 Nitrides for gas sensing applications

Bulk GaN and AlGaN/GaN heterostructures grown by the TS MOVPE system were used to fabricate standard Pt Schottky diodes. A comprehensive study of gas sensor design showed that the size and thickness of the Pt Schottky contact impact the gas sensitivity. Bulk GaN Schottky diodes with larger sensing area and thinner Schottky contact showed six times higher sensitivity than a reference sample for CO detection. This supports that CO sensing occurs through the grain boundaries in porous metal films.

Schottky diodes based on AlGaN/GaN heterostructures demonstrated the capability of gas detection even at room temperature while bulk GaN sensors barely detected anything. This excellent performance is due to the 2DEG formed by spontaneous and piezoelectric fields in nitride heterostructures as this is sensitive to the surface state. This is proved by AlGaN/GaN heterostructures Schottky didoes

with SiN_x surface passivation which did not show any response to gases.

GaN/air gap based Fabry-Pérot filters (FPFs) were explored as a potential detector in optical gas sensing systems and in particular for usage in the UV/VIS wavelength region. The deflection of the membrane, which is caused by strain relaxation after sacrificial layer etching, was found to be critical. Optimizing the membrane size and the thickness is proposed in order to enhance the membrane flatness while keeping its optical performance comparable to the thinner membranes.

In order to realize the AlN sacrificial layer, the correlation between etchability and AlN growth temperature was investigated. An etching rate of about 200 nm/min was obtained for AlN grown at 800 °C. The etching rate of AlN grown above 950 °C is less than 3 nm/min under the same conditions which makes this quality of AlN not applicable as sacrificial layers.

7.4 Impact of this work

This work presents a systematic analysis of the way how device characteristics are impacted by the material. More specifically, the correlation between defects in bulk GaN and its resistivity were studied in chapter III by carrying out a comprehensive growth and characterization study. Evidence was brought that the acceptors are formed by $V_{Ga}H_N$ and dislocations. As a consequence of changing the bulk GaN quality (resistivity), DC and RF characteristics of HFETs were improved as discussed in chapter IV. Effects of *in-situ* SiN_x deposited by MOVPE were also investigated from the material point of view. Wet and dry etching tests of SiN_x proved its good quality and important role in improving device characteristics. The study of non-

polar Nitrides presented in chapter V is important due to the fact that in contrast to studies for optical devices, their impact has not been studied extensively for electronic devices. While the surface morphology issues pertaining to non-polar GaN seem to be resolved in this work, the improvement of crystalline quality remains to be performed in order to obtain reasonable device characteristics. Finally, the realization of GaN/air gap based Fabry-Pérot filters (FPFs) was explored by using epitaxially grown AlN as a sacrificial layer. To our knowledge, AlN as sacrificial layer has so far only been studied using sputtering techniques. While theoretical studies showed the feasibility of this device type, experimental results of growth and etching tests showed that more extensive studies are necessary to define growth conditions which make AlN etchable while allowing at the same time subsequent growth of good quality GaN layers.

CHAPTER VIII

FUTURE WORK

8.1 Growth in non-polar directions

Recent reports found in literature on optoelectronic devices based on non-polar GaN demonstrate enhanced LED efficiency by eliminating polarization fields [136, 137]. In analogy with the successful growth of non-polar III-Nitrides for optoelectronic devices, it should be possible to grow and use non-polar Nitrides for electronic devices as explored in this work. Very little research has been done for this purpose and device results are also premature. Although this thesis presents some progress in non-polar heterostructure growth on *r*-plane sapphire substrates, further studies are important to obtain layers having device quality.

Issues pertaining to enhancing mobility must be tackled for high frequency devices due to the interest existing in using non-polar Nitrides for the realization of normally off transistors. In comparison to *c*-plane Nitrides, non-polar GaN layers have higher defect density. This poses a challenge concerning the realization of devices such as resonant tunneling diodes which will also benefit from the absence of the polarization field since defects drastically impede device performance in the form of trapping electrons. Therefore, a reduction of dislocation density must be considered as addressed in section 8.3. An alternative way to improve layer quality

would be growth on m-plane sapphire substrates. The range of MOVPE growth parameters to obtain good quality a-plane layers on r-plane sapphire substrates is narrow and highly sensitive to changes in growth pressure, temperature and precursor flow rates [194]. Compared to the growth on r-plane sapphire substrates, growth on m-plane sapphire substrates is believed to offer more flexible growth conditions and reproducible results [195].

8.2 Hybrid structures with Nitrides and ZnO

The lattice mismatch between ZnO and GaN is only $\sim 1.8\,\%$ and the crystal structure of the two materials is similar to each other [196]. This potentially leads to good layer quality of GaN grown on ZnO or vice versa. Recently, the interest in combining these two materials has increased because this hybrid structure can offer many promising applications.

GaN/ZnO structures are of potential interest for MEMS devices since wet chemical etching of ZnO is much easier in comparison to Nitride etching. Currently, most Nitride MEMS structures are studied with Si or SiC substrates because of high wet etching selectivity between GaN and the substrate. However, the improvement of Nitrides quality on Si is still underway and the usage of SiC is not cost effective. Specially, when devices need multiple sacrificial layers, using these substrates are not appropriate.

pn diodes using GaN and ZnO are very attractive for application to both optoelectronic devices and high frequency devices. Although lower threshold currents and better performance at high temperature are expected with ZnO based LEDs due to the larger exciton binding energy of ZnO (60 meV vs. 28 meV for GaN), the realization of stable and reproducible p-type ZnO hinders the progress. In spite of

its mature technology, GaN also has a problem. The higher growth temperature of GaN than that of InGaN impedes the high In incorporation since In is highly volatile. Therefore, LED structures consisting of n-ZnO/InGaN MQW/p-GaN is promising for green LEDs because good quality of ZnO layer can still be grown below 800 °C [98].

In Nitride heterojunction bipolar transistors (HBTs), the degradation of p-contact due to dry etching needs to be solved ; p-GaN surfaces are found to be sensitive to etch damage which causes point defects creating donor states and degrading contacts in etched p-GaN [197]. If the growth of reasonable quality of p-ZnO is possible, p-ZnO/n-GaN/p-ZnO devices will not have the issue pertaining to p-contact as p-ZnO will be removed by wet etching chemicals. However, for this purpose, the damage of ZnO layer during the growth of GaN has to be overcome along with ZnO p-doping issue. It is reported that ammonia and hydrogen which are standard gases for GaN growth process damage ZnO layer.

8.3 Growth on porous substrates

It is known that the density of threading dislocations of GaN is typically $10^9 \sim 10^{10}\,\mathrm{cm}^{-3}$. In order to reduce the defects, Epitaxial Lateral Overgrowth (ELO) using dielectric masks (SiN_x or SiO_2) of periodic geometries on a substrate has been studied. Since most dislocations tend to propagate upward along the vertical growth direction from the substrate, the mask opening area (window region) contains highly defective material. In contrast, the layers grown above the mask region (wing region) have fewer dislocations [198]. As a result, the defect density is reduced to $10^5 \sim 10^6\,\mathrm{cm}^{-3}$ in the wing region.

Growth on porous substrates such as porous SiC or porous GaN is also proposed

to improve the quality of Nitrides [199]. Nano pipes or nano pores were found to stop and/or bend dislocations. Recently, the growth using porous Si is also reported [200]. In addition to the reduction of dislocations, the reduction of strain in GaN was also reported. Incorporation of this growth technique in *a*-plane GaN growth is believed to improve the quality of *a*-GaN growth more effectively than the ELO technique. Due to the limited growth window of *a*-GaN, coalescence of the overgrowing ELO islands is known to be very difficult and the results are not reproducible [195]. Since the size of the pores is much smaller than the size of the dielectric mask, the defects can be reduced more effectively than by ELO technique. Moreover, the use of porous Si substrates enables the realization of vertical *pn* junction devices.

APPENDICES

APPENDIX A

Piezoelectric polarization calculation

The strain tensor describes the distortion of the unit cell with respect to the equilibrium structure. The tensors consist of normal strain components ϵ_{xx}, ϵ_{yy}, ϵ_{zz} as well as shear strain components ϵ_{xy}, ϵ_{xz}, ϵ_{yz}.

The stress tensor describes the pressure which has to be applied to the crystal in order to distort it. Similar to the strain tensor, the stress tensor has normal parts (σ_{xx}, σ_{yy}, σ_{zz}) and shear parts (σ_{xy}, σ_{xz}, σ_{yz}). The stress tensor is related to the strain tensor via the elastic constant according to Hook's law. In case of the C_6v symmetry of the wurtzite structure, the stress tensor is given by:

$$\begin{pmatrix} \sigma_{xx} \\ \sigma_{yy} \\ \sigma_{zz} \\ \sigma_{yz} \\ \sigma_{xz} \\ \sigma_{xy} \end{pmatrix} = \begin{pmatrix} C_{11} & C_{12} & C_{13} & 0 & 0 & 0 \\ C_{12} & C_{11} & C_{13} & 0 & 0 & 0 \\ C_{13} & C_{13} & C_{33} & 0 & 0 & 0 \\ 0 & 0 & 0 & C_{44} & 0 & 0 \\ 0 & 0 & 0 & 0 & C_{44} & 0 \\ 0 & 0 & 0 & 0 & 0 & C_{66} \end{pmatrix} \begin{pmatrix} \epsilon_{xx} \\ \epsilon_{yy} \\ \epsilon_{zz} \\ \epsilon_{yz} \\ \epsilon_{xz} \\ \epsilon_{xy} \end{pmatrix} \tag{A.1}$$

In the growth along the c-axis, the growth plane corresponds to the xy-plane and deposition takes place along the z-direction. Shear components of both stresses

and strains are absent. Thus the strain tensor has only three non-vanishing terms ϵ_{xx}, ϵ_{yy}, ϵ_{zz}. Considering the symmetry, strain can be simplified as in-plane strain $\epsilon_{\parallel}$ $= \epsilon_{xx} = \epsilon_{yy}$ and out-of-plane $\epsilon_{\perp} = \epsilon_{zz}$. Eq.A.1 becomes,

$$\begin{pmatrix} \sigma_{\parallel} \\ \sigma_{\perp} \end{pmatrix} = \begin{pmatrix} C_{11} + C_{12} & C_{13} \\ 2C_{13} & C_{33} \end{pmatrix} \begin{pmatrix} \epsilon_{\parallel} \\ \epsilon_{\perp} \end{pmatrix} \tag{A.2}$$

Since the film is free to expand or shrink along the growth direction, the out-of-plane stress $\sigma_{\perp}$ is equal to zero and we obtain

$$\frac{\epsilon_{\parallel}}{\epsilon_{\perp}} = -2\frac{C_{13}}{C_{33}} \tag{A.3}$$

The piezoelectric polarization can be obtained by relating the piezoelectric tensor (e_{ij}) of the space group $P6_3mc$ to the strain.

$$P_{PE} = \begin{pmatrix} 0 & 0 & 0 & 0 & e_{15} & 0 \\ 0 & 0 & 0 & e_{15} & 0 & 0 \\ e_{31} & e_{31} & e_{33} & 0 & 0 & 0 \end{pmatrix} \begin{pmatrix} \epsilon_{xx} \\ \epsilon_{yy} \\ \epsilon_{zz} \\ \epsilon_{yz} \\ \epsilon_{xz} \\ \epsilon_{xy} \end{pmatrix} = \begin{pmatrix} e_{15}\epsilon_{xz} \\ e_{15}\epsilon_{yz} \\ e_{31}(\epsilon_{xx} + \epsilon_{yy}) + e_{33}\epsilon_{zz} \end{pmatrix} \tag{A.4}$$

Since no shear strain is present in c-plane GaN, ϵ_{xz} and ϵ_{yz} are zero. The total polarization for the growth direction (0001) is given by:

$$P_{PE} = e_{33}\epsilon_{\perp} + 2e_{31}\epsilon_{\parallel} \tag{A.5}$$

By replacing $\epsilon_{\perp}$ with $\epsilon_{\parallel}$ from the Eq. A.3, P_{PZ} is now described as follows.

$$P_{PE} = 2\epsilon_{\parallel}\left(e_{31} - e_{33}\frac{C_{13}}{C_{33}}\right) \tag{A.6}$$

APPENDIX B

Electron mobility

	Bulk	2DEG
Polar Opical Phonon (μ_{opt}) [201]	$e^{E_0/kT}\left(1-\frac{5kT}{E_g}\right)^2$	
Acoustic Phonon (μ_{piezo}) [201]	$T^{-1/2}$	$T^{-1/2}{\cdot}n_s^{-1/2}$
Ionized impurity (μ_{ii}) [112]	$\frac{T^{3/2}}{N_i}$	$\frac{n_s^{3/2}}{N_i}$
Alloy Disorder (μ_{alloy})	$\frac{1}{x(1-x)T^{1/2}}$	$\frac{1}{x(1-x)n_s^{1/2}}$
Dislocation (μ_{dis}) [202]	-	$\frac{{n_s}^{3/2}}{N_{dis}}$
Interface (μ_{in})[203]	-	$\downarrow$ as $n_s \uparrow$

Table B.1: Electron mobilities limited by different scattering mechanisms. After Ref. [109].

E_0 : The energy of polar optical phonon
N_i : The density of ionized impurities
N_{dis} : The density of dislocations
n_s : sheet charge carrier density

APPENDIX C

Figure of Merits for various semiconductor materials

Material	JM	KM	BM	BHFM	QF1	QF2	QF3
Si	1.0	1.0	1.0	1.0	1.0	1.0	1.0
GaAs	11	0.45	28	16	9.4	16	28
GaN	790	1.8	910	100	910	10300	910
AlN($\mu = 14$)	5120	2.6	390	14	660	25520	390
InN($\mu = 3000$)	58	6	46	19	150	460	46
6HSiC	260	5.1	90	13	300	2440	90
4HSiC	410	5.1	290	34	950	9630	290

Table C.1: Normalized figure of merits for various semiconductors with respect to Si. After Ref. [111].

JM = $(E_c v_{sat}/\pi)^2$, here, E_c is critical breakdown field.
KM = $k_{th}(v_{sat}/\epsilon)^{1/2}$, here, k_{th} is thermal conductivity.
BM= $\mu\epsilon(E_c)^3$, μ is carrier mobility.
BHFM= $\mu(E_c)^2$
QF1= σ_A, here, σ_A is $\epsilon\mu E_c^3$
QF2= $\sigma_A E_c$
QF3=BM

BIBLIOGRAPHY

[1] H. P. Maruska and J. J. Tietjen. The Preparation and Properties of Vapor Deposited Single Crystalline GaN. *Appl. Phys. Lett.*, 15:327, 1969.

[2] S. Yoshida, S. Misawa, and S. Gonda. Improvements on the Electrical and Luminescent Properties of Reactive Molecular Beam Epitaxially Grown GaN Films by Using AlN-coated Sapphire Substrates. *Appl. Phys. Lett.*, 42:427, 1983.

[3] I. Akasaki, H. Amano, Y. Koide, H. Hiramatsu, and N. Sawak. Effects of AlN Buffer Layer on Crystallographic Structure and on Electrical and Optical Properties of GaN and GaAlN ($0 < x \leq 0.4$) Films Grown on Sapphire Substrate by MOVPE. *J. Cryst. Growth*, 98:209, 1989.

[4] S. Nakamura. GaN Growth Using GaN Buffer Layer. *Jpn. J. Appl. Phys.*, 30:L1705, 1991.

[5] I. Akasaki, T. Kozowa, H. Hiramatsu, N. Sawak, K. Ikeda, and Y. Ishii. Electron Beam Effects on Blue Luminescence of Zinc-doped GaN. *J. Lumin.*, 40:121, 1988.

[6] J. A. van Vechten, J. D. Zook, and R. D. Horning. Defeating Compensation in Wide Gap Semiconductors by Growing in H that is Removed by Low Temperature De-Ionizing Radiation. *Jpn. J. Appl. Phys*, 31:3662, 1992.

[7] S. Nakamura, N. Iwasa, M. Senoh, and T. Mukai. Hole Compensation Mechanism of p-Type GaN Films. *Jpn. J. Appl. Phys.*, 31:1258, 1992.

[8] H. Amano, M. Kitoh, K. Hiramatsu, and I. Akasaki. P-type Conduction in Mg-doped GaN Treated with Low-Energy Electron Beam Irradiation (LEEBI). *Jpn. J. Appl. Phys. Part 2-Letters*, 28:2112, 1997.

[9] S. Nakamura, T. Mukai, and M. Senoh. Candela-class High-Brightness InGaN/AlGaN Double-Heterostructure Blue-Light-Emitting Diodes. *Appl. Phys. Lett.*, 64:1687, 1994.

[10] S. Nakamura. High power InGaN Based Blue Laser Diodes with a Long Lifetime. *J. Cryst. Growth*, 195:242, 1998.

[11] Y. Otoki, T. Saitoh, T. Meguro, and H. Sakaguchi. Mass Production Technology of Large Size III-V Compound Semiconductor Epitaxial Wafers for Microwave Devices by MOVPE. Technical report, Hitachi Cable Review No. 20, 2001.

[12] A. A. Burk. Development of Multiwafer Warm Planetary VPE Reactors for SiC Device Production. *Chem. Vap. Deposition*, 12:465, 2006.

[13] O. Ambacher, J. Smart, J. R. Shealy, N. G. Weimann, K. Chu, M. Murphy, R. Dimitrov, L. Wittmer, M. Stutzmann, W. Rieger, and J. Hilsenbeck. Two-dimensional Electron Gases Induced by Spontaneous and Piezoelectric Polarization Charges in N- and Ga-face AlGaN/GaN Heterostructures. *J. Appl. Phys.*, 85:3222, 1999.

[14] I. Grzegory. High Pressure Growth of Bulk GaN from Solutions in Gallium. *J. Phys. Condens. Matter.*, 13:6875, 2001.

[15] P. Roussel. Si, Sapphire and GaN Materials Status unto Opto and RF Business. *CS MANTECH conference*, page 231, 2006.

[16] N. V. Edwards. *Residual Stress in III-Nitrides*. Elsevier, 2000.

[17] S. Nakamura and G. Fasol. *The Blue Laser Diode*. Springer, 1997.

[18] D. C. Look and J. R. Sizelove. Predicted Maximum Mobility in Bulk GaN. *Appl. Phys. Lett.*, 79:1133, 2001.

[19] Y. F. Wu, A. Saxler, M. Moore, R. P. Smith, S. Sheppard, P. M. Chavarkar, T. Wisleder, U. K. Mishra, and P. Parikh. 30W/mm GaN HEMTs by Field Plate Optimization. *IEEE Elec. Dev. Lett.*, 3:117, 2005.

[20] T. Palacios. High power AlGaN/GaN HEMTs for Ka-Band Applications. *IEEE Trans. Electron Device Lett.*, 11:781–783, 2005.

[21] R. Vetury, N. Q. Zhang, S. Keller, and U. Mishra. The Impact of Surface States on the DC and RF Characteristics of AlGaN/GaN HFETs. *IEEE Trans. Elec. Dev. Lett.*, 48:560, 2001.

[22] E. T. Yu. *Spontaneous and Piezoelectric Polarization in Nitride Heterostructures*. Taylor and Francis Books, INC, 2002.

[23] J. I. Pankove and T. D. Moustakas. *Gallium nitride (GaN) I*. Academic Press, 1998.

[24] C. Theodoropoulos, T. J. Mountziaris, H. K. Moffat, and J. Han. Design of Gas Inlets for the Growth of Gallium Nitride by Metalorganic Vapor Phase Epitaxy. *J. Cryst. Growth*, 217:65, 2000.

[25] D. H. Reep and S. K. Ghandhi. Electrical Properties of Organometallic Chemical Vapor Deposited GaAs Epitaxial Layers. *J. Electrochem. Soc.*, 131:2697, 1984.

[26] O. Briot, J. P. Alexis, M. Tchounkeu, and R. L. Aulombard. Optimization of the MOVPE Growth of GaN on Sapphire. *Mater. Sci. Eng.*, 43:147, 1997.

[27] M. Yoshida, H. Watanabe, and F. Uesugi. Mass Spectrometric Study of $Ga(CH_3)$ and $Ga(C_2H_5)$ Decomposition Reaction in H_2 and N_2. *J. Electrochem. Soc.*, 132:677, 1995.

[28] A. Thon and T. F. Keuch. High Temperature Adduct Formation of Trimethylgallium and Ammonia. *Appl. Phys. Lett.*, 69:55, 1996.

[29] S. M. Hubbard. *Metalorganic Vapor Phase Epitaxy (MOVPE) Growth and Characterization of III-Nitride Heterostructures for Application in Electronic Devices*. PhD thesis, The University of Michigan, 2005.

[30] P. Javorka. *Fabrication and Characterization of AlGaN/GaN High Electron Mobility Transistors*. PhD thesis, Technischen Hochschule Aachen, 2004.

[31] R. S. Muller and T. I. Kamins. *Device Electronics for Integrated Circuits*. John Wiley & Sons, 2003.

[32] T. H. Gfroerer. *Encyclopedia of Analytical Chemistry*. John Wiely and Sons Ltd, Chichester, 2000.

[33] B. D. Cullity. *Elements of X-ray Diffraction*. Addison-Wesley, 1978.

[34] M. Ohring. *The Materials Science of Thin Film*. Academic Press, 1992.

[35] V. S. Harutyunyan, A. P. Aivazyan, E. R. Weber, Y. Kim, Y. Park, and S. G. Subu-ramanya. High-Resolution X-ray Diffraction Strain-Stress Analysis of GaN/Sapphire Heterostructures. *J. Phys. D, Appl. Phys.*, 34:A37, 2001.

[36] D. Kapolnek. Structural Evolution in Epitaxial Metalorganic Chemical Vapor Deposition Grown GaN Films on Sapphire. *Appl. Phys. Lett.*, 67:1541, 1995.

[37] *Digital Instruments Multimode AFM Handbook*.

[38] J. I. Goldstein. *Scanning Electron Microscopy and X-ray Microanalysis*. New York, Plenum Press, 1981.

[39] *Thomas Swan in-situ Reflectance Monitor Manual*.

[40] K. Uchida, A. Watanabe, F. Yano, M. Kouguchi, T. Tanaka, and S. Minagawa. Nitridation Process of Sapphire Substrate Surface and its Effect on the Growth of GaN. *J. Appl. Phys.*, 79:3487, 1996.

[41] M. H. Kim, C. Son, J. H. Yi, and E. Yoon. Changes in the Growth Mode of Low Temperature GaN Buffer Layers with Nitrogen Plasma Nitridation of Sapphire Substrates. *Appl. Phys. Lett.*, 71:1228, 1997.

[42] C. Y. Hwang. Effects of Substrate Pretreatment on Growth of GaN on (0001) Sapphire by Low Pressure Metal Organic Chemical Vapor Deposition. *J. Vac. Sci. Technol.*, A.13(3):672, 1995.

[43] K. S. Kim, K. Y. Lim, and H. J. Lee. The Effects of Nitridation on Properties of GaN grown on Sapphire Substrate by Metal Organic Chemical Vapour Deposition. *Semicond. Sci. Technol.*, 14:557, 1999.

[44] N. Grandjean, J. Massies, and M. Leroux. Nitridation of Sapphire. Effect on the Optical Properties of GaN Epitaxial Overlayers. *Appl. Phys. Lett.*, 69:2071, 1996.

[45] K. Hiramatsu, S. Itoh, H. Amano, I. Akasaki, N. Kuwano, T. Shiraishi, and K. Oki. Growth Mechanism of GaN Grown on Sapphire with A1N Buffer Layer by MOVPE. *J. Cryst. Growth*, 115:628, 1991.

[46] M. Prutton. *Introduction to Surface Physics*. Clarendon Press, Oxford, 1994.

[47] L. B. Feund and S. Suresh. *Thin Film Materials*. Cambridge, 2006.

[48] L. Sugiura. Effects of Thermal Treatment of Low-Temperature GaN Buffer Layers on the Quality of Subsequent GaN Layers. *J. Appl. Phys.*, 82:4877, 1997.

[49] X. H. Wu, P. Fini, E. J. Tarsa, B. Heying, S. Keller, U. K. Mishra, S. P. DenBaars, and J. S. Speck. Dislocation Generation in GaN Heteroepitaxy. *J. Cryst. Growth*, 189-190:231, 1998.

[50] N. G. Weimann and L. F. Eastmann. IEEE Cornell Conf. Proc. Itchaca, New York. 1997.

[51] M. S. Yi. Effects of Growth Temperature on GaN Nucleation Layers. *Appl. Phys. Lett.*, 75:2187, 1999.

[52] S. Keller, E. J. Tarsa, B. P. Keller, Y. Wu, B. Heying, J. S. Speck, U. K. Mishra, and S. P. DenBaars. Effects of the Trimetalgallium Flow during Nucleation Layer Growth on the Properties of GaN grown on Sapphire. *Jpn. J. Appl. Phys.*, 35:L285, 1996.

[53] K. S. Kim. Effects of Growth Rate of a GaN Buffer Layer on the Properties of GaN on a Sapphire Substrate. *J. Appl. Phys.*, 85:8441, 1999.

[54] T. Hashimoto, M. I. Yur, M. Ishida, Y. Terakoshi, O. Imafuj, T. Sugino, and K. Itoh. Reduction of Threading Dislocations in GaN on Sapphire by Buffer Layer Annealing in Low-Pressure Metalorganic Chemical Vapor Deposition. *Jpn. J. Appl. Phys.*, 38:6605, 1999.

[55] A. E. Wickenden, D. K. Wickenden, and T. J. Kistenmacher. The Effect of Thermal Annealing on GaN Nucleation Layers Deposited on (0001) Sapphire by Metalorganic Chemical Vapor Deposition. *J. Appl. Phys.*, 75:5367, 1994.

[56] C. F. Lin and G. C. Chi. The dependence of the Electrical Characteristics of the GaN Epitaxial Layer on the Thermal Treatment of the GaN Buffer Layer. *Appl. Phys. Lett.*, 68:3758, 1996.

[57] J. Narayan. Characteristics of Nucleation Layer and Epitaxy in GaN/Sapphire Heterostructures. *J. Appl. Phys.*, 99:054313, 2006.

[58] T. Schmidtling. In situ Spectroscopic Ellipsometry Study of GaN Nucleation Layer Growth and Annealing on Sapphire in Metal-Organic Vapor-Phase Epitaxy. *J. Appl. Phys.*, 98:033522, 2005.

[59] Z. Bougrioua, I.Moerman, N. Sharma, R. H. Wallis, J. cheyns, K. Jacobs, E. J. Thrush, L. Considine, R. Beanland, J. L. Farvacque, and C. Humphreys. Material Optimization for AlGaN/GaN HFET Applications. *J. Cryst. Growth*, 230:573, 2001.

[60] S. M. Hubbard, G. Zhao, D. Pavlidis, W. Sutton, and E. Cho. High-resistivity GaN Buffer Templates and Their Optimization for GaN-Based HFETs. *J. Cryst. Growth*, 284:297, 2005.

[61] S. Lee, J. K. Son, H. S. Paek, T. Sakong, W. Lee, K. H. Kim, S. S. Kim, Y. J. Lee, D. Y. Noh, E. Yoon, O. H. Nam, and Y. Park. Growth Pressure Dependence of Residual Strain and Threading Dislocations in the GaN layer. *phys. stat. sol.(c)*, 1:2458, 2004.

[62] S. K. Mathis, A. E. Romanov, L. F. Chen, G. E. Beltz, W. Pomoe, and J. S. Speck. Modeling of Threading Dislocation Reduction in Growing GaN Layers. *Phys. Stat. Sol.(a)*, 179:125, 2000.

[63] S. Hearne, E. Chason, J. Han, J. A. Floro, J. Fiegle, J. Hunter, H. Amano, and I. S. T. Tong. Stress Evolution during Metalorganic Chemical Vapor Deposition of GaN. *Appl. Phys. Lett.*, 74:356, 1999.

[64] H. Heinke, V. Kirchner, S. Einfeldt, and D. Hommel. X-Ray Diffraction Analysis of the Defect Structure in Epitaxial GaN. *Appl. Phys. Lett.*, 77:2145, 2000.

[65] S. Heikman, S. Keller, S. P. DenBaars, and U. K. Mishra. Growth of Fe doped Semi-insulating GaN by Metalorganic Chemical Vapor Deposition. *Appl. Phys. Lett.*, 81:439, 2002.

[66] W. Götz, N. M. Johnson, C. Chen, H. Liu, C. Kuo, and W. Imler. Activation Energies of Si Donors in GaN. *Appl. Phys. Lett.*, 68:3144–3146, 1996.

[67] H. Wang and A. B. Chen. Calculation of Shallow Donor Levels in GaN. *J. Appl. Phys.*, 87:7859–7863, 2000.

[68] X. Xu, H. Liu, C. Shi, Y. Zhao, S. Fung, and C. D. Beling. Residual Donors and Compensation in Metalorganic Chemical Vapor Deposition As-Grown n-GaN. *J. Appl. Phys.*, 90:6130–6134, 2000.

[69] J. Oila, V. Ranki, J. Kivioja, K. Saarinen, P. Hautojaevi, J. Likonen, J. M. Baranowski, K. Pakula, T. Suski, M. Leszczynski, and I. Grzegory. Influence of Dopants and Substrate Material on the Formation of Ga Vacancies in Epitaxial GaN Layers. *Phys. Rev. B.*, 63:045205, 2001.

[70] W. J. Moore, Jr. J. A. Freitas, G. C. B. Braga, R. J. Molnar, S. K. Lee, K. Y. Lee, and I. J. Song. Identification of Si and O Donors in Hydride-Vapor-Phase Epitaxial GaN. *Appl. Phys. Lett.*, 79:2570–2572, 2001.

[71] M. A. di Forte-Poisson, F. Huet, A. Romann, M. Tordjman, D. Lancefield, E. Pereira, J. Di Persio, and B. Pecz. Relationship between Physical Properties and Gas Purification in GaN Grown by Metalorganic Vapor Phase Epitaxy. *J. Cryst. Growth*, 195:314–318, 1998.

[72] V. A. Joshkin, C. A. Parker, S. M. Bedair, J. F. Muth, I. K. Shmagin, R. M. Kolbas, E. L. Piner, and R. J. Molnar. Effect of Growth Temperature on Point Defect Density of Unintentionally doped GaN Grown by Metalorganic Chemical Vapor Deposition and Hydride Vapor Phase Epitaxy. *J. Appl. Phys.*, 86:281, 1999.

[73] S. Keller, Wu. Yi-Feng, G. Parish, Naiqian Ziang, J. J. Xu, B.P. Keller, S. P. DenBaars, and U. K. Mishra. Gallium Nitride based High Power Heterojunction Field Effect Transistors: Process Development and Present Status at UCSB. *IEEE Trans. Electron Device Lett.*, 48:552–559, 2001.

[74] P. B. Klein, S. C. Binari, K. Ikossi, A. E. Wickenden, D. D. Koleske, and R. L. Henry. Current Collapse and the Role of Carbon in AlGaN/GaN High Electron Mobility Transistors Grown by Metalorganic Vapor-Phase Epitaxy. *Appl. Phys. Lett.*, 79:3527, 2001.

[75] J. Neugenbauer and C. G. Van de Walle. Hydrogen in GaN: Novel Aspects of a Common Impurity. *Phys. Rev. Lett.*, 75:4452, 1995.

[76] C. Y. Hwang, M. J. Schurman, W. E. Mayo, Y-C. Yu, R. A. Stall, and T. Salagaj. Effect of Structural Defects and Chemical Impurities on Hall Mobilities in Low Pressure MOCVD Grown GaN. *J. Electron. Mater.*, 26:423, 1997.

[77] D. D. Koleske, A. E. Wickenden, R. L. Henry, and M. E. Twigg. Influence of MOVPE Growth Conditions on Carbon and Silicon Concentrations in GaN. *J. Cryst. Growth*, 242:55, 2002.

[78] J. Lee, M. Lee, S. Hahm, Y. Lee, J. Lee, Y. Bae, and H. Cho. Growth of Semi-insulating GaN Layer by Controlling Size of Nucleation Sites for SAW Devices Application. *MRS Internet J. Nitride Semicond. Res.*, 8:1, 2003.

[79] A. E. Wickenden, D. K. Wickenden, and T. J. Kistenmacher. Resistivity Control in Unintentionally Doped GaN Films Grown by MOCVD. *J. Cryst. Growth*, 260:54, 2004.

[80] T. Yang, K. Uchida, T. Mishima, J. Kasai, and J. Gotoh. Control of Initial Nucleation by Reducing the V/III Ratio during the Early Stages of GaN growth. *phys. stat. sol.(a)*, 180:45, 2000.

[81] K. Kornitzer, K. Thonke T. Ebner, R. Sauer, C. Kirchner, V. Schwegler, M. Kamp, M. Leszczynski, I. Grzegory, and S. Porowski. Photoluminescence and Reflectance Spectroscopy of Excitonic Transitions in High-Quality Homoepitaxial GaN. *Phys. Rev. B.*, 60:1471, 1999.

[82] E. Oh, H. Park, and Y. Park. Influence of Potential Fluctuation on Optical and Electrical Properties in GaN. *Appl. Phys. Lett.*, 72:1848, 1998.

[83] N. V. Edwards, S. D. Woo, M. D. Bresmer, T. W. Weeks Jr., O. H. Nam, H. Liu, R. A. Stall, M. N. Horton, N. R. Perkins, T. F. Kuech, and D. E. Aspnes. Variation of GaN Valence Bands with Biaxial Stress and Quantification of Residual Stress. *Appl. Phys. Lett.*, 70:2001, 1996.

[84] A. Cremades, L. AU Georgens, O. Ambacher, M. Stutzmann, and F. Scholz. Structural and Optical Properties of Si-doped GaN. *Phys. Rev. B.*, 61:1812, 2000.

[85] A. E. Wickenden D. D. Koleske, R. L. Henry, and M. E. Twigg. GaN Decomposition in H_2 and N_2 at MOVPE Temperatures and Pressures. *J. Cryst. Growth*, 223:466, 2001.

[86] M. A. Reshchikov and H. Morkoç. Luminescence Properties of Defects in GaN. *J. Appl. Phys.*, 97:061301, 2005.

[87] J. Neugebauer and C. G. Van de Walle. Gallium Vacancies and the Yellow Luminescence in GaN. *Appl. Phys. Lett.*, 69:503, 1996.

[88] J. Elsner, R. Jones, M. I. Heggie, S. Öberg, and P. R. Briddon. Deep Acceptors Trapped at Threading-Edge Dislocations in GaN. *Phys. Rev. B.*, 58:12571, 1998.

[89] R. Armitage, Q. Yang, H. Feick, and E. R. Weber. Evaluation of CCl_4 and CS_2 as Carbon Doping Sources in MBE Growth of GaN. *J. Cryst. Growth*, 263:132, 2004.

[90] C. H. Seager, A. F. Wright, J. Yu, and W. Götz. Role of Carbon in GaN. *J. Appl. Phys.*, 92:6553, 2002.

[91] H. C. Yang, T. Y. Lin, and Y. F. Chen. Nature of the 2.8eV Photoluminescence Band in Si-doped GaN. *Phys. Rev. B.*, 62:12593, 2000.

[92] M. Tosh, K. Fleischer, and M. R. Phillips. Direct Experimental Evidence for the Role of Oxygen in the Luminescent Properties of GaN. *Phys. Rev. B.*, 59:1575, 1999.

[93] Van de Walle and G. Chris. Interactions of Hydrogen with Native Defects in GaN. *Phys. Rev. B.*, 56:R10020, 1997.

[94] M. Albrecht, H. P. Strunk, J. M. Weyher, Y. Grezgory, S. Porowski, and T. Wosinski. Carrier Recombination at Single Dislocations in GaN Measured by Cathodluminescence in a Transmission Electron Microscope. *J. Cryst. Growth*, 92:2000, 2002.

[95] A. F. Wright. Substitutional and Interstitial Carbon in Wurtzite GaN. *J. Appl. Phys.*, 92:2575, 2002.

[96] U. Birkle, M. Fehrer, V. Kirchner, S. Einfeldt, D. Hommel, S. Strauf, P. Michler, and J. Gutowski. Studies on Carbon as Alternative p-type Dopant for GaN. *MRS Internet J. Nitride Semicond. Res.*, 4S1:G5.6, 1999.

[97] Allen M. West. *Effects of Dislocations on Electronic Properties of III-Nitrides Materials*. PhD thesis, The University of Florida, 2005.

[98] D. J. Rogers, F. Hosseini Teherani, A. Yasan, K. Minder, P. Kung, and M. Razeghi. Electroluminescence at 375nm from a ZnO/GaN:Mg/c-Al_2O_3 Heterojunction Light Emitting Diode. *Appl. Phys. Lett.*, 88:141918, 2006.

[99] L. W. Wong, S. J. Cai, R. Li, K. Wang, H. W. Jiang, and M. Chen. Magnetotransport Study on the Two-Dimensional Electron Gas in AlGaN/GaN Heterostructures. *Appl. Phys. Lett.*, 73:1391, 1998.

[100] R. Dimitrov, L. Wittmer, H. P. Felsl, A. Mitchell, O. Ambacher, and M. Stutzmann. Carrier Confinement in AlGaN/GaN Heterostructures Grown by Plasma Induced Molecular Beam Epitaxy. *phys. stat. sol.(a)*, 168:R7, 1998.

[101] R. Gaska, M. S. Shur, A. D. Bykhovski, A. O. Orlov, and G. L. Snider. Electron Mobility in Modulation-doped AlGaNGaN Heterostructures. *Appl. Phys. Lett.*, 74:287, 1999.

[102] J. P. Ibbetson, P. T. Fini, K. D. Ness, S. P. DenBaars, J. S. Speck, and U. K. Mishra. Polarization Effects, Surface States, and the Source of Electrons in AlGaN/GaN Heterostructure Field Effect Transistors. *Appl. Phys. Lett.*, 77:250, 2000.

[103] I. P. Smorchkova, C. R. Elsass, J. P. Ibbetson, R. Vetury, B. Heying, P. Fini, E. Haus, S. P. DenBaars, J. S. Speck, and U. K. Mishra. Polarization-induced Charge and Electron Mobility in AlGaN/GaN Heterostructures grown by Plasma-Assisted Molecular-Beam Epitaxy. *J. Appl. Phys.*, 86:4520, 1999.

[104] G. Koley and M. G. Spencer. Surface Potential Measurements on GaN and AlGaN/GaN Heterostructures by Scanning Kelvin Probe Microscopy. *J. Appl. Phys.*, 90:337, 2001.

[105] R. Vetury. *Polarization Induced 2DEG in AlGaN/GaN HEMTs : On the origin, DC and Transient Characterization*. PhD thesis, The University of California Santa Babara, 2000.

[106] N. Zhang. *High Voltage GaN HEMTs with Low on-Resistance for Switching Applications*. PhD thesis, The University of California Santa Barbara, 2002.

[107] E. T. Yu, X. Z. Dang, P. M. Asbeck, and S. S. Lau. Spontaneous and Piezoelectric Polarization Effects in III-V Nitride Heterostructures. *J. Vac. Sci. Technol. B.*, 17:1742, 1999.

[108] G. Martin, A. Botchkarev, A. Rockett, and H. Morkoç. Valence-Band Discontinuities of Wurtzite GaN, AlN, and InN Heterojunctions Measured by X-ray Photoemission Spectroscopy. *Appl. Phys. Lett.*, 68:2541, 1996.

[109] M. Kocan. *AlGaN/GaN MBE 2DEG Heterostructures:Interplay between Surface-, Interface and Device-Properties*. PhD thesis, Technischen Hochschule Aachen, 2003.

[110] U. Bhapkar and M. Shur. Monte Carlo Calculation of Velocity-Field Characteristics of Wurtzite GaN. *J. Appl. Phys.*, 82:1649, 1997.

[111] T.P. Chow and R. Tyagi. Wide Bandgap Compound Semiconductors for Superior High-Voltage Unipolar Power Devices. *IEEE Trans. Electron Device Lett.*, 41:1481, 1994.

[112] S. M. Sze. *Physics of Semiconductor Devices*. John Wiely and Sons Ltd, 1981.

[113] S. C. Binari, K. Ikossi, J. A. Roussos, W. Kruppa, D. Park, H. B. Dietrich, D. D. Koleske, A. E. Wickenden, and R. L. Henry. Trapping Effects and Microwave Power Performance in AlGaN/GaN HEMTs. *IEEE Trans. Electron Device Lett.*, 48:465, 2001.

[114] B. M. Green, K. K. Chu, E. M. Chumbes, J. A. Smart, J. R. Shealy, and L. F. Eastman. The Effect of Surface Passivation on the Microwave Characteristics of Undoped AlGaN/GaN HEMTs. *IEEE Elec. Dev. Lett.*, 21:268, 2000.

[115] S. C. Choi, J. H. Kim, J. Y. Choi, and G. M. Yang. Solid Incorporation of AlGaN and Influence of Growth Interruption on GaN/AlGaN Quantum Well Structures Grown by MOCVD. *phys. stat. sol.(a)*, 176:263, 1996.

[116] P. F. Fewster. *X-ray Scattering from Semiconductors*. Imperial College Press, London, 2003.

[117] R. Gaska, J. W. Yang, A. Osinsky, A. D. Bykhovski, and M. S. Shur. Piezoeffect and Gate Current in AlGaN/GaN High Electron Mobility Transistors. *Appl. Phys. Lett.*, 71:3673, 1997.

[118] Y. Yue, Y. Hao, J. Zhang, J. N, , W. Mao, Q. Feng, and L. Liu. AlGaN/GaN MOS-HEMT with HfO_2 Dielectric and Al_2O_3 Interfacial Passivation Layer Grown by Atomic Layer Deposition. *IEEE Elec. Dev. Lett.*, 29:838, 2008.

[119] M. Higashiwaki, T. Mimura, and T. Matshui. AlN/GaN Insulated-Gate HFETs Using Cat-CVD SiN. *IEEE Electron Device Lett.*, 27:719, 2006.

[120] E. Alekseev, A. Eisenbach, and D. Pavlidis. Low Interface State Density AlN/GaN MISFETs. *Electron. Lett.*, 35:2145, 1999.

[121] Yu. Cao and D. Jena. High-Mobility Window for Two-Dimensional Electron Gases at Ultrathin AlN/GaN Heterojunctions. *Appl. Phys. Lett.*, 90:182112, 2007.

[122] B. Heying, I. P. Smorchkova, R. Coffie, V. Gambin, Y. C. Chen, W. Sutten, T. Lam, M. S. Kahr, K. S. Sikorski, and M. Wojtowicz. In situ SiN Passivation of AlGaN/GaN HEMTs by Molecular Beam Epitaxy. *Electron. Lett.*, 43:779, 2007.

[123] J. Derluyn, S. Boeykens, K. Cheng, R. Vandersmissen, S. Degroote, M. R. Leys, M. Germain, and G. Borghs. Improvement of AlGaN/GaN High Electron Mobility Transistor Structures by in situ Deposition of a Si_3N_4 Surface Layer. *J. Appl. Phys.*, 98:054501–5, 2005.

[124] B. Heying, X. H. Wu, Y. Li S. Keller, D. Kapolneak, B. P. Keller, S. P. DenBaars, and J. S. Speck. Role of Threading Dislocation Structure on the X-ray Diffraction Peak widths in Epitaxial GaN films. *Appl. Phys. Lett.*, 68:643, 1996.

[125] H. Haegawa, T. Inagaki, S. Ootomo, and T. Hashizume. Mechanisms of Current Collapse and Gate Leakage Currents in AlGaN/GaN Heterostructure Field Effect Transistors. *J. Vac. Sci. Technol. B.*, 21:1844, 2003.

[126] S. Seo, E. Cho, and D. Pavlidis. Improvement of AlN/GaN MISFETs DC and RF characteristics with in-situ Si_3N_4. *Electron. Lett.*, 2008.

[127] N. Okamoto, K. Hoshino, N. Hara, M. Takikawa, and Y. Arakawa. MOCVD Grown InGaN Channel HEMT Structures with Electron Mobility of Over 1000cm^2/Vs. *J. Cryst. Growth*, 272:278, 2004.

[128] A. Koukitu, M. Takahashi, T. Taki, and H. Seki. Thermodynamic Analysis of $In_xGa_{1-x}N$ Alloy Composition Grown by Metalorganic Vapor Phase Epitaxy. *Jpn. J. Appl. Phys.*, 35:L673, 1996.

[129] E. L. Piner, M. K. Behbehani, N. A. El-Masry, F. G. McIntosh, J. C. Roberts, K. S. Boutros, and S. M. Bedair. Effect of Hydrogen on the Indium Incorporation in InGaN Epitaxial Films. *Appl. Phys. Lett.*, 70:461, 1997.

[130] S. Keller, B. P. Keller, D. Kapolnek, A. C. Abare, H. Masui, L. A. Coldren, U. K. Mishra, and S. P. Den Baars. Growth and Characterization of Bulk InGaN Films and Quantum Wells. *Appl. Phys. Lett.*, 68:3147, 1998.

[131] T. Takeuchi, C. Wetzel, S. Yamaguchi, H. Sakai, H. Amano, I. Akasaki, Y. Kaneko, S. Nakagawa, Y. Yamaoka, and N. Yamada. Determination of Piezoelectric Fields in Strained GaInN Quantum Wells Using the Quantum-Confined Stark Effect. *Appl. Phys. Lett.*, 73:1691, 1998.

[132] S. Ghosh, P. Waltereit, O. Brandt, H. T. Grahn, and K. H. Ploog. Electronic Band Structure of Wurtzite GaN under Biaxial Strain in the M Plane Investigated with Photoreflectance Spectroscopy. *Phys. Rev. B.*, 65:075202, 2002.

[133] F. Sacconi, A. Di Carlo, and P. Lugli. Modeling of GaN-Based Resonant Tunneling Diodes: Influence of Polarization Fields. *phys. stat. sol.(a)*, 190:295, 2002.

[134] M. Saglam, K. Mutamba, A. Megej, C. Sydlo, H. L. Hartnagel, and I. Daumiller. Influence of Polarization Charges in $Al_{0.4}Ga_{0.6}N$/GaN Barrier Varactors. *Appl. Phys. Lett.*, 82:227, 2003.

[135] P. Waltereit, O. Brandt, M. Ramsteiner, A. Trampert, H.T. Grahn, J. Menniger, M. Reiche, R. Uecker, P. Reiche, and K.H. Ploog. Growth of M-Plane GaN(11-00): A Way to Evade Electrical Polarization in Nitrides. *phys. stat. sol.(a)*, 180:133, 2000.

[136] A. Chakraborty, B. A. Haskell, S. Keller, J. S. Speck, S. P. DenBaars, S. Nakamura, and U. K. Mishra. Nonpolar InGaN/GaN Emitters on Reduced-Defect Lateral Epitaxially Overgrown a-Plane GaN with Drive-Current-Independent Electroluminescence Emission Peak. *Appl. Phys. Lett.*, 85:5143, 2004.

[137] A. Chakraborty, B. A. Haskell, S. Keller, J. S. Speck, S. P. DenBaars, S. Nakamura, and U. K. Mishra. Demonstration of Nonpolar m-Plane InGaN/GaN Light-Emitting Diodes on Free-Standing m-Plane GaN Substrates. *Jpn. J. Appl. Phys.*, 44:L173, 2004.

[138] N. F. Gardner, J. C. Kim, J. J. Wierer, Y. C. Shen, and M. R. Krames. Polarization Anisotropy in the Electroluminescence of m-Plane InGaNGaN Multiple-Quantum-Well Light-Emitting Diodes. *Appl. Phys. Lett.*, 86:111101, 2005.

[139] D. Li, H. Chen, H. B. Yu, Y. J. Han, X. H. Zheng, Q. Huang, and J. M. Zhou. Effects of Carrier Gas on the Stress of a-Plane GaN Films Grown on r-Plane Sapphire Substrates by Metalorganic Chemical Vapor Deposition. *J. Cryst. Growth*, 263:76, 2004.

[140] M. Araki, N. Mochimizo, K. Hoshino, and K. Tadatomo. Direct Growth of a-Plane GaN on r-Plane Sapphire Substrate by Metalorganic Vapor Phase Epitaxy. *Jpn. J. Appl. Phys.*, 46:555, 2007.

[141] S. Lee, H.S. Paek, J.K. Son, T. Sakong, O.H. Nam, and Y. Park. Characteristics of Si and Mg doping in a-Plane GaN Grown on r-Plane Sapphire. *J. Cryst. Growth*, 307:358, 2007.

[142] J. L. Hollander, M. J. Kappers, C. McAleese, and C. J. Humphreys. Improvements in a-Plane GaN Crystal Quality by a Two-Step Growth Process. *Appl. Phys. Lett.*, 92:101104, 2008.

[143] J. Huang, T. Tang, C. Huang, and C.C. Yang. High Quality a-Plane GaN grown with Flow-rate Modulation Epitaxy on r-Plane Sapphire Substrate. *J. Cryst. Growth*, 310:2712, 2008.

[144] X. Ni, Y. Fu, Y. T. Moon, N. Biyikli, and H. Morkoç. Optimization of a-Plane GaN Growth by MOCVD on r-Plane Sapphire. *J. Cryst. Growth*, 290:166, 2006.

[145] T. S. Ko, T. C. Wang, R. C. Gao, H.G. Chen, G.S. Huang, T. C. Lu, H. C. Kuo, and S. C. Wang. Study on Optimal Growth Conditions of a-Plane GaN Grown on r-Plane Sapphire by Metal-Organic Chemical Vapor Deposition. *J. Cryst. Growth*, 300:308, 2007.

[146] T. Aschenbrenner, K. Goepel, C. Kruse, S. Figge, and D. Hommel. Direct MOVPE and MBE Growth of a-Plane GaN on r-Plane Sapphire. *phys. stat. sol.(c)*, 5:1836, 2008.

[147] F. Wu, M. D. Craven, S. H. Lim, and J. S. Speck. Polarity Determination of a-Plane GaN on r-Plane Sapphire and its Effects on Lateral Overgrowth and Heteroepitaxy. *J. Appl. Phys.*, 94:942, 2003.

[148] K. Uchida, K. Nishida, M. Kondo, and H. Munekata. Characterization of Double-Buffer Layers and Its Application for the Metalorganic Vapor Phase Epitaxial Growth of GaN. *Jpn. J. Appl. Phys.*, 37:3882, 1998.

[149] H. M. Wang, J. P. Zhang, C. Q. Chen, Q. Fareed, J. W. Yang, and M. A. Khan. AlN/AlGaN Superlattices as Dislocation Filter for Low-Threading-Dislocation Thick AlGaN Layers on Sapphire. *Appl. Phys. Lett.*, 81:604, 2005.

[150] R. Armitage, H. Hirayama, and Y. Kondo. Reduced Structural Defect Densities in a-plane GaN Layers on r-Plane Sapphire through Buffer Layer Engineering. *phys. stat. sol.(c)*, 4:2524, 2007.

[151] M. AsifKhan, Q. Chen, C. J. Sun, J. W. Yang, M. S. Shur, and H. Park. Enhancement and Depletion Mode GaN/AlGaN Heterostructure Field Effect Transistors. *Appl. Phys. Lett.*, 68:514, 1996.

[152] A. Endo, Y. Yamashita, K. Ikeda, M. Higashiwaki, K. Ikosaka, T. Matsui, S. Hiyamizu, and T. Mimura. Non-Recessed-Gate Enhancement-Mode AlGaN/GaN High Electron Mobility Transistors with High RF Performance. *Jpn. J. Appl. Phys.*, 43:2255, 2004.

[153] V. Kumar, A. Kuliev, T. Tanaka, Y. Otoki, and I. Adesida. High Transconductance Enhancement-mode AlGaN/GaN HEMT on SiC Substrate. *Electron. Lett.*, 39:1758, 2003.

[154] W. B. Lanford, T. Tanaka, Y. Otoki, and I. Adesida. Recessed Gate Enhancement-Mode GaN HEMT with High Threshold Voltage. *Electron. Lett.*, 41:449, 2005.

[155] X. A. Cao, H. Cho, S. J. Pearton, G. T. Dang, A. P. Zhang, F. Ren, R. J. Shul, L. Zhang, R. Hickman, and J. M. Van Hove. Depth and Thermal Stability of Dry Etch Damage in GaN Schottky Diodes. *Appl. Phys. Lett.*, 75:232, 1999.

[156] M. Kuroda, H. Ishida, T. Ueda, and T. Tanaka. Nonpolar (11-20) Plane AlGaN/GaN Heterojunction Field Effect Transistors on (1-102) Plane Sapphire. *J. Appl. Phys.*, 102:093703, 2007.

[157] S. J. Pearton, B. S. Kang, S. Kim, F. Ren, B. P. Gila, C. R. Abernathy, J. Lin, and S. N. G. Chu. GaN-Based Diodes and Transistors for Chemical, Gas, Biological and Pressure Sensing. *J. Phys. Condens. Matter.*, 16:R961, 2004.

[158] G. Y. Zhao, W. Sutton, D. Pavlidis, E. L. Pinner, J. Schwank, and S. M. Hubbard. A Novel Pt-AlGaN/GaN Heterostructure Schottky Diode Gas Sensor on Si. *IEICE Trans. Electron.*, E86-C (10):2027, 2003.

[159] E. Cho, D. Pavlidis, G. Y. Zhao, S. M. Hubbard, and J. Schwank. Improvement of CO Sensitivity in GaN-based Gas Sensors. *IEICE Trans. Electron.*, E89-C:1047, 2006.

[160] F. Yun, S. Schevtchenko, Y. Moon, H. Morkoç, T. J. Fawcett, and J. T. Wolan. GaN Resistive Hydrogen Gas Sensors. *Appl. Phys. Lett.*, 87:073507, 2005.

[161] V. Tilak, K. Matocha, and P. Sandvik. Pt/GaN Schottky Diodes for Harsh Environment NO Sensing Applications. *phys. stat. sol.(c)*, 2:2555, 2005.

[162] J. Song and W. Lu. AlGaN/GaN Heterostructure Field Effect Transistors for High Temperature Hydrogen Sensing with Enhanced Sensitivity. In *IEEE IEDM Wachington, DC, 7-10 December 2007 pp835-838*, 2007.

[163] B. S. Kang, H. Wang, L. Tien, F. Ren, B. P. Gila, D. P. Norton, C. R. Abernathy, J. Lin, and S. Pearton. Wide Bandgap Semiconductor Nanorod and Thin Film Gas Sensors. *Sensors.*, 6:643–666, 2006.

[164] S. Capone, A. Forleo, L. Francioso, R. Rella, P. Siciliano, J. Spadavecchia, D. S. Presicce, and A. M. Taurino. Solid State Gas Sensors: State of the Art and Future Activities. *Journal of Optoelectronics and Advanced Materials*, 5:1335, 2003.

[165] J. Fogelberg, M. Eriksson, H. Dannetun, and L. G. Petersson. Kinetic Modeling of Hydrogen Adsorption/Absorption in Thin Films on Hydrogen-Sensitive Field-Effect Devices: Observation of Large Hydrogen-Induced Dipoles at the Pd-SiO_2 Interface. *J. Appl. Phys.*, 78 (7):988, 1995.

[166] L. G. Ekedah, M. Eriksson, and I. Lundström. Hydrogen Sensing Mechanism of Metal-Insulator Interfaces. *Acc. Chem. Res.*, 31(5):249, 1998.

[167] J. Schalwig, G. Müller, U. Karrer, M. Eickhoff, O. Ambacher, L. Görgens, and G. Dollinger. Hydrogen Response Mechanism of Pt-GaN Schottky diodes. *Appl. Phys. Lett.*, 80:1222, 2002.

[168] O. Weidemann, M. Hermann, G. Steinhoff, H. Wingbrant, A. Lloyd Spetz, M. Stutzmann, and M. Eickhoff. Influence of Surface Oxides on Hydrogen-Sensitive Pd:GaN Schottky Diodes. *Appl. Phys. Lett.*, 83:773, 2003.

[169] G. A. Somorjai. *Introduction to Surface Chemistry and Catalysis*. Wiely Inter Science, 1993.

[170] I. Lundström and L. Petersson. Chemical Sensors with Catalytic Metal. *J. Vac. Sci. Technol. A.*, 14:1539–1545, 1996.

[171] A. Spetz, M. Armgarth, and I. Lundström. Hydrogen and Ammonia Response of Metal-Silicon Dioxide-Silicon Structures with Thin Platinum Gates. *J. Appl. Phys.*, 64(3):1274, 1988.

[172] V. Tilak, M. Ali, V. Cimalla, V. Manivannan, P. Sandvik, J. Fedison, O. Ambacher, and D. Merfeld. Influence of Metal Thickness to Sensitivity of Pt/GaN Schottky Diodes for Gas Sensing Application. In *Proc. of. Mater. Res. Soc., Boston, USA*, 2004.

[173] I. Lundström, A. Spetz, F. Winquist, U. Ackelid, and H. Sundgren. Catalytic Metals and Field-Effect Devices-a Useful Combination. *Sens. Actuators*, B1:15, 1990.

[174] A. E. Hudeish, A. A. Aziz, Z. Hassan, C. K. Tan, H. Abu Hassan, and K. Ibrahim. Investigations of Surface Roughness of GaN Based Gas Sensors Using Atomic Force Microscope. In *2005 Asian Conference on Sensors and the International Conference on new Techniques in Pharmaceutical and Biomedical Research*, 2005.

[175] M. Strassner, J. C. Esnault, L. Leroy, J. L. Leclercq, M. Carrigues, and I. Sagnes. Fabrication of Ultrathin and Highly Flexible InP-based Membranes for Microopto-electromechanical Systems at 1.55μm. *IEEE Photon. Technol. Lett.*, 17:804, 2005.

[176] P. Bondavalli, T. Benyattou, M. Garrigues, Jean Louis Leclercq, S. Jourba, C. Pautet, and X. Hugon. Opto-mechanical Design of Tunable InP-based Fabry-Pérot filter for Gas Analysis. *Sens. Actuators*, 94:136, 2005.

[177] M. Mello, B. Poti. A de Risi, A. Passaseo, M. Lomascolo, and M. De Vittorio. GaN Optical System for CO and NO Gas Detection in the Exhaust Manifold of Combustion Engines. *J. Opt. A : Pure Appl. Opt.*, 8:S545, 2006.

[178] P. Kotidis, W. Atia, M. Kuznetsov, S. Fawcett, D. Nislick, R. Crocombe, and D. C. Flanders. Optical, Tunable Filter-Based Micro-Instrumentation for Industrial Applications. Technical report, AXSUN Technologies.

[179] A. J. Steckl and I. Chyr. Focused Ion Beam Micromilling of GaN and Related Substrate Materials (Sapphire, SiC and Si). *J. Vac. Sci. Technol. B.*, 17:362, 1999.

[180] Y. Gao. *Highly Selective PEC Etching of GaN Device Structures*. PhD thesis, The University of California Santa Babara, 2004.

[181] R. Sharma, E. D. Haberer, C. Meier. E. L. Hu, and S. Nakamura. Vertically Oriented GaN-based Air-Gap Distributed Bragg Reflector Structure Fabricated Using Band-Gap-Selective Photoelectrochemical Etching. *Appl. Phys. Lett.*, 87:051107, 2005.

[182] T. E. Sale. *Vertical Cavity Surface Emitting Laser*. Research Studies Press, 1995.

[183] C. Lin. *Surface Micromachined Tunable Optoelectronic Devices*. PhD thesis, Standford University, 2002.

[184] H. A. Macled. *Thin Film Optical Filters*. McGraw-Hill New York, 2nd edition, 1989.

[185] A. Bhattacharyya, S. Iyer, E. Iliopoulos, A. V. Sampath, J. Cabalu, T. D. Moustakas, and I. Friel. High Reflectivity and Crack-free AlGaN/AlN Ultraviolet Distributed Bragg Reflectors. *J. Vac. Sci. Technol.*, B 20:1229, 2002.

[186] D. Brunner, H. Angerer, E. Bustarret, F. Freudenberg, R. Höpler, R. Dimitrov, O. Ambacher, and M. Stutzmann. Optical Constants of Epitaxial AlGaN Films and Their Temperature Dependence. *J. Appl. Phys.*, 82:5090, 1997.

[187] M. Shubert, T. E. Tiwald, and C. M. Herzinger. Infrared Dielectric Anisotropy and Phonon Modes of Sapphire. *Phys. Rev. B.*, 61:8187, 2000.

[188] H. M. Ng, T. D. Moustakas, and S. N. G. Chu. High Reflectivity and Broad Bandwidth AlN/GaN Distributed Bragg Reflectors Grown by Molecular-Beam Epitaxy. *Appl. Phys. Lett.*, 76:2818, 2000.

[189] J. Dorsaz, J. F. Carlin, S. Gradecak, and M. Ilegems. Progress in AlInN-GaN Bragg Reflectors: Application to a Microcavity Light Emitting Diode. *J. Appl. Phys.*, 97:84505, 2005.

[190] A. Polian, M. Grimsditch, and I. Grzegory. Elastic Constants of Gallium Nitride. *J. Appl. Phys.*, 79:3343, 1996.

[191] E. Bellet-Amalric, C. Adelmann, E. Sarigiannidou, J. L. Rouvière, G. Feuillet, E. Monroy, and B. Daudin. Plastic Strain Relaxation of Nitride Heterostructures. *J. Appl. Phys.*, 95:1127, 2004.

[192] E. Cho, D. Pavlidis, and E. Sillero. GaN/Air Gap Based Micro Opto Electro Mechanical (MOEM) Fabry-Pérot Filters. *phys. stat. sol. (c)*, 7:1047, 2007.

[193] J. R. Mileham, S. J. Peatron, C. R. Abernathy, J. D. Mackenzie, R. J. Shul, and S. P. Kikoyne. Wet Chemical Etching of AlN. *Appl. Phys. Lett.*, 67:1119, 1995.

[194] M. D. Craven. *a-plane Oriented Gallium Nitride Thin Films : Heteroepitaxy, Quantum wells, and Lateral Overgrowth*. PhD thesis, The University of California Santa Babara, 2003.

[195] B. Imer. *Improved Quality Non-polar III-Nitride Heteroepitaxial Films and Devices*. PhD thesis, The University of California Santa Babara, 2006.

[196] R. D. Vispute, V. Talyansky, S. Choopun, R. P. Sharma, T. Venkatesan, M. He, X. Tang, J. B. Halpern, M. G. Spencer, Y. X. Li, L. G. Salamanca-Riba, A. A. Iliadis, and K. A. Jones. Heteroepitaxy of ZnO on GaN and its Implications for Fabrication of Hybrid Optoelectronic Devices. *Appl. Phys. Lett.*, 73:348, 1998.

[197] L. S. McCarthy, I. P. Smorchkova, H. Xing, P. Kozodoy, P. Fini, J. Limb, D. L. Pulfrey, J. S. Speck, M. J. W. Rodwell, S. P. DenBaars, and U. K. Mishra. GaN HBT: Toward an RF Device. *IEEE Trans. Eleclectron Device Lett.*, 48:543, 2001.

[198] P. Gibart. Organic Vapour Phase Epitaxy of GaN and Lateral Overgrowth. *Rep. Prog. Phys.*, 67:667, 2004.

[199] C. K. Inoki, T. S. Kuan, C. D. Lee, A. Sagar, R. M. Feenstra, D. D. Koleske, D. J. Diaz, P. W. Bohn, and I. Adesida. Growth of GaN on Porous SiC and GaN Substrates. *J. Electron. Mater.*, 32:855, 2003.

[200] H. Ishikawa, K. Shimanaka, F. Tokura, Y. Hayashi, Y. Hara, and M. Nakanishi. MOCVD growth of GaN on Porous Silicon Substrates. *J. Cryst. Growth*, 2008.

[201] M. Shur, B. Gelmont, and M. Asif Kahn. Electron Mobility in Two-Dimensional Electron Gas in AlGaN/GaN Heterostructures and in Bulk GaN. *J. Electr. Mat*, 25:777, 1996.

[202] D. Jena, A. C. Gossard, and U. K. Mishra. Dislocation Scattering in a Two-Dimensional Electron Gas. *Appl. Phys. Lett.*, 76:1707, 2000.

[203] R. Oberhuber, G. Zandler, and P. Vogl. Mobility of Two-Dimensional Electrons in AlGaN/GaN Modulation-doped Field-Effect Transistors. *Appl. Phys. Lett.*, 78:818, 1998.